UNIVERSITAT POLITÉCNICA DE CATALUNYA

PROGRAMA DE DOCTORADO EN INGENIERÍA AMBIENTAL

Departament de Projectes d'Enginyeria

Turbulent Structure in Environmental Flows:

Effects of Stratification and Rotation

ANNA MAGDALENA MATULKA

Barcelona, December 2009

Director: Prof. José Manuel Redondo Apraíz

High enstrophy eddies

Eat small enstrophy eddies

But sometimes

Little eddies crowd up

And make up

A really high enstrophy eddies

Till the size of the planet

Or the Hurricane or the Tornado

Or in internal or inertial waves

Saves from destruction the little 3D

Richardson's and Kraichnan's Cascades

Dedicated to my parents Teresa and Zdzislaw

And to my brother Marek

INDEX

i

ACKNOWLEDGEMENTS

CHAPTER 1. Introduction

1.1. Introduction 1

1.2. Description of the Thesis 9

CHAPTER 2. Theory of Turbulence

2.1. Turbulent Flows 10

2.1.1. Kolmogorov 1941 Theory 11

2.1.2. Kolmogorov 1962 Theory 17

2.1.3. The Taylor Microscale 21

2.2. Dimensionless Numbers and Boussinesq approximation 24

2.2.1. Richardson Number and Gradient Richardson Number 26

2.2.2. Reynolds Number 29

2.2.3. Froude Number 32

2.2.4. Rossby Number and Ekman Number 34

CHAPTER 3. Stratified Fluids

3.1. Basic concepts 35

3.2. Internal Waves 39

3.3. The Entrainment E 44

3.4. Previous related results and comparative analysis 48

CHAPTER 4. Rotating Fluids and Vorticity

4.1. Flow in Rotating Fluids 53

4.1.1. Introduction 53

4.1.2. Centrifugal and Coriolis forces 55

4.1.3. Intrinsic stability and inertial waves 57

4.2. Internal and Inertial waves 59

4.3. Vorticity in 2D flows 61

4.3.1. Basic Equations in environmental flows 62

4.3.2. Basic instabilities compare to Average Turbulent Continuity Reynolds Equations (RANS) 66

4.3.3. Turbulent Energy and Transport Equations 72

4.4. Turbulence Vorticity in 3D flows 75

CHAPTER 5. Fractal and Multifractal Analysis in Environmental Turbulence

5.1. Dimensional Analysis and Scales 81

5.2. Fractal analysis and turbulent cascades 82

5.3. Ima – Calc – The Box counting Method 86

5.4. Theory of Multi-Fractal measurements 90

5.5. Symmetries of the Navier-Stokes equation 93

CHAPTER 6. Methodology and Laboratory experimental setup

6.1. Experimental Methodology 98

6.1.1. Image processing for fluid dynamics – DigiFlow/DigImage 103

6.2. Mixing Efficiency 106

6.3. The Laboratory non-rotating stratified Experiments 108

CHAPTER 7. Experimental Results

7.1. Introduction 112
7.2. Results without stratification (low Richardson number) 119
7.2.1. Interfacial flows 119
7.3. Results with significant (strong and medium) stratification 121
7.3.1. The evolution of the positive (anticlockwise) and negative (clockwise) vorticity in time 134
7.3.2. The evolution of vorticity and enstrophy in one line for different experiments 139
7.3.3. The evolution of integral scale in time 148
7.3.4. The histograms of local vorticity measured by PIV 153
7.4. Decay and merging of vortices with significant stratification 159
7.5. Decay and merging without significant stratification (with low Richardson number) 178
7.6. Mixing Efficiency – Entrainment 184
7.5. General Parameterization of Stratified non-rotating flows 187

CHAPTER 8. Satellite observations of vortices in the Ocean

8.1. Use of SAR images in ocean studies 193
8.2. Introduction 194
8.3. Image analysis and descriptions 196
8.4. Statistical analysis of vortices 198
8.5. Results on vortex multifractal measurements of the ocean 204

8.6. Other geometrical Topological Fractal measurements 208
8.7. Summary and conclusions 213

CHAPTER 9. Discussion

9.1. General Discussion 215
9.2. New aspect of the research 218
9.3. Discussion on energy decay in stratified flows 220
9.4. Topology of the Vortex Interaction 227
9.5. Models of Vortex evolution 229

CHAPTER 10. Conclusions

10.1. General Conclusions 237
10.2. Conclusions on the vortex structure and evolution 244
10.3. Conclusions on the Kinetic Energy decay 247
10.4. Conclusions on the Number of Vortices and their interactions 250
10.5. Conclusions on Mixing in Stratified Flows 252
10.6. Conclusions on Satellite observation of the environment 253
10.7. Further Work 255

References 256

Appendix 1. Basic Review of Remote Sensing 275

A1.1. The digital processing of the satellite images 275

A1.1.1. *Satellite type* 276

A1.1.2. *Sensor type* 279

A1.1.2.1. *Microwaves sensors* 280

A1.1.2.2. *Visible and Infrared sensors* 281

A1.1.3. *Band type* 283

A1.1.3.1. *Techniques in the visible and near infrared* 284

A1.1.3.2. *Infrared* 286

A1.2. References 289

Appendix 2. Descriptive plots of a High Richardson number experiment 293

Appendix 3. Examples of DigiFlow analysis 300

Appendix 4. The Local structure of turbulence for large Reynolds Numbers (Based in Kolmogorov 1941 and Monin & Yaglom 1975) 309

A4.1. Dissipation of energy in locally isotropic turbulence 315

Appendix 5. Horizontal non-homogeneous flow: coastal mixing 319

Appendix 6. Molecular mixing and mixing efficiency 324

A6.1**.** Definition of Mixing Efficiency 327

A6.2. Scales of Turbulent Mixing 341

Acknowledgements

I especially would like to thank my director Professor Jose Manuel Redondo Apraiz for his support and his help with the PhD thesis and with the laboratory experiments done at the Applied Physics Department at UPC and at Trondheim SINTEF Laboratory. I would like to thank Filip Ciesinski from Warsaw University of Technology for help with the initial experiments reported in this PhD and Dr. Alejandro Carrillo and Dr. Alexei Platonov for there assistance with the analysis of the Trondheim experiments and for the SAR images from the ESA.

Thanks to Dr. Stuart Dalziel (DAMPT, Cambridge) and Dr. Joan Grau and for the help offered with DigImage, DigiFlow and Ima-Calc programs; also to Dr. Roberto Castilla, Dr. Daniel Cano (AEMET, Madrid), Dr. Claude Cambon (Ecole Centrale, Lyon) and Dr. Luca Sorriso-Valvo (Calabria, Italy) for helping me to understand my experiments thanks to their numerical simulations of vorticity and velocity.

Many thanks to Emil Sekula, Cristian Peco, Raffaele Marino (Calabria, Italy) and all students and staff from the Fluids Mechanics and Applied Physic departments for the knowledge that they shared with me and all my friends from Universidad Politécnica de Catalunya as Tanya, Mariella, Max, Israel and others.

I would like to thank Professor Jose María Baldasano Recio for his support during the development of this PhD thesis. Also, I would like to thank my colleagues from the Laboratory of Environmental Modelling at the University of Catalonia (Doctorat en Enginyeria Medi Ambiental) for the time that we shared.

Thanks also to Professor Jan Wojciechowski for his support during all my education in Warsaw, during my Master project and the beginning of this thesis.

Last but not least, special thanks to Miguel for his support during the elaboration of this thesis.

CHAPTER 1

Introduction

1.1. Introduction

Turbulence is one of the most ubiquitous phenomena in the discipline of fluid mechanics and of far reaching influence in the atmosphere and ocean likewise. Regarding the latter the interplay between the ocean stratification and the diffusive turbulent motions is often crucial in determining the structure of the environment. Again, the response of the ocean to large-scale wind and thermal disturbances and the development of ocean currents is dependent on the transfer of matter, momentum and energy by irregular smaller scale motions of one kind or another.

Not all of the random motions found in the ocean, however, can be properly described as turbulence. The characteristic properties of turbulent motions are that they possess a random distribution of vorticity in which there is no unique relation between the frequency and wave number of the Fourier modes; that they are diffusive and dissipative. A distinction is drawn between turbulence in a stably stratified fluid on the one hand and random field of internal gravity waves on the other. This differentiation is useful, not only conceptually but also observationally since the mechanisms of energy transfer (in both physical and Fourier space) are essentially different.

The effect of the atmosphere on the ocean is also important. When the wind blows across the surface of the water, a tangential surface stress is developed both directly from the interfacial stress, and indirectly by the rate of momentum loss from the surface waves by such processes as wave breaking. Below the surface, a turbulent mixed layer develops. In case the underlying region is statically stable or neutral, the interface between turbulent and non-turbulent fluid is very sharp, and remains so as the turbulence erodes the lower fluid by entrainment. The temperature and salinity in the mixed layer are virtually uniform as a result of turbulent diffusion. Also, the continued erosion results in an increasing contrast between the properties of the water in the mixed layer and the layer immediately below. In this way, a thermocline develops. If, on the other hand, there is substantial surface cooling, there may be a region below the mixed layer in which the density decreases with depth and which is statically unstable. Convective motions can develop and, particularly in polar waters, can extend to considerable depths, forming the important buoyancy driven ocean-wide circulation.

Examples of turbulence in the Atmosphere, Ocean and real life:

- Smoke rising from a cigarette. For the first few centimetres, the flow remains laminar, and then becomes unstable and turbulent as the rising hot air accelerates upwards. Similarly, the dispersion of pollutants in the atmosphere is governed by turbulent processes.
- Flow over a golf ball. If the golf ball had a smooth surface, the boundary layer flow over the front of the sphere would be laminar at typical conditions. However, the boundary layer would separate early, as the pressure gradient switched from favourable (pressure decreasing in the flow direction) to unfavourable (pressure increasing in the flow direction), creating a large region of low pressure behind the ball that creates high form drag.
- The mixing of warm and cold air in the atmosphere by wind, which causes clear-air turbulence experienced during airplane flight, as well as poor astronomical seeing (the blurring of images seen through the atmosphere.)
- Most of the terrestrial atmospheric circulation.
- The oceanic and atmospheric mixed layers and intense oceanic currents.
- The flow conditions in many industrial equipment (such as pipes, ducts, precipitators, gas scrubbers, dynamic scraped surface heat exchangers, etc.) and machines (for instance, internal combustion engines and gas turbines).
- The external flow over all kind of vehicles such as cars, airplanes, ships and submarines.
- The motions of matter in stellar atmospheres.
- A jet exhausting from a nozzle into a quiescent fluid. As the flow emerges into this external fluid, shear layers originating at the lips of the nozzle are created. These layers separate the fast moving jet from the external fluid, and at a certain critical Reynolds number they become unstable and break down to turbulence.

Figure 1.1: Effect of turbulent flow in the world that was observed from Mount St. Hellens on May 18, 1980. It is a power full example of turbulent dispersion of small particles as the pumice and ash erupting. (Matulka 2003).

The motion of particles in a turbulent flow is an issue of crucial importance. In technological processes one often wants to mix fluids in a short time, with the combustion chamber of the internal combustion engine being a familiar example. In addition, as we become increasingly concerned about environmental problems, it is critical that we understand how turbulence in our atmosphere or the oceans transports dust and pollutants. Another example would be the understanding of cloud formation which is very important for climate modeling. We can see a powerful example of turbulent dispersion of small particles at figure 1.1. Here we can observe the pumice and ash erupting from St Hellens Mount on 18th May of 1980.

Natural and man-made distributions of tensioactive substance concentrations in the sea surface features exhibit self-similarity at all radar reflectivity levels when

illuminated by SAR. This allows the investigation of the traces produced by vortices and other features in the ocean surface. Most mixing processes in the ocean depend both on advection and diffusion characteristics with energetic inputs at many different scales, the topology of tracers in the ocean surface probable depends on the local characteristics of the turbulent cascades. For examples, in the detected vortices in the ocean, local shear will transform slicks in the surface to align and follow the local flow so the resulting pattern is spiral as show by Munk 2001. The first spiral eddies were seen on the Apollo Mission 30 years ago. They have since been recorded on SAR missions and in the infrared. The spirals are globally distributed, 10-25 km in size. On SAR images the streaks are always dark, indicating a reduced scattering cross-section and for this spirals are visible.

Despite the importance and abundance of turbulent flows, the community of scientists as Reynolds (1883) or Richardson (1922, 1929) has encountered many difficulties in developing satisfactory scientific descriptions of them. One of the most important steps in our understanding came in 1941 when Kolmogorov developed his theory (K41) about how the energy that is put into large turbulent motions cascades down to very small scales where it is converted into heat by viscosity.

Over the past 50 years measurements have allowed to test various aspects of K41 theory. For example, by putting small heated wires in the flow, researchers have measured many properties of the turbulent velocity in a fixed reference frame. These measurements have found that Kolmogorov's theory is useful in predicting the essential phenomena, although it fails to account for some of the subtleties, such as intermittency.

But there are other aspects of Kolmogorov's theory that have proven to be much more difficult to test experimentally. When his ideas are applied to the properties of turbulence as seen by a small particle moving with the fluid (for example a snowflake or dust particle), they yield predictions about the statistics of the particle accelerations and velocities that are needed in calculating turbulent transport such as the dispersal of pollutants. These predictions have not been tested and there are constants in the theory that have never been accurately measured.

Turbulent mixing, and especially turbulent mixing in a density stratified fluid, and in rotating fluids is a considerable problem in geophysical fluid mechanics, as well as in environmental and industrial studies. Of particular interest is the mixing in the vicinity of relatively sharp density interfaces in the oceans, lakes, reservoirs, and in the

atmosphere with regard to many applications of environmental fluid mechanics, both at large and at small scales.

Laboratory experiments on turbulent mixing in a stratified rotating fluid are essential for the development of computer models of geophysical phenomena, for, if better predictions are to be made, the distributions of potential and kinetic energy have to be correctly assessed for each process under study. Oceanic and atmospheric flows due to this high Reynolds number may be considered as turbulent motions under the constraints of geometry, stratification and rotation. At large scales these flows tend to be along isopycnal surfaces due to the combined effects of the very low aspect ratio of the flows (the motion is mostly confined to thin layers of fluid) and the existence of stable density stratification. The effect of the Earth's rotation is to reduce the vertical shear in these almost planar flows. The combined effects of these constraints are to produce approximately two-dimensional turbulent flows termed as geophysical turbulence.

In a strictly two-dimensional flow with weak dissipation, energy input at a given scale is transferred to larger scales, because these constraints stop vortex lines being stretched or twisted. Physically, this upscale energy transfer occurs by merging of vortices and leads to the production of coherent structures in the flow that contain the energy the appearance of order from chaos, Flor et al. (1996). This scenario is an attractive model for geophysical flows which are known to contain very energetic vortices, mesoscale oceanic eddies and atmospheric highs and lows such as those depicted in figure 1.2 that show the dominant length scale at the Rossby deformation Radius. The upscale transfer of energy is inhibited at the Rossby deformation scale by baroclinic instability at larger scales, which accounts for the dominant observed size of geophysical vortices.

Recent advances in laboratory techniques Dalziel and Redondo et al. (2007) and Fraunie et al. (2008) allow nowadays investigating in detail the velocity of the turbulent flow. This is also true for remote sensing observation at the environment (Gade & Redondo 1999). So we will use laboratory experiments and field observation to investigate environmental turbulence.

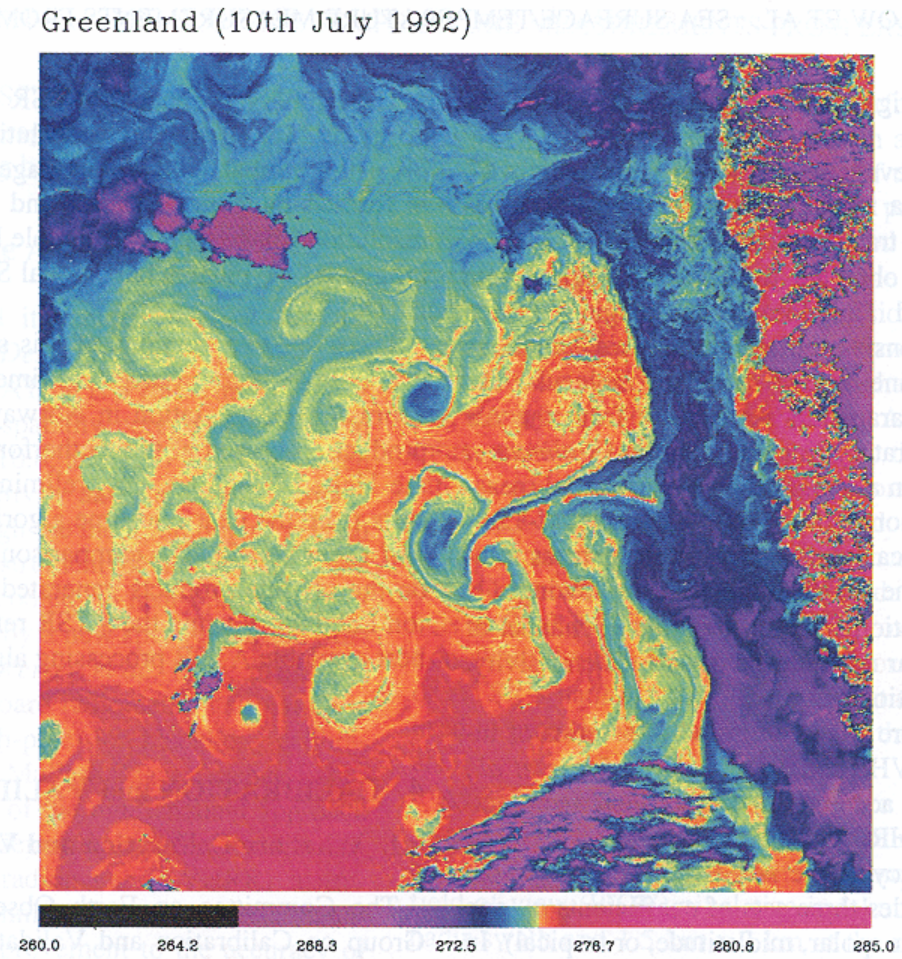

Figure 1.2: Structure of Ocean vortices. The picture is taken over Greenland on 10th July, 1992. (Matulka 2003).

Previous work on annulus flow, pioneered by Hide et al. (1958) and Fultz (1959) where the flow is driven in a rotating annulus by differential heating of the lateral walls of the annulus, or by internal heating of the fluid has long been used to simulate planetary circulation. A horizontal temperature gradient is established which drives a zonal flow via the 'thermal wind' balance. For certain values of the parameters this flow is unstable to baroclinic modes that feed on the energy in the temperature field. At finite amplitude the instabilities can lead to large amplitude waves and vortex structures. Many features have been identified with structures and phenomena observed in the annulus experiments, and understanding of atmospheric and ocean dynamics has become significantly advanced. The experiments have provided new insights about the dynamics and revealed a wide range of nonlinear behaviour. Experiments performed by Boubnov et al. (1994) and Linden et al. (1996) showed the effect of mixing from the edge on a rotating stratified system. When the instability is caused by differential

heating or by buoyancy there seems to be a range of very different dynamic regimes, including as in many experiments: The zonally-symmetric circulation (ZC), anticyclonic gap-scale vortices (AGV), azimuthal wave/vacillation regimes (WR), and geostrophic turbulence regimes (GT). This complexity of the interactions between the different forcing is even more evident when the turbulent cascades are simultaneously affected by rotation and stable stratification.

Turbulence or quasi-geostrophic turbulence has been the focus of numerous mathematics and physics papers during the past fifty years. In a landmark paper Onsager (1949) studied an ensemble of point vortices and argued that they cluster into a coherent large-scale vortex in the negative temperature regime corresponding to sufficiently large kinetic energies. The quantitative aspects of the point vortex model and subsequently predictions were compared with direct numerical simulations of the end state of freely decaying turbulence. Another approach by Kraichnan (1975), called the energy-enstrophy model, was based on spectral truncation of the underlying fluid dynamics equations, leading to the two dimensional turbulent energy-enstrophy cascades as an extension of Kolmogorov's K41 and K62 theories.

Many experimental and theoretical studies have been devoted to the understanding of non-homogeneous turbulent dynamics. Activity in this area intensified when the basic self-similar theory was extended to two-dimensional or quasi 2D turbulent flows such as those appearing in the environment, that seem to control ocean mixing in coastal areas, the synoptic atmospheric flows and many other layered and/or rotating flows. The statistical description and the dynamics of these geophysical flows depend strongly on the distribution of long lived organized (coherent) structures. These flows show a complex topology, but their basic structure may be subdivided and quantified in terms of strongly elliptical domains (high vorticity regions), strong hyperbolic domains (deformation cells with high energy condensations) and the background turbulent field of moderate elliptic and hyperbolic characteristics. It is of fundamental importance to investigate the different influence of these topological diverse regions on the eddy diffusivity. The scalar concentration of pollutants (tracers) within the flow can also be analyzed in the same fashion, as the advection takes place in a self-similar, fractal way, so that tracers shed relevant information on the velocity and vorticity dynamics.

Large-scale atmospheric models rely on small scale parameterisation of vertical mixing, and the ability to identify the local processes, which determine mixing, is very important in order to increase the accuracy of forecasting. To highlight the role of small

scale stratification we just have to look at atmospheric inversions, which often reduce drastically the dilution of contaminants, so that in order to reduce local atmospheric pollution, we have to take into account the changing mixing efficiency of the process with regard to industrial emissions. In many cases the thermal stratification affects the dilution rates, even if the pollutants themselves are not denser than air.

Sharp density interfaces are commonly found in the ocean and transport through them is very important in determining the residence times of deep water. The dynamics of the thermocline is controlled by the mixing through many different processes. Also, benthic boundary layer results from mixing near the bottom of the sea. These processes merge near coastal regions, where tides often produce fronts. Sometimes exchanges between two different masses of water are locally controlled by interfacial mixing. The same is true in estuaries and river basins where fresh river water is mixed with all seawater.

1.2. Description of the Thesis

The present work is divided in 10 chapters and 6 appendices. After this introductory chapter, in chapter 2, some basic theory of turbulence that will be used throughout this thesis is presented and discussed, such as the general concepts about scaling, the basic theories of Richardson and Kolomgorov (K41 and K62) and the basic role of external body forces that lead to the many relevant dimensionless numbers for stratified and rotating flows. The aim of this chapter is to give a quick review of turbulence, of the standard accepted theories, on the state of art of the subject and to understand basic concepts and new criticisms relevant to non-homogeneous flows.

In chapters 3 and 4 is shown the understanding of stratified and rotating fluids, theirs basic equations, internal and inertial waves. Also turbulence vorticity in 2D and 3D flows is presented for further analysis in this part.

In chapter 5 basic concepts about fractal and multifractal analysis are presented together with some applications on environmental turbulence, including scaling and dimensional analysis, different scales and turbulent cascades.

Chapter 6 presents detailed experimental configuration with experimental methodology setup, image processing system – DigiFlow and complete process of the laboratory experiments in stratified and rotating fluids.

All experiments results are given in chapter 7. There are different sub chapters for analysis with and without stratification, rotating and no – stratified flows, or rotating and stratified fluids. There are made some analysis of decay and merging of vortices and general parameterization of presented results.

In chapter 8 we concentrate on observations of vortices in the ocean by mean of satellites, where a new technique has proved very powerful because of the irrelevance of cloud. Covering and solar position is the use of SAR images. We are able to perform a statistical analysis and a description of vortices.

The discussion and conclusions are described and presented in chapters 9 and 10, as future proposal for upcoming investigations.

There are six appendices dealing with specific issues, both experimental and theoretical but marginal to the main issue at this thesis.

CHAPTER 2

Theory of Turbulence

2.1. Turbulent Flows

In fluid dynamics, turbulence or turbulent flow is a fluid regime characterized by chaotic, stochastic property changes. This includes low momentum diffusion, high momentum convection, and rapid variation of pressure and velocity in space and time. Flow that is not turbulent is called laminar flow. The (dimensionless) Reynolds number characterizes whether flow conditions lead to laminar or turbulent flow; e.g. for pipe flow, a Reynolds number above about 4000 (A Reynolds number between 2100 and 4000 is known as transitional flow) will be turbulent. At very low speeds the flow is laminar, i.e., the flow is smooth (though it may involve vortices on a large scale). As the speed increases, at some point the transition is made to turbulent flow. In turbulent flow, unsteady vortices appear on many scales and interact with each other. Drag due to boundary layer skin friction increases. The structure and location of boundary layer separation often changes, sometimes resulting in a reduction of overall drag. Because laminar-turbulent transition is governed by Reynolds number, the same transition occurs if the size of the object is gradually increased, or the viscosity of the fluid is decreased, or if the density of the fluid is increased.

Turbulence causes the formation of eddies of many different length scales. Most of the kinetic energy of the turbulent motion is contained in the large scale structures. The energy "cascades" from these large scale structures to smaller scale structures change by an inertial and essentially inviscid mechanism. This process continues, creating smaller and smaller structures which produces a hierarchy of eddies. Eventually this process creates structures that are small enough that molecular diffusion becomes important and viscous dissipation of energy finally takes place. The scale at which this happens is the Kolmogorov length scale.

It is really difficult to define turbulence and Tennekes et al. (1972) proposed a list of some basic characteristics of turbulent flows like:

- *Irregularity or randomness* – The turbulent flow is unpredictable, irregular, and chaotic and these force us to use statistical methods.
- *Diffusivity* – Due to the macroscopic mixing of fluid particles and that turbulence generates a large diffusivity, the turbulent flow is characterized by diffusion of momentum, heat, salinity, contaminants and mass transfer. If there

doesn't exist an increase of diffusivity, the flow isn't turbulent, although it may be irregular or chaotic.

- *High Reynolds number* – Laminar flows become turbulent when increase the Reynolds number.
- *Three-Dimensional vorticity fluctuations* – Turbulence is rotational and three-dimensional, and is characterized by big high levels of fluctuating vorticity.
- *Dissipation* – Turbulent flows are always dissipative. To keep the flow turbulent, it needs a continuous supply of energy because viscosity acts in efficient way over small whirls. Richardson et al. (1922) described that the energy come from big whirls to small whirls, and from small whirls to lesser whirls, and so on to viscosity and that expound the cascade theory of energy proposed by Kolmogorov in 1941. This energy cascade we can observe in figure 2.1.

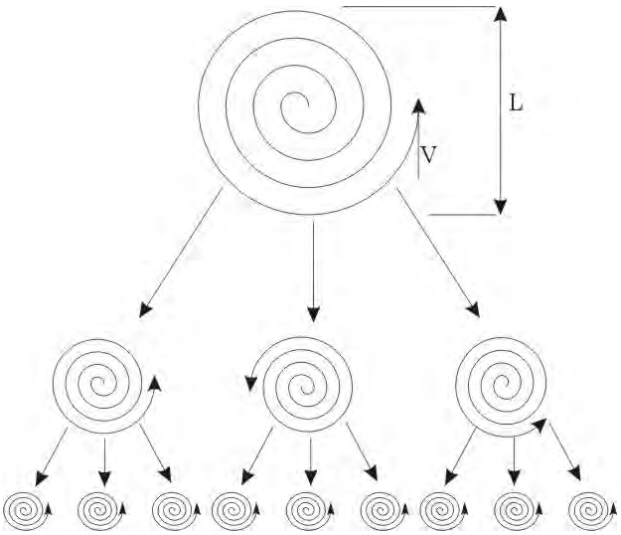

Figure 2.1: Cascade of energy by Kolmogorov. The energy comes from big to small whirls and without any source of energy, turbulence decay quickly.

The inverse energy cascade (shown at figure 2.2.) in two-dimensional Navier-Stokes turbulence over which kinetic energy is transferred from small to large length scales (as can be approximated in the atmosphere or ocean) is one of the most important phenomena in fluid dynamics. In agreement with Kraichnan (1967) the energy and enstrophy conservation make that energy actually flow to larger scales and this is a basic difference between 2D and 3D turbulence, where energy flows toward small scales in a direct cascade. Almost forty years ago Kraichnan predicted an inverse cascade of energy in two-dimensional fluid turbulence and proposed an inertial range

with a $k^{-(5/3)}$ power-law energy spectrum, just as in three-dimensional turbulence, but with a flux of energy from small to large scales rather than the reverse.

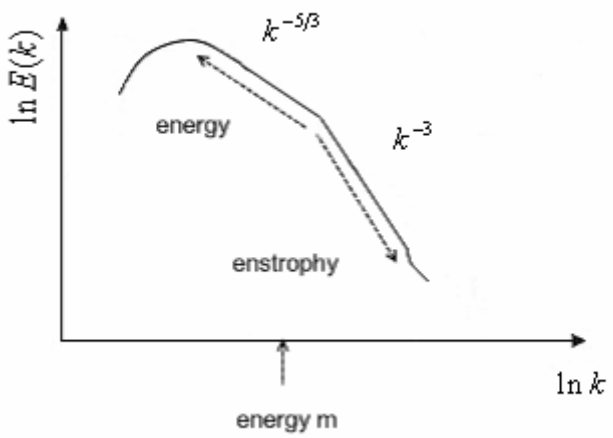

Figure 2.2: The inverse energy cascade characterized by $k^{-(5/3)}$ in the power spectrum.

Turbulent diffusion is usually described by a turbulent diffusion coefficient. This turbulent diffusion coefficient is defined in a phenomenological sense, by analogy with the molecular diffusivities, but it does not have a true physical meaning, being dependent on the flow conditions, and not a property of the fluid itself. In addition, the turbulent diffusivity concept assumes a constitutive relation between a turbulent flux and the gradient of a mean variable similar to the relation between flux and gradient that exists for molecular transport. In the best case, this assumption is only an approximation. Nevertheless, the turbulent diffusivity is the simplest approach for the quantitative analysis of turbulent flows, and many models have been postulated to calculate it. k^{-3}

2.1.1. Kolmogorov 1941 Theory

Richardson's notion of turbulence was that a turbulent flow is composed by "eddies" of different sizes as shown conceptually in figure 2.3. The sizes define a characteristic length scale for eddies, which are also characterized by velocity scales and time scales (turnover time) dependent on the length scale. The large eddies are unstable in 3D flows and eventually break up originating smaller eddies, and the kinetic energy of the initial large eddy is divided into the smaller eddies that stemmed from them. These smaller eddies undergo the same process, giving rise to even smaller eddies which inherit the energy of their predecessor eddy, and so on. In this way, the energy is passed down from the large scales of the motion to smaller scales until reaching a sufficiently small length scale so that the viscosity of the fluid can effectively dissipate kinetic energy into internal energy.

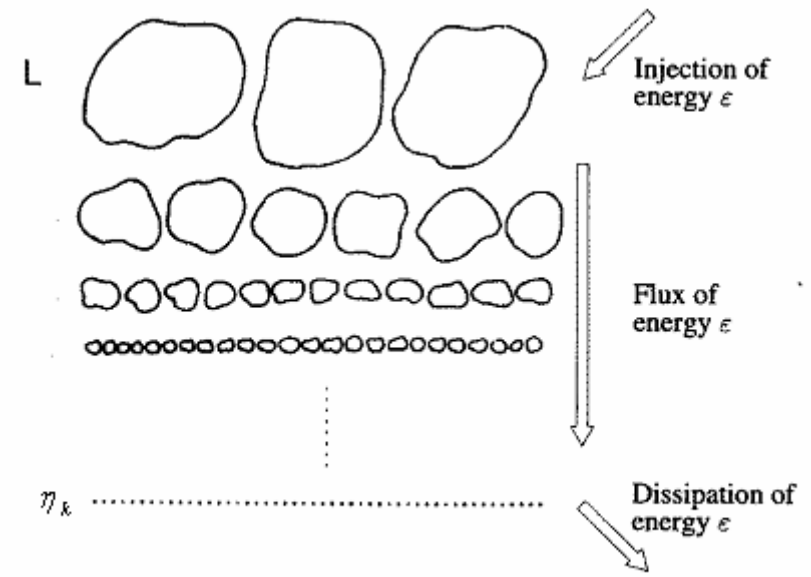

Figure 2.3: The Richardson idea of energy cascade, where the energy is transferred to small scales in steps. At eddies of size *L* energy is injected, then energy is transmitted to smaller and smaller eddies, until it is dissipated into heat at smallest eddies of size η_k. (Mahjoub et al. 2000).

In his original theory of 1941, Kolmogorov postulated that for very high Reynolds number, the small scale turbulent motions are statistically isotropic (i.e. no preferential spatial direction could be discerned). In general, the large scales of a flow are not isotropic, since they are determined by the particular geometrical features of the

boundaries (the size characterizing the large scales will be denoted as *L*). Kolmogorov's idea was that in the Richardson's energy cascade this geometrical and directional information is lost, while the scale is reduced, so that the statistics of the small scales have universal character: they are the same for all turbulent flows when the Reynolds number is sufficiently high.

Thus, Kolmogorov introduced a second hypothesis: for very high Reynolds numbers the statistics of small scales are universally and uniquely determined by the viscosity (v) and the rate of energy dissipation (ε). With only these two parameters, the unique length that can be formed by dimensional analysis is the equation 2.1 today known as the Kolmogorov length scale:

$$\eta_k = \left(\frac{\nu^3}{\varepsilon} \right)^{1/4} \tag{2.1}$$

A turbulent flow is characterized by a hierarchy of scales through which the energy cascade takes place. Dissipation of kinetic energy takes place at scales of the order of Kolmogorov length η_k, while the input of energy into the cascade comes from the decay of the large scales, of order *L* (as we can observe in figure 2.3). These two scales at the extremes of the cascade can differ by several orders of magnitude at high Reynolds numbers. In between there is a range of scales (each one with its own characteristic length *l*) formed at the expense of the energy of the large ones. These scales are very large compared with the Kolmogorov length, but still very small compared with the large scale of the flow (i.e. $\eta_k \langle\langle l \langle\langle L$). Since eddies in this range are much larger than the dissipative eddies that exist at Kolmogorov scales, kinetic energy is essentially not dissipated in this range, but merely transferred to smaller scales until viscous effects become important as the order of the Kolmogorov scale is approached. Within this range inertial effects are still much larger than viscous effects, and it is possible to assume that viscosity does not play a role in their internal dynamics (for this reason this range is called "inertial range”). In figure 2.4 we can observe the energy spectrum in function of Kolmogorov scale.

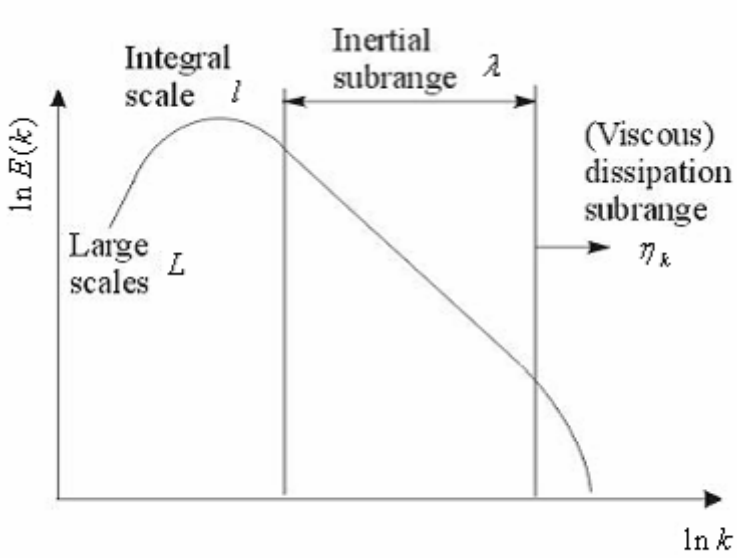

Figure 2.4: The energy spectrum in function of Kolmogorov scale. The minimum corresponds to Kolmogorov scale and the maximum is related with Reynolds number.

Hence, a third hypothesis of Kolmogorov was that at very high Reynolds number the statistics of scales in the range $\eta_k \langle\langle l \langle\langle L$ are universally $\ln k$ and λ uniquely determined by the scale *l* and the rate of energy dissipation ε.

The way kinetic energy is distributed over the multiplicity of scales is a fundamental characterization of a turbulent flow. For homogeneous turbulence this is usually studied by means of the energy spectrum function $E(k)$, where *k* is the modulus of the wave vector corresponding to some harmonics in a Fourier representation of the flow velocity field *u(x)*:

$$u(x) = \iiint_{R^3} \hat{u}(k) e^{ik \cdot x} \, d^3k \tag{2.2}$$

where $\hat{u}(k)$ is the Fourier transform of the velocity field. Thus, $E(k)dk$ represents the contribution to the kinetic energy from all the Fourier modes with $k \langle |k| \langle k + dk$, and therefore:

$$Total\ kinetic\ energy = \int_0^\infty E(k)dk \tag{2.3}$$

The wavenumber k corresponding to length scale l is $k = 2\pi/l$. Therefore, by dimensional analysis, the only possible form for the energy spectrum function according with third Kolmogorov´s hypothesis is (see in appendix 4 a detailed description of Kolmogorov theory; he only used the structure function analysis):

$$E(k) = C\,\varepsilon^{2/3}\,k^{-5/3} \tag{2.4}$$

where C is a constant whose value can depend on the dimensionality and $E(k)$ is defined so that the mean kinetic energy per unit mass. Kolmogorov's K41 theory implicitly assumes that the turbulence is statistically self-similar at different scales. This essentially means that the statistics are scale-invariant in the inertial range. A usual way of studying turbulent velocity fields is by means of the so called structure functions, namely the moments of order p of the velocity increments δu_l:

$$S_q(l) = \left\langle \left(u\left(\vec{x}+\vec{l}\right) - u\left(\vec{x}\right)\right)^q \right\rangle = \left\langle \left(\delta u_l\right)^q \right\rangle \tag{2.5}$$

where u is the velocity component parallel to the separation l, in the case of longitudinal structure function. These powers of the velocity differences are very useful to determine the type of the flow and refer to the amplitude of the typical turbulent fluctuations of the velocity field. The statistical scale-invariance implies that the scaling of velocity increments should occur with a unique scaling exponent ξ_q of the structure function of order q, as:

$$\xi_q = \frac{q}{3} \tag{2.6}$$

Mahjoub et al. (2000), following Benzi et al. (1992) and Frisch et al. (1995) described that the scaling exponents of structure function of order q are scale-independent and universal quantities for the Kolmogorov K41 theory. From this fact, it follows that the structure functions in turbulence should scale as (see appendix 4):

$$\left\langle \left(\delta u_l\right)^q \right\rangle = C_q\,\varepsilon^{q/3}\,l^{q/3} = C_q\left(\langle\varepsilon\rangle l\right)^{q/3} \tag{2.7}$$

where the brackets denote the statistical average, and the C_q are universal constants. There is considerable evidence that turbulent flows deviate from this behaviour. The scaling exponents deviate from the q/3 value predicted by the theory, becoming a non-linear function of the order *p* of the structure function. For low orders the discrepancy with the Kolmogorov q/3 value is very small, which explain the success of Kolmogorov theory with regard to low order statistical moments. In particular, it can be shown that when the energy spectrum follows a power law

$$E(k) \propto k^{-p}, \tag{2.8}$$

with $1 < p < 3$ and $p - 1 = \frac{q}{3}$, the second order structure function has also a power law, with the form

$$\left\langle [\delta u(l)]^2 \right\rangle \propto l^{p-1}. \tag{2.9}$$

Since the experimental values obtained for the second order structure function only deviate slightly from the 2/3 value predicted by Kolmogorov theory the value for *p* is very near to 5/3. Thus the "Kolmogorov -5/3 spectrum" is generally observed in turbulence. However, for high order structure functions the difference with the Kolmogorov scaling is significant, and the breakdown of the statistical self-similarity is clear. This behaviour and the lack of universality of the C_q constants are related to the phenomenon of intermittency in turbulence. Kolmogorov microscales are the smallest scales in turbulent flow, defined by Table 2.1 where ε the average rate of energy dissipation per unit mass is, and ν is the kinetic viscosity of the fluid.

Table 2.1: Kolmogorov microscales in turbulent flow.

Kolmogorov length scale	$\eta_k = \left(\frac{\nu^3}{\varepsilon} \right)^{1/4}$
Kolmogorov time scale	$\tau_{\eta_k} = \left(\frac{\nu}{\varepsilon} \right)^{1/2}$
Kolmogorov velocity scale	$u_{\eta_k} = (\nu \varepsilon)^{1/4}$

In fully developed turbulence at scale *l*, Kolmogorov's local similarity theory K41 assumed that all statistically averaged quantities depend only on the mean dissipation rate ε and *l*, where *l* is located in the inertial sub-range.

2.1.2. Kolmogorov 1962 Theory

Kolmogorov (1941) suggested local similarity theory for locally homogeneous, isotropic and stationary turbulence, using velocity structure function. In 1962 Kolmogorov and Obuhkov introduced very important modification to K41 theory and found experimental and numerical results that deviate from the $q/3$ law. This was so-called intermittency correction to K41 in the framework of Kolmogorov's K62 theory. Mahjoub and Redondo et al. (1998) studied the variation of the absolute scaling exponents ξ_q as a function of distance from the source of turbulence, and they found that these exponents depend on the location of the flow and that deviations from the K41 scaling were related to the intermittency.

Kolmogorov (1962) introduced a hypothesis relating the moments of the PDF of velocity increments δu_l to the moments of ε_l, taking into consideration only intermittency. The velocity differences δu_l depend on the length scale *l* and the scaling exponents of the *q*-order is given by

$$\left\langle \delta u_l^{\,q} \right\rangle \sim \left\langle \varepsilon_l^{\,q/3} \right\rangle l^{q/3} \sim l^{\xi_q} \tag{2.10}$$

Assuming that:

$$\left\langle \varepsilon_l^{\,q/3} \right\rangle \sim l^{\tau_{q/3}} \tag{2.11}$$

the scaling exponents are defined as:

$$\xi_q = q/3 + \tau_{q/3} \tag{2.12}$$

where ε_l is the locally defined energy dissipation per unit mass over a volume of size *l*, $\tau_{q/3}$ is the scaling exponent of $\left\langle \varepsilon_l^{\,q/3} \right\rangle$. This relation assures the basic result $\xi_3 = 1$ for locally homogenous, isotropic turbulence and stationary energy cascade and the correction $\tau_{q/3}$ for $q \neq 3$ in equation 2.12 caused by intermittency. In the original K62 theory, the scale-dependency of the energy transfer rate ε_l is proposed as stemming

from a multiplicative cascade process, with local random transfer, leading to a lognormal distribution.

2.1.3. The Taylor Microscale

The Taylor microscale λ_T is a length scale which may be defined even if Kolmgorov (K41 and K62) hypothesis are not met. It is used to characterize a turbulent flow and may be considered the largest length scale at which fluid viscosity affects the dynamics of turbulent eddies in the flow. This microscale is characterized by being in the middle of a typical Kolmogorov spectrum of velocity fluctuations, normally near to the dissipative scale. There exist length scales, referred to inertial range larger than the Taylor microscale, such as the integral scale l which is not strongly affected by viscosity. Below the Taylor microscale, in the dissipation range, there are shorter length scale displacements and the turbulent motion is there subject to strong viscous forces and most of the kinetic energy is dissipated into heat.

Thus we have

$$l \rangle \lambda_T \rangle \eta_k \tag{2.13}$$

Turbulence is dissipative and can't exist without any supply of energy. When turbulence is stable (i.e. stationary) the turbulent energy production at any scale has to equal to the viscosity dissipation at small scales.

$$P = \varepsilon \tag{2.14}$$

where P is production of turbulent energy by shear, hydrostatic pressure or any another mechanism and ε the viscosity dissipation of energy. If turbulence is isotropic at small scale (local isotropy), in according to the equation energy, that

$$P = -\overline{u_i u_j S_{ij}} \tag{2.15}$$

$$\varepsilon = 2\nu \overline{s_{ij} s_{ij}} \tag{2.16}$$

when

$$S_{ij} = \frac{1}{2}\left(\frac{\partial U_i}{\partial x_j} + \frac{\partial U_j}{\partial x_i} \right) \tag{2.17}$$

is a mean velocity of deformation or mean shear and

$$s_{ij} = \frac{1}{2}\left(\frac{\partial u_i}{\partial x_j} + \frac{\partial u_j}{\partial x_i} \right) \tag{2.18}$$

is a deformation velocity or shear produced by velocity fluctuation in the flow (bars indicate temporary and spatial means). Interpreting dimensionally these terms $s_{ij} = u/l\, S$ and $\overline{u_i u_j} \approx u^2$, and being *u* and *l* mean shear scales that produce turbulence (it can't be confuse with flow mean scales *L* and *V*) nevertheless scales that affect S_{ij} should be much smaller. Equalizing and substituting the production and dissipation of turbulent energy and substituting characteristics scales

$$ul\, S_{ij} S_{ij} = 2c\nu\, \overline{s_{ij} s_{ij}} \tag{2.19}$$

being c an order one constant. As the Reynolds number ul/ν is generally high:

$$S_{ij} S_{ij} << \overline{s_{ij} s_{ij}} \tag{2.20}$$

That it is common to define a length scale λ_T such than as $S_{ij} = u/\lambda_T$ and we have

$$\frac{u^2}{\lambda_T^2} >> \frac{u^2}{l^2} \Rightarrow \lambda_T << l \tag{2.21}$$

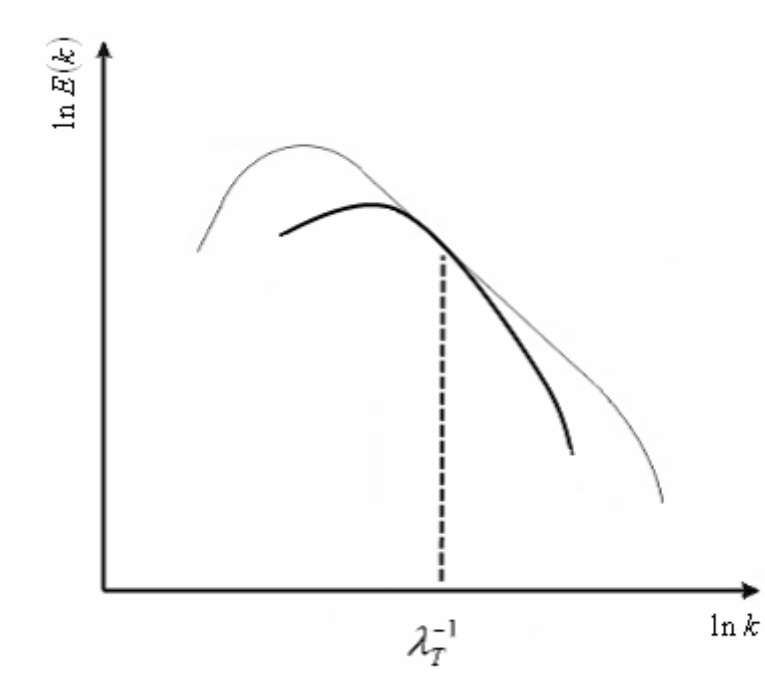

Figure 2.5: The energy spectrum in function of Taylor microscale.

This convenient scale is called the Taylor microscale and is associated to the curvature of the spatial correlations of velocity, and is connected with Kolmogorov theory for the turbulence spectrum, but may be defined independently at the existence of an inertial subrange, as indicated in figure 2.5, which may be compared with figure 2.4.

2.2. Dimensionless Numbers and Boussinesq approximation (Buoyancy)

In order to compare results between different experiments, dimensionless parameters must be used. In this Thesis many dimensionless numbers exist, and some of them are described below. The Richardson number that describes effects of stratification in stable situation; the Reynolds number that controls if the flow is turbulent or laminar; the Froude number which is used to describe the effect of gravity and described hydraulic flow patterns over an obstacle; and the Rossby and Ekman numbers used to describe the effects of rotation.

In fluid dynamics, the Boussinesq approximation is used in the field of buoyancy-driven flow (also known as natural convection or in stratification). It states that density differences are sufficiently small to be neglected, except where they appear in terms multiplied by *g*, the acceleration due to gravity. The essence of the Boussinesq approximation is that the difference in inertia is negligible but gravity is sufficiently strong to make the specific weight appreciably different between the two fluids. Sound waves are impossible when the Boussinesq approximation is used since sound waves move via inertial density variations.

Boussinesq flows are common in nature (such as atmospheric fronts, oceanic circulation, katabatic winds[1]), industry (dense gas dispersion, fume cupboard ventilation), and the built environment (natural ventilation, central heating). The approximation is extremely accurate for many of such flows, and makes the mathematics and physics simpler. The approximation's advantage arises because when considering a flow of, say, warm and cold water of density ρ_1 and ρ_2 one needs only to consider a single average density $\overline{\rho}$: the difference $\Delta\rho = \rho_1 - \rho_2$ is negligible compared with $\overline{\rho}$. Dimensional analysis shows that, under these circumstances, the only sensible way that acceleration due to gravity *g* should enter into the equations of motions as the reduce gravity *g'* where

$$g' = g\frac{\rho_1 - \rho_2}{\overline{\rho}} \tag{2.22}$$

[1] Is the technical name for a drainage wind, a wind that carries high density air from a higher elevation down a slope under the force of gravity. Such winds are sometimes also called *fall winds.*

An equivalent (save for a factor at 2) method is to use the Atwood number

$$A=\frac{\rho_1-\rho_2}{\rho_1+\rho_2} \tag{2.23}$$

and then, as $\bar{\rho}=\frac{\rho_1+\rho_2}{2}$ we have also $g'=2Ag$.

The role of buoyancy depends strongly on whether the stratification is stable or unstable. In the first case it is a sink of energy and in the second case it is a source of energy, but the contribution to the vorticity or enstrophy is not that clear due to the presence of the baroclinic term and the non-linear effects of internal waves.

2.2.1. Richardson Number and Gradient Richardson Number

The basic non-dimensional parameters that describe effects of stratification in a sheared stable situation is the Richardson number, *Ri*, described as a gradient or as a flux that relates buoyancy flux to turbulent production by shear or the other causes. The Richardson number is often used to indicate the stability of the shear flows (Turner 1973). It is the main variable that controls the mixing at a density interface (Redondo 1990).

The characteristic properties of turbulent motions are that they possess a random distribution of vorticity in which there is no unique relation between the frequency and wave number of the Fourier modes; this means that turbulent related mixing is diffusive and dissipative. A distinction is drawn between turbulence in a stably stratified fluid on the one hand and random field of internal gravity waves on the other. This differentiation is useful, not only conceptually but also observationally since the mechanisms of energy transfer (in both physical and Fourier space) are essentially different. The stratification may be sufficiently important so that the Richardson number is large enough to prevent the onset of dynamical instability everywhere.

The likelihood of Kelvin-Helmholtz instability can be evaluated by means of the Richardson's number (*Ri*), the ratio of the static stability (N^2) to the square of the wind shear (dU/dz):

$$Ri = \frac{N^2}{\left(dU/dz\right)^2} \tag{2.24}$$

where

$$N^2 = \left(g/\rho\right)\cdot\left(d\rho/dz\right) \tag{2.25}$$

here U is the wind speed, g the gravitational acceleration (about 9.8 m/s^2), ρ density and z height. N is called the Brunt-Väisälä frequency or static stability parameter: the higher N, the more stable the flow. In case the N^2 is positive there is a stable

stratification, while, in the negative case the stratification is unstable. Both stability and wind shear are calculated locally, and Ri may vary rapidly across a sheared boundary, such as on top of the stable nocturnal boundary layer. Even under these statically stable conditions, instability is possible when the wind shear is strong enough to break up the stable layer and produce breaking waves. This occurs when $Ri \langle 0.25$ for linear 2D instabilities but the non-linear processes when rotation and stratification act together are far from clear, Redondo (2002).

The Gradient Richardson Number is the basic non dimensional parameter that describes the effects of stratification in stable situation is the Richardson number. It can be described as a gradient Richardson (*Rig*) or as flux Richardson (*Rif*) numbers. The Flux Richardson number relates buoyancy flux to turbulent production by shear or the other causes. While a gradient Richardson number parameterization of the effects of buoyancy; is often used to indicate the stability of the shear flows, it relates the variables that control the mixing at interface as follow:

$$Rig = \frac{g}{\rho} \frac{\partial \rho / \partial z}{\left(\partial u / \partial z\right)^2} \tag{2.26}$$

The relationship between the flux Richardson number, that may be considered as a mixing efficiency, and different, local as global forms of the gradient Richardson number may be explained directly from the turbulent energy equation. This dimensionless parameter represents the ratio between the potential energy required for vertical mixing *W* and the turbulent kinetic energy E_c available in the flow for mixing:

$$Rig = \frac{\frac{g}{\rho}\frac{d\rho}{dz}}{\left(\frac{du}{dz}\right)^2} = \frac{W}{E_c} \tag{2.27}$$

with $W = gV \frac{d\rho}{dz} \frac{l^2}{2}$ and

$$E_c = \frac{1}{2}\rho V\left(\frac{du}{dz}l\right)^2 \qquad (2.28)$$

where E_c is the kinetic energy, associated to the vertical motion of fluid parcel of density and volume *V*.

2.2.2. Reynolds Number

The Reynolds number *Re* is a dimensionless number that gives a measure of the ratio of inertial forces to viscous forces and it quantifies the relative importance of these two types of forces for given flow conditions. At small values of *Re* above 2000 the flow exhibits small instabilities. At values of about 4000 we can say that the flow is truly turbulent. Over the past 100 years many experiments have shown this phenomenon of limits of *Re* for many different Newtonian fluids - including gases. We can define Reynolds number with the Navier-Stokes equation. In order to make some progress in understanding the possible solutions, it is useful to do some dimensional analysis and to make a couple of estimates. For this purpose, we want to compare the inertial terms on the left hand side to the viscous terms on the right hand side. Let's assume that the flow is steady, so that $\frac{\partial V}{\partial t}=0$. Let *U* be a characteristic speed of the flow (usually taken to be the free-stream speed far from the object), and let *L* be some characteristic dimension of the flow (the typical size of an object in the fluid, say). Then for the inertial term,

$$\rho\left|(V\cdot\nabla)V\right|\sim\frac{\rho U^2}{L} \tag{2.29}$$

For the viscous term,

$$\mu\left|\nabla^2 V\right|\sim\frac{\mu U}{L^2} \tag{2.30}$$

Both of these quantities have the same dimension, so we can define a dimensionless number, the Reynolds number *Re*, by taking the ratio:

$$\mathrm{Re} = \frac{inertial\ terms}{viscous\ terms} = \frac{\rho\left(U^2/L\right)}{\mu\left(U/L^2\right)} = \frac{UL}{\nu} \tag{2.31}$$

with $\nu = \frac{\mu}{\rho}$ the kinematics viscosity.

Here, *L* is the characteristic flow scale, *U* the wind speed, ρ the air density, and ν the kinematics viscosity. The ratio *Re* is proportional to the wind speed; viscous forces dominate at low speeds, so that *Re* is small, whilst inertia is great at high speeds, making *Re* large. It is observed that fluid flow becomes turbulent when *Re* exceeds about 2300. This can be seen in cigarette smoke, which accelerates upwards from the burning tip, eventually reaching a speed at which the rising filament breaks into turbulence. *Re* is important in aeronautical sciences (the airflow around a wing) and in a variety of engineering applications. For instance, an oil pipeline needs to be designed so that *Re*>1, otherwise frictional retardation gains the upper hand. The viscosity increases as temperature decreases. In other words, when the inertial forces dominate over the viscous forces (when the fluid is flowing faster and *Re* is larger) then the flow is turbulent. On the other hand, when the viscous forces are dominant (slow flow, low *Re*) they are sufficient enough to keep all the fluid particles in line and then the flow is laminar.

In a turbulent flow, there is a range of time-varying scales of fluid motion. The size of the largest scales of fluid motion (called eddies) are set by the overall geometry of the flow. For instance, in an industrial smoke stack, the largest scales of fluid motion are as big as the diameter of the stack itself. The size of the smallest scales is set by the Reynolds number. As the Reynolds number increases, smaller and smaller scales of the flow are visible. In a smoke stack, the smoke may appear to have many very small velocity perturbations or eddies, in addition to large bulky eddies. In this sense, the Reynolds number is an indicator of the range of scales in the flow. The higher Reynolds number the greater range of scales. The largest eddies, determined by the geometry of the flow, will always be the same size, while the smallest eddies are determined by the Reynolds number. A large Reynolds number indicates that viscous forces are not important at large scales of the flow. With a strong predominance of inertial forces over viscous forces, the largest scales of fluid motion are undamped and there is not enough viscosity to dissipate their motions. The kinetic energy must "cascade" from these large

scales to progressively smaller scales until a level is reached for which the scale is small enough for viscosity to become important (that is, viscous forces become of the order of inertial ones). It is at these small scales that the dissipation of energy by viscous action finally takes place. The Reynolds number indicates at what scale this viscous dissipation occurs. Therefore, since the largest eddies are dictated by the flow geometry and the smallest scales are dictated by the viscosity, the Reynolds number defines the ratio of the largest scales of the turbulent motion to the smallest scales. It is easy to show that:

$$\frac{L}{\eta_k} = c\,\mathrm{Re}^{3/4} \tag{2.32}$$

with c as a constant.

2.2.3. Froude Number

Another non-dimensional number is the Froude number (*Fr*) which is used to describe the flow pattern over an obstacle. In the case of airflow over a mountain ridge (or water over a weir), the current may change accelerate and thin, and then suddenly decelerate, thereby producing a hydraulic jump (figure 2.6). This jump is sometimes visible as a rotor cloud in the atmosphere but always visible in water, as a bore. *Fr* is the ratio of the flow speed (*U*) to the speed of shallow water waves. If *Fr* > 1, the flow is supercritical: the current is strong and the water shallow. Waves do not travel upstream and the flow thickens when crossing an obstacle. If *Fr* < 1, the flow is subcritical: it thins when it approaches an obstacle.

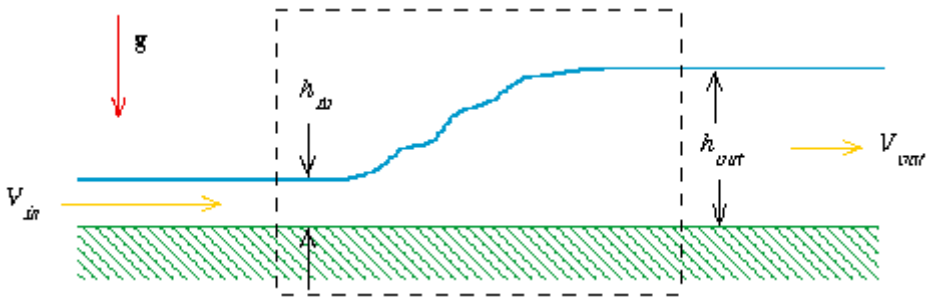

Figure 2.6: A hydraulic jump, i.e. a discontinuous transition from supercritical flow (left) to subcritical flow (right).

The speed of linear shallow water waves is $c = \sqrt{gh}$, where *h* is the depth of the flow, or, equivalently, the amplitude of the waves (i.e. the height of the obstacle *L* that triggered the waves). In the case of surface waves, the restoring force is the gravity *g*, but for waves internal to the atmosphere, the restoring force is the reduced gravity *g'*

$$g' = g\frac{\rho'}{\rho} = \tilde{g}\frac{\rho_o'}{\rho_o} = L\left(\frac{g}{\rho_o}\frac{d\rho_o}{dz}\right) = LN^2 \qquad (2.33)$$

where N is the Brunt-Väisälä frequency. Therefore $c = NL$, and the Fr can be expressed as

$$Fr_1 = \frac{U}{\sqrt{gL}} = \frac{U}{NL} \tag{2.34}$$

where U is the speed of open channel flow, g is gravity, and L is the length scale (at this example the height of the mountain). This is the first Froude number, which is the dimensionless parameter. If $Fr << 1$, i.e. when the airflow is slow, stably stratified, and/or the mountain high, the air will flow around the mountain, not over it (if the mountain is too wide, the flow will be blocked). If however $Fr >> 1$, the air readily flows over the mountain with very little lateral displacement. The second Froude number is defined as the ratio of inertial force to gravitational force. It therefore applies to wave and surface behavior, and is defined by

$$Fr_2 = \frac{U^2}{gL} \tag{2.35}$$

i.e., the square of Fr_1.

Finally, we can say that Froude number is proportional to inertial force divide by gravitational force and is used in momentum transfer in general and open channel flow and wave and surface behavior calculations in particular. We can write as

$$Fr = \frac{U^2}{gL} \tag{2.36}$$

2.2.4. Rossby Number and Ekman Number

The basic non-dimensional parameter used to describe the effects of rotation is the Rossby number defined as the ratio of the local fluid induced vorticity to the part of the absolute vorticity induced by the overall internal rotation

$$R_o = \frac{\omega}{f} \tag{2.37}$$

where ω, is the vorticity in small scale and *f*, is the coriolis parameter defined as $f = 2\Omega$. Furthermore we can define the Rossby number which characterizes the external rotation as $R_{oT} = U/\left(T^{-1}L\right)$ but in case of balance between the acceleration and the Coriolis force we can write as:

$$R_o = \frac{U}{\Omega L} \tag{2.38}$$

Ekman number is used to describe effect in oceans and atmosphere phenomena. Formally is described as:

$$Ek = \frac{\nu}{f\,L^2} \tag{2.39}$$

where *v* is the kinematic eddy viscosity, *f* is the coriolis parameter and *L* is the relevant eddy length scale. The same for the Eckman number with external rotation we can write as:

$$Ek = \frac{\nu}{\Omega L^2} \tag{2.40}$$

CHAPTER 3

Stratified Fluids

3.1. Basic concepts

The name stratified flow is applied to a flow primarily in the horizontal direction that is affected by a vertical variation of the density. Such flows are of considerable importance in geophysical fluid mechanics. The obvious case of the effect of vertical temperature variations on the wind near the ground is only one of a number of examples in the atmosphere, and the effects of both temperature and salinity variations play an important role in many aspects of dynamical oceanography.

The density may, in general, either increase or decrease with height. The former case gives rise to an interaction between the mean flow and the convection that would occur in the absence of mean flow. One example is the alignment of Benard cells by a mean shear, Tritton 1999, illustrated in the laboratory by figure 3.1. This shows an illuminated cross-section, perpendicular to the flow, of an air channel with heated bottom and cooled top; the smoke has been introduced a long way upstream and so the pattern indicates the occurrence of regular rolls with their axes along the flow.

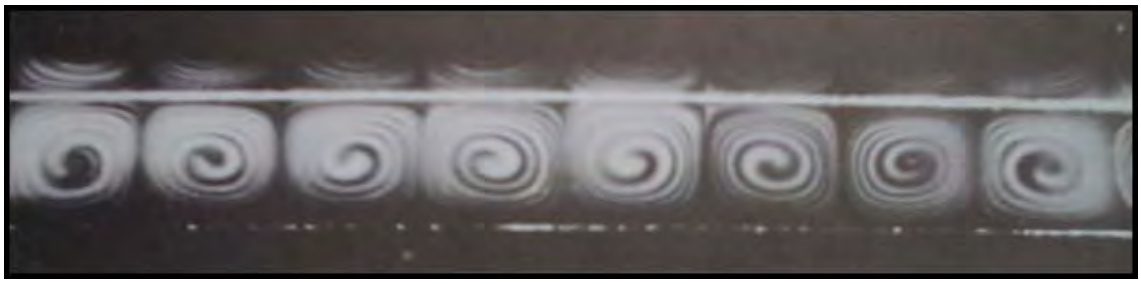

Figure 3.1: Cross section of convection cells in channel flow; Ra = 4.16×10^3, Re = 8.3. (Tritton 1999).

However, in this chapter we are primarily concerned with the case of stable stratification, that is to say the density decreases with height. Vertical motions then tend to carry heavier fluid upwards and lighter fluid downwards, and are thus inhibited. This inhibition may take the form of modifying the pattern of the laminar motion or of preventing or modifying its instability.

We require a quantitative criterion for this to be a strong effect. Since most of the experiments on stratified flows have used salt rather than heat as the stratifying agent we shall retain the density variations explicitly, rather than relating them to temperature variations. We consider the case of flow outside boundary layers at high Reynolds and

Peclet[1] numbers, so that both viscous and diffusive processes are negligible. Thus we write the momentum and density equations (for steady flow)

$$\rho u \cdot \nabla u = -\nabla p + \rho g \tag{3.1}$$

$$u \cdot \nabla \rho = 0 \tag{3.2}$$

We take *z* vertically upwards and suppose that the basic stratification consists of a uniform density gradient $-d\rho_o/dz$. Because ρ_o does not vary horizontally, the balance between $\rho_o g$ and the hydrostatic pressure can be subtracted out from equation 3.1 just as for an entirely uniform density.

We now consider, superimposed on this basic configuration, a flow with length and velocity scales *L* and *U*, produced, for example, by moving an obstacle of size *L* horizontally through the fluid at speed *U*. This will produce a modification of the density field which we denote by ρ', related to the stratification by equation 3.2 in the form

$$u \cdot \nabla \rho' + w\, d\rho_o/dz = 0 \tag{3.3}$$

In order of magnitude

$$\rho' \sim \frac{WL}{U}\left|\frac{d\rho_o}{dz}\right| \tag{3.4}$$

W is constant, and restricted by the fact the flow cannot produce buoyancy forces associated with ρ' that are larger forces involved. Since the buoyancy force does not contribute directly to the horizontal component of equation 3.1 it is convenient to work in terms of the vorticity form of this equation:

[1] For brevity, we retain the names, Peclet number and (subsequently) Prandtl number, although, when salt is the stratifying agent these now refer to UL/D and ν/D (the Schmidt number), where D is the diffusivity of the salt.

$$\rho\left(\mathrm{u}\cdot\nabla\omega-\omega\cdot\nabla u\right)=-g\left(\hat{x}\frac{\partial\rho^{'}}{\partial y}-\hat{y}\frac{\partial\rho^{'}}{\partial x}\right) \tag{3.5}$$

Since the order of magnitude of ω is *U/L* this indicates that the order of magnitude of ρ' must remain not greater than

$$\rho'\sim\rho_o U^2/g\,L \tag{3.6}$$

Comparison of this with (3.4) indicates that

$$W\Big/U\sim\rho_o U^2\Big/\left(gL^2\left|\frac{d\rho_o}{dz}\right|\right)=\left(Fr_{\text{internal}}\right)^2 \tag{3.7}$$

When $\left(Fr_{\text{internal}}\right)^2$ is small the horizontal motion has only weaker vertical motion associated with it. Fr_{internal} is called the internal Froude number: when, as at present, there is no danger of confusion with the Froude number associated with free surface effects, it is simply called the Froude number. $1/\left(Fr_{\text{internal}}\right)^2$ is sometimes known as the Richardson number.

Similar analysis can be given for flows in which viscous and/or diffusive effects are strong. This is a matter of some complexity, since different detailed treatments are appropriate for low, intermediate and high Prandtl number. Thus we do not consider it here; when we talk below of low Froude number flows, it is assumed that any other criterion for the flow to be strongly constrained by stratification is also fulfilled.

Often low Froude number motion can be considered to be entirely two-dimensional in horizontal planes. For example, in the relative moment between a spherical obstacle and a stratified fluid, nearly all the fluid is deflected to the sides of the sphere, sligthly above and below it. Thus the flow pattern in a horizontal plane has a closer resemblance to unstratified flow past a cylinder than to unstratified flow past a sphere.

Geophysical problems of interest frequently involve horizontal and vertical scales, *L* and *d*, of very different sizes; e.g. flow of a stratified ocean of depth *d* over topography of horizontal scale *L*, with $L>>d$. It is therefore worth pointing out parenthetically that, in these circumstances, the relative importance of stratification is

determined by the Froude number based on the vertical scale. In the above analysis, the relevant length scale is L at all points of the argument, except that the order of magnitude of ω is U/d. Hence, (3.7) becomes

$$W \Big/ U \sim \rho_o U^2 \Big/ \left(gL\, d \left| \frac{d\rho_o}{dz} \right| \right) \tag{3.8}$$

However, even without stratification, the geometry (via the continuity equation) constrains W/U to be of order d/L. Stratification is important when it provides a constraint at least as strong as this; i.e. when

$$\rho_o U^2 \Big/ \left(g\, d \left| \frac{d\rho_o}{dz} \right| \right) \leq 1 \tag{3.9}$$

3.2. Internal Waves

An important associated parameter may be introduced (and its physical significance illustrated) by considering first the behavior of a small fluid particle that is vertically displaced. Suppose its density, which it conserves, is $\rho_o(0)$. If it is displaced a distance Δz upwards, the density of the fluid surrounding it is $\rho_o(0)+\Delta z\, d\rho_o/dz$ and the net gravitational force on it is $-g\,\Delta z\, d\rho_o/dz$. Hence, its motion is governed by the equation

$$\rho_o \frac{d^2\Delta z}{dt^2} = g\frac{d\rho_o}{dz}\Delta z \tag{3.10}$$

and it oscillates about its original position with an angular frequency

$$N = \left(-\frac{g}{\rho_o}\frac{d\rho_o}{dz} \right)^{1/2} \tag{3.11}$$

($d\rho_o/dz$ being negative). N is called the Brunt-Väisälä frequency for stratified flows (see § 2.25). When the density variations are due to temperature variations,

$$N = \left(g\,\alpha\, dT_o/dz\right)^{1/2} \tag{3.12}$$

When, in addition, the adiabatic temperature gradient is significant,

$$N = \left[g\,\alpha \left(\frac{dT_o}{dz} + \frac{g\,\alpha\, T_o}{C_p} \right) \right]^{1/2} \tag{3.13}$$

The above analysis does not describe any actual fluid dynamical situation. For that we must turn to the full equations of motion. We consider a wave of small amplitude in an inviscid, non-diffusive fluid. Hence, we require the equations of unsteady motion, but we omit the non-linear terms on the basis that these must be negligible when the amplitude is small enough:

$$\rho_o \, \partial u / \partial t = -\nabla p + g \, \Delta\rho \tag{3.14}$$

$$\nabla \cdot u = 0 \tag{3.15}$$

$$\partial \Delta\rho / \partial t + w \, d\rho_o / dz = 0 \tag{3.16}$$

where $\Delta\rho$ is the departure of the density from its basic distribution, $\rho_o(z)$, and p is the corresponding departure from the hydrostatic pressure. We note that, although the problem is linearized, the term $u \cdot \nabla\rho$ in the density equation still enters through the interaction between the vertical velocity component and the basic stratification.

We look for wavelike solutions, periodic in both space and time:

$$u = U \exp i(\omega t - k_x x - k_y y - k_z z) \tag{3.17}$$

$$p = P \exp i(\omega t - k_x x - k_y y - k_z z) \tag{3.18}$$

$$\Delta\rho = Q \exp i(\omega t - k_x x - k_y y - k_z z) \tag{3.19}$$

where k_x, k_y, k_z are wave numbers in three directions *x*, *y*, *z* (where, the real parts correspond to the physical quantities). Substitution of these into equations (3.14) - (3.16) gives

$$i\omega\rho_o U = ik_x P \tag{3.20}$$

$$i\omega\rho_o V = ik_y P \tag{3.21}$$

$$i\omega\rho_o W = ik_z P - gQ \tag{3.22}$$

$$ik_x U + ik_y V + ik_z W = 0 \tag{3.23}$$

$$i\omega Q + \frac{d\rho_o}{dz} W = 0 \tag{3.24}$$

were (*U, V, W*) are the components of *U*. Elimination of *U, V, W, P* and *Q* from these homogeneous equations shows that they are consistent when and only when

$$\omega = N\left(1 - \frac{k_z^2}{k_x^2 + k_y^2 + k_z^2}\right)^{1/2} \tag{3.25}$$

which may also be written

$$\omega = N\left(k^2 - k_z^2\right)^{1/2} / k \tag{3.26}$$

or

$$\omega = N\left|\sin\theta\right| \tag{3.27}$$

where θ is the inclination to the vertical of the vertical wave number $k = \hat{x}k_x + \hat{y}k_y + \hat{z}k_z$ and $k = |k|$.

Thus waves exist for any value of the angular frequency from zero up to the Brunt-Väisälä frequency[2] N. Above N there are no wavelike solutions (since, in an unstratified fluid, $N = 0$, this gives confirmation that the waves are essentially a consequence of the stratification.). When $k_z = 0$, corresponding to a wave pattern without vertical variation, $\omega = N$; an array of vertical columns, with the velocity varying in the horizontal direction, oscillates at the Brunt-Väisälä frequency, as might be expected from its simple derivation above. When $k_x = k_y = 0$, corresponding to a wave pattern without horizontal variation, $\omega = 0$. The phase velocity of the waves is in the direction of *k* and has *ω/k.*

Of greater physical importance is the group velocity, indicating the speed and direction with which kinetic and potential energy are transmitted through the fluid. The

[2] Also called the buoyancy frequency, isthe frequency at which a vertically displaced parcel will oscillate within a statically stable environment.

waves are dispersive in a rather unusual way; the frequency does not depend on the magnitude of the wave number but it does depend on its direction. The standard result that for a wave in one dimension the group velocity is $d\omega/dk$ may be extended to three dimensions giving

$$c_g = \hat{x}\frac{\partial \omega}{\partial k_x} + \hat{y}\frac{\partial \omega}{\partial k_y} + \hat{z}\frac{\partial \omega}{\partial k_z} \tag{3.28}$$

For the present situation

$$c_g = \frac{N k_z}{k^3\left(k^2 - k_z^2\right)^{1/2}}\left[\hat{x}\,k_x k_z + \hat{y}\,k_y k_z - \hat{z}\left(k^2 - k_z^2\right)\right] \tag{3.29}$$

Since the properties of the waves are obviously axisymmetric about the vertical in case of no variation in the y – direction that is $k_y = 0$ then

$$c_g = \frac{N\cos\theta}{k}\left(\hat{x}\cos\theta - \hat{z}\sin\theta\right) \tag{3.30}$$

This is perpendicular to the wave number

$$k = k\left(\hat{x}\sin\theta + \hat{z}\cos\theta\right) \tag{3.31}$$

and thus to the phase velocity. Energy is thus transmitted along lines in the planes of the wave fronts. This is what gives the waves their rather unfamiliar character, analogous to waves occurring in a rotating fluid.

The other interesting direction in providing an understanding of the structure of the wave motion is the direction of motion of the fluid particles. Equation (3.23), which may be written

$$\vec{U}\cdot\vec{k} = 0 \tag{3.32}$$

shows that this motion is always perpendicular to the wave number. The waves are

essentially transverse. Moreover, since when $k_y = 0$, then $V = 0$ (equation 3.21), the motion is along the same line as the group velocity.

No prediction about the wave numbers present is given by the theory. For a single ω, all values of k are possible and all transmit in the same direction. In the experiments, there will have been a range of wave numbers present that Fourier synthesize to give the narrow rays with undisturbed fluid elsewhere. The detailed structure depends on the motion in the immediate vicinity of the oscillating cylinder.

3.3. The Entrainment E

Several mechanisms exist that produce mixing across density interfaces; it depends on the rate of transfer from kinetic to potential energy, elevating the center of gravity of the initially stratified flow. The Prandtl number $\left(\mathrm{Pr}=\frac{\nu}{\kappa}\right)$ is also important relating the momentum diffusivity and the mass ν and the mass diffusivity κ, which effect is the general entrainment law, Redondo et al. 1996, as

$$E=\frac{Ve}{u'}=C\left(\mathrm{Pr}\right)\cdot Ri^{-n(Ri,\mathrm{Pr})} \tag{3.33}$$

For oscillating grid experiments, Turner et al. 1973, proposed that the entrainment velocity Ve defined as $Ve=dD/dt$, where D is the depth of the turbulent layer, is given by a simple law of the form

$$E\propto Ri^{-n} \tag{3.34}$$

where E, the entrainment rate is defined as $E=Ve/V$, V being some global or local reference velocity. The Richardson number, Ri, measures the relative importance of buoyancy forces which usually act so as to stabilize the flow, and velocity fluctuations which tends to destabilize it. A global Richardson number (equivalent to the inverse square of the Froude numb, Fr_{internal}) can be defined as $Ri_o=Fr_{\text{internal}}^{-2}=\frac{g'D}{V}g'$ being the reduced gravity $g'=\frac{\Delta\rho}{\rho}g$ where $\Delta\rho$ is the density difference producing the buoyancy effects. The Richardson number can be used in various ways as defined in § 2.2.1., here we consider appropriate definitions for each of the experimental situations investigated such as in grid generated turbulence. Turner 1973, defined a global Richardson number in terms of local turbulent parameters as:

$$Ri_o = \frac{g\,\Delta\rho\,l}{\rho\,u^{'2}} \tag{3.35}$$

where $\Delta\rho$ is the buoyancy jump across a density interface, $u^{'}$ is the turbulent velocity and l is an integral length scale of the turbulence defined as the area under the cross-correlation coefficient curve for the parallel velocity components.

In general

$$l = \int_0^{\infty} R(\delta)\, d\delta \tag{3.36}$$

when δ is the distance between the density or velocity probes and $R(\delta)$ is the cross correlation coefficient

$$R(\delta) = \frac{\overline{u_i^{'}(x)\,u_i^{'}(x+\delta)}}{u^{'2}} \tag{3.37}$$

The relationship between the integral length scale and the Taylor microscale define in §2.1.3 is seen in figure 3.2.

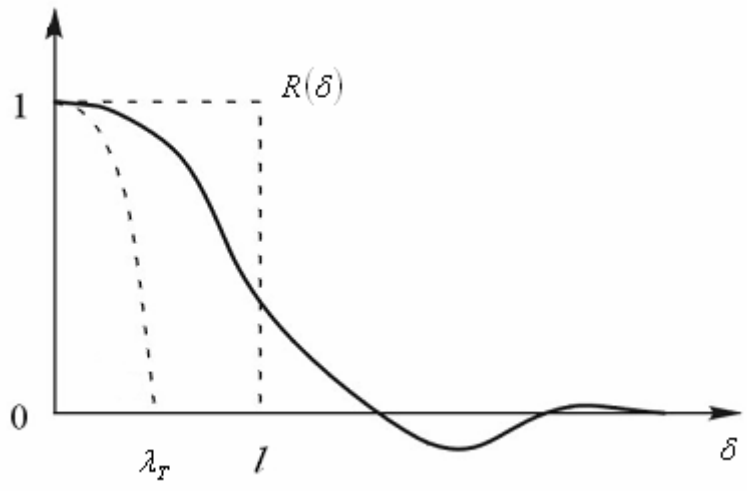

Figure 3.2: The relationship between the integral length scale and the Taylor microscale.

Turner 1973 and Redondo et al. 1996, found that the value of *n* in equation 3.34

was 3/2 when the stratification was due to salt, and 5/3 when was due to sugar, but the density-stratification resulted from a temperature gradient, the value of *n* was found to be close to 1. Turner also suggested that viscosity differences cannot be used to explain the different values of *n*, and proposed that the differences in Ve that occur when using salt and heat as the stratifying agents can only be explained by consideration of the molecular diffusion of mass and heat as defined by the appropriate diffusivity κ, and proposed that the entrainment velocity would be a function of both a Richardson number and the Peclet number $Pe = \frac{u' l}{\kappa}$. Turner initially suggested that $E \propto Ri^{-1}$, which he found for temperature stratification was the basic entrainment law, but he also found $E \propto Ri^{-3/2}$, for salt stratification, showing the influence of the molecular diffusivity on turbulent transport. This experiment studies the horizontal characteristics of a larger scale mixing front both in a stratified and in a homogeneous flow, modeling the coastal stirring associated to a coastal current and based on the work by Carrillo et al. (2001).

The entrainment as a function of the Richardson number confirms the Turner (1973) and Redondo et al. (1987) results, shown in figure 3.3 showing power law dependence with $n = 3/2$ for large range of Ri values. It is apparent that there are more than 3 decades of variation in the values of entrainment which are reflected in a similar range of variation for the mixing efficiency. For salty interfaces the relationship between the mixing efficiency and the local Richardson number (Ri) is a function of entrainment as

$$\eta = E\,Ri = Ri^{1-n} \tag{3.38}$$

This is a non lineal effect that can be explained by the complex resonances between waves and turbulence (Linden 1980, Redondo et al. 1995, Redondo et al. 2001).

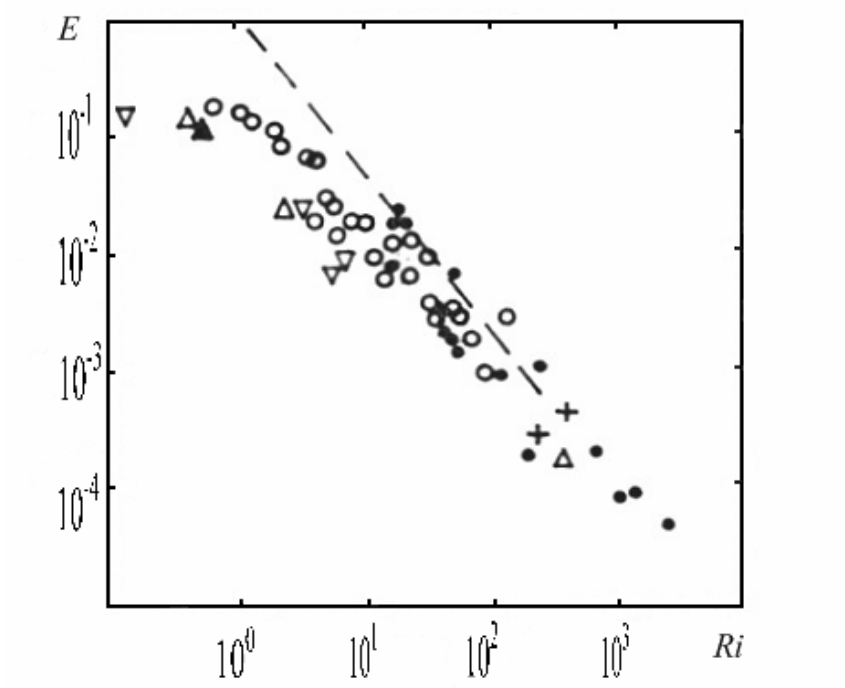

Figure 3.3: Entrainment versus Richardson Number for oscillating grid turbulent mixing. Redondo (1987), Turner (1973) Results for salt are indicated as black dots.

3.4. Previous related results and comparative analysis

The Entrainment law is modified, provided there is a close boundary layer as demonstrated by Redondo (1990) as seen in figure 3.4, however to our knowledge, no experiments have been performed measuring Entrainment with grid stirred turbulence on a rotating frame in non homogenous-turbulence.

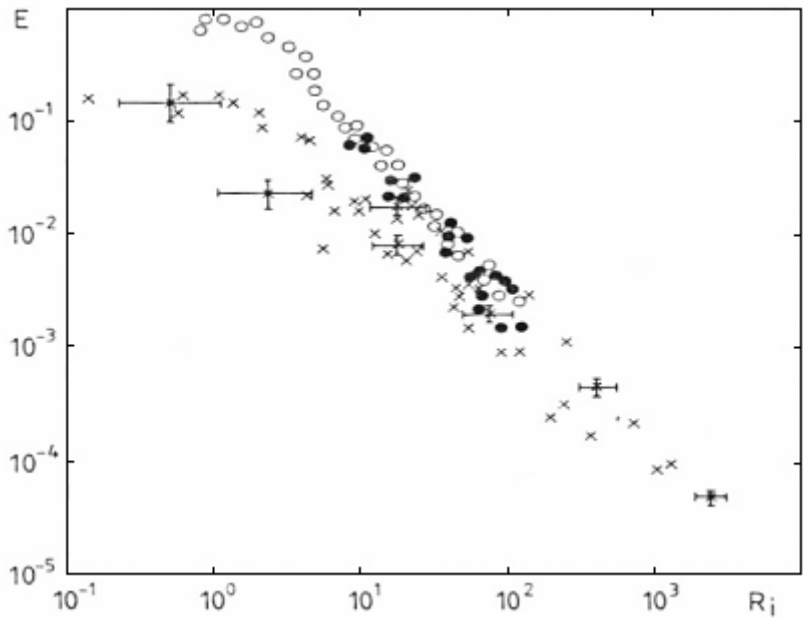

Figure 3.4: Changes in Entrainment due to a boundary Layer, x and ● - experiments by Redondo (1990), ○ - experiments by Turner (1973).

The preliminary results from the Trondheim Rotating Stratified flow experiments lead to the expectation that both stratification and rotation produce changes in the spectra of both the velocity components and of the density at the centre of the interface. The density also shows a marked skewness as we move away from the centre as seen in figure 3.5. The Kurthosis also increases strongly as a function of the Richardson number as seen in figure 3.6 so an important feature of the experimental analysis of this thesis will be to consider measurements, long enough to be able to calculate not only turbulent velocities and densities and their RMS, but also their higher order moments. The ESS technique will be used Babiano (2002) to calculate Structure functions with enough accuracy, using the Mahjoub et al. (1998, 2001) technique.

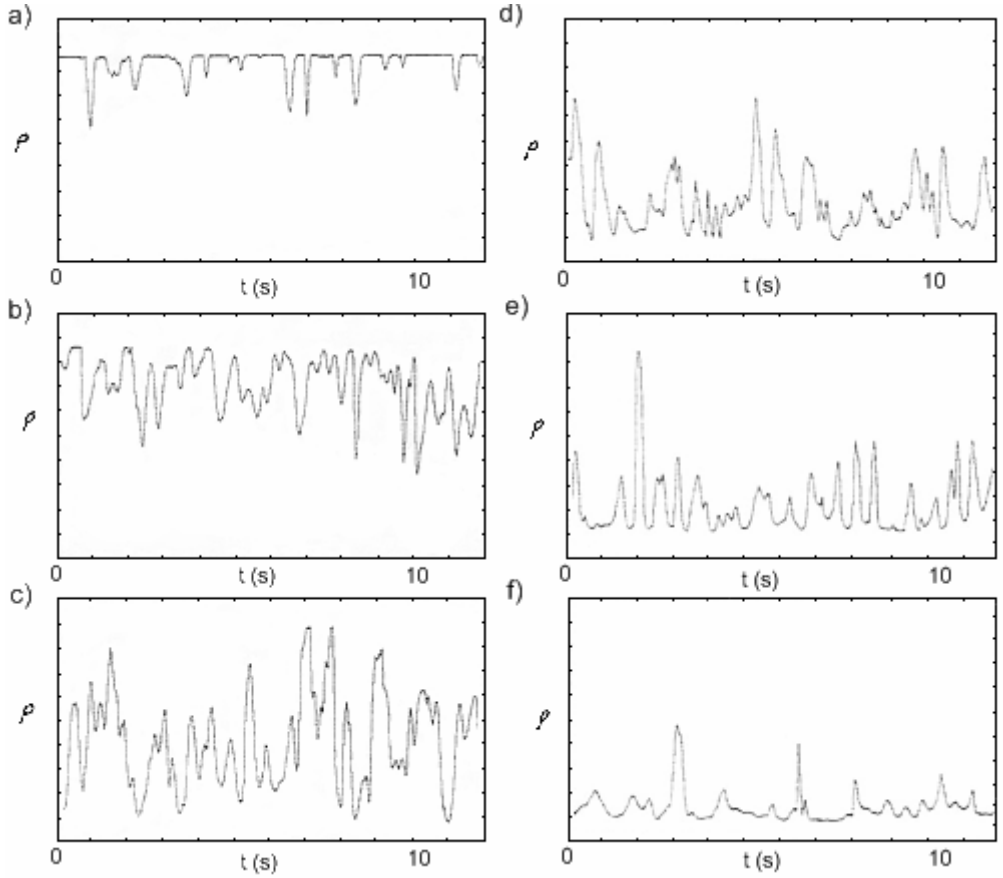

Figure 3.5: Density fluctuations at the centre of an interface, note the skeweness. a) 1cm below the interface, b) 0.5cm below the interface, c) at the average interface, d), e) and f) above the interface.

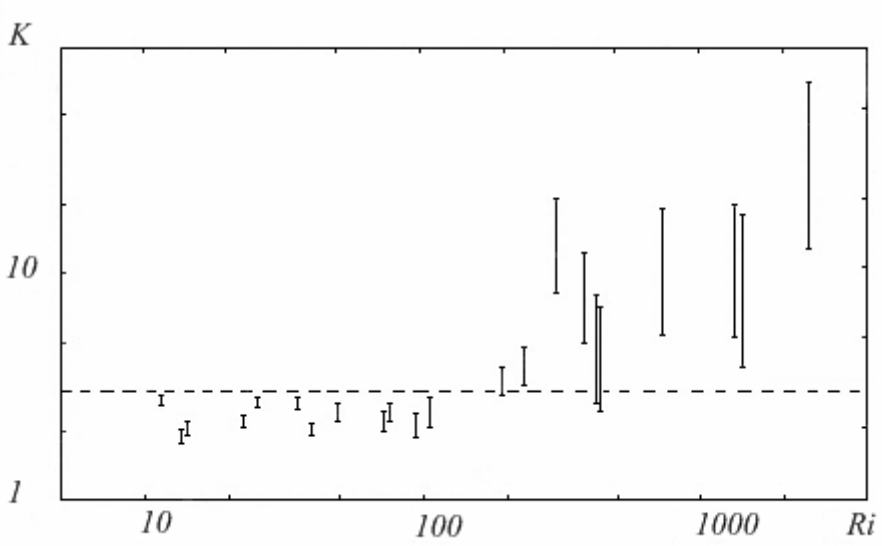

Figure 3.6: Kurthosis of the density fluctuations measured at the centre of a density interface in oscillating grid turbulence, Redondo et al. (1988) [Rev. de Geophisc].

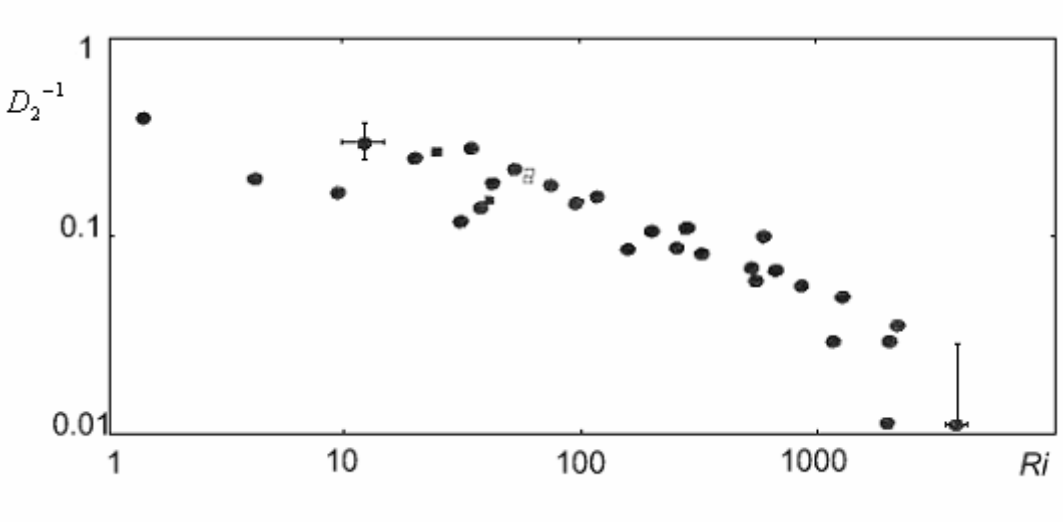

Figure 3.7: Fractal dimension D_2^{-1}, as a function of the Richardson number.

It was shown by Redondo (1990) (see figures 3.7 and 3.8) that density interfaces may be distinguished by their Fractal dimension D_2 and their thickness and both are functions of the Richardson number. The same analysis will be extended to Rotating flows using the Rossby number to parameterize the geometrical changes.

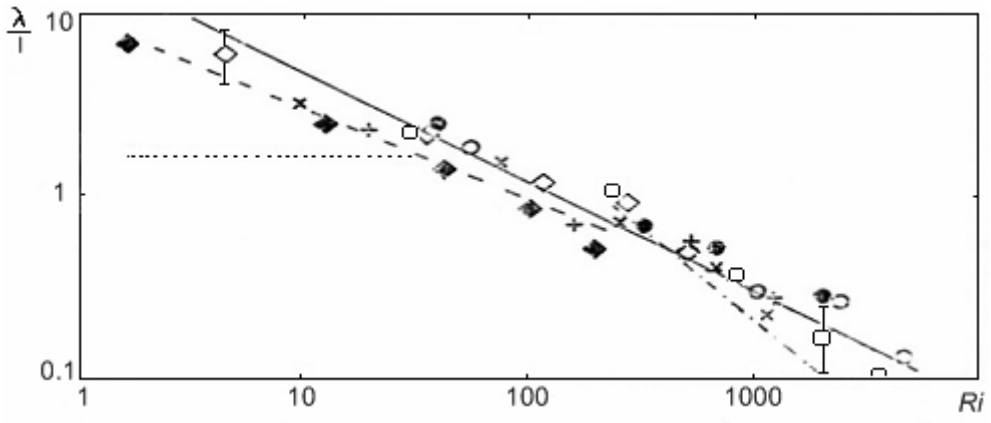

Figure 3.8: Vertical length scale versus Ri, different symbols correspond to different distance between an oscillating grid and a sharp density interface.

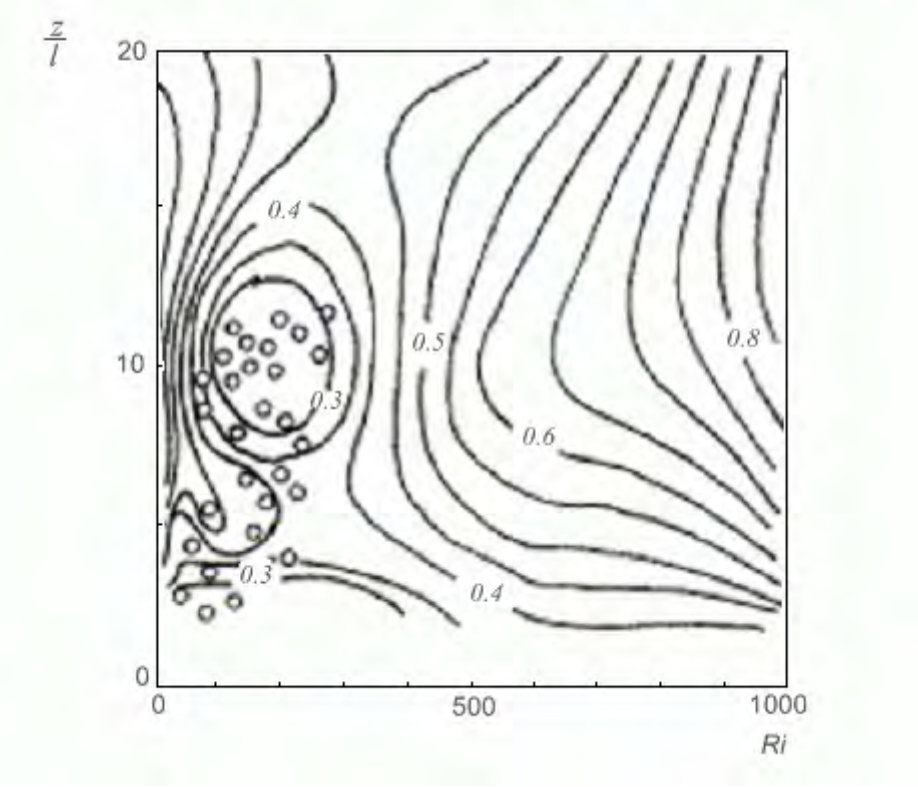

Figure 3.9: Mixedness contours as a function of Richardson number.

In figure 3.9 the parameterization of the Mixedness with *Ri* and z/l, which may be considered as the grid action or Reynolds number per unit viscosity shows a region of resonance due to internal waves. The extension of these measures to a rotating flow would also introduce the inertial waves and the Coriolis parameter creating more complex resonances. From top views such as that shown in figure 3.10 of tracer evolution in the surface, the vortex structure on a stratified-rotating flow may be analyzed and the Rossby deformation radius and the fractal dimension calculated in a similar way as the satellite images both from the atmosphere and ocean.

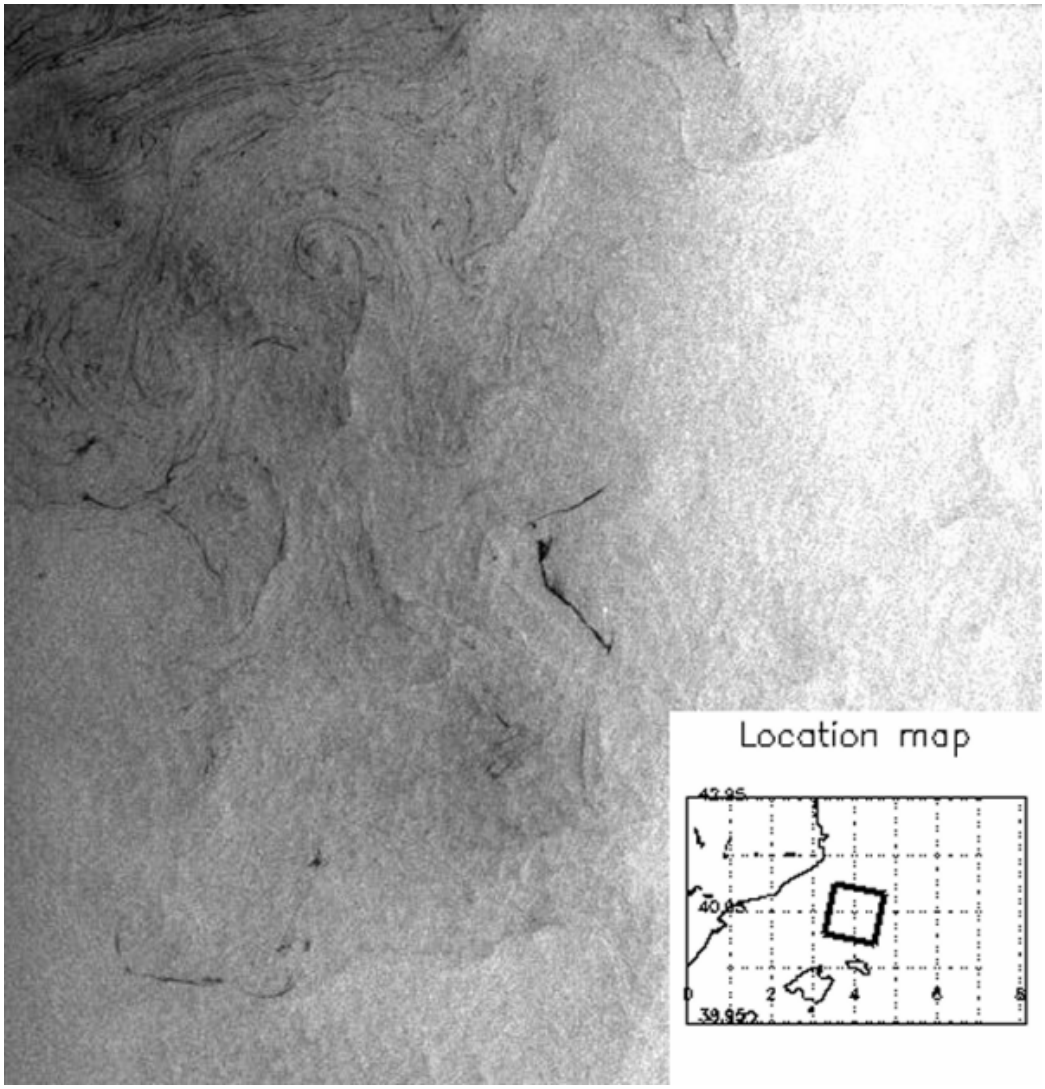

Figure 3.10: Example of ERS-2 SAR images (left) with a recent, but distorted, oil spill in the North Western Mediterranean near Barcelona. The image's box size is approximately 100 Km (other similar images are available in chapter 8 and appendix 3).

CHAPTER 4

Rotating Fluids and Vorticity

4.1. Flow in Rotating Fluids

4.1.1. Introduction

This chapter is concerned with the dynamic of fluids in rotating systems. This branch of fluids mechanics has developed rapidly in recent years as an obvious consequence of interest in geophysical flow problems. Evaluation of the parameters shows that the motions, particularly on the large scale, of the Earth's atmosphere, oceans, and core and of stars and galaxies will all exhibit the effects discussed in this chapter. The rotation gives rise to a range of new phenomena; here we consider a small selection of these. For the most part of this introduction we consider constant density flows, but further on we will consider the coupled effect of rotation and stratification specially when discussing the rotating stratification experiments (see chapter 9 and appendix 5). The whole subject could be formulated as seen by an observer external to the rotation. Since, however, all boundary conditions will be specified in terms of the rotating frame of reference it is easier to modify the equations of motion so that they apply in such a frame.

To consider how rotation forces the flow topology characteristics, let us consider a body of fluid and rotate its boundaries at a constant angular velocity Ω, then at any time sufficiently long after starting the rotation, the whole body is rotating with this angular velocity, moving as if it were a rigid body. There are then no viscous stresses acting within the fluid. Any disturbance – i.e. anything that would produce a motion in a non-rotating system – will produce motion relative to this rigid body rotation. This relative motion can be considered as the flow pattern; it is the pattern that will be observed by an observer fixed to the rotating boundaries (Tritton 1999).

The Taylor-Proudman theorem has simple and striking consequences, illustrating the fact that rotating fluids exhibit a range of phenomena not found in non-rotating fluids. The principal of these is the formation of 'Taylor columns' that lead to a 2D like structure. These occur when there is relative motion between an obstacle and the fluid in a strongly rotating system. We consider first the case in which this motion is perpendicular to the axis of rotation (giving what is called a transverse Taylor column). The fluid is deflected past the obstacle. Since the flow must be two-dimensional this deflection also occurs above and below the obstacle (visualizing the axis of rotation as vertical). There are thus columns of fluid, extending parallel to the axis from the

obstacle, round which the fluid is deflected just as if the solid walls themselves extended there.

4.1.2. Centrifugal and Coriolis forces

The basic non-dimensional parameter used to describe the effects of rotation is the Rossby number considered as the ratio of the local fluid induced vorticity to the part of the absolute vorticity induced by the overall external rotation and is shown in 2.2.4. A small Rossby number signifies a system which is strongly affected by Coriolis forces, and a large Rossby number signifies a system in which inertial and centrifugal forces dominate.

The effect of using a rotating frame of reference is well known from the mechanics of solid systems; there are accelerations associated with the use of a non-inertial frame that can be taken into account by introducing centrifugal Coriolis forces. That statement may be expressed in a form appropriate to fluid systems by

$$\left(\frac{Du}{Dt}\right)_I = \left(\frac{Du}{Dt}\right)_R + \Omega \times \left(\Omega \times r\right) + 2\Omega \times u_R \tag{4.1}$$

The subscripts *I* and *R* refer to inertial and rotating frames of reference. $\left(Du/Dt\right)_I$ is the acceleration relative to the rotating frame and can thus be expanded in the usual way:

$$\left(\frac{Du}{Dt}\right)_R = \frac{\partial u_R}{\partial t} + \left(u \cdot \nabla u\right)_R \tag{4.2}$$

Dropping the subscript *R*, as all velocities will be referred to the rotating frame throughout the rest of this chapter, the equation of motion is

$$\frac{\partial u}{\partial t} + u \cdot \nabla u = -\frac{1}{\rho}\nabla \rho - \Omega \times \left(\Omega \times r\right) - 2\Omega \times u + v\nabla^2 u \tag{4.3}$$

The second and third terms on the right-hand side of (4.1) are, of course, respectively the centrifugal and Coriolis forces. In many problems the centrifugal force is unimportant. This is because it can be expressed as the gradient of a scalar quantity,

$$\Omega \times (\Omega \times r) = -\nabla\left(\frac{1}{2}\Omega^2 r'^2\right) \tag{4.4}$$

where r' is the distance from the axis of rotation (figure 4.1). Hence replacing the pressure by $\left(p - \frac{1}{2}\rho\Omega^2 r'^2\right)$ reduces the problem to one that is identical except that the centrifugal force is absent. This is entirely analogous to the procedure of subtracting out the hydrostatic pressure to remove the effect of gravitational forces. The centrifugal force is balanced by a radial pressure gradient, which is present, whether or not there is any flow relative to the rotating frame and which does not interact with any such flow. The limitations to this statement are just the same as for the gravitational case. First, the pressure must not appear explicitly in the boundary conditions. Second (since ρ has been taken through ∇), the density must be constant; centrifugal forces variations associated with density variations do give rise to body forces that can alter or even cause a flow.

It should be emphasized that the centrifugal force under discussion here is associated with the rotation of the frame of reference as a whole. In the other contexts it is sometimes convenient to talk about the centrifugal force associated with circular motion relative to the frame of reference (either inertial or rotating). This is then a way of discussing physically effects that are contained mathematically in one or both of $(u \cdot \nabla u)$ and the Coriolis term.

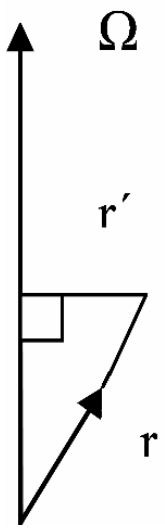

Figure 4.1: Definition sketch.

4.1.3. Intrinsic stability and inertial waves

Rotating fluids have an intrinsic stability, in the sense that if a fluid particle is displaced there is a tendency for it to return in a way that would not occur in a non-rotating fluid. Consider an isolated particle of unit mass, which, as a result of some disturbance, moves with a speed u in any direction perpendicular to the axis of rotation. (We are not considering here a genuine fluid motion or even a particular physical situation, but merely illustrating a general feature in the simplest way). A Coriolis force of magnitude $2\Omega u$ acts on it, always at right angles to its direction of motion. It thus moves on a circular path of radius r given by

$$u^2/r = 2\Omega u \tag{4.5}$$

that is

$$r = u/2\Omega \tag{4.6}$$

It goes once round the circle in a time

$$T = 2\pi r/u = \pi/\Omega \tag{4.7}$$

independent of u. It thus returns to its original position periodically, twice during every revolution of the fluid. It is thus often said that a rotating fluid has an intrinsic angular frequency, $2\pi/T = \Omega$.

In a complete system, the effect of this constraining tendency acting on every fluid particle is that rotating fluids can support wave motions, known as inertial waves that would not arise in the absence of rotation. Inertial waves are in many ways closely similar to internal waves in a stratified fluid. Just as internal waves occur with values of the angular frequency from zero up to the Brunt-Väisälä frequency, so inertial waves occur with the values from zero up to 2Ω:

$$\omega = 2\Omega|\cos\theta| \tag{4.8}$$

where θ is now the angle between the wave number vector and the rotation axis. Again the frequency is related to the orientation and not the magnitude of the wave number. Consequently, the property of the group velocity being perpendicular to the phase velocity is also exhibited by inertial waves. We can thus allow the analogy between inertial and internal waves (§ 3.2) to indicate the nature of inertial waves without the need of a separate detailed analysis of them.

4.2. Internal and Inertial waves

In stratified-rotating fluids, both types of moments act at the same time. The linear internal waves propagate at an angle θ with a dispersion relationship given by $\omega^2 = N^2 \sin\theta$ that propagate at an angle among a layered stratified structure as shown in figure 4.2. On the other hand rotating structures dissipate energy through inertial waves limited by the coriolis parameter *f*. That process is a powerful mechanism for the radiation of energy away from the mixing front or density produced by the local velocity gradient $(\partial u/\partial z)$.

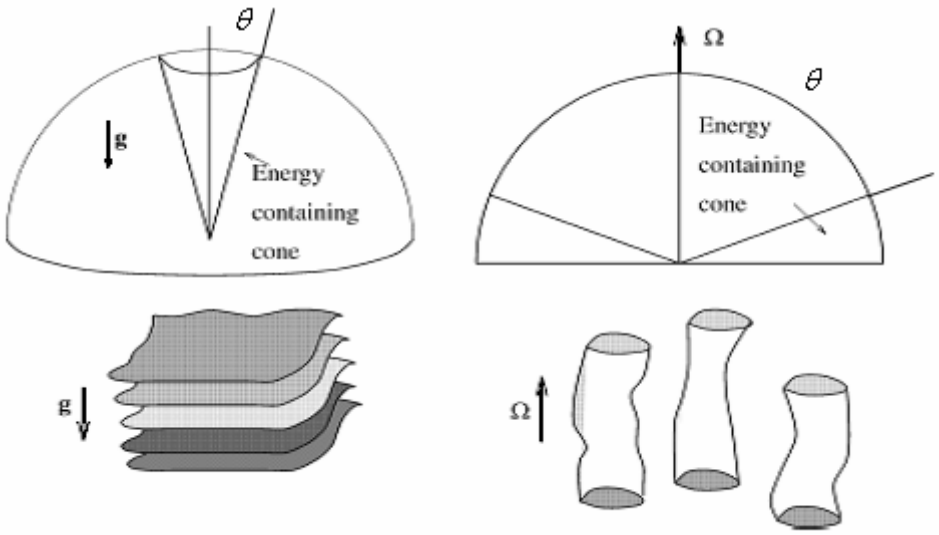

Figure 4.2: Internal and Inertial wave propagation cones.

The quasi-bidimensional (2D) approximations can not be applied directly to the mesoscale dynamic, dominated by stable stratification and rotation. In spite of numerical tools and theories for lineal approximations; high resolution direct numeric simulation and non-linear theories as wave turbulence for 3D predictions. Those tools can be used to compare with results at laboratories experiments and are adapted to well defined problems such as the quantification of elongated or flat eddy structures by an extended range of parameters like *N* or *f* (characteristic frequency of stratification and Coriolis respectively).

Any solenoidal two-dimensional motion satisfies the geostrophic equations. The

Taylor-Proudman theorem[1] for fast rotation is the limit of the information to be obtained in this way. Both the Rossby number ($R_o = U/\Omega L$) and the Ekman number ($Ek = \nu/\Omega L^2$) increase as the length scale is decreased. So, if therefore there are regions in which the flow parameters vary over a distance small compared with the imposed length scales, then inertia forces and/or viscous forces may be locally important. Then, there may be local violations of the Taylor-Proudman theorem. An obvious place for such a development to occur is between the two flows which, according to the theorem, do not interact, that is at the edge of the Taylor column. Thin shear layers are observed here. The whole structure of the detailed flow in the Taylor column is determined by these shears layers together with the boundary layer on the obstacle's surface. Because the two regions are separated by a layer in which the Taylor-Proudman theorem does not apply, there is in fact some interchange of fluid between the integer and the exterior of a transverse Taylor column. It is the shear layers that also govern the length of a Taylor column (either transverse or longitudinal) so that, although it is long at low Rossby and Ekman numbers, it does not extend to infinity as predicted by the Taylor-Proudman theorem. A flow in a rotating fluid in which viscous forces are important but which is much simpler than the shear layers mentioned above. This is the Ekman layer, the boundary layer between a geostrophic flow and a solid boundary at which the no-slip condition applies. This turns out to be actually simpler than the corresponding problem in a non-rotating fluid. The results have the added interest of direct application to the atmosphere and the oceans.

Several kinds of experiments developed with jet induced turbulence Boubnov et al. (1994), Linden et al. (1995) and Dalziel et al. (1995), or with grid stirred turbulence show a slow front advance adverted by the presence of a steady general circulation on the tank (Carrillo et al. 2001).

[1] States that when a solid body is moved slowly within a fluid that is steadily rotated with a high Ω, the fluid velocity will be uniform along any line parallel to the axis of rotation. Ω must be relatively large compared to the movement of the solid body in order to make the coriolis force large compared to the acceleration terms.

4.3. Vorticity in 3D/2D flows

Vorticity as a mathematical concept is used in fluid dynamics. It can be related to the amount of "circulation" or "rotation" (or more strictly, the local angular rate of rotation) in a fluid. Vorticity we can write in vector form as:

$$\vec{\omega}=\nabla\times\vec{v} \tag{4.9}$$

being $\vec{\omega}=(\zeta,\eta,\omega)$ and $\vec{v}=(u,v,w)$ vorticity and velocity vectors respectively.

In fluid dynamics, vorticity is the curl of the fluid velocity. It can also be considered as the circulation per unit area at a point in a fluid flow field. It is a vector quantity, whose direction is along the axis of the fluid's rotation. For a two-dimensional flow, the vorticity vector is perpendicular to the plane. For a fluid having locally a "rigid rotation" around an axis, vorticity is twice the angular velocity of a fluid element.

In general, vorticity is an especially powerful concept, in case viscosity is low (i.e. high Reynolds number). In such cases, even when the velocity field is relatively complicated, the vorticity field can be well approximated as zero nearly everywhere except in a small region in space. This is clearly true in the case of 2D potential flow (i.e. 2D zero viscosity flow), in which case the flow field can be identified with the complex plane, and questions about those sorts of flows can be posed as questions in complex analysis which can often be solved analytically.

Even for real flows (3D and finite Re), the idea of viewing things in terms of vorticity is still very powerful. In particular, one restricts attention to the vortex dynamics, which presumes that the vorticity field can be well modelled in terms of discrete vortices. In general, the presence of viscosity causes a diffusion of vorticity away from these small regions into the general flow field. This can be seen by the diffusion term in the vorticity transport equation. Thus, in cases of very viscous flows, the vorticity will be diffused throughout the flow field and it is probably simpler to look at the velocity field rather than to look at the vorticity field. One of the advantage of using the vorticity equation is that pressure term are avoided in homogeneous flows ($\rho=cte.$) because $\nabla\times\nabla p=0$. In 2D flows $(x,y,0)$ $(u,v,0)$ the vertical vector is reduced to the vertical component $\vec{\omega}=(0,0,\omega)$ and it may be treated as a scalar.

4.3.1. Basic Equations in environmental flows

The basic equations are the continuity and momentum equations using Boussinesq approximation[2], and will be used to show some aspects at the scale to scale energy transfer in a 2D flow. For an incompressible fluid the continuity equation reduces to

$$\nabla \cdot \vec{u} = 0 \tag{4.10}$$

The equation of motion of an incompressible, homogeneous geophysical fluid with constant viscosity is:

$$\frac{\partial \vec{u}}{\partial t} + u_i \frac{\partial \vec{u}}{\partial x_i} = -\frac{1}{\rho} \overrightarrow{\nabla p} + \overrightarrow{\nabla \phi} - 2\vec{\Omega} * \vec{u} + \nu \nabla^2 \vec{u} \tag{4.11}$$

where p is the pressure, ϕ the gravitational potential, Ω the angular velocity of Earth and ν kinematic viscosity. If the motion is primarily horizontal, then the flow is approximately two-dimensional i.e. $\vec{u} = (u, v, 0)$ where u and v are independent of depth.

In a strictly 2D flow of this form there is only one non-zero component of vorticity (the vertical) and $\vec{\omega} = (0, 0, \omega)$ in the absence of dissipation vorticity is conserved (Kelvin's Law)

$$\frac{D\omega}{Dt} = 0 \tag{4.12}$$

Note that this is true away from the boundaries that act as sources of vorticity.

[2] Boussinesq approximation neglects variations in density except to calculate buoyancy forces. It is often used in free convection problems where density changes are small (see chapter 2).

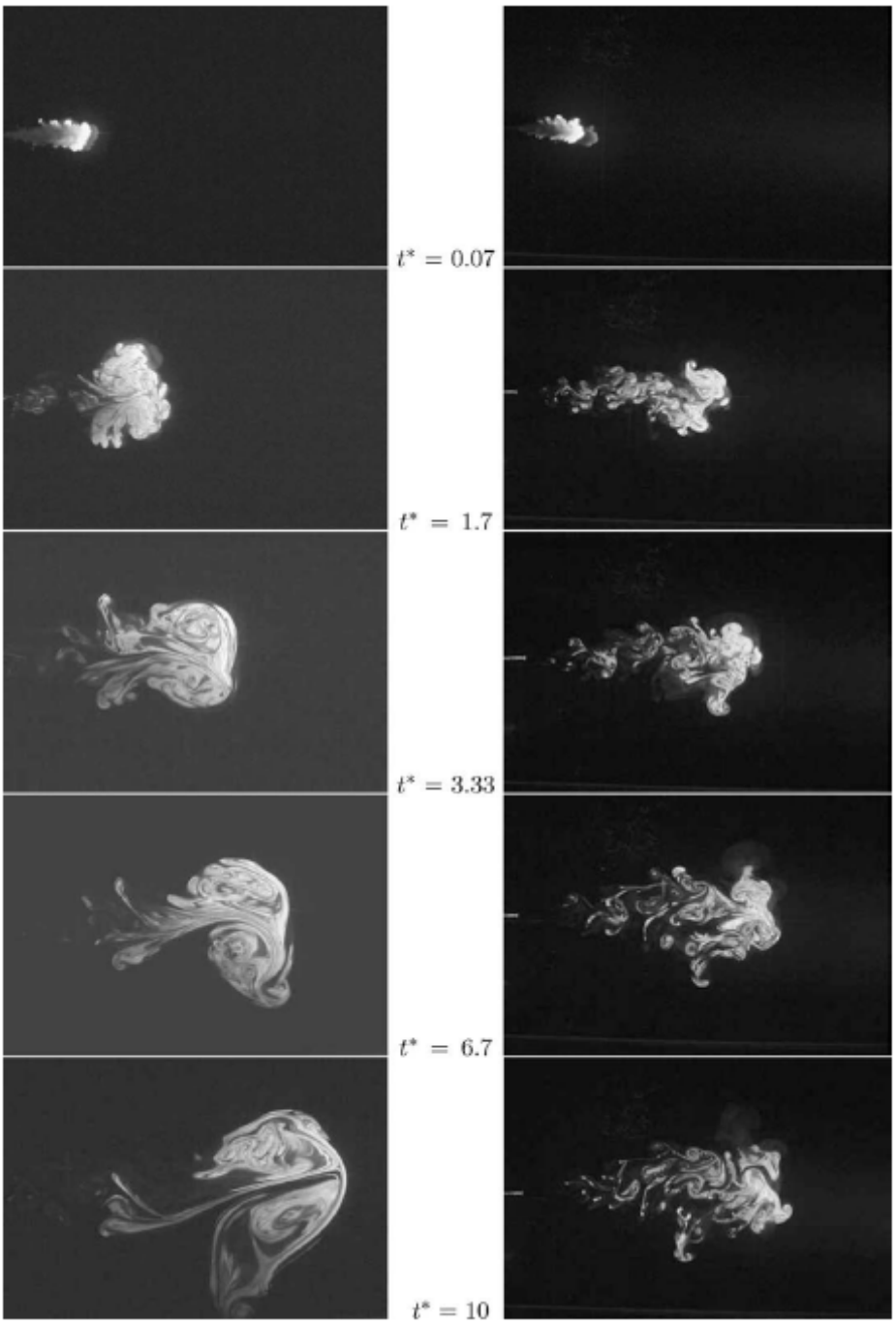

Figure 4.4: Comparison of a Turbulent Jet in a Stratified (left) and a Neutral (right) environment, showing the formation of a stable 2D vortex dipole.

So we may define a stream function ψ, such that

$$u = \left(\frac{\partial \psi}{\partial y}, -\frac{\partial \psi}{\partial x}, 0 \right) \qquad (4.13)$$
$$\omega = -\nabla^2 \psi$$

The intensification of vertical vorticity can be seen in a stratified fluid such as that seen at the left of figure 4.4. The use of the vorticity and the stream function calculated experimentally such as the plot of figure 4.5 can be used to distinguish between the different coherent structures in the 2D turbulent flows (Flor et al. 1996).

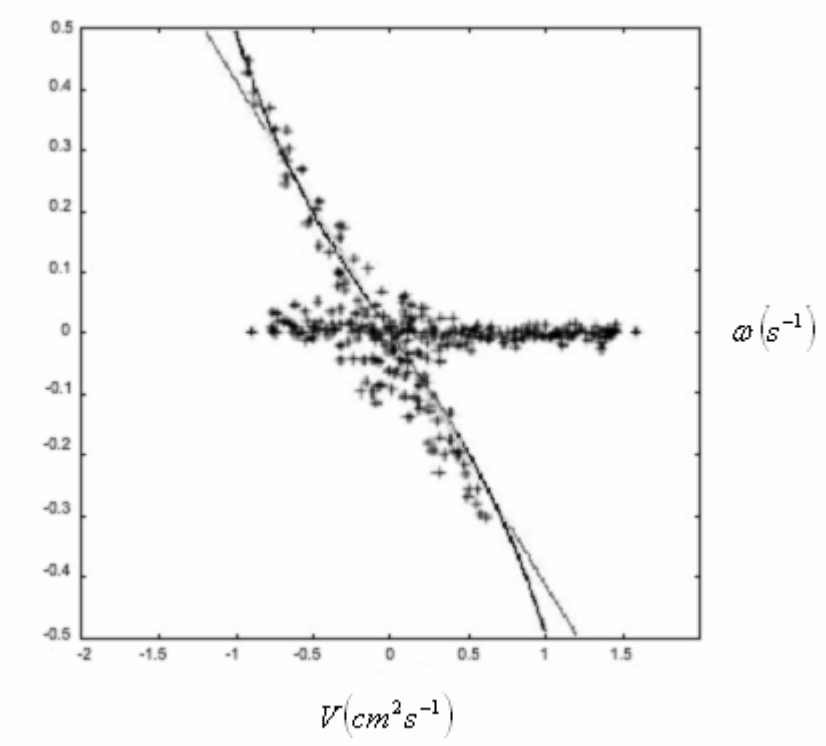

Figure 4.5: Vorticity-Stream function plot for a dipole structure.

Then, using ω and ψ, the equation of vorticity conservation becomes

$$\frac{\partial \omega}{\partial t} + J(\omega, \psi) = 0 \tag{4.14}$$

where ψ is the $\omega\left(s^{-1}\right)$stream function as defined previously and J denotes the Jacobian. So that in 2D flows with no dissipation we have conservation of (observed in figure 4.6)

Energy $$\overline{u^2} = \int_0^\infty E(k,t)dk \tag{4.15}$$

Enstrophy $$\overline{\omega^2} = \int_0^\infty k^2 E(k,t)dk \tag{4.16}$$

These simple relations, will be revised in the case of non-local dominant vortices (Cano et al. 2008), in the discussion chapter.

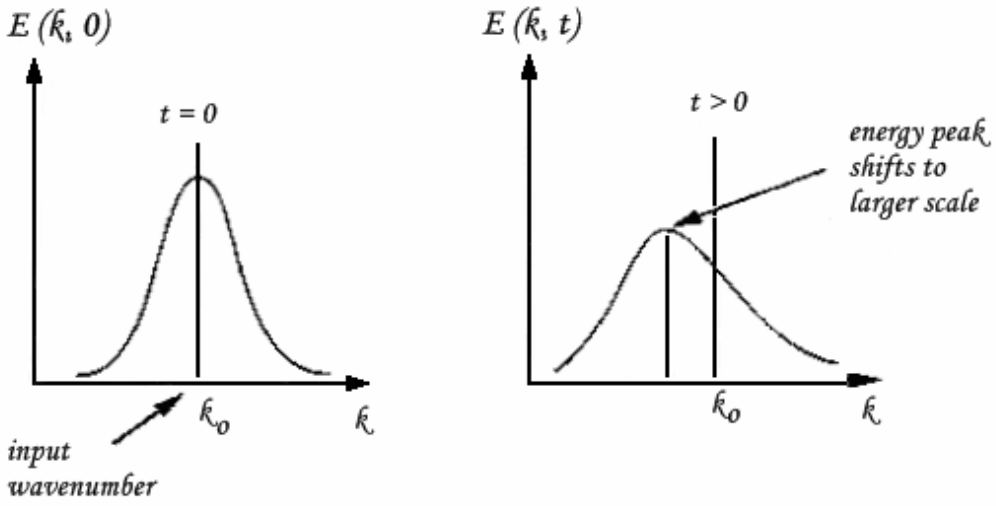

Figure 4.6: Energy peak shifts to larger scales (inverse energy cascade). Low rates of energy dissipation.

Conservation of enstrophy results from conservation of vorticity ω (no stretching or twisting). In a 2D flow with weak dissipation the above results hold approximately, when the 2D flow is not strict, but rotation and stratification force some form of laminarization as column structure, energy and enstrophy transfers are much more complicated, Cambon (2000).

4.3.2. Basic instabilities compare to Average Turbulent Continuity Reynolds Equations (RANS)

Each time a flow changes as a result of an instability, the ability to predict the details of the motion is reduced. The flow is turbulent, in case successive instabilities have reduced the level of predictability so much that it is appropriate to describe a flow statistically rather than in every detail. This implies that random features of the flow are dominant. One cannot however say that a turbulent flow is 'completely random'; to do so would define turbulence out of existences.

This approach seems likely to leave a 'grey area' of flows that one might or might not choose to call turbulent. It is in fact a moot point whether one would expect to be able to classify all flows as either turbulent or non-turbulent, equivalently, whether during transition to turbulence one should be able to designate the point at which turbulent motion begins.

The notion of loss of predictability is better understood through an example. Consider the motion in a Kármán vortex street[3] in the wake of an obstacle. The velocity at a point fixed relative to the obstacle varies periodically and roughly sinusoidally. The phase of this variation is arbitrary, depending on the small disturbances at the time the flow commenced. If, therefore, a prediction of the instantaneous velocity should be conducted, without making any observation, it cannot be given within certain limits. The degree of unpredictability is small. Only a single observation indicating the phase of the fluctuations is required for all the details of the flow to be determined. When, with increasing Reynolds number, a further instability causes loss of regularity in the array of vortices, the unpredictability is increased.

There is every reason to suppose that this loss of predictability occurs as a property of the Navier-Stokes and continuity equations, although these equations contain the determinism of classical mechanics. In the meantime, it is useful to illustrate the essential reason why a deterministic treatment of turbulent flows is not possible.

Static instability in the atmosphere leads to spontaneous vertical mixing (convection) in the form of thermals and possibly cumulus clouds. Vertical mixing may occur in a stable environment, in particular in the form of breaking waves. These breaking waves are a major cause of turbulence aloft, especially just above the planetary

[3] Is a term used for a repeating pattern of swirling vortices caused by the unsteady separation of flow of a fluid over bluff bodies.

boundary layer or near the jet stream, where they often produce clear-air turbulence dreaded by aviators. The evolution of these breaking waves has been described mathematically by Kelvin and Helmholtz, hence the term Kelvin-Helmholtz billows, the evolution of which is shown in figure 4.7.

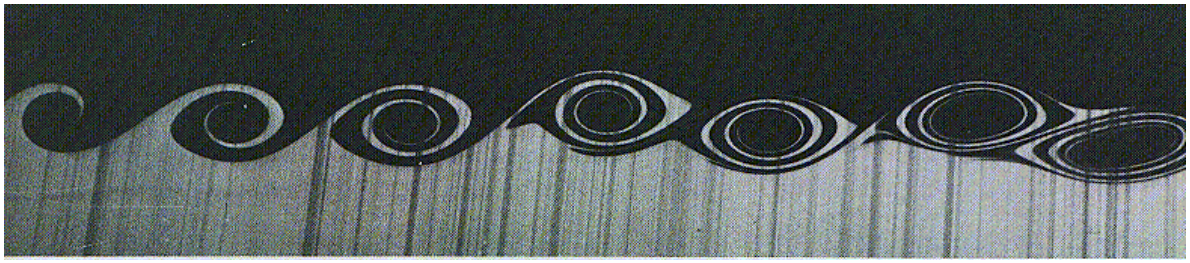

Figure 4.7: Idealized evolution of a Kelvin-Helmholtz billow when Ri < 0.25.

The likelihood of Kelvin-Helmholtz instability[4] can be evaluated by means of the Richardson's number, *Ri*, but other parameters may modify the flow topology.

The first analysis of shear instabilities was made by Kelvin (1898) and Helmholtz (1887). Richardson (1922) introduced the numbers named after him; although Taylor (1932) shows that he had derived similar parameters in 1914. Taylor published his results at the same time as Goldstein (1931). Analysing the stability of a piecewise stratified shear layer, they introduced what is now called the Taylor-Goldstein equation

$$\frac{d^2 w}{dz^2} = \left(\alpha^2 - \frac{1}{(c-U)} \frac{d^2 U}{dz^2} + \frac{Ri}{(c-U)^2} \left(\frac{dU}{dz} \right)^2 \right) w \qquad (4.17)$$

by applying normal modes to a homogenous inviscid two dimensional flow in the x-direction, and vertical density and velocity variations. The mean velocity is only allowed to vary in the vertical direction, but in the case of very weak acceleration or deceleration of the flow, or span-wise non uniformities of the mean velocity, which can be ignored, $\frac{\partial U}{\partial z}$ may be used instead of $\frac{dU}{dz}$. The Taylor-Goldstein equation is reduced to the Rayleigh equation

[4] Can occur when velocity shear is present within a continuous fluid or, when there is sufficient velocity difference across the interface between two fluids. One example is a wind blowing over a water surface, where the wind causes the relative motion between the stratified layers (i.e. water and air).

$$\frac{d^2}{dz^2} w = (U - c)\left(\frac{d^2}{dz^2} - \alpha^2 \right) w \tag{4.18}$$

The basic instabilities that the N-S equation can sustain, that depend mostly on the geometry (or topology) of the forcing and on the body forces such as buoyancy, rotation or magnetic fields. Unfortunately this "coherent structure" information is partly lost when we perform a statistical analysis on the equation for large Reynolds numbers. This procedure is called Reynolds averaging (RANS) and provides the average effect of the turbulent fluctuations on the average flow[5].

With the velocity divided into its mean and fluctuating parts, the continuity equation for incompressible fluids is

$$div(U + u) = 0 \tag{4.19}$$

that is

$$\partial (U_i + u_i) / \partial x_i = 0 \tag{4.20}$$

Averaging this equation,

$$\partial U_i / \partial x_i = 0 \tag{4.21}$$

Subtracting this result from the original equation, we have

$$\partial u_i / \partial x_i = 0 \tag{4.22}$$

The mean and fluctuating parts of the velocity field thus individually satisfy the usual form of the continuity equation. The same division applied to the Navier-Stokes equation gives

[5] New techniques that allow to sample only selected parts of the flow (VITA) or to model directly the large eddies (LES), or use averages of different size are very usefull (CHASSAIGN 2002, Redondo 1987).

$$\frac{\partial(U_i+u_i)}{\partial t}+(U_j+u_j)\frac{\partial(U_i+u_i)}{\partial x_j}=-\frac{1}{\rho}\frac{\partial(P+p)}{\partial x_i}+\nu\frac{\partial^2(U_i+u_i)}{\partial x_j^2} \qquad (4.23)$$

Carrying out the averaging process throughout this equation gives

$$\frac{\partial U_i}{\partial t}+U_j\frac{\partial U_i}{\partial x_j}+\overline{u_j\frac{\partial u_i}{\partial x_j}}=-\frac{1}{\rho}\frac{\partial P}{\partial x_i}+\nu\frac{\partial^2 U_i}{\partial x_j^2} \qquad (4.24)$$

which, with the help of the continuity equation (4.19), may be rewritten

$$U_j\frac{\partial U_i}{\partial x_j}=-\frac{1}{\rho}\frac{\partial P}{\partial x_i}+\nu\frac{\partial^2 U_i}{\partial x_j^2}-\frac{\partial}{\partial x_j}\left(\overline{u_i\,u_j}\right) \qquad (4.25)$$

This equation for the mean velocity U_i differs from the laminar flow equation by the addition of the last term. This term represents the action of the velocity fluctuations on the mean flow arising from the non-linearity of the Navier-Stokes equation. It is frequently large compared with the viscous term, with the result that the mean velocity distribution is very different from the corresponding laminar flow.

The character of this interaction between the mean flow and the fluctuations can more simply see in the context of a flow for which the two-dimensional boundary layer approximation applies. The turbulent fluctuations are always three-dimensional, but if the imposed conditions are two-dimensional, there is no variation of mean quantities in the third direction and terms such as $\partial\left(\overline{uw}\right)/\partial z$ are zero. Omitting such terms and terms that are small on the boundary layer approximation[6] in equation (4.25) gives

$$U\frac{\partial U}{\partial x}+V\frac{\partial U}{\partial y}=-\frac{1}{\rho}\frac{\partial P}{\partial x}+\nu\frac{\partial^2 U}{\partial y^2}-\frac{\partial}{\partial y}\left(\overline{uv}\right) \qquad (4.26)$$

This equation is applied to turbulent boundary layers, jets, wakes, etc.

[6] The boundary layer approximation is used here to its fullest extent. In studies of turbulent flows, some further terms (e.g. $\partial\left(\overline{u^2}\right)/\partial x$) are retained because measurements indicate that they are not so very small. Trinitron (1999).

Writing the last two terms of (4.26) as

$$\frac{1}{\rho}\frac{\partial}{\partial y}\left(\mu\frac{\partial U}{\partial y}-\rho\overline{uv}\right) \tag{4.27}$$

shows that the velocity fluctuations produce a stress on the mean flow. A gradient of this produces a net acceleration of the fluid in the same way as a gradient of the viscous stress. The quantity $\left(-\rho\overline{uv}\right)$, and more generally the quantity $\left(-\rho\overline{u_i\, v_j}\right)$, is called a Reynolds stress.

The Reynolds stress arises from the correlation of two components of the velocity fluctuation at the same point. A non-zero value of this correlation implies that the two components are not independent of one another. For example, if $\overline{uv}$ is negative, then at moments at which *u* is positive, υ is more likely to be negative than positive; conversely when *u* is negative. Putting

$$u' = (u+v)/\sqrt{2} \quad v' = (v-u)/\sqrt{2} \tag{4.28}$$

gives

$$\overline{uv} = \frac{1}{2}\left(\overline{u'^2} - \overline{v'^2}\right) \tag{4.29}$$

Figure 4.8 shows the geometrical significance of this.

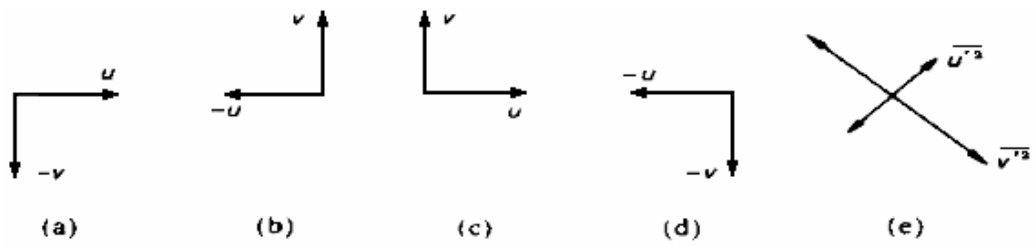

Figure 4.8: Geometrical interpretation of Reynolds stress if patterns of velocity fluctuations shown in (a) and (b) occur more frequently than those in (c) and (d), giving negative $\overline{uv}$, then $\overline{v'^2}$ is larger than $\overline{u'^2}$ as indicated by (e), Tritton (1999).

One can readily see how a correlation of this kind can arise in a mean shear flow. We may consider the case of positive $\partial U/\partial y$ as shown in figure 4.8. A fluid particle with positive v is being carried by the turbulence in the positive *y*-direction. It is coming from a region where the mean velocity is smaller and it is thus likely to be moving downstream more slowly than its new environment, i.e. it is more likely to have negative *u* than positive. Similarly negative *v* is more likely to be associated with positive *u*. The analogy has led to the definition of a quantity ν_T such that

$$-\overline{uv} = \nu_T \, \partial U/\partial y \tag{4.30}$$

ν_T is called the eddy viscosity. It is important to realize that ν_T is a representation of the action of the turbulence on the mean flow and not a property of the fluid. It is moreover a representation that simplifies the dynamics of that action, because of the large-scale coherent motions. The Reynolds stress (shown in figure 4.9) at any point depends on the whole velocity profile, not just on the local gradient. Although it is sometimes useful for approximate calculations to suppose that ν_T is an (empirical) constant, in general (equation 4.30) should be regarded as the defining equation of ν_T rather than an equation for $\overline{uv}$.

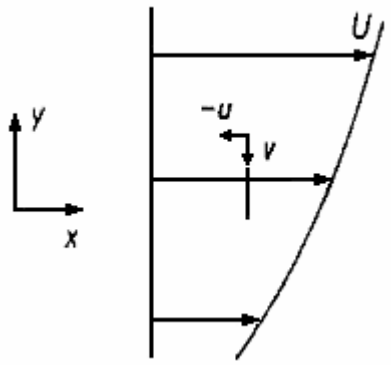

Figure 4.9: To illustrate the generation of a Reynolds stress in a mean velocity gradient.

4.3.3. Turbulent Energy and Transport Equations

Further understanding of the interaction between the mean flow and the fluctuations is obtained from the equation for the kinetic energy of the turbulence. Subtracting equation (4.24) from equation (4.23) to investigate just the velocity fluctuation gives

$$\frac{\partial u_i}{\partial t}+U_j\frac{\partial u_i}{\partial x_j}+u_j\frac{\partial U_i}{\partial x_j}+u_j\frac{\partial u_i}{\partial x_j}-\overline{u_j\frac{\partial u_i}{\partial x_j}}=-\frac{1}{\rho}\frac{\partial p}{\partial x_i}+\nu\frac{\partial^2 u_i}{\partial x_j^2} \qquad (4.31)$$

Multiplying this by u_i and averaging

$$\frac{1}{2}\frac{\partial\overline{\left(u_i^2\right)}}{\partial t}+\frac{1}{2}U_j\frac{\partial\overline{\left(u_i^2\right)}}{\partial x_j}=-\overline{u_i u_j}\frac{\partial U_i}{\partial x_j}-\frac{1}{2}\frac{\partial}{\partial x_j}\left(\overline{u_i^2 u_j}\right)-\frac{1}{\rho}\frac{\partial}{\partial x_i}\left(\overline{p u_i}\right)+\nu\overline{u_i\frac{\partial^2 u_i}{\partial x_j^2}} \qquad (4.32)$$

(where the rearrangement of terms has made use of the continuity equation 4.19). Since the summation convention is being applied, the mathematics involves multiplying each component of the dynamical equation (4.31) by the corresponding velocity component and then adding the three resulting equations. For steady mean conditions the first term of equation (4.32) is zero, but it indicates the physical significance of the equation, in view of the summation convention

$$\overline{u_i^2}=\overline{q^2}=\sum_{i=1}^{3}u_i^2=2E_c \qquad (4.33)$$

and so each term in the equation represents some process tending to increase or decrease the kinetic energy of the turbulence.

With the boundary layer approximation applied to a flow, which is steady and two-dimensional in the mean, with just horizontal shear $\frac{dV}{dy}$ equation (4.32) becomes

$$\frac{1}{2}U\frac{\partial\overline{\left(q^2\right)}}{\partial x}+\frac{1}{2}V\frac{\partial\overline{\left(q^2\right)}}{\partial y}=-\overline{u\upsilon}\frac{\partial U}{\partial y}-\frac{\partial}{\partial y}\left(\frac{1}{2}\overline{q^2 v}+\frac{1}{\rho}\overline{pv}\right)+\nu\overline{u_i\frac{\partial^2 u_i}{\partial x_j^2}} \qquad (4.34)$$

The left-hand side and the second term on the right-hand side are terms that show the interaction between the turbulent kinetic energy and the mean flow $(u,v,0)$ and become zero when integrated over the whole flow. They represent the transfer of energy from place to place, respectively transfer by the mean motion and transfer by the turbulence itself. As in a laminar flow, the viscous term can be divided into two parts: one is essentially negative and thus represents viscous dissipation; the other (usually small) integrates to zero and so is another energy transfer process. The input of energy to compensate for the dissipation must be provided by the only remaining term, $\left(-\overline{uv}\,\partial U/\partial y\right)$. We have seen that $\overline{uv}$ is likely to be negative where $\partial U/\partial y$ is positive, giving this term the required sign. Although local regions of positive $\left(\overline{uv}\,\partial U/\partial y\right)$ can occur, they cannot occupy the majority of the flow or the turbulence cannot be maintained.

The equation for the energy of the mean flow contains a corresponding term of the opposite sign. The term thus represents a transfer of energy from the mean flow to the turbulence. One can therefore say that the Reynolds stress works against the mean velocity gradient to remove energy from the mean flow, just as the viscous stress works against the velocity gradient. However, the energy removed by the latter process is directly dissipated, reappearing as beat, whereas the action of the Reynolds stress provides energy for the turbulence. This energy is ultimately dissipated by the action of viscosity on the turbulent fluctuations. Frequently, the loss of mean flow energy to turbulence is large compared with the direct viscous dissipation.

The more general transport equations are obtained for each of the term of the correlation $\overline{u_i' u_j'}$. After manipulating the product of each component at the velocity time the Navier-Stokes equation applies to the other component in the following fashion:

$$\overline{u_i' \, NS\left(u_j'\right) + u_j' \, NS\left(u_i'\right)} \tag{4.35}$$

we obtain the following equations:

$$
\begin{aligned}
&\frac{\partial}{\partial t}\left(\frac{\overline{u_i u_j}}{2}\right)+U_l\frac{\partial\overline{u_i u_j}}{\partial x_l}= \\
&-\left(\overline{u_i u_l}\frac{\partial U_j}{\partial x_l}+\overline{u_j u_l}\frac{\partial U_i}{\partial x_l}\right)+\overline{\frac{p'}{\rho}\left(\frac{\partial u_i}{\partial x_j}+\frac{\partial u_j}{\partial x_i}\right)} \\
&-\frac{\partial}{\partial x_l}\left(\overline{u_i u_j u_l}\right)-\frac{1}{\rho}\left(\frac{\partial}{\partial x_i}\overline{p'u'_j}+\frac{\partial}{\partial x_j}\overline{p'u'_i}\right) \\
&+\nu\left(\overline{u_i\frac{\partial^2 u_j}{\partial x_l^2}}+\overline{u_j\frac{\partial^2 u_i}{\partial x_l^2}}\right)+\left(\overline{f'_i u_j}+\overline{f'_j u_i}\right)
\end{aligned}
\tag{4.36}
$$

where the meaning of each of the term (shown in figure 4.10) is: the first term at right of equality corresponds to the creation by mean shear (1), the second to the return to isotropy by action of pressure fluctuation *p'* (2), the third to the transport of fluctuations (of correlations) (3), the fourth to the pressure transport (4), fifth to the viscosity destruction and transport by $\nu(\varepsilon)$ (5), and the sixth to the generation or destruction by massive forces (*f* if is rotation and *g* if is gravitation – stratification) (6).

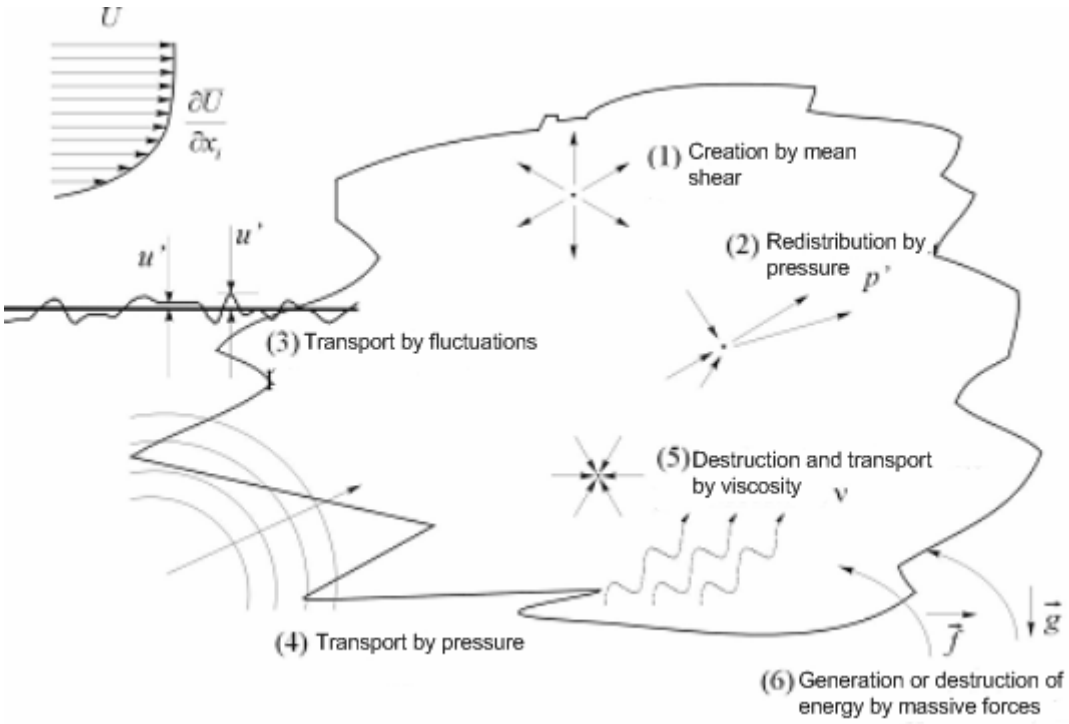

Figure 4.10: The generation and destruction of energy.

4.4. Turbulence Vorticity in 3D flows

Vorticity is the rotation of air around a vertical axis. Relative and absolute vorticity are defined as the z-components of the curls of relative (i.e., in relation to Earth's surface) and absolute wind velocity, respectively.
This gives:

$$\omega' = \frac{\partial \upsilon_r'}{\partial x} - \frac{\partial u_r'}{\partial y} \tag{4.37}$$

for relative vorticity and

$$\omega = \frac{\partial \upsilon_a}{\partial x} - \frac{\partial u_a}{\partial y} \tag{4.38}$$

for absolute vorticity, where u and υ are the zonal (x direction) and meridian (y direction) components of wind velocity. The absolute vorticity at a point can also be expressed as the sum of the relative vorticity at that point and the Coriolis parameter at that latitude.

A useful related quantity is potential vorticity. The absolute vorticity of an air mass will change if the air mass is stretched (or compressed) in the z direction. But if the absolute vorticity is divided by the vertical spacing between levels of constant entropy (or potential temperature), the result is a conserved quantity of adiabatic flow, termed potential vorticity.

Cano et al. (2008) recaptures the hypothesis developed by Reynolds and Taylor (1932) and decomposes the flow in mean and fluctuations and applies it to the vorticity vector for turbulent flow as:

$$\omega = \overline{\omega} + \omega' \tag{4.39}$$

being ω the vorticity vector, $\overline{\omega}$ the average vorticity vector and ω' the turbulent perturbation of the vorticity vector. From this moment $\overline{\omega}$ is interpreted as the average rotation at which a turbulent eddy would be developed. ω is the rotation imposed by

turbulent flow for each of flowing volume elements that constitute. Therefore ω' is the difference between the actual and the average rotation of the eddy. Using this kind of decomposition to different components of vorticity vortex is obtained:

$$\omega=\left(\overline{\zeta}+\zeta',\overline{\eta}+\eta',\overline{\omega}+\omega'\right) \tag{4.40}$$

where (ζ,η,ω) are the three components mentioned on the (x,y,z) axes respectively. Using the corresponding algebra to average values and derivatives it is possible to prove easily the relations among the average and perturbed components of the vorticity vector and the corresponding velocity vector components (for the average components equation 4.41 and for the fluctuating ones 4.42):

$$\begin{aligned}\overline{\zeta}&=\left(\frac{\partial\overline{w}}{\partial y}-\frac{\partial\overline{v}}{\partial z}\right)\\ \overline{\eta}&=\left(\frac{\partial\overline{u}}{\partial z}-\frac{\partial\overline{w}}{\partial x}\right)\\ \overline{\omega}&=\left(\frac{\partial\overline{v}}{\partial x}-\frac{\partial\overline{u}}{\partial y}\right)\end{aligned} \tag{4.41}$$

$$\begin{aligned}\zeta'&=\left(\frac{\partial w'}{\partial y}-\frac{\partial v'}{\partial z}\right)\\ \eta'&=\left(\frac{\partial u'}{\partial z}-\frac{\partial w'}{\partial x}\right)\\ \omega'&=\left(\frac{\partial v'}{\partial x}-\frac{\partial u'}{\partial y}\right)\end{aligned} \tag{4.42}$$

Considering an isotropic turbulent flow is easy to obtain the following condition for the three perturbed components of the vorticity vector:

$$u'=v'=-w' \tag{4.43}$$

This condition can take place in a geophysical, Ocean or Atmospheric flow, only far from thermal generators or mechanical turbulence. Using this isotropy expression is deduced:

$$\begin{aligned}\zeta' &= \left(\frac{\partial w'}{\partial y} - \frac{\partial v'}{\partial z}\right) = \left(\frac{\partial(-u')}{\partial y} - \frac{\partial u'}{\partial z}\right) \\ \eta' &= \left(\frac{\partial u'}{\partial z} - \frac{\partial w'}{\partial x}\right) = \left(\frac{\partial u'}{\partial z} - \frac{\partial(-u')}{\partial x}\right) \\ \omega' &= \left(\frac{\partial v'}{\partial x} - \frac{\partial u'}{\partial y}\right) = \left(\frac{\partial u'}{\partial x} - \frac{\partial u'}{\partial y}\right)\end{aligned} \tag{4.44}$$

and further is shown a new characteristic of perturbed components of vorticity vector in isotropy without any body forces:

$$\zeta' + \eta' - \omega' = 0 \rightarrow \zeta' + \eta' = \omega' \tag{4.45}$$

Applying the rotational operator to the Navier-Stokes equation, the vorticity equation with no body forces is obtained:

$$\frac{d\omega}{dt} = \nabla p \times \nabla\left(\frac{1}{\rho}\right) + \omega \cdot \nabla v - \omega \, div v \tag{4.46}$$

The new form of the motion equation of the kinetic energy and vorticity is:

$$\begin{aligned}\frac{\partial u}{\partial t} + \frac{1}{2}\frac{\partial}{\partial x}\left(u^2 + v^2 + w^2\right) + w\eta - v\omega &= -\frac{1}{\rho}\frac{\partial p}{\partial x} \\ \frac{\partial v}{\partial t} + \frac{1}{2}\frac{\partial}{\partial y}\left(u^2 + v^2 + w^2\right) + u\omega - w\zeta &= -\frac{1}{\rho}\frac{\partial p}{\partial y} \\ \frac{\partial w}{\partial t} + \frac{1}{2}\frac{\partial}{\partial z}\left(u^2 + v^2 + w^2\right) + v\zeta - u\eta &= -\frac{1}{\rho}\frac{\partial p}{\partial z}\end{aligned} \tag{4.47}$$

Considering the O. Reynolds decomposition applied this time to vorticity:

$$\begin{aligned}
&\frac{\partial \bar{u}}{\partial t}+\frac{\partial}{\partial x}\left(\overline{E_c}\right)+\frac{\partial}{\partial x}\left(\overline{E_c}'\right)+\bar{w}\bar{\eta}+\overline{w'\eta'}-\bar{v}\bar{\omega}-\overline{v'\omega'}=-\frac{1}{\rho}\frac{\partial p}{\partial x}\\
&\frac{\partial \bar{v}}{\partial t}+\frac{\partial}{\partial y}\left(\overline{E_c}\right)+\frac{\partial}{\partial y}\left(\overline{E_c}'\right)+\bar{u}\bar{\omega}+\overline{u'\omega'}-\bar{w}\bar{\zeta}-\overline{w'\zeta'}=-\frac{1}{\rho}\frac{\partial p}{\partial y}\\
&\frac{\partial \bar{w}}{\partial t}+\frac{\partial}{\partial z}\left(\overline{E_c}\right)+\frac{\partial}{\partial z}\left(\overline{E_c}'\right)+\bar{v}\bar{\zeta}+\overline{v'\zeta'}-\bar{u}\bar{\eta}-\overline{u'\eta'}=-\frac{1}{\rho}\frac{\partial p}{\partial z}
\end{aligned} \tag{4.48}$$

where $\bar{u},\bar{v},\bar{w}$ are the three components of velocity vector; $\bar{\zeta},\bar{\eta},\bar{\omega}$ are the three components of the average vorticity vector; $\overline{E_c}$ the average kinetic energy of motion; u',v',w' the three perturbed components of velocity vector; ζ',η',ω' the three perturbed components of vorticity vector; $\overline{E_c'}$ the average of the perturbed kinetic energy, that is to say $\frac{1}{2}\left(\overline{u'^2}+\overline{v'^2}+\overline{w'^2}\right)$ and *P* the pressure. Considering steady mean flow and such coordinates system than $\bar{v}=\left(\bar{u},0,0\right)$ this system is simplified to:

$$\begin{aligned}
&\frac{\partial}{\partial x}\left(\overline{E_c}\right)+\frac{\partial}{\partial x}\left(\overline{E_c}'\right)+\overline{w'\eta'}-\overline{v'\omega'}=-\frac{1}{\rho}\frac{\partial p}{\partial x}\\
&\frac{\partial}{\partial y}\left(\overline{E_c}\right)+\frac{\partial}{\partial y}\left(\overline{E_c}'\right)+\bar{u}\bar{\omega}+\overline{u'\omega'}-\overline{w'\zeta'}=-\frac{1}{\rho}\frac{\partial p}{\partial y}\\
&\frac{\partial}{\partial z}\left(\overline{E_c}\right)+\frac{\partial}{\partial z}\left(\overline{E_c}'\right)+\overline{v'\zeta'}-\bar{u}\bar{\eta}-\overline{u'\eta'}=-\frac{1}{\rho}\frac{\partial p}{\partial z}
\end{aligned} \tag{4.49}$$

in the same way, using $\bar{u}=\bar{u}\left(y,z\right)$ in a 3D coordinate system, we obtain:

$$\begin{aligned}
&\frac{\partial}{\partial x}\left(\overline{E_c}'\right)+\overline{w'\eta'}-\overline{v'\omega'}=-\frac{1}{\rho}\frac{\partial p}{\partial x}\\
&\frac{\partial}{\partial y}\left(\overline{E_c}\right)+\bar{u}\frac{\partial}{\partial y}\left(\overline{E_c}'\right)+\bar{u}\bar{\omega}+\overline{u'\omega'}-\overline{w'\zeta'}=-\frac{1}{\rho}\frac{\partial p}{\partial y}\\
&\frac{\partial}{\partial z}\left(\overline{E_c}\right)+\bar{u}\frac{\partial}{\partial z}\left(\overline{E_c}'\right)+\overline{v'\zeta'}-\bar{u}\bar{\eta}-\overline{u'\eta'}=-\frac{1}{\rho}\frac{\partial p}{\partial z}
\end{aligned} \tag{4.50}$$

finally, it can be written in vector form as:

$$\nabla\left(\overline{E_c'}\right)+\nabla\bar{v}\cdot\bar{v}+\bar{\omega}\times\bar{v}+\overline{\omega'\times v'}=-\frac{\nabla p}{\rho} \tag{4.51}$$

or

$$\nabla\left(\overline{E_c'}\right)+\bar{v}\nabla\bar{v}+\overline{\omega'\times v'}=-\frac{\nabla p}{\rho} \tag{4.52}$$

From equation 4.52 it is possible to obtain a sample equation with the non-linear terms and similar flow conditions and coordinate system $\bar{v}=\left(\bar{u},0,0\right)$ as:

$$\frac{\partial\bar{v}}{\partial t}+\bar{v}\cdot\nabla\bar{v}=-\frac{1}{\rho}\nabla p-\overline{v'\cdot\nabla v'} \tag{4.53}$$

using the corresponding components of vectors (Cano et al. 2008) obtain the following system, that avoid pressure fluctuation ($P=\bar{P}$) and baroclinic terms.

$$\begin{aligned}
&\frac{\partial}{\partial x}\left(\overline{u'u'}\right)+\frac{\partial}{\partial y}\left(\overline{u'v'}\right)+\frac{\partial}{\partial z}\left(\overline{u'w'}\right)=-\frac{1}{\rho}\frac{\partial\bar{p}}{\partial x}\\
&\bar{u}\frac{\partial\bar{v}}{\partial x}+\frac{\partial}{\partial x}\left(\overline{v'u'}\right)+\frac{\partial}{\partial y}\left(\overline{v'v'}\right)+\frac{\partial}{\partial z}\left(\overline{v'w'}\right)=-\frac{1}{\rho}\frac{\partial\bar{p}}{\partial x}\\
&\bar{u}\frac{\partial\bar{w}}{\partial x}+\frac{\partial}{\partial x}\left(\overline{w'u'}\right)+\frac{\partial}{\partial y}\left(\overline{w'v'}\right)+\frac{\partial}{\partial z}\left(\overline{w'w'}\right)=-\frac{1}{\rho}\frac{\partial\bar{p}}{\partial x}
\end{aligned} \tag{4.54}$$

If we suppose that for the small scales this system admits the local isotropic hypothesis, we may then use:

$$\overline{u'u'}=\overline{u'v'}=\overline{w'w'}=\overline{v'v'}=-\overline{v'w'}=-\overline{u'w'} \tag{4.55}$$

Therefore, equation (4.54) may be simplified to:

$$
\begin{aligned}
&-2\overline{w'\frac{\partial u'}{\partial x}}-2\overline{w'\frac{\partial u'}{\partial y}}+2\overline{w\frac{\partial u'}{\partial z}}=-\frac{1}{\rho}\frac{\partial \bar{p}}{\partial x}\\
&\bar{u}\frac{\partial \bar{v}}{\partial x}-2\overline{w'\frac{\partial u'}{\partial x}}-2\overline{w'\frac{\partial u'}{\partial y}}+2\overline{w\frac{\partial u'}{\partial z}}=-\frac{1}{\rho}\frac{\partial \bar{p}}{\partial x}\\
&\bar{u}\frac{\partial \bar{w}}{\partial x}-2\overline{w'\frac{\partial u'}{\partial x}}-2\overline{w'\frac{\partial u'}{\partial y}}+2\overline{w\frac{\partial u'}{\partial z}}=-\frac{1}{\rho}\frac{\partial \bar{p}}{\partial x}
\end{aligned}
\tag{4.56}
$$

and we also have for the average pressure:

$$
-\frac{1}{\rho}\frac{\partial \bar{p}}{\partial x}=-\frac{1}{\rho}\frac{\partial \bar{p}}{\partial y}-\bar{u}\frac{\partial \bar{v}}{\partial x}=\frac{1}{\rho}\frac{\partial \bar{p}}{\partial z}+\bar{u}\frac{\partial \bar{w}}{\partial x} \tag{4.57}
$$

Finally through the turbulent vorticity components the following system of equations is proposed to relate velocity, vorticity components and pressure:

$$
\begin{aligned}
\overline{2w'(\omega'+\eta')}&=-\frac{1}{\rho}\frac{\partial \bar{p}}{\partial x}\\
\bar{u}\frac{\partial \bar{v}}{\partial x}+\overline{2w'(\omega'+\eta')}&=-\frac{1}{\rho}\frac{\partial \bar{p}}{\partial y}\\
\bar{u}\frac{\partial \bar{w}}{\partial x}+\overline{2w'(\omega'+\eta')}&=-\frac{1}{\rho}\frac{\partial \bar{p}}{\partial z}
\end{aligned}
\tag{4.58}
$$

This system indeed does not consider body forces, nor the anisotropy induced by them, but assuming that small scales are not affected as much as the large scales and force a vertical squashing in case of stable buoyancy, or a vertical elongation in case of the fast rotation.

It is important to investigate the topology of the flow, especially when non-homogeneous turbulence is produced by one or several body forces like buoyancy, rotation or magnetic fields. The role of internal or inertial waves could affect the locality of the cascade processes and these effects will be discussed after the presentation of the experimental results in chapter 7.

CHAPTER 5

Fractal and Multifractal Analysis in Environmental Turbulence

5.1. Dimensional Analysis and Scales

In order to compare scales of molecular and turbulent diffusion, we first take an imposed length scale to compare times and next an imposed time scale to compare lengths. Take as an example the diffusion of a gas in a room with dimension L. From the diffusion equation one may estimate the order of magnitude

$$\frac{\delta C}{T_m} \propto D\frac{\delta C}{L^2} \tag{5.1}$$

where δC is a concentration difference, which will be reached by molecular diffusion at distance L after time T_m. If the velocity of the major eddies in the room is u, the corresponding time scale T_t becomes

$$T_t = \frac{L}{u} \tag{5.2}$$

The ratio of both times may be expressed as

$$\frac{T_t}{T_m} \propto \frac{L}{u}\frac{D}{L^2} = \frac{D}{uL} \propto \frac{\nu}{uL} = \frac{1}{\mathrm{Re}} \tag{5.3}$$

where it was used that the diffusion coefficient D for air and kinematics viscosity for air ν are of the same order of magnitude. The interesting point is that turbulent transport usually is much quicker than molecular diffusion, for instance, we can smell a cigar 10 metres away after few minutes.

If we focus in the smallest eddies, the rate of energy dissipation ε per unit of mass has the dimension of m^2s^{-3}. The dynamic factor governing this dissipation must be the kinematic viscosity ν with a dimension of m^2s^{-1}. It is now possible to identify the Kolmogorov scales for length η_k, time τ and velocity u as

$$\eta_k = \left(\frac{\nu^3}{\varepsilon}\right)^{1/4}$$
$$\tau = \left(\frac{\nu}{\varepsilon}\right)^{\frac{1}{2}} \qquad (5.4)$$
$$u = (\nu\varepsilon)^{\frac{1}{4}}$$

The Reynolds number on this scale becomes

$$\mathrm{Re} = \frac{u\eta_k}{\nu} = 1 \qquad (5.5)$$

which illustrates that viscosity dominates the processes on this scale. The basic assumption, which agrees with observation, is that large eddies with length and velocity scales *l* and *u* lose their energy when they have travelled a distance of the order of *l*. The associated time is l/u. The kinetic energy of a unit of mass is of the order u^2, so the energy a unit of mass is losing per second becomes u^3/l. On average this should be equal to the rate ε with the smallest eddies are dissipating their kinetic energy into head,

$$\varepsilon = \frac{u^3}{l} \qquad (5.6)$$

Then the relation between the sizes of small and large eddies become (already mentioned in chapter 1):

$$\frac{\eta_k}{l} = \left(\frac{\nu^3}{u^3 l^3}\right)^{1/4} = \mathrm{Re}^{-3/4} \qquad (5.7)$$

With Reynolds numbers in the order of $Re \approx 10^4$, length scales differ by an order of 10^3. Numerical grids to perform calculations should describe both eddies at the same time, which is computationally out of reach nowadays. This illustrates the need for physically sensible approximations. A similar relation holds for the time scales:

$$\frac{\tau}{t} = \frac{\tau}{l/u} = \mathrm{Re}^{-1/4} \tag{5.8}$$

The angular velocities in eddies are inversely proportional to the time scales. Therefore, they will be the largest for the smallest eddies.

This observation is also related to the notion that there is more energy dissipation ε at the smallest scales. The experimental observation that the scaling laws in turbulence depended on size led to the fractal (Mandelbrot 1985) and multifractal models of turbulence (Frisch 1995). It was only natural to relate the physical and spectral (in Fourier space) approaches in the study of turbulence and to relate fractal (geometrical aspects) to the concept of intermittency.

5.2. *Fractal analysis and turbulent cascades*

The analysis of convoluted surfaces and its application to turbulence was followed by a rapid expansion mostly due to the works of Mandelbrot 1985 who gave practical definitions of fractal dimensions of real objects. Fractal objects, as they are called, display self-similarity over a range. The Hausdorff dimension can be used to describe them for physical objects. In general, there is a limited range where self-similarity applies. In turbulence this range is found between the largest scale and the Kolomogorow scale. A practical definition of the fractal dimension, D_i can be given as

$$D_i = \frac{\log N}{\log\left(\frac{1}{\sigma}\right)} \tag{5.9}$$

where N is the number of self-similar parts or covering boxes at size σ. An extension of the fractal dimension to a set where different isolines have different fractal dimensions may be done using multifractals. For a fractal curve, its measured length L will have a power law dependence on the measuring yardstick as:

$$L \propto \sigma^{1-D_i} \tag{5.10}$$

The exponent D_i is called the fractal dimension of the curve and is a measure of the roughness of fragmentation of the curve and have the subindex i represents the Euclidean dimension of the embedding space $i = \{1,2,3,.....n\}$. The fractal convolutions of turbulent interfaces will increase the area between different marked regions of the flow. In similar way as above we can express the area determined by the fractal set as

$$A \propto \sigma^{2-D_2} \tag{5.11}$$

If the range of scales where self-similarity is exhibited is limited by, say, a large scale l and a small scale, say the Kolomogorow length scale η_k, then the increase in area of a turbulent interface due to the fractal behaviour, which at scales comparable to l measures A_l, is

$$A_l \left(\left(\frac{l}{\eta} \right)^{2-D_2} - 1 \right) \tag{5.12}$$

This increase in contact area needs to be taken into account when mixing through density interfaces is discussed. This geometrical descriptor is useful in different circumstances as higher fractal dimensions generally indicate more flow convolutions. Multifractal analysis will aid in the parameterizations of the different mixing efficiencies produced by the different basic instabilities.

For example if we perform a box-counting algorithm count to the different energy and vorticity contours in decaying turbulence on the wake of an interface (Redondo et al. (2009)). We realize that the flow is dominated by less and less vortices considered as coherent structures and at the same time, as the spectra becomes more non-local (i.e. steeper), the fractal dimension decreases as first realised by Redondo (1990) and Vassilicos et al. (1991).

5.3. Ima – Calc – The Box counting Method

The software *Ima-Calc* will be used here to calculate the fractal dimension of images through a Box-counting algorithm. Furthermore, it includes simple processing tools and images analysis. Consider putting the fractal on a sheet of graph paper, where the side of each box is size *h*. Instead of finding the exact size of the fractal we count the number of boxes that are not empty. Let this number be *n*. Making the boxes smaller gives you more detail, which is the same as increasing the magnification. In fact, the magnification, *e*, is equal to *1/h*. The formula for fractal dimension is $D_i = \log n / \log e$, or, equivalently: $D_i = \log n / \log(1/h)$. If *h* is smaller, the dimension will be more accurate. For 3-D_2 fractals we can do the same with cubes instead of squares, and for 1-D_1 fractals we can use line segments. For example, we can calculate the fractal dimension of an object using the Box-Counting Fractal method (see in figure 5.1) by counting numerically all boxes that intersect a certain value of the scalar value of the image.

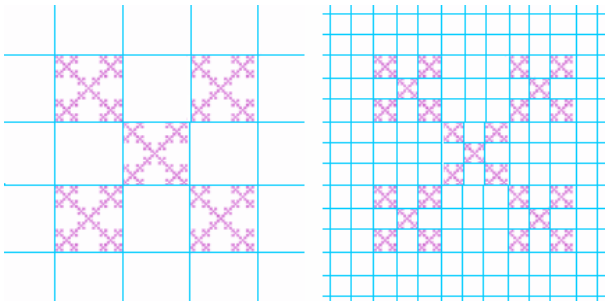

Figure 5.1: The Box-counting method for a fractal set.

It is very interesting to relate the fractal dimension D_i to the frequency spectrum or to the spatial spectra obtained from the Fourier transform of the time or spatial correlation functions usual in studies of turbulence. The reason is that from such frequency spectrum the corresponding fractal dimension may be derived, if the tracer scalar is passively adverted by a turbulent flow. Then the fractal dimension might be related to the energy of the turbulence with a certain spatial or temporal dependence, and then the frequency spectrum exponent, provided an inertial subrange exists, is a function of the box-counting fractal dimension as demonstrated by Redondo (1990).

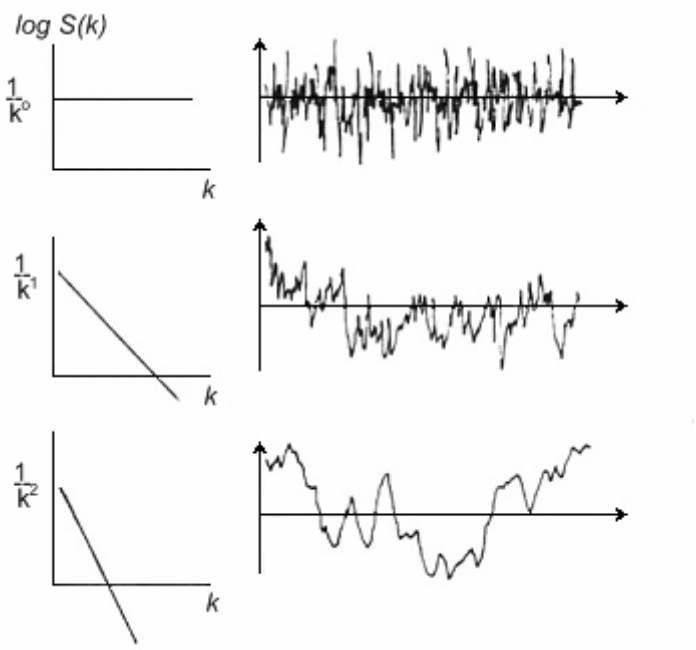

Figure 5.2: Relationship between the spectral slope and the signal.

If we assume that the frequency spectrum has a well defined shape over a significant range of frequencies, similar to ($E(k) \propto k^{-p}$)

$$S(f) = f^{-p} \tag{5.13}$$

In figure 5.2 we can see the dependence between the structure of the signal and its furrier power spectra, the three signals would correspond to noise (top), fractional Brownian motion (centre) which is close to a turbulent measurement and Brownian motion (bottom), which is much smoother. Even steeper spectra are dominated by the low wavenumber (large) structures and tend to be non-local.

Using the variance of the signal $\rho(t)$ defined from:

$$V(T) = \left\langle \left(\rho(t+T) - \rho(t)^2 \right) \right\rangle \tag{5.14}$$

where $\langle\ \rangle$ denotes the average over the entire period, T and the dependence for fractal time series $V(T) \approx T^{2H}$ (Voss 1985, 1988). Using $T = 1/f$ and the description of the spectral density function, $S(f)$, we have equivalently

$$S(f) \approx T^{p} \tag{5.15}$$

and

$$S \alpha T \int_{0}^{T} \rho^{2}(t) e^{-ift}\, dt \approx TV \tag{5.16}$$

so we can relate

$$S(f) \approx TV \approx T^{2H+1} \approx T^{2E_u+1-2D} \tag{5.17}$$

so the relationship between the exponent of the spectral density function and the fractal dimension is:

$$p = 2E_u + 1 - 2D_{E_u} \qquad D_{E_u} = E_u + \frac{1-p}{2} \tag{5.18}$$

These geometrical-dynamical equivalences may be used to check different methodologies of fractal dimension calculations. The multifractal analysis gives even more information on the scaling of the different intensity levels of the image. Each set of values of an image property, which in the case of SAR image is the level of reflectivity indicating surface roughness, of the temperature in case of Atmospheric infrared images, or concentration in a laboratory experiment, etc. has a certain fractal dimension, D_{E_u} embedded in a space of Euclidian dimension E_u, which expresses the level of self-similarity in space. This topological property may be studied. To calculate the single or maximum fractal dimension, as discussed above, the Box-Counting method used produces coverage of the object and the simplest method is to characterize it with boxes of side *e*. For the plane, these boxes will be square and for an object in space they will be cubes. The distribution of the boxes is accomplished systematically; the intersection of these with the object shows that we have n boxes with a non void intersection.

For each one of the possible ranges of intensity in the selected images, we can apply in an iterative fashion, the usual fractal dimension calculation with the box-counting method and we will obtain a corresponding fractal dimension for each intensity level. The result of the process will be a set of dimension values, function of the local intensity relating the coverage of E_u sized boxes with their number as

$$D_{E_u}(i) = -\frac{\ln n(e,i)}{\ln e(i)} \tag{5.19}$$

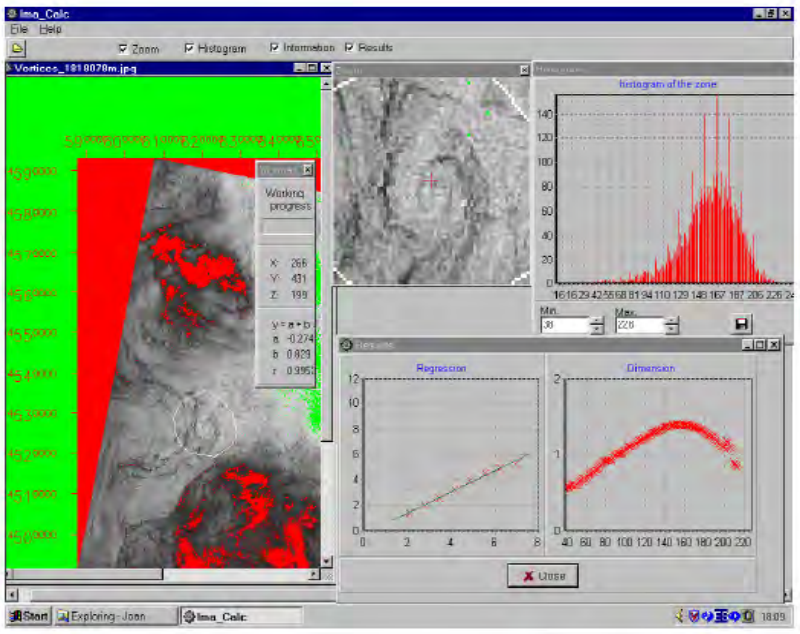

Figure 5.3: Description of a typical analysis of the multifractal structure of a vortex with the Imacalc program showing the screen display and options.

By means of this methodology we have for each Laboratory or Satellite image intensity level, the corresponding value of the fractal dimension for different groupings of the levels that allow a multi-fractal characterisation of the feature under study. In figure 5.3 a typical analysis of the multifractal structure of a vortex is shown in the Imacalc program, dialog box, Grau et al. (2005).

5.4. Theory of Multi-Fractal measurements

The measurement of multifractals is mainly the measurement of a statistic distribution which is why the results yield useful information even if the underlying structure does not show a self similar or self affine behaviour as shown by Plotnick et al. (1996). For a mono-fractal object, as mentioned above, the number n of features of a certain size δ varies as

$$n(\delta) \propto \delta^{-D_0} \quad , \tag{5.20}$$

where the fractal dimension D_0

$$D_0 = \lim_{\delta \to 0} \frac{\log n(\delta)}{\log \frac{1}{\delta}} \tag{5.21}$$

can be measured by counting the number n of boxes needed to cover the object under investigation for increasing box sizes δ and estimating the slope of a log-log plot.

There are several methods for implementing multifractal analysis; in this section the moment method is explained. This method use mainly three functions: $\tau(q)$, called the mass exponent function, α ,which is known as the coarse Hölder exponent, and finally the function $f(\alpha)$, or multifractal spectrum. For a measure (or field) defined in a two-dimensional support of the $L \times L$ pixels image, μ (may be considered as the grey tone from 0 to 255 in a normal 8 bit image), it could be spatially decomposed in terms of infinitely many intertwined sets of fractal dimensions. If that is the case, one fractal dimension cannot characterize all the complexity and several fractal dimensions will be estimated depending on the position.

Applying box counting “up-scaling” partitioning process we can get the partition function $\chi(q,\delta)$ defined as:

$$\chi(q,\delta) = \sum_{i=1}^{n(\delta)} \mu_i^q(\delta) = \sum_{i=1}^{n(\delta)} m_i^q \tag{5.22}$$

Where m is the mass of the measure, q is the mass exponent, δ is the length size of the box and $n(\delta)$ is the number of boxes in which $m_i \rangle 0$. Based on this, the mass exponent function $\tau(q)$ shows how the moments of the measure scales with the box size:

$$< \tau(q) >= \lim_{\delta \to 0} \frac{\log < \chi(q,\delta) >}{\log(\delta)} = \lim_{\delta \to 0} \frac{\log < \sum_{i=1}^{n(\delta)} m_i^q >}{\log(\delta)} \tag{5.23}$$

where <> represents statistical moment of the measure $\mu_i(\delta)$ defined on a group of non overlapping boxes of the same size partitioning the area studied. D_q are related as $\tau(q)=(1-q)D_q$.

This characterization of multifractal measures is the concept of generalized dimensions D_q, which corresponds to the scaling exponents for the *qth* moment of the measure. Based on the work of Rényi (1955) they are defined as:

$$D_q = \lim_{\delta \to 0} \frac{1}{1-q} \frac{\log \sum_{i=1}^{n(\delta)} m_i^{\,q}}{\log \delta} \tag{5.24}$$

The singularity index (α) can be determined by Legendre transformation of the $\tau(q)$ curve as:

$$< \alpha(q) >= \frac{d < \tau(q) >}{dq} \tag{5.25}$$

The number of cells of size δ with the same α, $n_\alpha(\delta)$, is related to the cell size as $n_\alpha(\delta) \propto \delta^{-f(\alpha)}$, where $f(\alpha)$ is a scaling exponent of the cells with common α. Parameter $f(\alpha)$ can be calculated as:

$$< f(\alpha) >= q < \alpha(q) > - < \tau(q) > \tag{5.26}$$

Multifractal spectrum (MFS), a graph of α vs. $f(\alpha)$, quantitatively characterizes variability of the measure studied with asymmetry to the right and left indicating domination of small and large values respectively. The width of the MF spectrum indicates overall variability.

MFA in 2-D images involves partitioning the plane into boxes to construct samples with multiple scales. The box-counting method combines pixels to form larger mutually exclusive boxes each containing different set of pixels. If we have an image of $L \times L$ pixels and a partitioned process is applied with a box size $\delta \times \delta$ then the number of boxes with linear size δ ($\eta_k(\delta)$) will follow the proportion:

$$n(\delta) \propto \left(\frac{L}{\delta}\right)^2 \tag{5.27}$$

The larger is δ the larger the number of samples needed to carry out a convergent statistical analysis.

5.5. Symmetries of the Navier-Stokes equation

Even turbulent flows are considered to be correctly modelled by Direct Numerical Simulation (DNS) from the Navier-Stokes (NS) and continuity equations, which are simplification of Newton Laws applied to a fluid. Indeed they contain spatio-temporal symmetries that are not evident at a first glance. We may write the NS equation in a general way as:

$$\partial_t \vec{v} + \vec{v}\nabla\vec{v} = -\frac{1}{\rho}\nabla\vec{p} + \nu\nabla^2 v + \vec{F} \tag{5.28}$$

where v is the velocity, p denote the pressure, $\vec{F}$ the body forces, ρ the density and ν the kinematic viscosity. If we introduce a scaling factor λ raised to the scaling exponent H (that we call the Hölder factor or the Hurst exponent) in the velocity field we can study the behaviour of the system under the following transformations arising from a simple change in scale

$$v \to \lambda^H v' \tag{5.29}$$

$$t \to \lambda^{1-H} T' \tag{5.30}$$

$$r \to \lambda r' \tag{5.31}$$

$$p \to \lambda^{2H} p' \tag{5.32}$$

$$F \to \lambda^{2H-1} F' \tag{5.33}$$

By simple mathematics we can see that, if we consider $v = 0$ in equation 5.29, the scaling of coordinates in an inviscid flow (Euler's equation) brings to:

$$\lambda^{2H-1}\left[\partial_T v + v\nabla v + \nabla p\right] = 0 \tag{5.34}$$

That is: the Euler equation behaves in the same way at scales as $\mathrm{Re} \to \infty$ and viscosity tends to zero. To see whether this symmetry is conserved when viscosity is present, we can study the following hypothesis:

A) $\nu \to \lambda^{H+1} \nu$: the viscosity scales with other variables, good for LES.

B) $\nu = const$: the viscosity remains constant at every scale, good for DNS.

Hypothesis A) satisfies the scale invariance for every value of H, while hypothesis B) holds only for $H = -1$. This symmetry is due to the law of conservation of the circulation of the velocity field. According to the self-similarity principle of the NS equation, we can claim that there is an energy flux from one scale to another until the Kolmogorov scale is reached; the Kolmogorov scale is the length scale at which the viscous dissipation is equal to the dissipation of energy and is the lower bound for the energy transfer. We can study the NS equation applying projection operators which function is that of a high/low pass filter. In this way a scale-by-scale energy budget equation is obtained and we can write the most important terms this way:

$$\text{Energy variation} + \text{energy flux} = \text{enstrophy} + \text{energy injection}$$

it can be interpreted as follows: the rate of change of energy at scales down to a certain length, is equal to the energy injected at such scale by a force minus the energy dissipated at such scales minus the flux of energy to smaller scales. This last term is due to nonlinear interactions between scales arising from the nonlinear term in the NS equation. As a matter of fact this nonlinear term is responsible of the unpredictable behaviour of turbulent flows.

We may also treat in this way the scalar (ρ) detection - diffusion equation and the vorticity equation so assuming G is the scalar production term, and J the baroclinic vorticity production term:

$$\frac{\partial \rho}{\partial t} = G - (u \cdot \nabla)\rho - D\nabla^2 \rho \qquad (5.35)$$

and

$$\frac{\partial \omega}{\partial t} = J - (u \cdot \nabla)\omega + [(\omega + 2\Omega) \cdot \nabla] - \nu_{\omega} \nabla^2 \omega \tag{5.36}$$

with $J = \frac{1}{\rho^2} \nabla\rho \times \nabla p$ the baroclinic source of vorticity. We can derive the following scaling

$$\begin{aligned} r &\to \lambda r' \\ v &\to \lambda^H v' \\ t &\to \lambda^{1-H} t' \\ \rho &\to \lambda^{H'} \rho' \\ D &\to \lambda^{H+1} D' \\ p &\to \lambda^0 p' \\ f &\to \lambda^{2H-1} f' \\ G &\to \lambda^{H+H'} G' \end{aligned} \tag{5.37}$$

But for the scaling of vorticity we have to consider also the hypothesis A) and B) mentioned previously, and generalize slightly the similarity laws to include the possibility, say that the derivatives, or integrals, or in general the higher order moments scale in a different way, so using the definition of the order q, structures functions(equation 2.5) now in time $S_q(z) = \left\langle |u(t+\tau) - u(t)|^q \right\rangle$ so that

$$S_q(z) = C_q \tau^{\xi(q)} \tag{5.38}$$

The generalized Hurst exponent $H(q)$ for order q is defined as:

$$H(q) = \frac{\xi(q)}{q} \tag{5.39}$$

Because, of course, the second order structure function, like the correlation scale like the variance of equation 5.14 we have

$$u = \lambda^{2H(2)} \tag{5.40}$$

and for the poer exponent

$$p = 2H(2) + 1 \tag{5.41}$$

as mentioned in equations 5.16 and 5.17, because a relationship holds between vorticity and velocity:

$$\omega = \vec{\nabla} \times \vec{u} \tag{5.42}$$

its behaviour is not that of a passive scales (Zauri and Babiano 1994) and its scaling will not be the same as $\rho = \lambda^{H'} \rho'$ nor $u = \lambda^{H} u'$.

In the simplest case using that $[\omega] \equiv T^{-1}$ with constant $\nu = \nu_{\omega}$

$$\omega = \lambda^{H-1} \omega' \tag{5.43}$$

If we want to apply these scaling to, say the vortex size evolution, it would be interesting to compare the spectra with the Hurst exponent of second order. We know (Tarquis et al. 2009) that if $H(2) = \frac{1}{3}$, (Kolmogorov, 3D scaling) then the power exponent is $p = \frac{5}{3}$ in a similar way for Kraichnan´s 2D enstrophy cascade region where $p = 3$ then $H_{2D}(2) = 1$.

If we use the maximum fractal dimension like Redondo (1990, 1996) then from equation 5.18

$$p = 2E_u + 1 - 2D_{E_u} \tag{5.44}$$

so for 3D flows $p = 7 - 2D_3$ and for 2D flows $p = 5 - 2D_2$. So if $p = \frac{5}{3}$ in a fully 3D flow $D_3 = 2.66$ and if $p = 3$ then $D_2 = 1$. If a Kolomogorov spectra at $p = \frac{5}{3}$ appears

in a 2D flow then $D_2 = 1.66$. Both types of flows can co-exist both in the Atmosphere and the Ocean as indicated by Platonov et al. (2008). The role of intermittency would give other values.

CHAPTER 6

Methodology and Laboratory experimental setup

6.1. Experimental Methodology

The laboratory experiments on mixing tend to fall into four categories: Those where the turbulence is generated by oscillating grid and hence exhibits no mean shear; those produced by a sudden energy release, as in the dropping of grid, where the turbulence is decaying in time; those where the mixed layer is driven over the non-turbulent layer thus creating a mean velocity shear: and those where the turbulence is generated by convective heating or cooling at a surface. All of these experiments may also be performed in a rotating frame of reference (i.e. Rotating Table) where Coriolis forces are also important in a certain parameter space, mostly at low Rossby number.

The role of stratification has been parametrized using the Richardson number, while the Reynolds number is used to compare cascade processes at different size. The evolution and behavior of all experiments was studied using several techniques. Shadowgraph was also used taking advantage of the change in the refractive index to detect the interface. In other experiments the change in the refractive index was corrected with alcohol to prevent the distortions of the image and then the interface was observed by putting dye in the turbulent layer. But this technique presents some problems related with the shadowgraph, namely the image obtained is integrate of the whole width of the tank where the flow takes place. Laser Induced Fluorescence was used to make a Thin Lit Layer, by adding fluorescent to the mixed layer.

Several experiments show the dramatic effect that a strong density interface has both on vertical and horizontal mixing. The effect of density interfaces also tend to spread further the non-homogeneous lateral mixing akin to that taking place near the coastline. An intrusion spreading along the initially sharp interface generates strong vertical vorticity and may be used to define the limit of a coastal mixing front, like the study of Carrillo at al. (2001).

All the experiments (see § 6.3) were videotaped, then digitized and analyzed with the fluid mechanics packages DigImage, DigiFlow and ImaCalc. Filter, contouring and some other geometrical operations were applied using the facilities provided by the software to measure the advance of the turbulent interface as described in Redondo et al. 1996. Plastic particles of plyolite that previously had been treated in salty water to have neutral buoyancy were placed on the liquid in order to observe the behaviour of water motions as lateral mixing takes place. The image was recorded by a video camera with the experimental set up seen in figure 6.1; the signal is then also digitalized by a

DT - 2861 data translation frame grabber and a personal computer with DigImage. Figure 6.2 shows in a flux diagram the image analysis configuration shown in real time on both TV and monitor where the processed images allow visualizing the particle streaks and the interface.

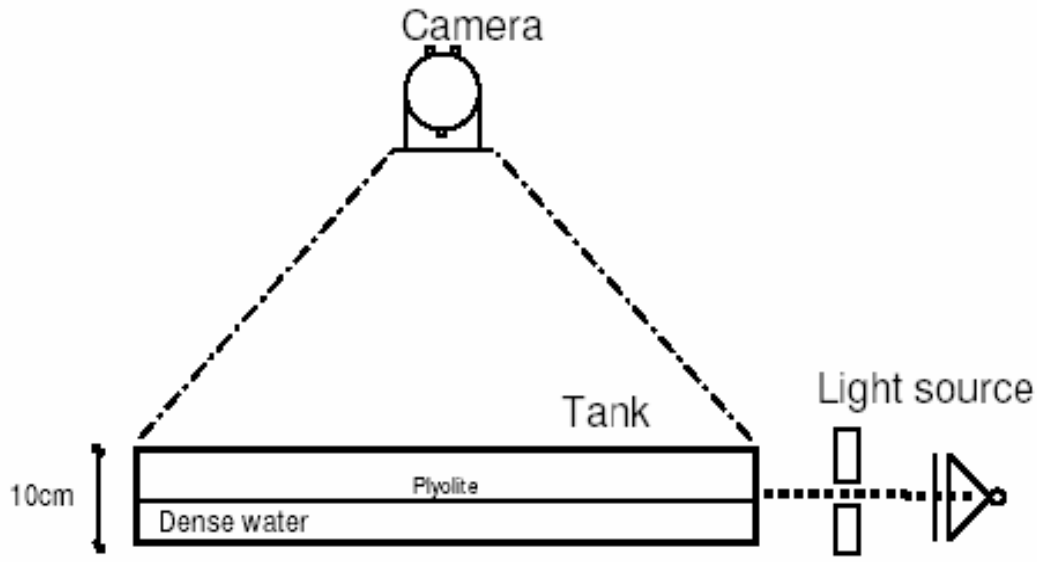

Figure 6.1: Experimental vertical tank set up, film camera and light position. In the case of LIF the laser or light source was positioned in one side only. Lateral view of the experimental tank 1x1m. A density interface was created with 5 cm of salty water and 5 cm of clean water. Carefully a third layer of plastic plyolite particles was placed in the middle of the salty and clean water.

The software *DigImage*, *ImaCalc* and *Digiflow* are used at UPC to analyze the Laboratory experiments in a quantitative way. DigiFlow offers the same characteristics from digital image sequences and ImaCalc is able to perform multiscale and Fractal analysis on Image sequences. These programs used currently at UPC and at DAMTP at Cambridge University result of a continuous program of development, enhancement and support.

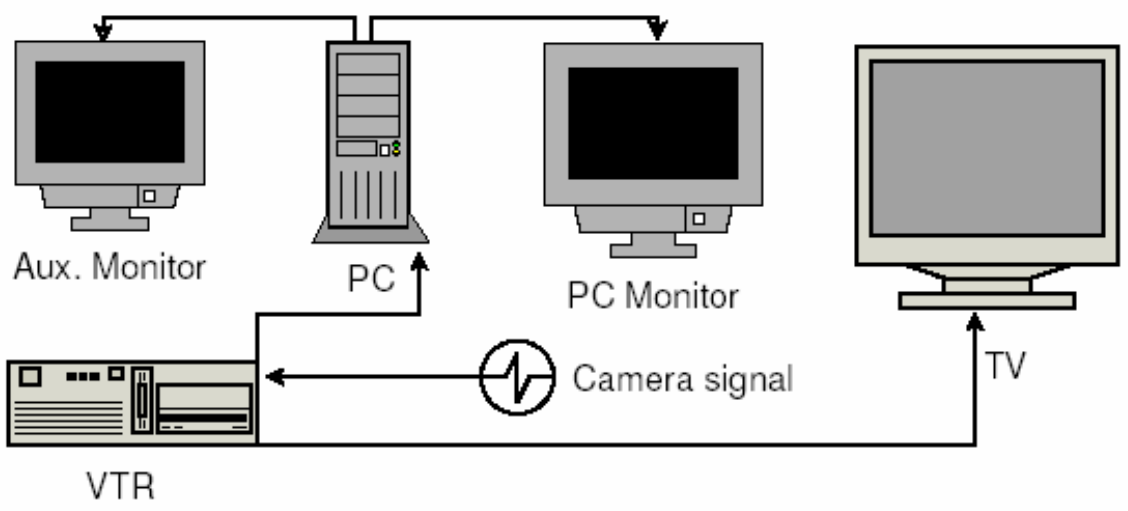

Figure 6.2: Image process with the DigImage software. It allows processing and visualizing images on both the monitor and the TV monitor in real time.

Through this on-going effort they have remained at the forefront of image processing for fluid dynamics for the past ten years. The unique combination of particle tracking, PIV, optical thickness, refractive index analysis, LIF enhancement, time series generation, and many more capabilities enable greatly enhanced visualisations and allows previously qualitative experiments to yield accurate quantitative data. Efficient and easy to use, they are employed by an increasing number of research laboratories world wide for qualitative and quantitative analyses. Up to date technical details describing the abilities and requirements along with sample output are available for this research.

The image analysis configuration is shown in real time on both TV and monitor where the processed images allow visualizing the particle streaks and the interface. Figure 6.3 is an Eulerian interpolation of the Lagrangian data produced from the tracking of neutral particles at the interface. For heat stratified experiments, on the other hand the mixing efficiency does not seem to depend on Richardson number as shown in Redondo (2002) in the case of steady input (for example in the grid stirred experiments).

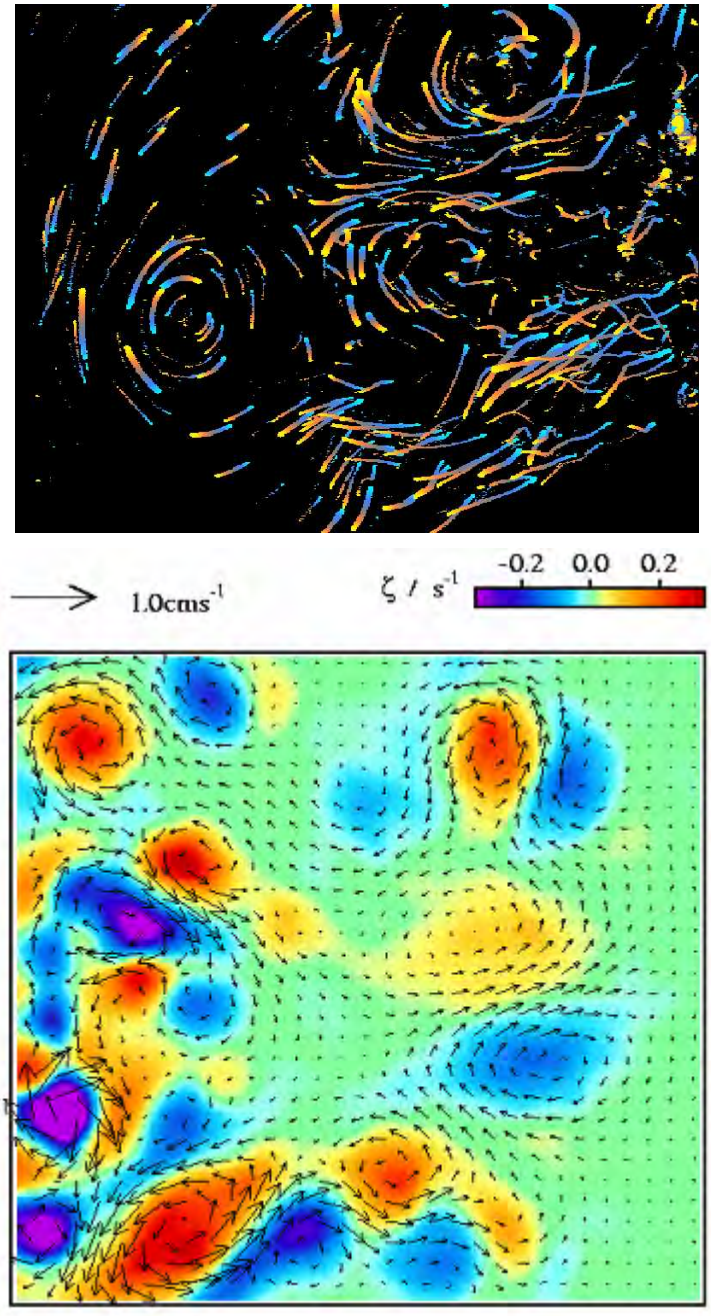

Figure 6.3: Example of Image processing by DigImage of a grid stirred flow. (top) Particle paths, (bottom) Velocity Vectors and vertical vorticity.

In figure 6.3 we can observe an example of image processing by DigImage of a grid stirred flow. At the top it is shown the particle paths as particle tracking and at the bottom the velocity field as velocity vectors. Colors (red and blue) and vectors indicate positive (anticlockwise) and negative (clockwise) vortices.

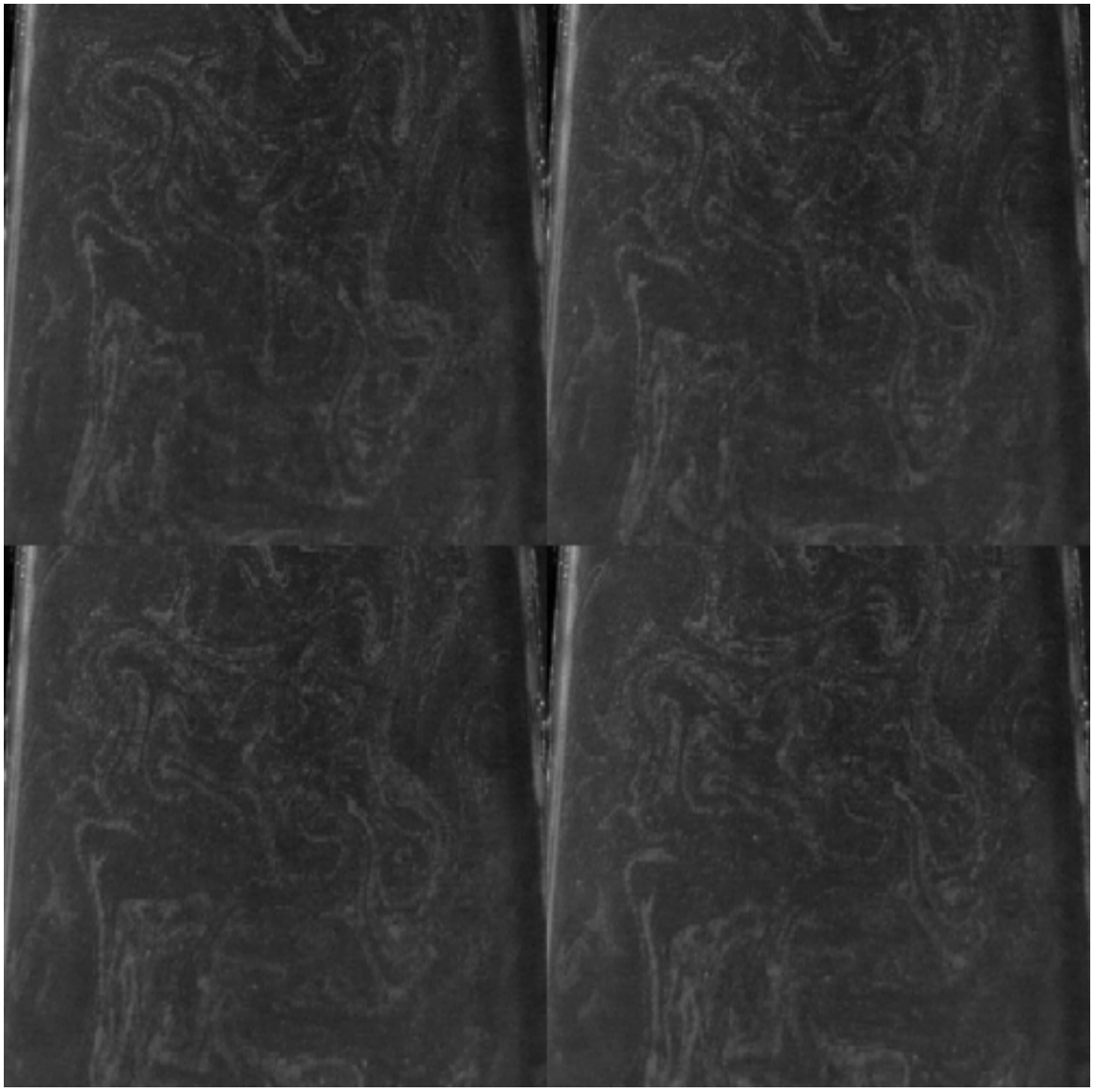

Figure 6.4: Evolution of the structure of a surface 2D flow in a Laboratory tank 1mx1m, pliolite beads show streaks comparable to SAR ocean observations.

The evolution of the structure of a 2D flow in a laboratory tank 1m x 1m and pliolite beads particle tracking results are shown in figures 6.4. This is an example of particle tracking in the experimental tank. Clearly we can observe vortices at different times in the picture.

6.1.1. Image processing for fluid dynamics – DigiFlow and DigImage

DigiFlow-DigImage is much more than just an image processing system; it is a video sequence processing system. For fluid flows time is just as important as the spatial dimensions. In this sense, DigFlow offers unrivalled functionality for extracting temporal as well as spatial information; it includes both standard image processing techniques and specialised techniques tailored specifically for analysing fluid flows. No other system offers the breadth of functionality for a broad range of laboratory and observational measurements.

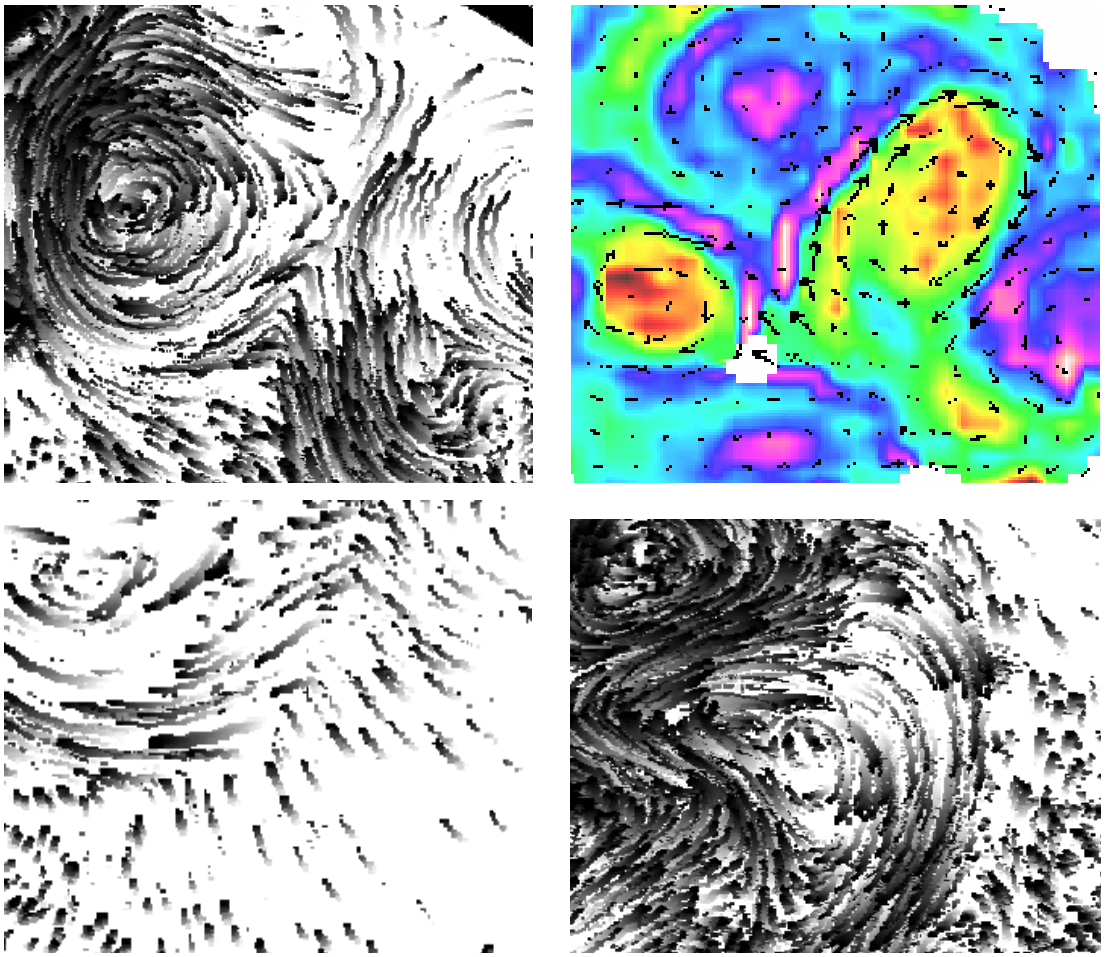

Figure 6.5: Example of particle tracking near a density interface

Efficient and easy to use, DigImage and DigiFlow are employed by an increasing number of research laboratories world wide for qualitative and quantitative analyses. To obtain the necessary performance of image processing on desktop computers, DigImage required a framegrabber card to be installed to provide not only image capture, but also

image display and some of the processing. While this close coupling allowed efficient real-time processing and frame-accurate control of a video recorder, it ultimately restricted the development and deployment of the technology.

The continuation of DigImage is Digiflow. Digiflow provides a range of image processing features designed specifically for analysing fluid flows. The package is designed to be easy to use, yet flexible and efficient. Whereas most image processing systems are intended for analysing or processing single images, Digiflow is designed from the start for dealing with sequences or collections of images (see on figure 6.5) in a straightforward manner. DigiFlow retains the potential DigImage released by the control of a frame grabber. Not only does this greatly simplify the process of running experiments, acquiring images, processing them, extracting and plotting data, but it also enables real-time processing of particle streaks and synthetic schlieren.

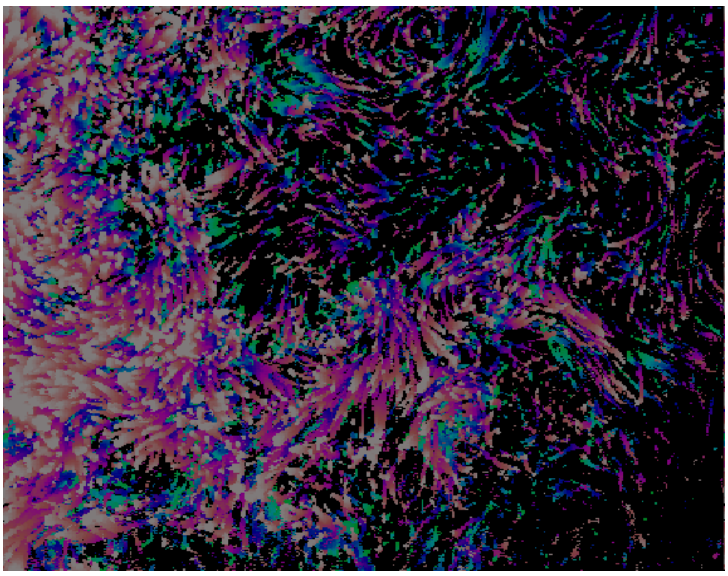

Figure 6.6: Pliolite particles and its traces 10 s after the passage of the Grid perpendicularly to the centre of a sharp density interface.

The main aim of this research is to understand and describe key aspects of the structure of non-homogeneous turbulence affected by stratification and rotation, in particular turbulent jets and plumes and their interaction with coherent structures such as vortices. Other effects connected with non-homogeneity are presented. Most predictive models fail when forcing at the Rossby deformation Radius is important and a large range of scales have to be taken into account. Figures 6.6 and 6.7 are examples of particle tracking from DigImage the first 6.6 shows the evolution of the density

interface, pliolite particles and its traces 10 sec after the passage of the Grid perpendicularly to the center of a sharp density interface and the second 6.7 shows an example of technique that is used to track the pliolite particles and produce the velocity and vorticity plots used to calculate temporal and spatial correlations vortex topology and spectra, side view.

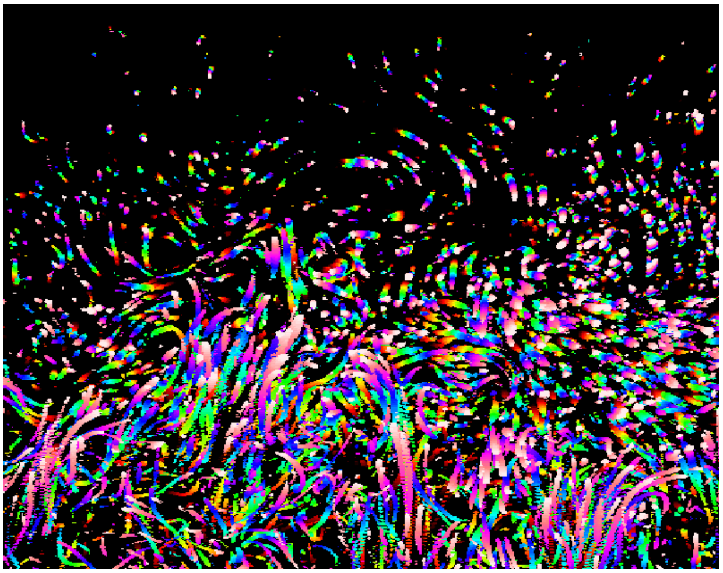

Figure 6.7: Example of particle tracking near a density interface, side view.

6.2. Mixing Efficiency

Studies of mixing in the laboratory and in the environment have been made using the non-dimensional parameters discussed in chapter 2 as well as relevant spatial and temporal scales. These depend on the relevant body forces that act on the fluid. Examples are the Rossby Deformation radius: $R_D = Nh/f$, when both buoyancy and rotation act together; the Rossby number $R_o = U/fl$ and the flux or gradient Richardson numbers induced by the relevant velocity *U*, the Coriolis parameter *f*, the buoyancy frequency *N*, the lateral *L*, and vertical, *h* scales. In order to describe the structure of density interfaces, fronts and their hydrodynamic behavior, different mixing processes near density interfaces where analyzed in laboratory conditions to investigate experimentally the structure of these interfaces.

The observation of the dynamics of fluids near densities interfaces is important in order to model how local mixing affects pollutant or biological organism dispersion under different environmental conditions. These complex non-homogenous environmental mixing processes are obviously responsible for the maintenance of the ecosystems in areas like estuaries, lagoons and costal systems where both lateral and vertical mixing occurs.

Horizontal circulation takes place with a great dynamic effect, often coupled with the presence of recirculation patrons, natural river discharges, internal waves and their influences as water mixes. Depending on the rank of detected scales and their spectral shape, bi-dimensional or three-dimensional turbulence features detected as vortices are good indicators of the dynamic processes taking place.

The mixing efficiency (η) is defined as the ratio between the gain of potential energy (ΔPE) and the kinetic energy input (ΔKE) during the mixing process. It is equivalent to the Richardson flux number as

$$\eta = R_f = \frac{\Delta PE}{\Delta KE} \tag{6.1}$$

The gain in potential energy is calculated from the advance of the interface $\left(\frac{dD}{dt} = Eu'\right)$ and the kinetic energy is estimated from the work done by the grid as

discussed by Turner (1973), Linden (1980), Redondo and Cantalapiedra (1993).

The values of the mixing efficiency are comparable with other experiments, Redondo (2002), but further work is needed to investigate the effect of intermittency on the mixing process. The sequence shown in figure 6.4 shows the generation of the coastal mixing front from the experiment on Jet injection and extraction reported in Matulka (2003).

When mixing of reactants or pollutants has to be accounted, the range of scales spans from hundreds of kilometres to the Bachelor or Kolmogorov sub millimetre scales. Effect of intermittent eddies and non-homogeneity of diffusion is also an important issue in the environment because both stratification and rotation body forces are important and cause anisotropy/non-homogeneity. These problems need further approaches and we maximize the relevant geometrical fractal information in order to understand and therefore predict these complex environmental dispersive flows. The present thesis is based principally on laboratory experiments producing turbulence by means of wakes. We aim at comparing the different series of detailed experiments that have been performed in the Laboratory of Fluid Dynamics of UPC and in Trondheim on wake generated turbulence and its decay. Measurements of the 3 components of turbulent velocity and their spatial multifractal and Fourier spectra will also be used in order to obtain a basic understanding on local diffusion, mixing and mass transport. A detailed definition of the mixing efficiency and recent discussion on available kinetic (AKE) and potential energy (APE) is presented in appendix 6.

6.3. The Laboratory non-rotating stratified Experiments

The set of non-rotating experiments were performed on a square tank of dimensions $1m \times 1m$. Inside of this tank (figure 6.8) $100\,kg\,H_2O$ were arranged in two layers: $5\,cm$ bottom layer of salty water (brine) of different concentration with density between $\rho = 1.000 - 1.087\,gr/cm^3$ and $5\,cm$ of fresh water $\left(\rho = 1.000\,gr/cm^3\right)$. Between these two layers, a thin layer of plastic particles of pliolite was seeded, marking the separation layer between salty and fresh water. In order to mix these two layers, a traversing grid (figure 6.8) was used, which was built from thick pipe sections (pipes were located every $10cm$, their length were $30cm$ and diameter $3.5cm$). This configuration ensured strong vorticity produced by the Karman vortices of the round pipe array.

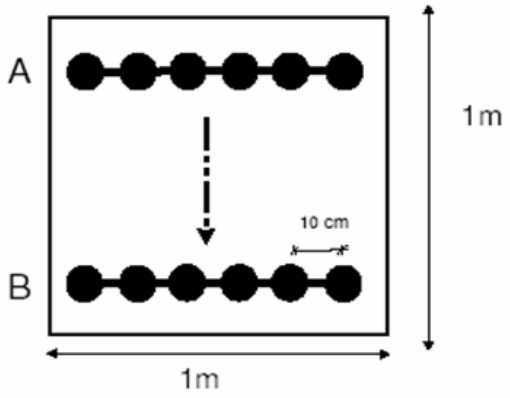

Figure 6.8: Plan view of a stirred grid experimental set up to generate turbulence with density stratification in 1x1m tank. Where a traversing grid of 30cm with bars of 3.5cm of diameter, separated 10cm, moved from A to B at time Δt.

This experiment had five sub sets arranged in terms of different initial density interface before experiments started. In each one, the measurements of the densities lead to profiles obtained from point measurements at heights chosen as $1,3,5,7,8,9,10\,cm$ inside the tank. Every experiment was made at different salinity in the brine fresh water interface. All measurements used calibrated conductivity probes and refractometer on a small drawn sample to be able to check on mass conservation. The precision of the

refractometer, that was oscillated against densmeter was at $\pm 5x10^{-5}\ g/cm^3$. All small scale measures had seven or eight profiles between the different passages of the grid.

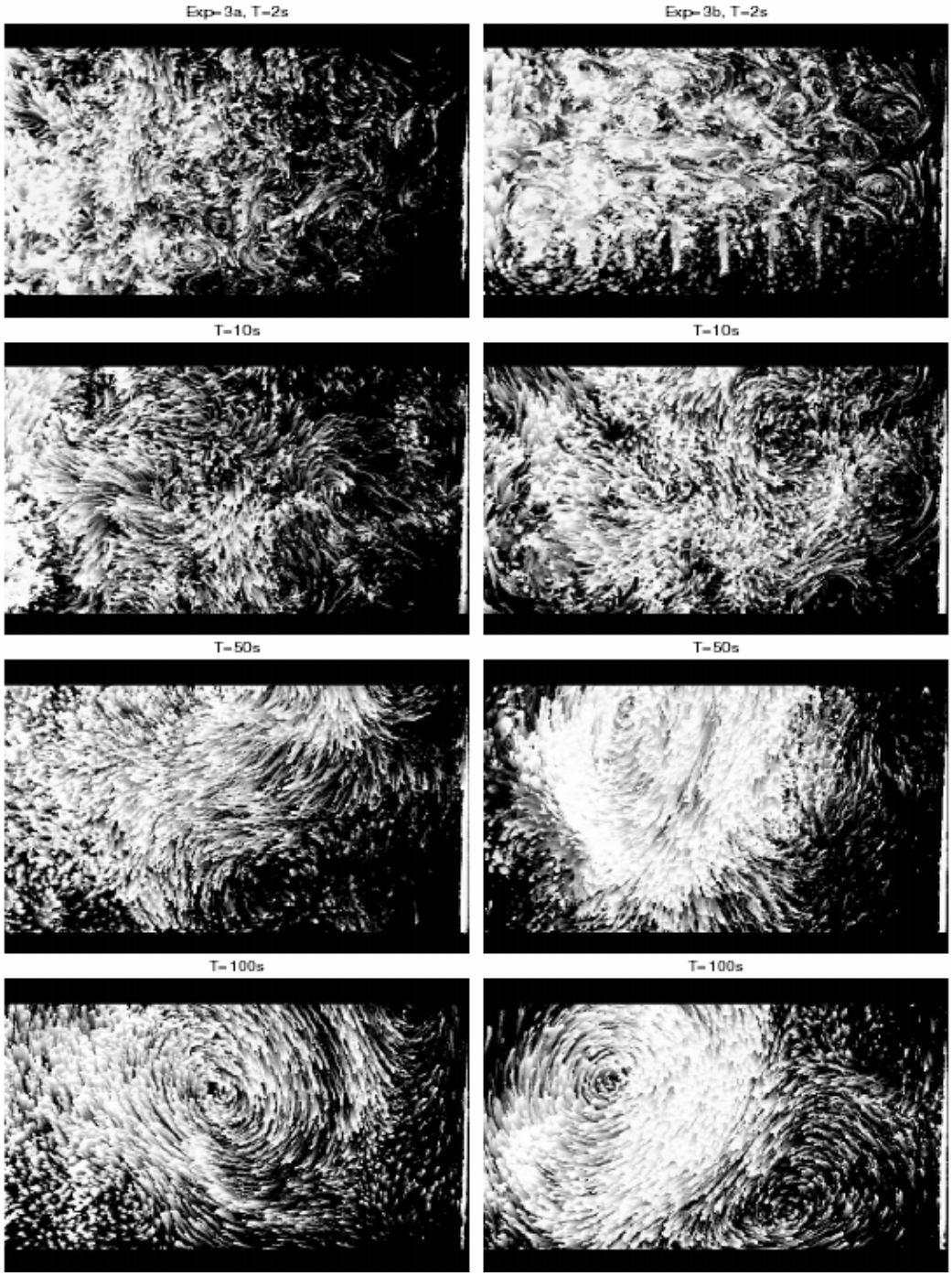

Figure 6.9: The laboratory experiments after *DigiFlow* analysis (example of particle tracking near a density interface). Experiment time series from Left 3a and Right 3b, at times 2, 10, 50 and 100 seconds. Note the evolution of the size of the vortex from small at the beginning to large at the end. Matulka et al. (2008)

Figure 6.9 presents a time series of density profiles from laboratory experiments showing the evolution of structures at 2, 10, 50 and 100 seconds, and a sequence of pliolite particles showing tracks after the horizontal traverse of the grid across the sharp density interface is seen.

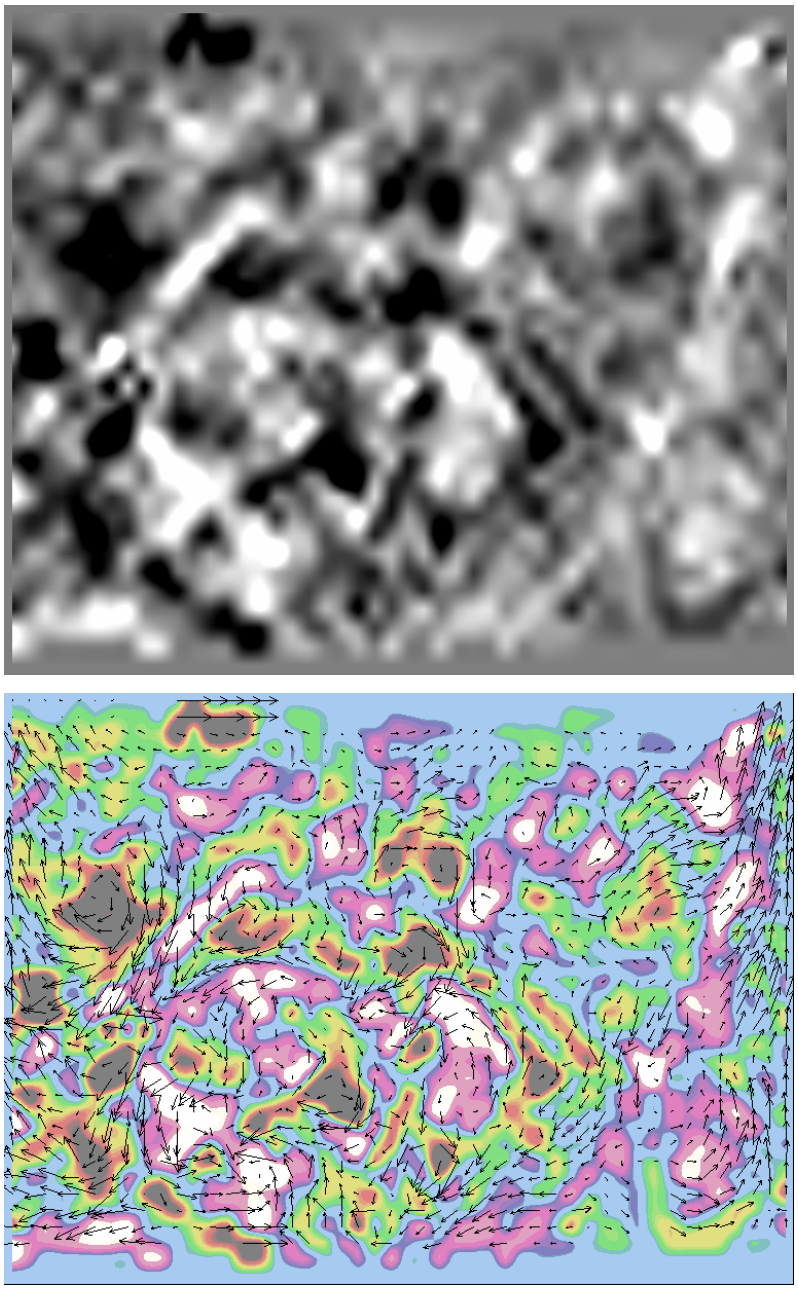

Figure 6.10: The experiment results from *DigImage*. Examples of the vorticity (up) and velocity (bottom) evolution in stratified fluids. One of the characteristics of the flow is the development of strong vertical structures.

One of the most important role of stratification and in general in all body forces, including magnetic fields, is to modify the slope of the spectral energy cascade. In the

following part of this PhD thesis results of the PIV laboratory experiments will be presented. They will allow calculating velocity spectra, the velocity and vorticity PDFs and the evolution of the structure of stratified decaying (and steady flows) as shown in figure 6.10.

CHAPTER 7

Experimental Results

7.1. Introduction

In this chapter, the main new experimental results will be presented using the techniques described in previous chapters. We will focus here on the results from the decaying non-rotating stratified experiments, the rotating experiments, done in collaboration under the TMR European Hidralab III project in Trondheim will be discussed further in the chapter of discussions and in appendix, because the experiments were performed as member of a larger international research team.

The set of turbulence decaying experiments have been performed, with the aim of focusing on the flow in the middle of a strongly stratified density interface. These experiments have been done under one condition: Stirring (Non-Rotating) Decaying 2D Turbulence experiments and were performed in a 1x1m tank. This set of experiments is a compilation of five series of grid wake mixing experiments; their classification will depend on the initial interfacial Richardson number as criteria for the varying role of buoyancy on the decay process. The Total time of mixing for the experiment sub sets was between 53 and 72 minutes, so diffusive molecular mixing of salt was negligible in all cases. The density of the brine in the bottom layer used in the experiment before total mixing took place between 1.0001 and $1.082\, g/cm^3$. These differences were due to the fact that the experiments had different initial densities, in all cases mass conservation was ensured by calculating it from the average density profiles. These differences in initial density profiles and in grid forcing (18-24 cm/s) produced a wide range of mixing efficiencies, the study of the relationship between flow topology and molecular mixing and diffusion is also an aim of this thesis.

In tables 7.1, 7.2, 7.3, 7.4 and 7.5 we present some relevant information on the initial conditions from all of the experiments; we denote λ the characteristic length scale, $\Delta\rho_{initial}$ the initial interface density difference, U is the horizontal velocity of the grid, ρ is the initial bottom layer density, *Rig* is the Gradient Richardson numbers, *Re* the dimensionless Reynolds numbers, N the Brunt-Väisälä frequency and T is the temperature in Celsius degrees. Figures from 7.1 to 7.5 show the density profile for the 5 different sets of experiments with different initial conditions, the five sequences, starting from a sharp density interface. Here as examples of the evolution of the density profiles after each passage of the grid in the laboratory experiments, we can see that an

elevation of the centre of gravity takes place due to the irreversible molecular mixing of the salt.

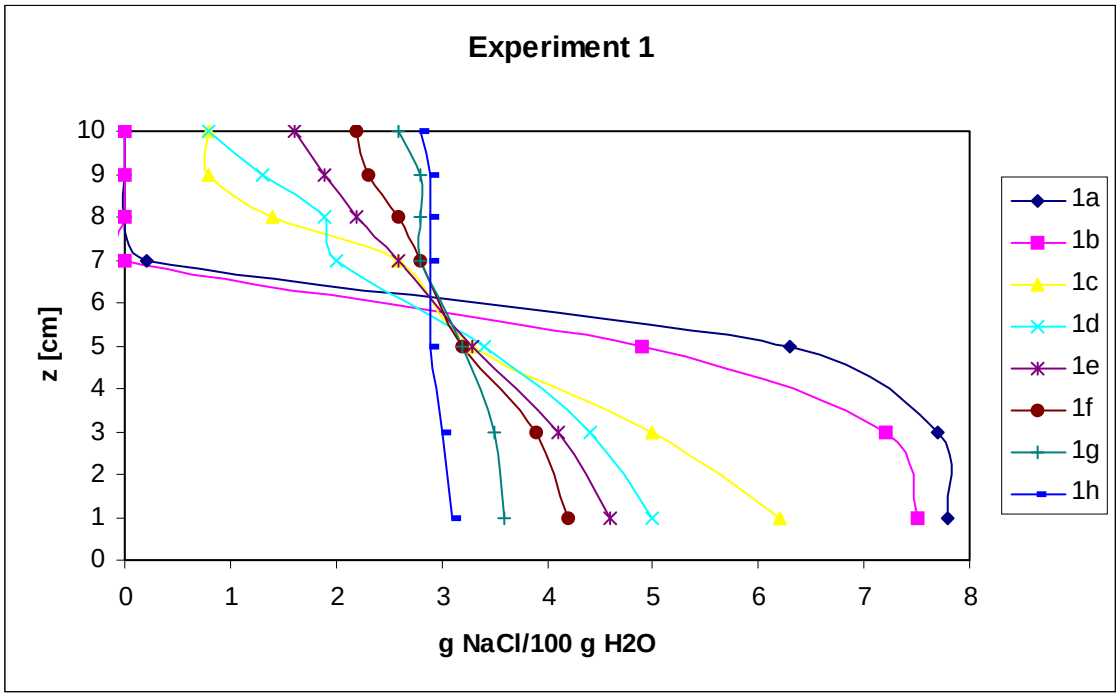

Figure 7.1: Stratified experiments. Total mixing experiments with NaCl from 1a with a lower layer ρ=1029, throughout 1a, 1b… until 1h.The totally mixed density in this experiment was for ρ=1070.

Table 7.1: Initial conditions from the first set of stirring experiments where *U* is velocity, *N* Brunt-Väisälä frequency, *Re* dimensionless Reynolds number, *Rig* Gradient Richardson numbers etc.

Experiment Number	1a	1b	1c	1d	1e	1f	1g	1h
λ [cm]	2	2	10	10	10	10	10	10
$\Delta\rho_{initial}$ [g/cm^3]	0,078	0,078	0,078	0,078	0,078	0,078	0,078	0,078
$\Delta\rho/\Delta z$ [g/cm^4]	0,03	0,025	0,007	0,005	0,0035	0,0022	0,0009	0,0002
U [cm/s]	18	19	19	20	20	21	22	22
ρ [g/cm^3]	1,03	1,03	1,03	1,03	1,03	1,03	1,03	1,03
Rig	8,8	6,58	1,84	1,189	0,83	0,47	0,17	0,039
Re	18 x 10^3	19 x 10^3	19 x 10^3	20 x 10^3	20 x 10^3	21 x 10^3	22 x 10^3	22 x 10^3
$\Delta\rho$ [g/cm^3]	0,061	0,05	0,07	0,05	0,035	0,022	0,009	0,002
N [s^{-1}]	3,778	3,449	0,816	0,690	0,577	0,458	0,293	0,138
T [°C]	19							

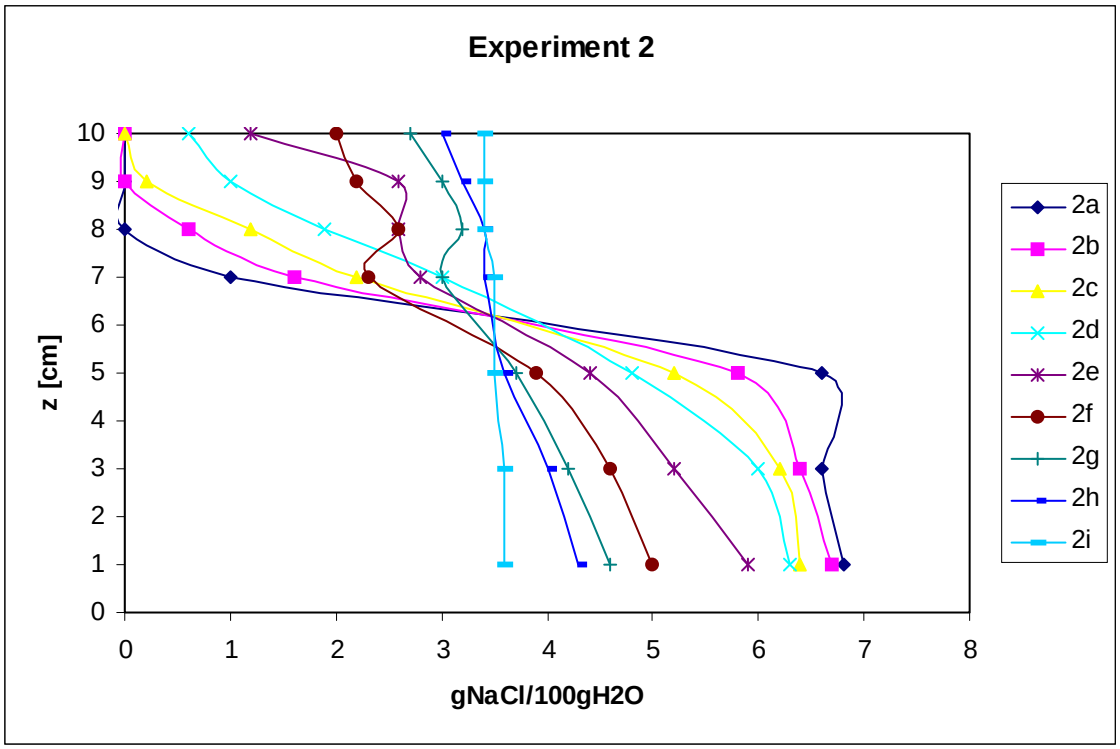

Figure 7.2: Stratified experiments. Total mixing experiments with NaCl from 2a with ρ=1035, throughout 2a, 2b… until 2i. The totally mixed density in this experiment was for ρ=1060.

Table 7.2: Initial conditions from second stirred experiments where *u* is velocity, *N* Brunt-Väisälä frequency, *Re* dimensionless number Reynolds, *Rig* Gradient Richardson numbers etc.

Experiment Number	2a	2b	2c	2d	2e	2f	2g	2h	2i
λ [cm]	2	2	3	3	10	10	10	10	10
$\Delta\rho_{initial}$ [g/cm^3]	0,07	0,07	0,07	0,07	0,07	0,07	0,07	0,07	0,07
$\Delta\rho/\Delta z$ [g/cm^4]	0,028	0,029	0,0133	0,00967	0,0041	0,0031	0,002	0,0014	0,0002
U [cm/s]	19	19	19	21	22	22	23	23	24
ρ [g/cm^3]	0,98	0,98	0,98	0,98	0,98	0,98	0,98	0,98	0,98
Rig	7,756	8,033	3,68	2,17	0,847	0,64	0,378	0,264	0,347
Re	19 x 10^3	19 x 10^3	19 x 10^3	21 x 10^3	22 x 10^3	22 x 10^3	22 x 10^3	23 x 10^3	24 x 10^3
$\Delta\rho$ [g/cm^3]	0,056	0,058	0,04	0,029	0,041	0,031	0,02	0,014	0,002
N [s^{-1}]	3,742	3,808	2,106	1,795	0,64	0,557	0,447	0,374	0,141
T [^{o}C]	19								

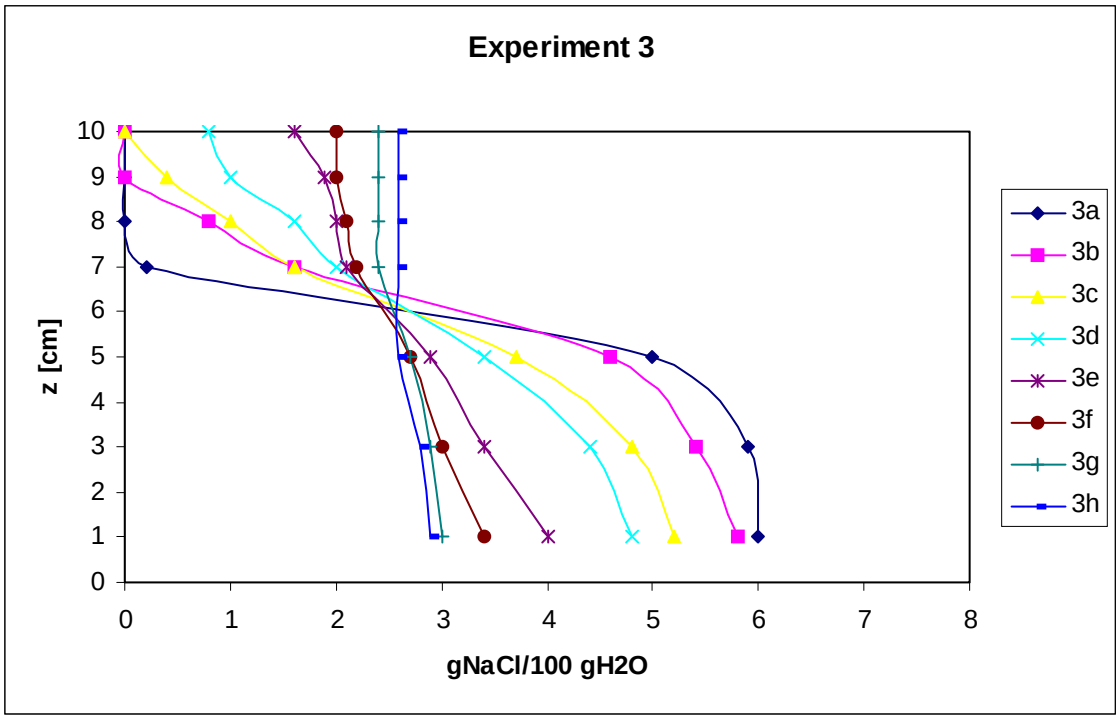

Figure 7.3: Stratified experiments. Total mixing experiments with NaCl from 3a with ρ=1060, throughout 3b, 3c, 3d… until 3h. The totally mixed density in this experiment was for ρ=1026.

Table 7.3: Initial conditions from third stirred experiments where *u* is velocity, *N* Brunt-Väisälä frequency, *Re* dimensionless number Reynolds, *Rig* Gradient Richardson numbers etc.

Experiment Number	3a	3b	3c	3d	3e	3f	3g	3h
λ [cm]	2	2	10	10	10	10	10	10
$\Delta\rho_{initial}$ [g/cm^3]	0.06	0.07	0.08	0.09	0.10	0.11	0.12	0.13
$\Delta\rho/\Delta z$ [g/cm^4]	0,0275	0,0215	0,005	0,0038	0,0022	0,0014	0,0008	0,0005
U [cm/s]	20	20	20	20	20	20	20	20
ρ [g/cm^3]	0,82	0,82	0,82	0,82	0,82	0,82	0,82	0,82
Rig	8,21	6,42	1,49	1,13	0,65	0,42	0,24	0,15
Re	20 x 10^3	20 x 10^3	20 x 10^3	20 x 10^3	20 x 10^3	20 x 10^3	20 x 10^3	20 x 10^3
$\Delta\rho$ [g/cm^3]	0,055	0,043	0,05	0,038	0,022	0,014	0,008	0,005
N [s^{-1}]	5,732	5,069	2,443	2,131	1,622	1,292	0,975	0,768
T [^{o}C]	21							

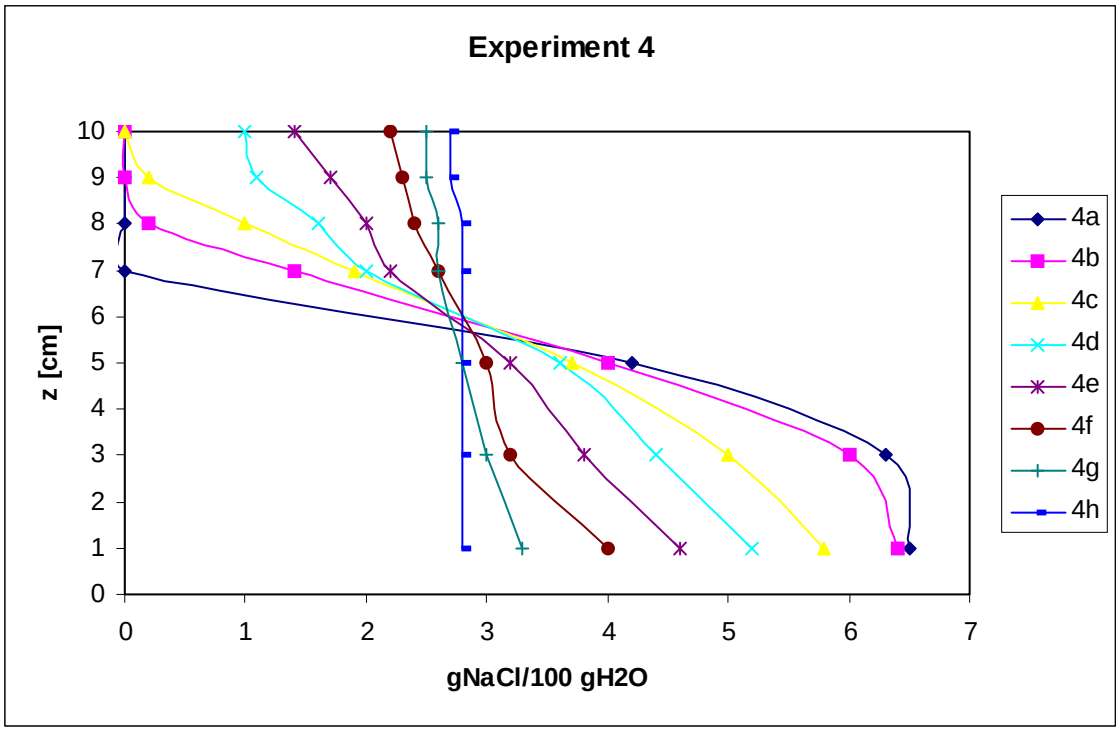

Figure 7.4: Stratified experiments. Total mixing experiments with NaCl from 4a with ρ=1065, throughout 4b, 4c, 4d… until 4h. The totally mixed density in this experiment was for ρ=1028.

Table 7.4: Initial conditions from forth stirred experiments where *u* is velocity, *N* Brunt-Väisälä frequency, *Re* dimensionless number Reynolds, *Rig* Gradient Richardson numbers etc.

Experiment Number	4a	4b	4c	4d	4e	4f	4g	4h
λ [cm]	4	10	10	10	10	10	10	10
$\Delta\rho_{initial}$ [g/cm^3]	0,065	0,065	0,065	0,065	0,065	0,065	0,065	0,065
$\Delta\rho/\Delta z$ [g/cm^4]	0,016	0,0062	0,0058	0,004	0,0031	0,0017	0,0009	0,0001
U [cm/s]	20	20	20	20	20	20	20	20
ρ [g/cm^3]	0,87	0,87	0,87	0,87	0,87	0,87	0,87	0,87
Rig	4,5	1,74	1,63	1,13	0,87	0,48	0,25	0,028
Re	20 x 10^3	20 x 10^3	20 x 10^3	20 x 10^3	20 x 10^3	20 x 10^3	20 x 10^3	20 x 10^3
$\Delta\rho$ [g/cm^3]	0,065	0,062	0,058	0,04	0,031	0,017	0,009	0,001
N [s^{-1}]	4,243	2,642	2,555	2,121	1,868	1,382	1,005	0,332
T [^{o}C]	21							

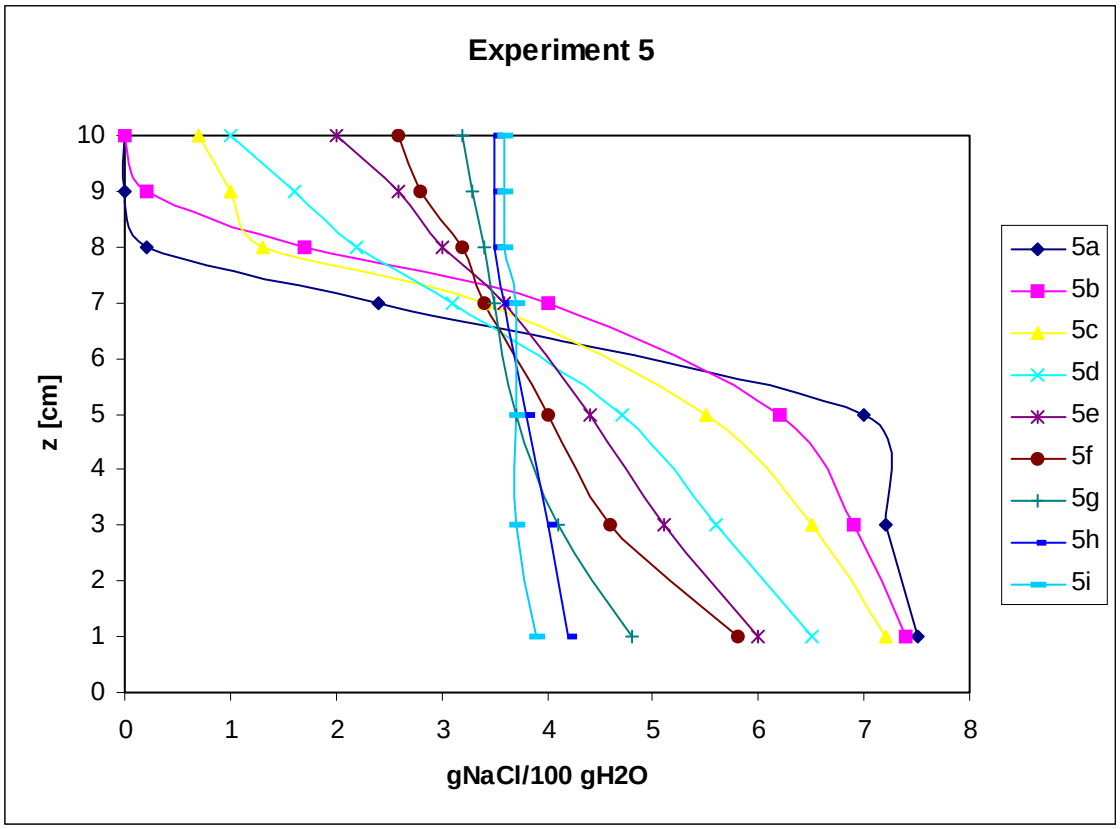

Figure 7.5: Stratified experiments. Total mixing experiments with NaCl from 5a with ρ=1075 throughout 5b, 5c, 5d… until 5i. The totally mixed density in this experiment was for fifth ρ=1037.

Table 7.5: Initial conditions from fifth stirred experiments where u is velocity, N Brunt-Väisälä frequency, *Re* dimensionless number Reynolds, *Rig* Gradient Richardson numbers etc.

Experiment Number	5a	5b	5c	5d	5s	5f	5g	5h	5i
λ [cm]	10	10	10	10	10	10	10	10	10
$\Delta\rho_{initial}$ [g/cm^3]	0,075	0,075	0,075	0,075	0,075	0,075	0,075	0,075	0,075
$\Delta\rho/\Delta z$ [g/cm^4]	0,008	0,0073	0,006	0,0053	0,004	0,0034	0,002	0,0007	0,0002
U [cm/s]	20	20	20	20	20	20	20	20	20
ρ [g/cm^3]	0,83	0,83	0,83	0,83	0,83	0,83	0,83	0,83	0,83
Rig	2,36	2,14	1,77	1,56	1,18	1	0,59	0,206	0,059
Re	20 x 10^3	20 x 10^3	20 x 10^3	20 x 10^3	20 x 10^3	20 x 10^3	20 x 10^3	20 x 10^3	20 x 10^3
$\Delta\rho$ [g/cm^3]	0,075	0,073	0,06	0,053	0,04	0,034	0,02	0,007	0,002
N [s^{-1}]	3,072	2,936	2,661	2,500	2,173	2,002	1,536	0,906	0,480
T [^{o}C]	22								

When the density profiles are vertical, after several passages of the grid, then these two layers are completely mixed. As the mixing takes place, the Richardson number at the interface decreases until we have a homogeneous layer. In further sections of this chapter we present different chosen analysis that aid to the understanding of the ensuing grid decay stratified flow and its mixing.

In table 7.6 we can see dimensionless numbers *Rig* and Re for all analysed experiments.

Table 7.6: Dimensionless numbers; *Re* Reynolds and *Rig* Gradient Richardson numbers for all experiments.

Experiment Number	Rig	Re	Experiment Number	Rig	Re
1a	8,8	18×10^3	3e	0,65	20×10^3
1b	6,58	19×10^3	3f	0,42	20×10^3
1c	1,84	19×10^3	3g	0,24	20×10^3
1d	1,189	20×10^3	3h	0,15	20×10^3
1e	0,83	20×10^3	4a	4,50	20×10^3
1f	0,47	21×10^3	4b	1,74	20×10^3
1g	0,17	22×10^3	4c	1,63	20×10^3
1h	0,039	22×10^3	4d	1,13	20×10^3
2a	7,756	19×10^3	4e	0,87	20×10^3
2b	8,033	19×10^3	4f	0,48	20×10^3
2c	3,68	19×10^3	4g	0,25	20×10^3
2d	2,17	21×10^3	4h	0,028	20×10^3
2e	0,847	22×10^3	5a	2,36	20×10^3
2f	0,64	22×10^3	5b	2,14	20×10^3
2g	0,378	22×10^3	5c	1,77	20×10^3
2h	0,264	23×10^3	5d	1,56	20×10^3
2i	0,347	24×10^3	5e	1,18	20×10^3
3a	8,21	20×10^3	5f	1	20×10^3
3b	6,42	20×10^3	5g	0,59	20×10^3
3c	1,49	20×10^3	5h	0,206	20×10^3
3d	1,13	20×10^3	5i	0,059	20×10^3

7.2. Results without significant stratification (low Richardson number)

7.2.1. Interfacial Flows

At first we present the analysis of experiments without buoyant effect or with weak buoyancy, inducted by low Richardson numbers. One interesting way to analyse the evolution of the vorticity is to visualize different graphics which they can give us an idea by the colour scale and the shape of the vorticity and velocity fields that generate it. In figure 7.6 as sequence is shown in time of the evolution of the velocity field, the evolution of a plane 2D vorticity false colour map, where white is positive vorticity and black negative. Finally it is very useful to generate a 3D vorticity plot as well as an integrated side view profile of vorticity, where the peaks, both positive and negative can be easily measured and counted. These four different plots for the low Richardson number $Rig = 0.039$ experiment at different times selected to be almost equally spaced in a logarithmic time sequence such as: 2, 5, 10, 20, 50 and 100 seconds.

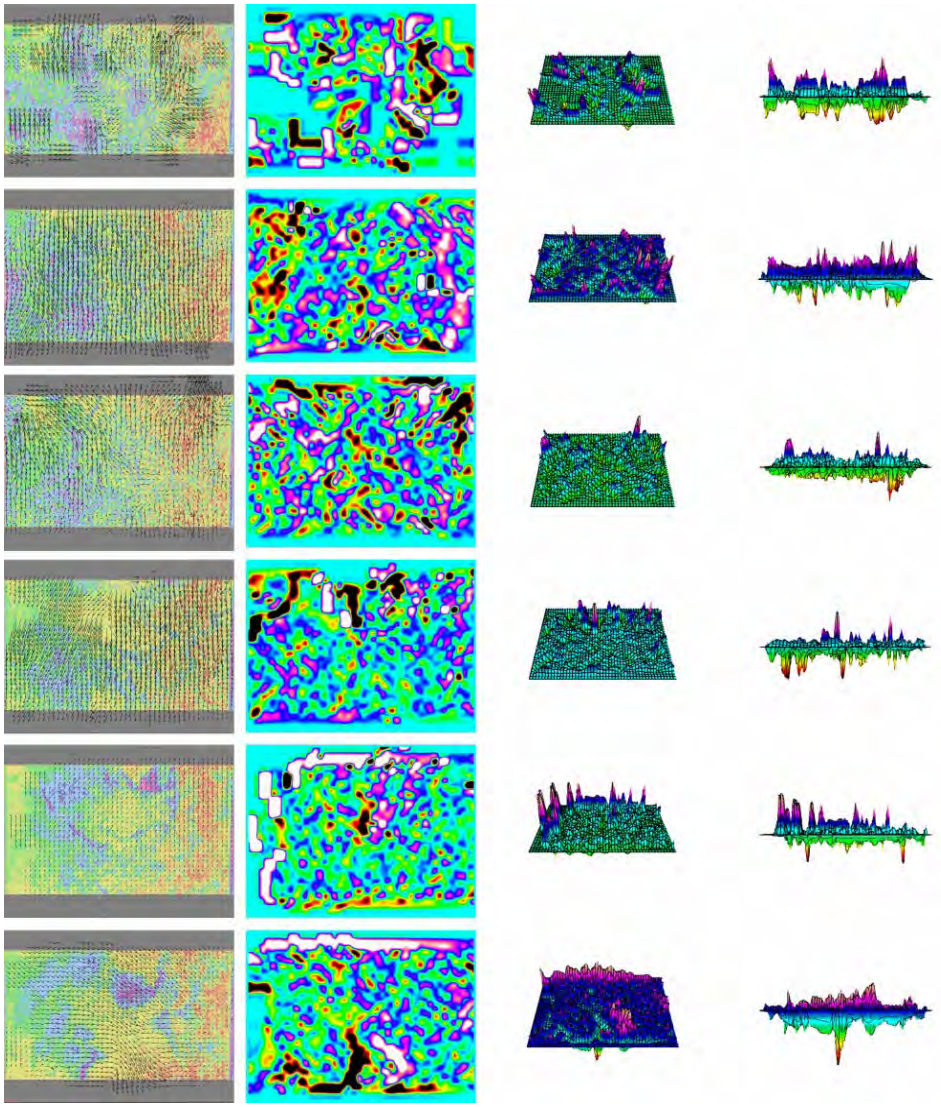

Figure 7.6: The evolution of velocity field, 2D vorticity field, 3D vorticity and profiles of vorticity 3D for experiment 1h at times 2, 5, 10, 20, 50 and 100 seconds, with small Richardson number $Rig = 0.039$.

The behaviour of vortices in other cases without stratification is quite similar to this with a weak stratification, and low Richardson number. In the evolution graphs we may observe a slight change of tendency between 20 and 50 seconds two last cases (50 and 100 seconds), both with very little vorticity, and large horizontal scales. Besides, it can be noticed a quite strong decrease in the vorticity between 2 and 5 seconds. This decrease is visualised well in the 2D vorticity maps.

7.3. Results with significant (strong and medium) stratification

In this section, the comparative analysis of the vorticity evolution is presented. One interesting way to analyse the vorticity evolution is to visualise different graphics which they can give an idea of the scale and the shape of vorticity and velocity fields. Here we analyse the evolution of different experiments and we try to explain the behaviour related to observed changes with different types of visualizations and their presented graphics.

The parameter ranges for the stratified flows are presented, in all experiments PIV and particle tracking on horizontal planes video taped from above were used to evaluate the velocity and vorticity fields.

Below we present columns with temporal evolution with four different figures in every line, corresponding to the velocity maps, bidimensional vorticity maps, threedimensional vorticity maps and the vortices profiles.

Figures 7.7, 7.8, 7.9 and 7.10 show the flow structure from experiments at time 2, 5, 10, 20, 50 and 100 seconds. It is interesting to notice in the graph of vorticity evolution how the vorticity does not vary much in the weakly stratified cases but it decreases strongly (see section 7.3.4) in the high Rig experiments as clearly seen in the last image of the figure 7.8. Close to the end of the experiment, this is even more evident in the bidimensional and one line vorticity maps. We observe that precisely, the behaviour of vorticity of strong stratification is quite different than in the other cases and also very different to the pure 2D flows (Bracco et al. 2004).

Also it can be detected one certain background of vorticity in the profiles graphs, which theory define as hardly active and is maintaining as the base during all process. With profiles graphs we can make general idea about the real size of vorticity peaks. In the threedimensional figures it can be displayed as well as the progressive increase of vorticity scale, especially in this with high energy and with tendency to merge. The velocity graphs show the velocity distribution associated to vortices, and permit the identification of vortices with high energy and their scale approximation.

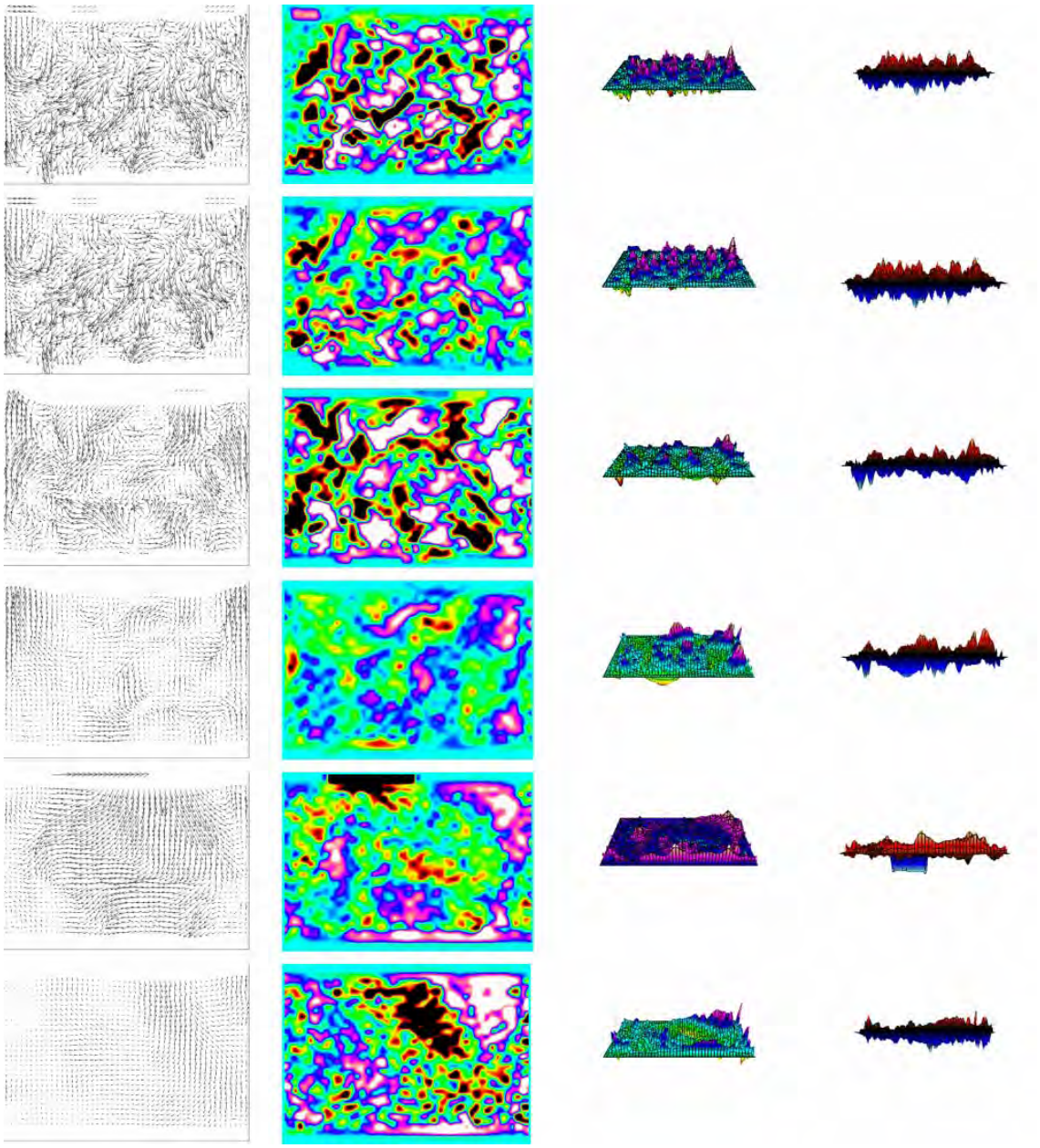

Figure 7.7: The evolution of velocity field, 2D vorticity field, 3D vorticity and profiles of vorticity 3D for experiment 1a with $Rig = 8.8$ at times 2, 5, 10, 20, 50 and 100 seconds.

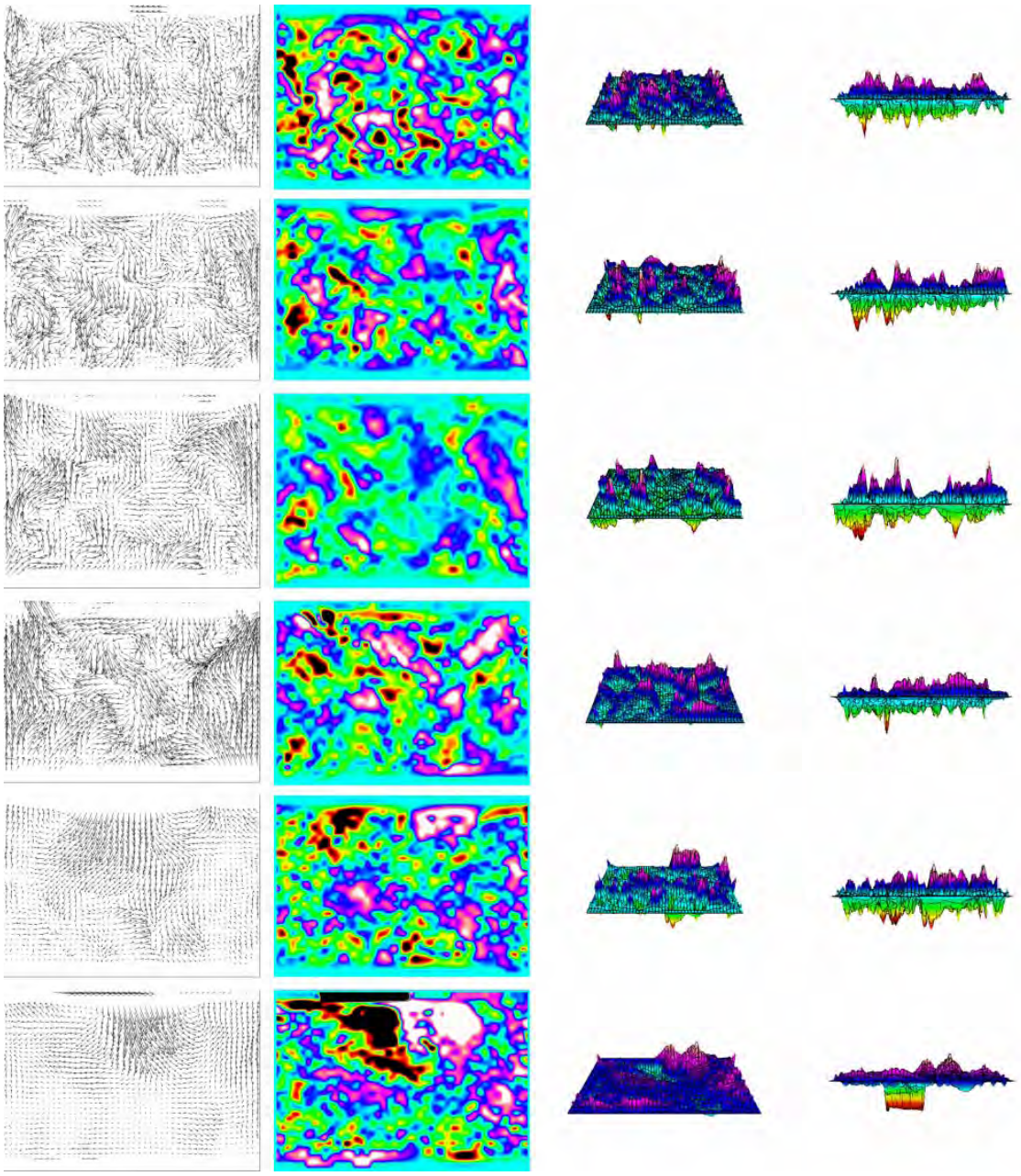

Figure 7.8: The evolution of velocity field, vorticity 2D field, vorticity 3D and profiles of vorticity 3D for experiment 1b with $Rig = 6.58$ at times 2, 5, 10, 20, 50 and 100 seconds.

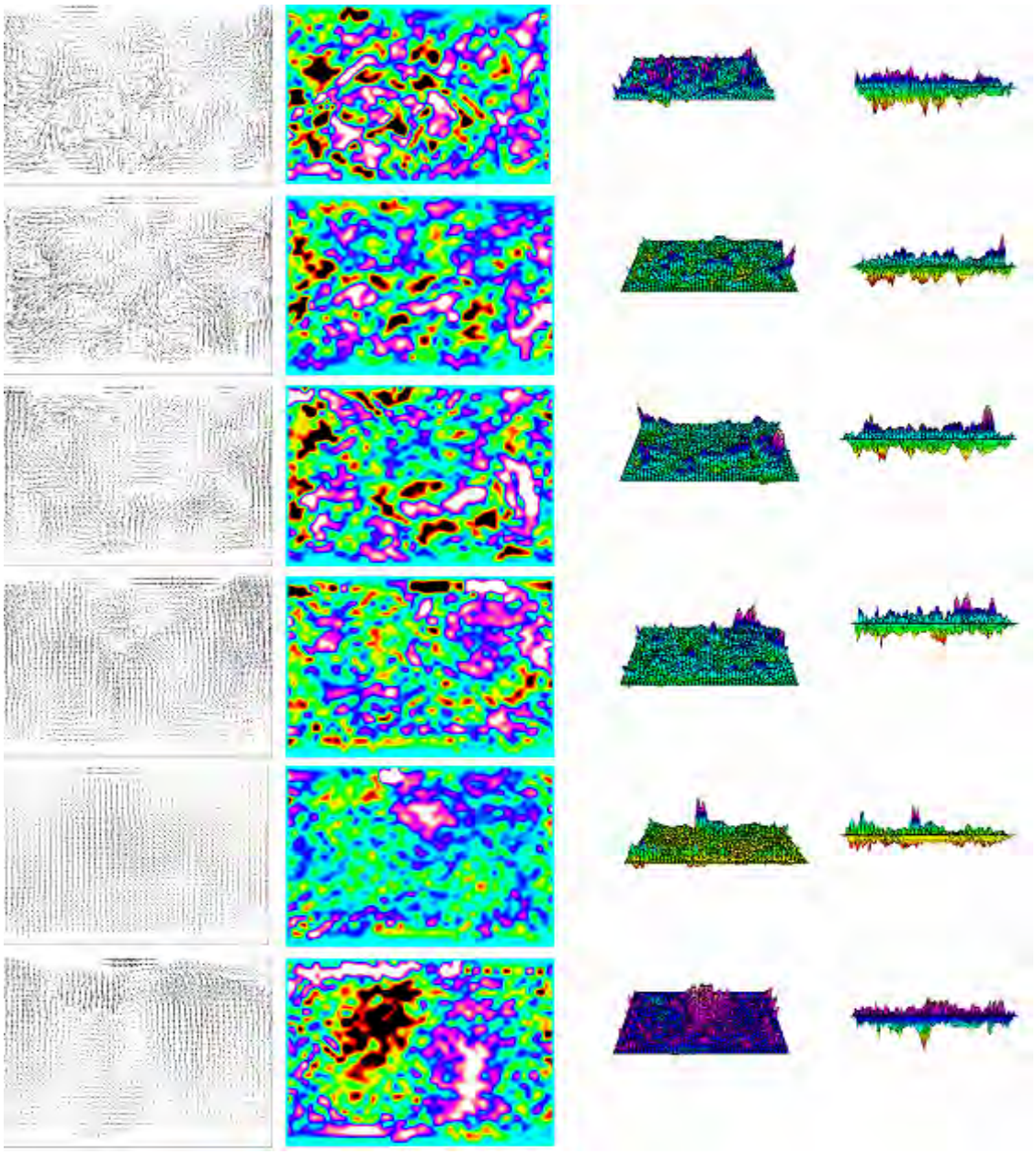

Figure 7.9: The evolution of velocity field, vorticity 2D field, vorticity 3D and profiles of vorticity 3D for experiment 2a with $Rig = 8.03$ at times 2, 5, 10, 20, 50 and 100 seconds.

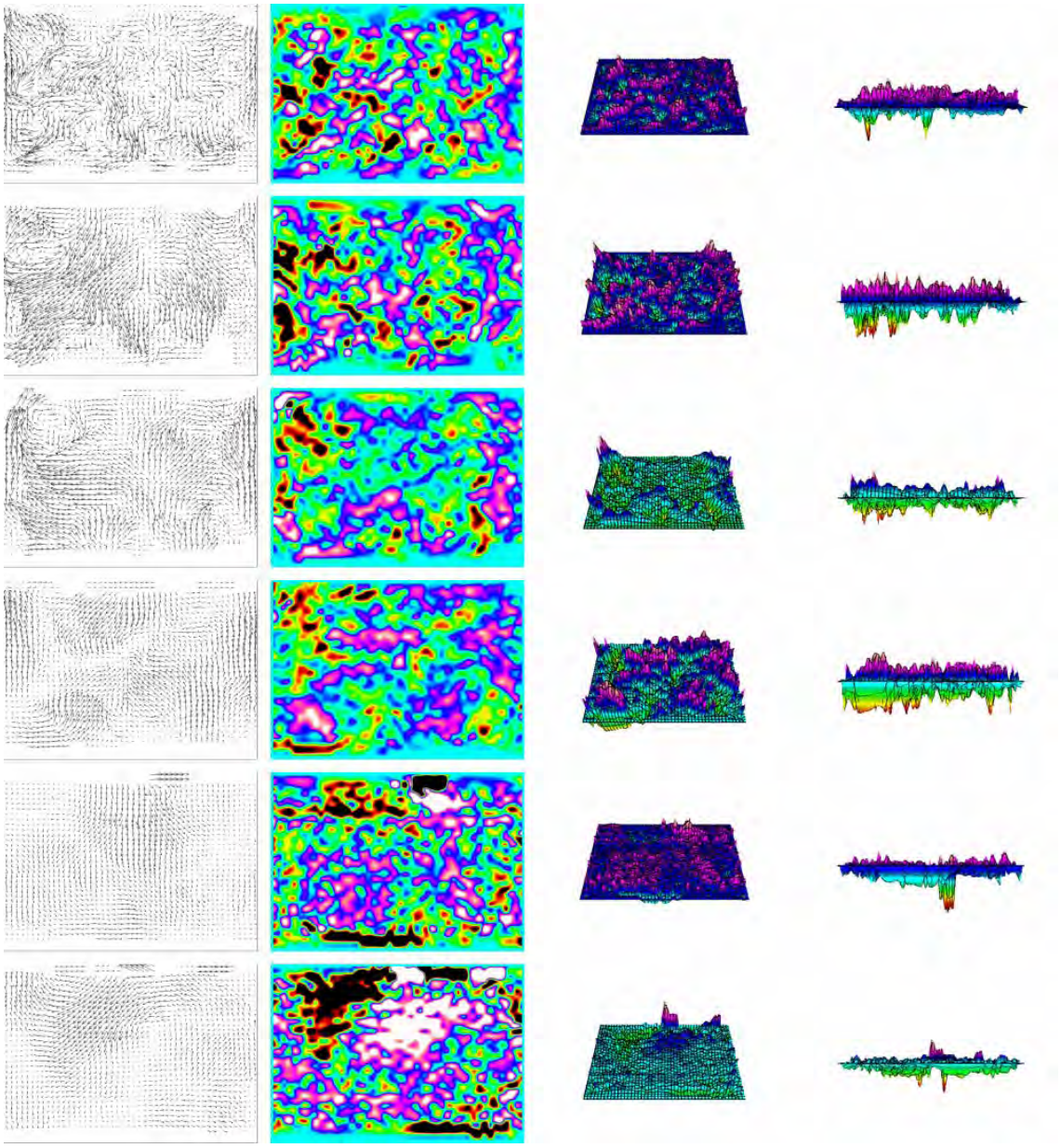

Figure 7.10: The evolution of velocity field, vorticity 2D field, vorticity 3D and profiles of vorticity 3D for experiment 2b with $Rig = 3.68$ at times 2, 5, 10, 20, 50 and 100 seconds.

In figures 7.11, 7.12, 7.13 and 7.14 the same type of results mentioned above are shown for experiments with moderate stratification, with the mean Richardson number ($1.0 \langle Rig \langle 4.0$). Again we have a good indicator of the behaviour of the vorticity, maintaining the same standard visual aspect in the bidimensional (2D) and threedimensional (3D) vorticity maps during the six times chosen for comparison in a logarithmic time scale $t = \{2, 5, 10, 20, 50, 100\}$. In all of the experiments for different Richardson number the number of vortices decreases in time until at time $50 - 100\,s$

and after that time there are only one or two large vortices which begin to be affected by the sides of the experimental tank, so all scales are smaller than 1m, the size of the square tank.

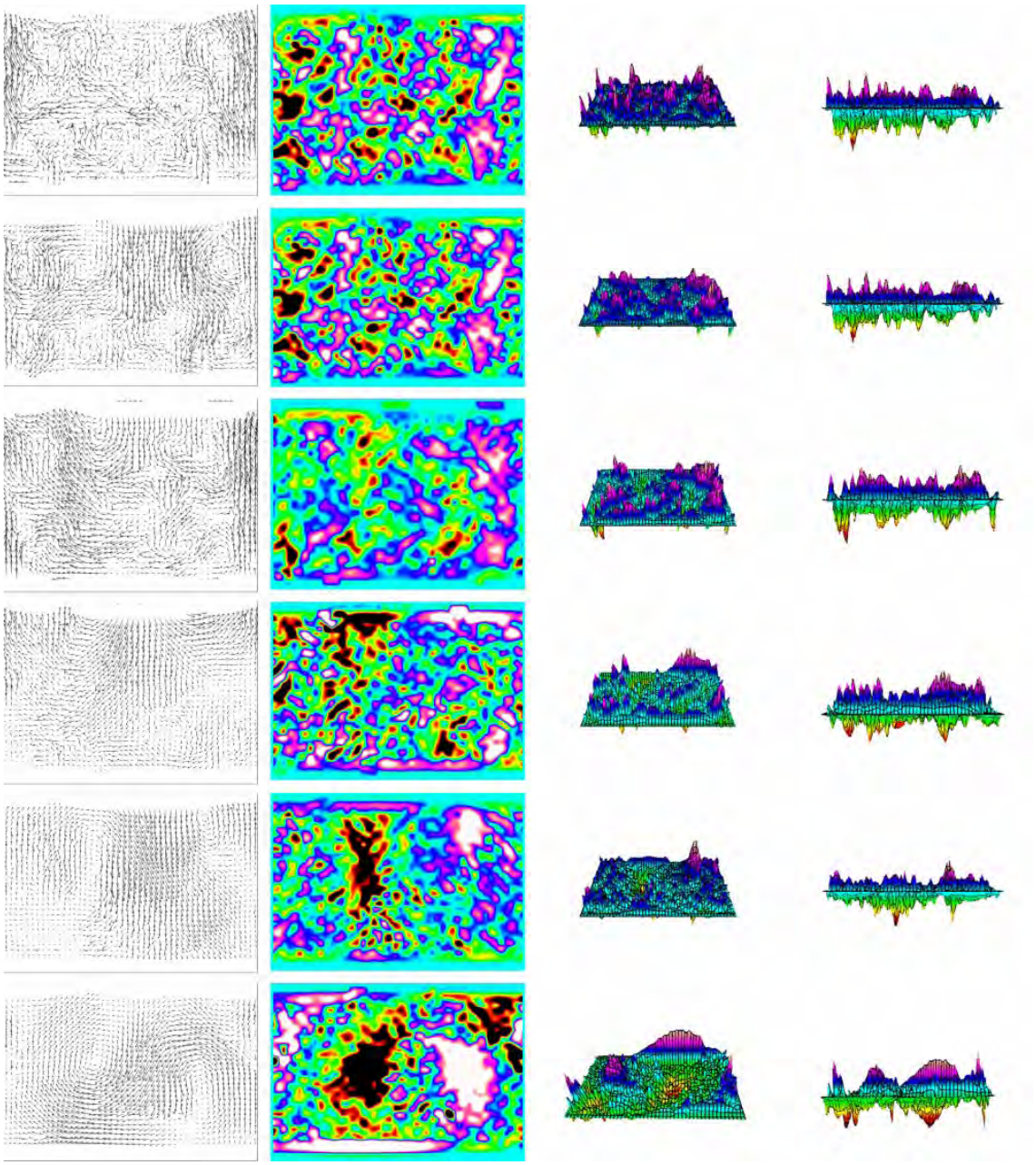

Figure 7.11: The evolution of velocity field, vorticity 2D field, vorticity 3D and profiles of vorticity 3D for experiment 1c with $Rig = 1.84$ at times 2, 5, 10, 20, 50 and 100 seconds.

Comparing the qualitative behaviour of the strongest vortices for the different Richardson number experiments, we may notice that for the more stratified experiments

after 50s the large coherent vortices are very dominant, this is quite clear for $Rig \geq 2$. On the other hand for lower Richardson number (weak stratification) this merging mechanism is not so evident ($Rig \leq 0.8$). For example in figure 7.15, even at time $t = 100\,s$, there are many disorganized small vortices, which in contrast for a strong density interface with $Rig = 8.0$ as shown in figure 7.10 we notice a large dominant vortex dipole at time $t = 100\,s$.

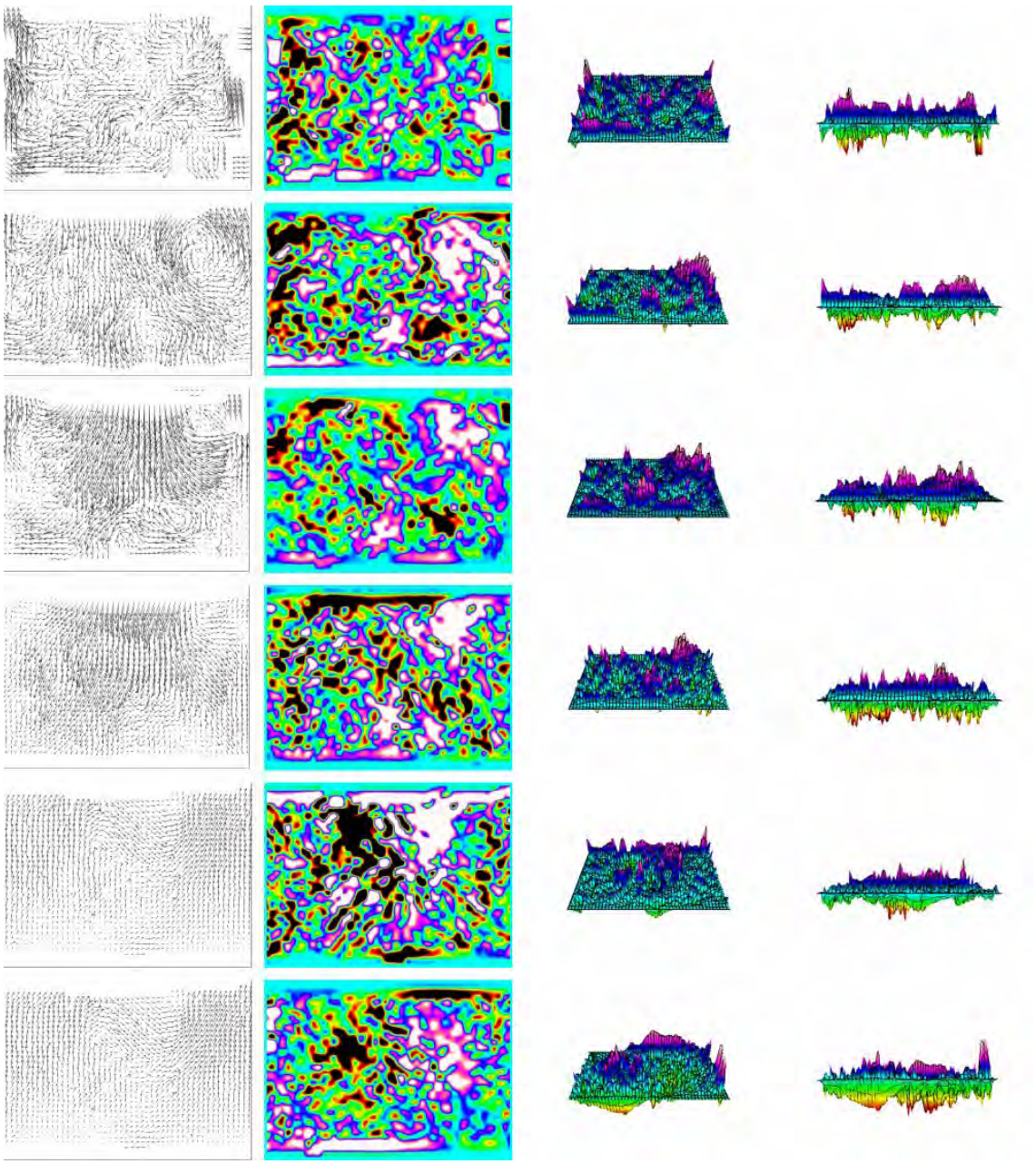

Figure 7.12: The evolution of velocity field, vorticity 2D field, vorticity 3D and profiles of vorticity 3D for experiment 1d with $Rig = 1.19$ at times 2, 5, 10, 20, 50 and 100 seconds.

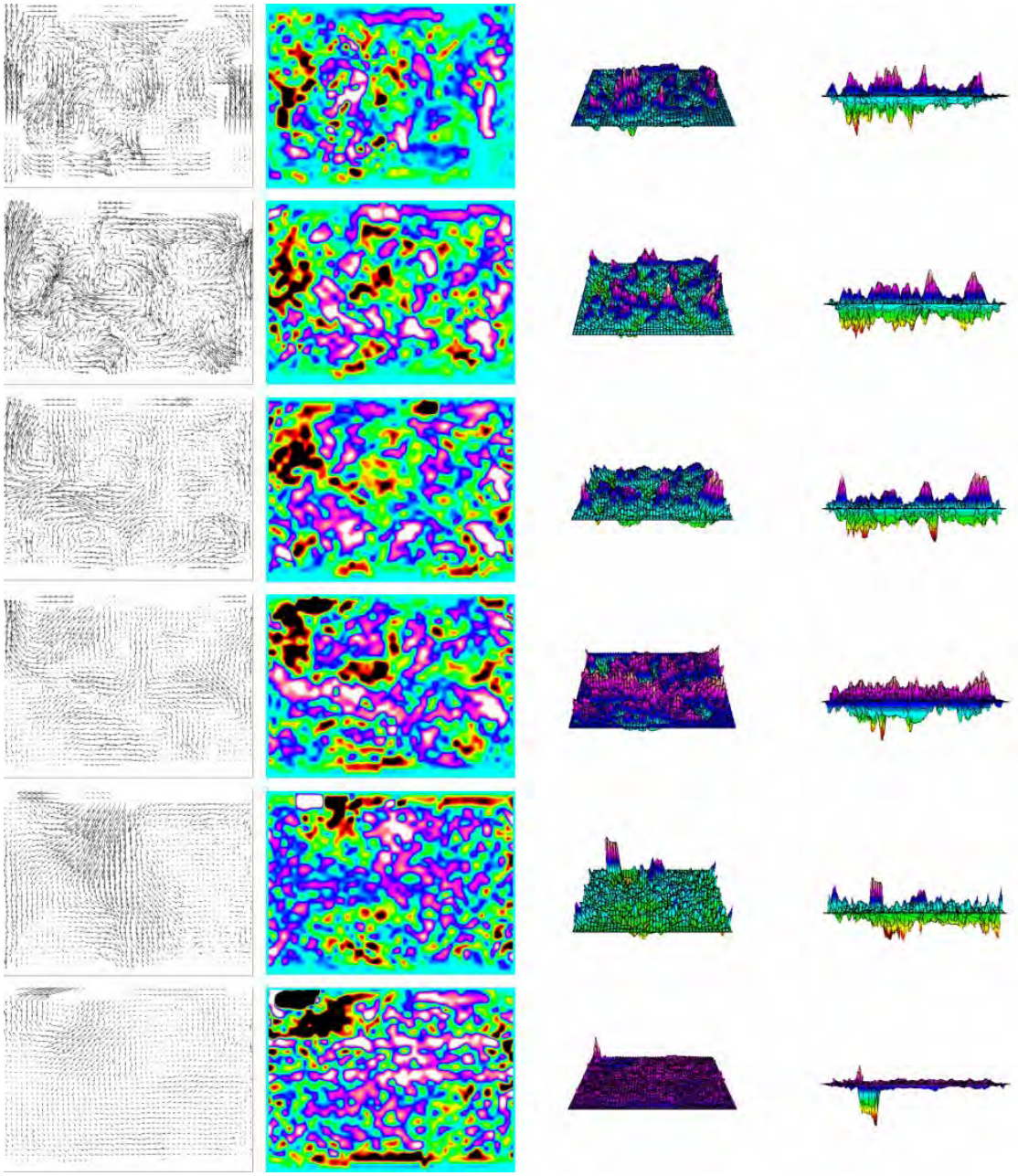

Figure 7.13: The evolution of velocity field, vorticity 2D field, vorticity 3D and profiles of vorticity 3D for experiment 2c with $Rig = 3.68$ at times 2, 5, 10, 20, 50 and 100 seconds.

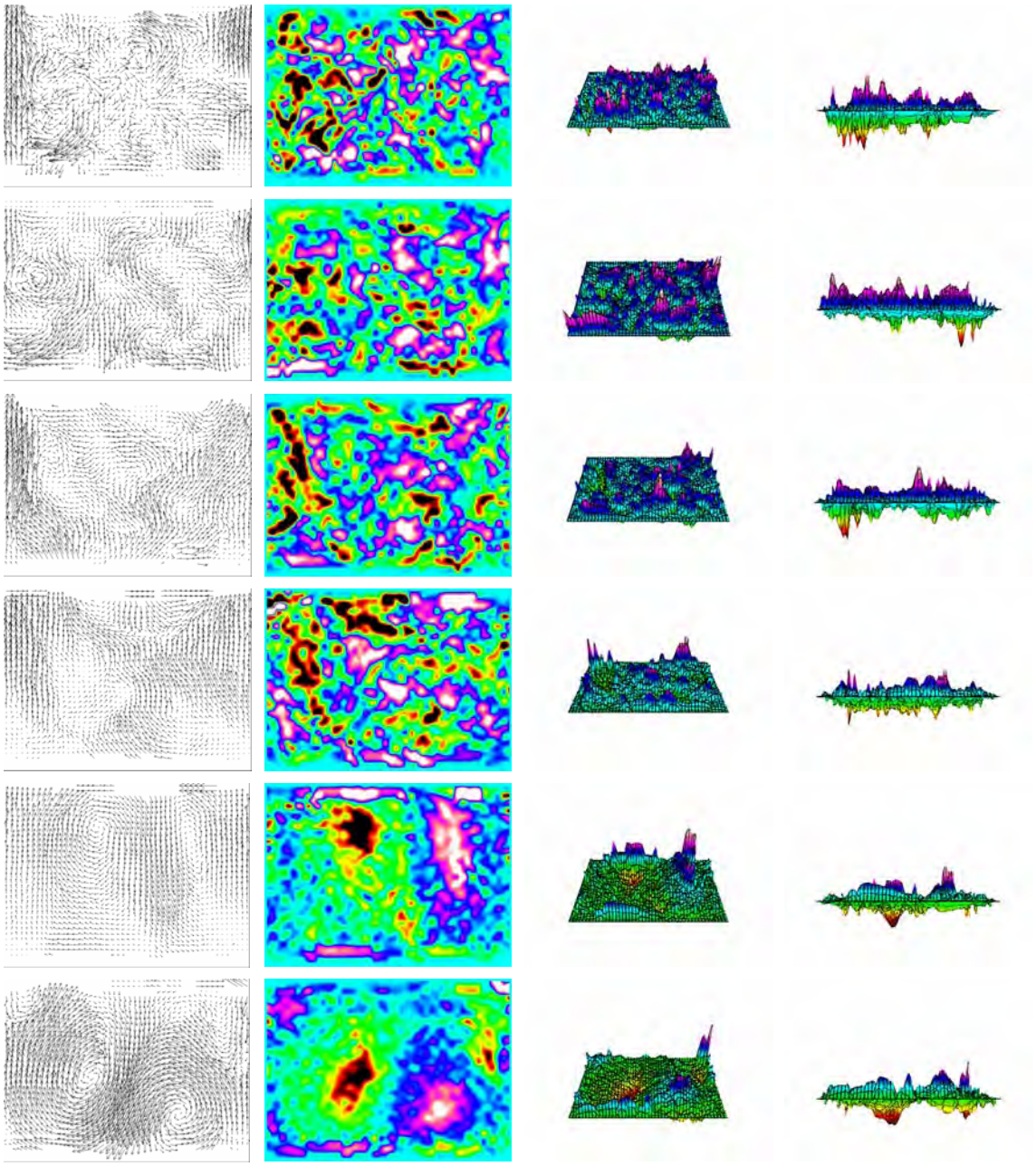

Figure 7.14: The evolution of velocity field, vorticity 2D field, vorticity 3D and profiles of vorticity 3D for experiment 2d with $Rig = 2.17$ at times 2, 5, 10, 20, 50 and 100 seconds.

In the following figures 7.15, 7.16 and 7.17 we can observe the structure of the flow for weak stratification experiments, with low Richardson number ($0.6 \langle Rig \langle 1.0$). The behaviour is quite similar to cases without stratification, and shows evident changes with the previous more stratified cases. It can be easily identified in the evolution graphs that there exist an obvious change of the tendency between 20s and 50s (two last graphs in all figures), both with little vorticity. Besides, it can be noticed

in the three first graphs there the vorticity change is quite strong. It is well visualised in the bidimensional vorticity maps, even more so in higher resolution visualizations.

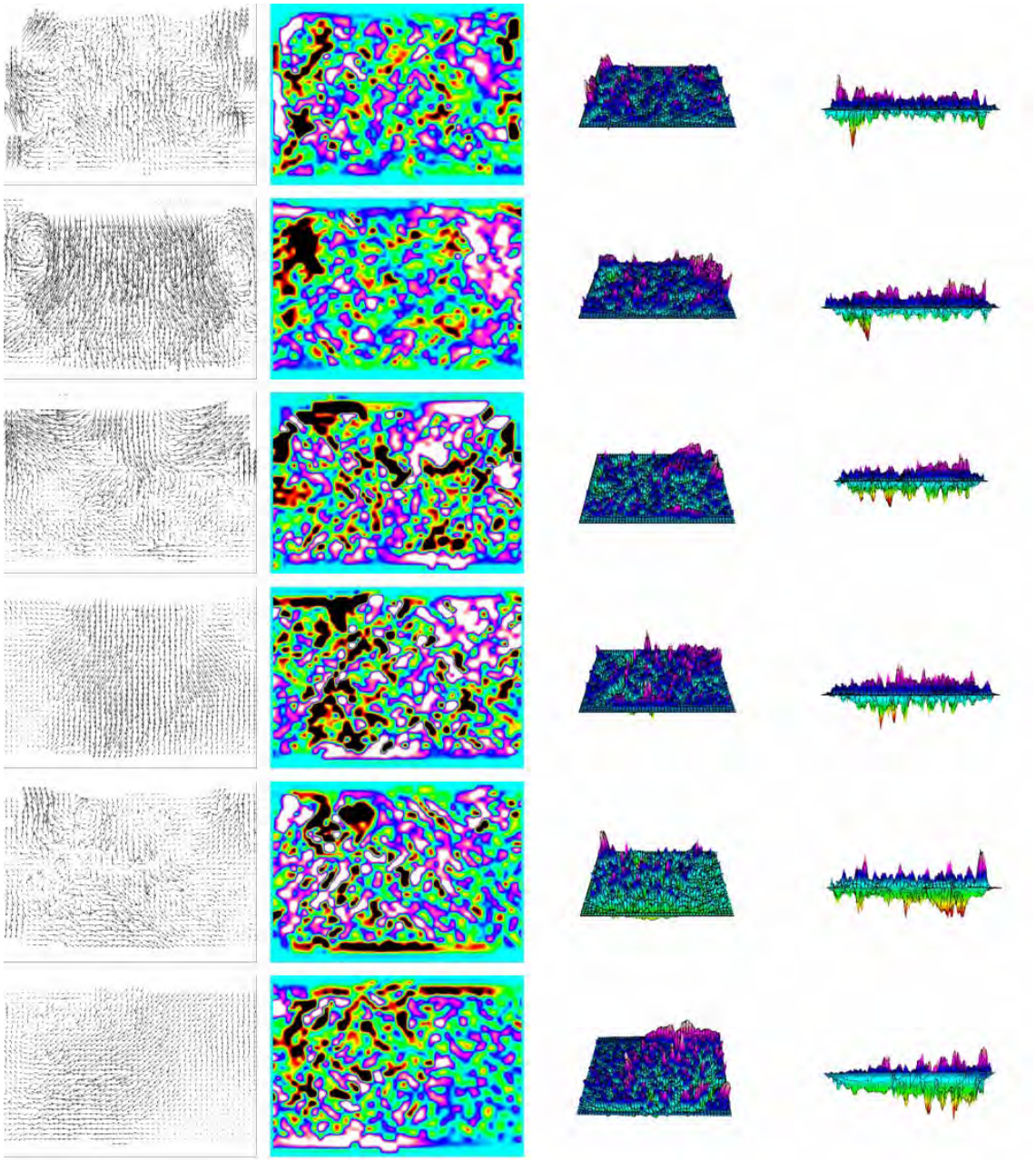

Figure 7.15: The evolution of velocity field, vorticity 2D field, vorticity 3D and profiles of vorticity 3D for experiment 1e with $Rig = 0.83$ at times 2, 5, 10, 20, 50 and 100 seconds.

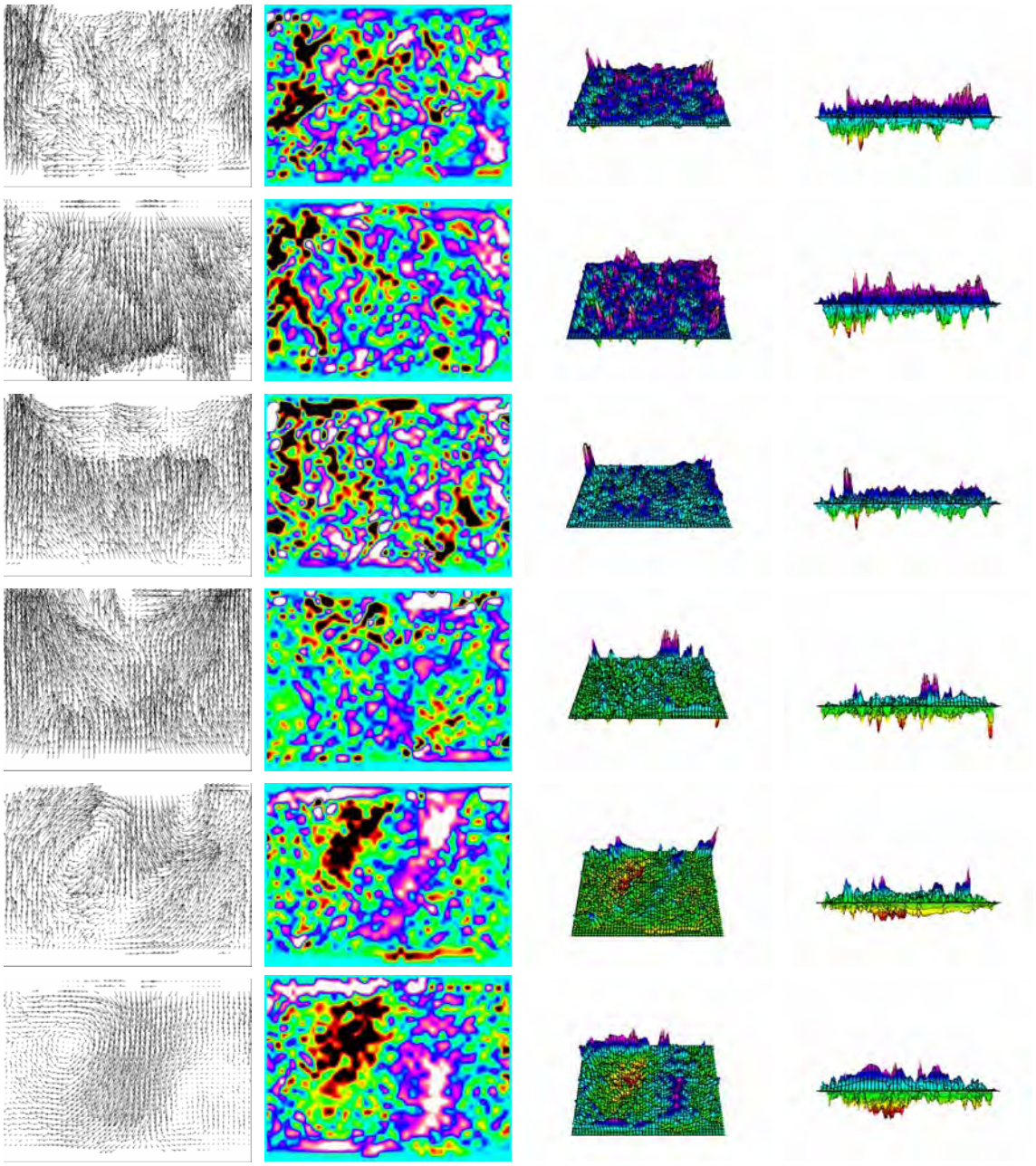

Figure 7.16: The evolution of velocity field, vorticity 2D field, vorticity 3D and profiles of vorticity 3D for experiment 2e with $Rig = 0.85$ at times 2, 5, 10, 20, 50 and 100 seconds.

In figure 7.18 we can see the example of the velocity field of a high resolution experiment with high Richardson number $Rig = 7{,}756$. Here the wave and vortices were detected with PIV and later were taken through the analysis process. The non-local interactions are clearly detected trough a combination of waves and vortices. In figure 7.19 we present examples of 2D velocity local zooms showing the velocity in the

PIV illuminated horizontal plane. At left we can see a locally dominant vortex structure and at right a strong shear region.

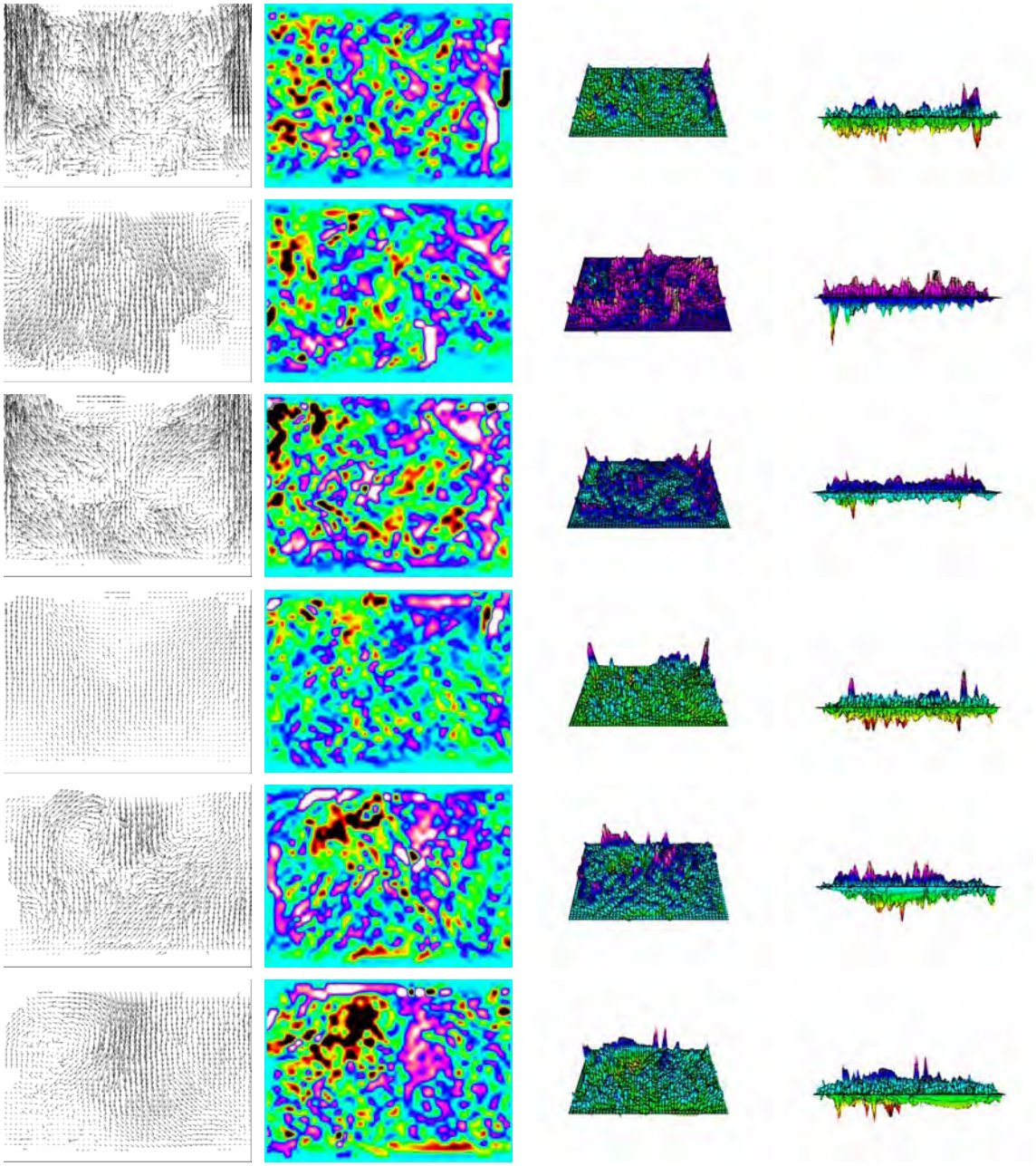

Figure 7.17: The evolution of velocity field, vorticity 2D field, vorticity 3D and profiles of vorticity 3D for experiment 2f $Rig = 0.64$ at times 2, 5, 10, 20, 50 and 100 seconds.

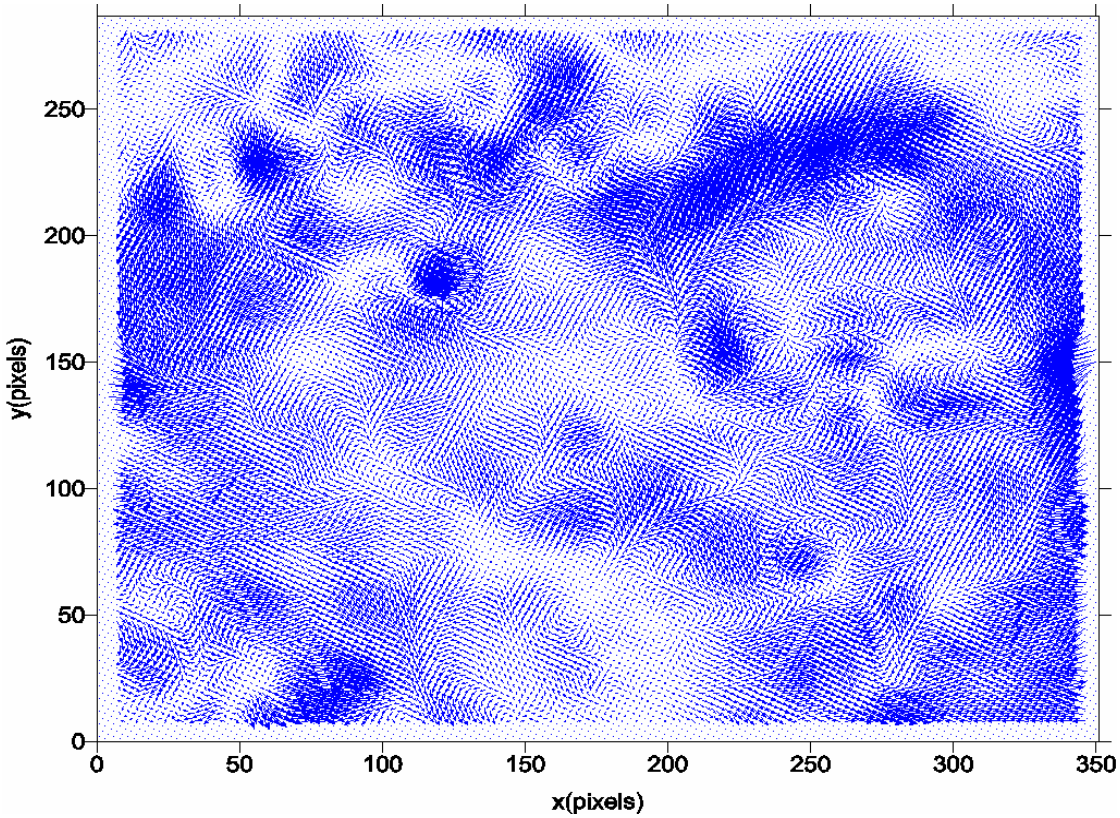

Figure 7.18: Example of a high resolution velocity mal in false colour for experiment with a high Richardson number $Rig = 7{,}756$, where waves and vortices may be detected with PIV and showing non-local interactions trough a combination of waves and vortices.

Further results on the topological analysis of the decaying stratified flows may be seen in Matulka et al. (2009) and in discussion.

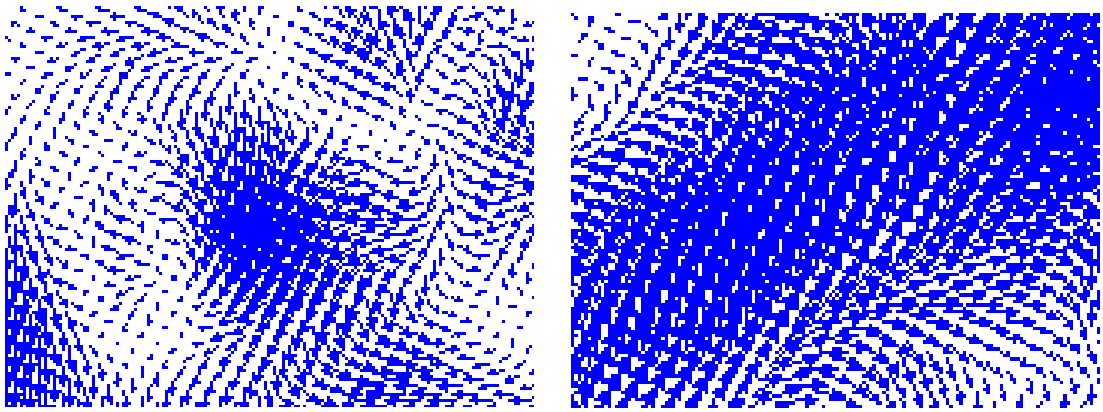

Figure 7.19: Example of 2D velocity local zooms showing the velocity in the PIV illuminated horizontal plane, (left) a locally dominant vortex structure, (right) a strong shear region.

7.3.1. The evolution of the positive (anticlockwise) and negative (clockwise) vorticity in time

Using DigiFlow program it was possible to use sequences of pairs of video frames in order to obtain the velocity and vorticity fields for all experiments in chosen times. The velocity and vorticity fields depend on the principal characteristics of experiments like temperature, grid velocity, salinity etc. Once chosen some consecutive frames in time we were able to plot in detail the vorticity values and to calculate their PDF´s. With these vorticity 2D fields it was also possible to see how the vorticity changes in time ($\frac{\partial \omega}{\partial t}$) comparing graph sequences, and also to calculate the different areas covered with either positive or negative vorticity and we compared, both the values and the area covered by these vortices as well as their ratio ($A\omega^{+}/A\omega^{-}$). The positive and negative vorticity regions in the images were obtained using the ImaCalc program.

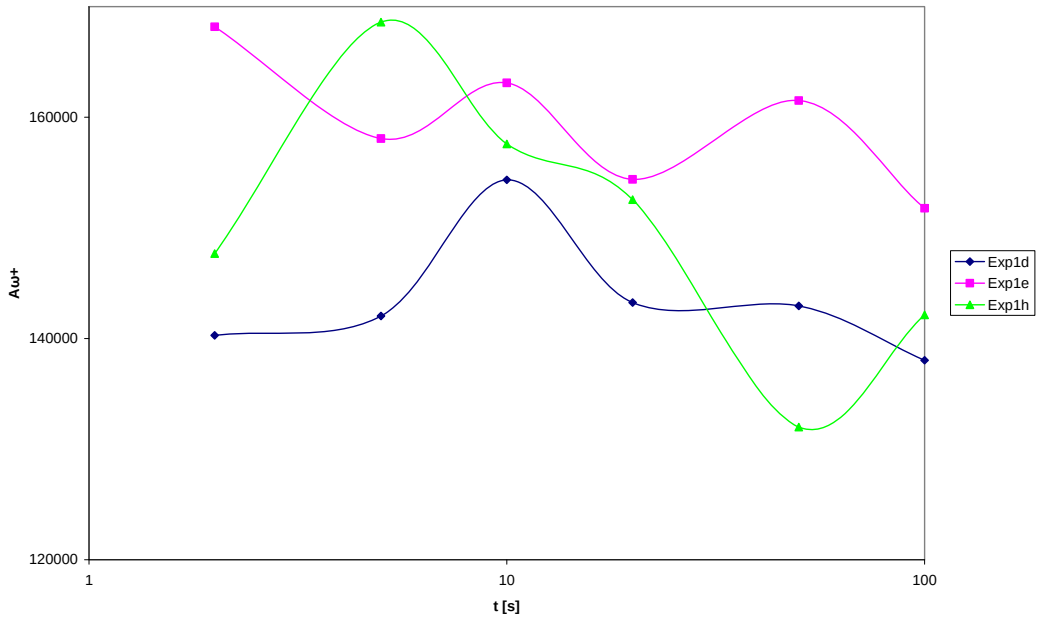

Figure 7.20: The evolution of positive vorticity area in time, comparison of experiments 1d ($Rig = 1.19$), 1e ($Rig = 0.83$) and 1h ($Rig = 0.04$) for different Richardson numbers.

In figures 7.20 and 7.21 we can observe the evolution of the positive vorticity in different experiments. We can see that the flow is clearly

oscillatory. It is clear that the experiment with the lowest Richardson number shows the largest overall decrease in vorticity at $\frac{\partial \omega}{\partial t} = 0.1 s^{-2}$.

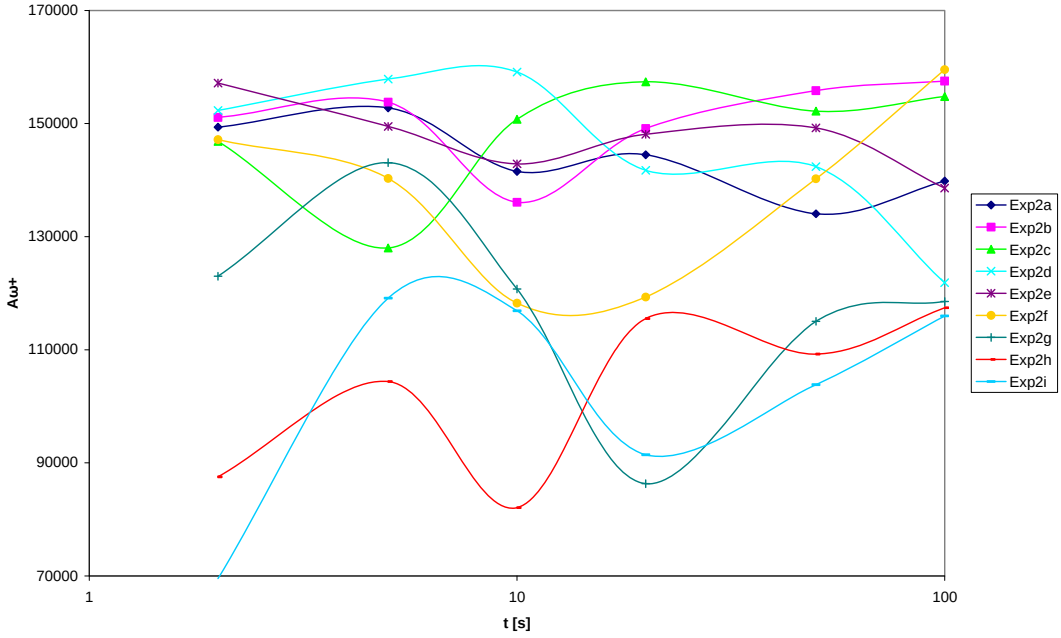

Figure 7.21: The evolution of positive vorticity area in time, comparison of experiments 2a through 2b … to 2i, from high to small Richardson numbers ($7.76 \leq Rig \leq 0.039$).

In figures 7.22 and 7.23 we can observe and compare the evolution of the negative vorticity in different experiments. We can also see that the flow is clearly oscillatory.

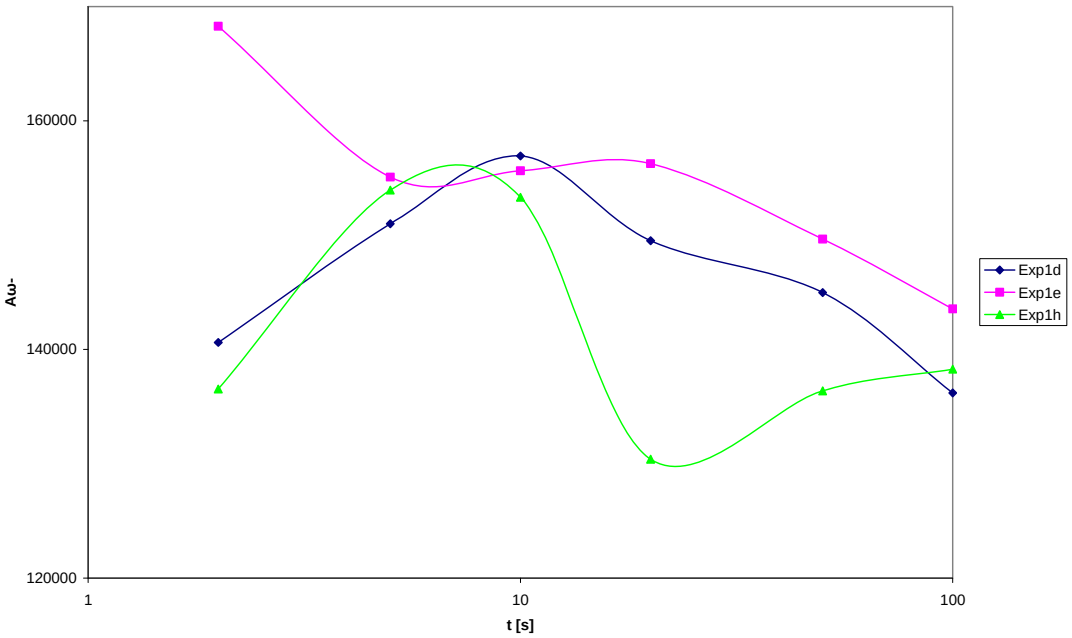

Figure 7.22: The evolution of negative vorticity area in time, comparison of experiments 1d ($Rig = 1.19$), 1e ($Rig = 0.83$) and 1h ($Rig = 0.04$) for different (average to low) Richardson numbers.

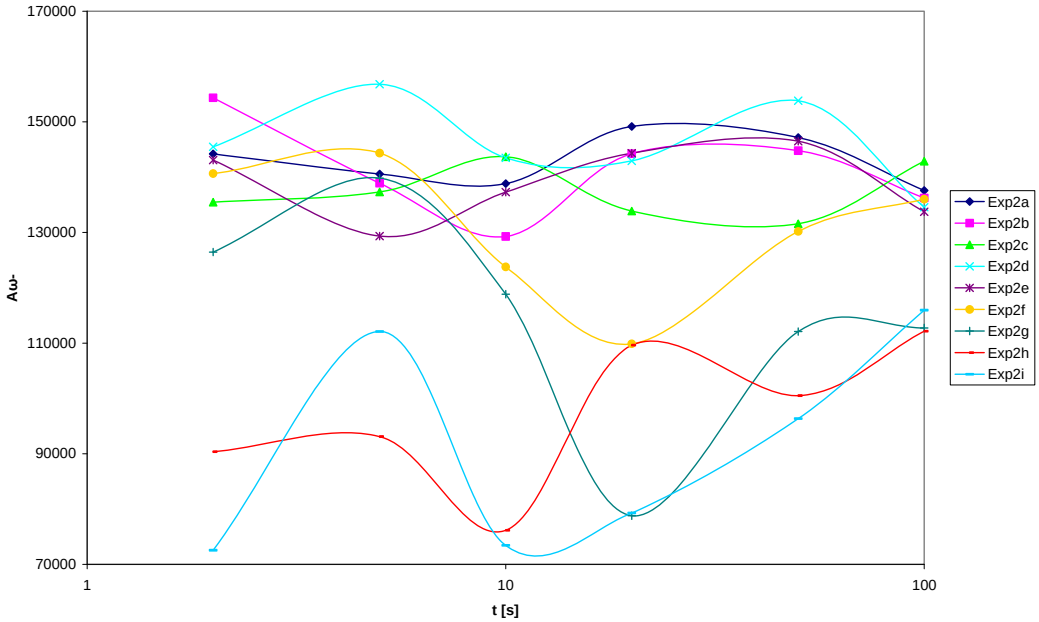

Figure 7.23: The evolution of negative vorticity area in time, comparison of experiments 2a through 2b … to 2i, from high to small Richardson numbers.

The flow is clearly oscillatory in nature, for all stratified experiments in contrast to what theoretical values of pure homogeneous 2D vorticity predicted for different

theories (LaCasce 2008). This will be discussed further when measuring in detail the number of vortices and discussed in chapter 9. Our main hypothesis is that this oscillatory behaviour is due to the presence of an internal wave field that increases the non-linear interactions between vortices, both of similar and opposite sign. This effect can be also valued by plotting the ratio of the area covered by positive (anticlockwise) vorticity, to the area covered by negative (clockwise) vorticity. This results are presented as it evolves in logarithmic time in figure 7.24 for medium-low experiments 1d, 1e and 1h and in figure 7.25 for a wide range of Richardson number ($7.76 \leq Rig \leq 0.039$) experiments from 2a, 2b to 2i.

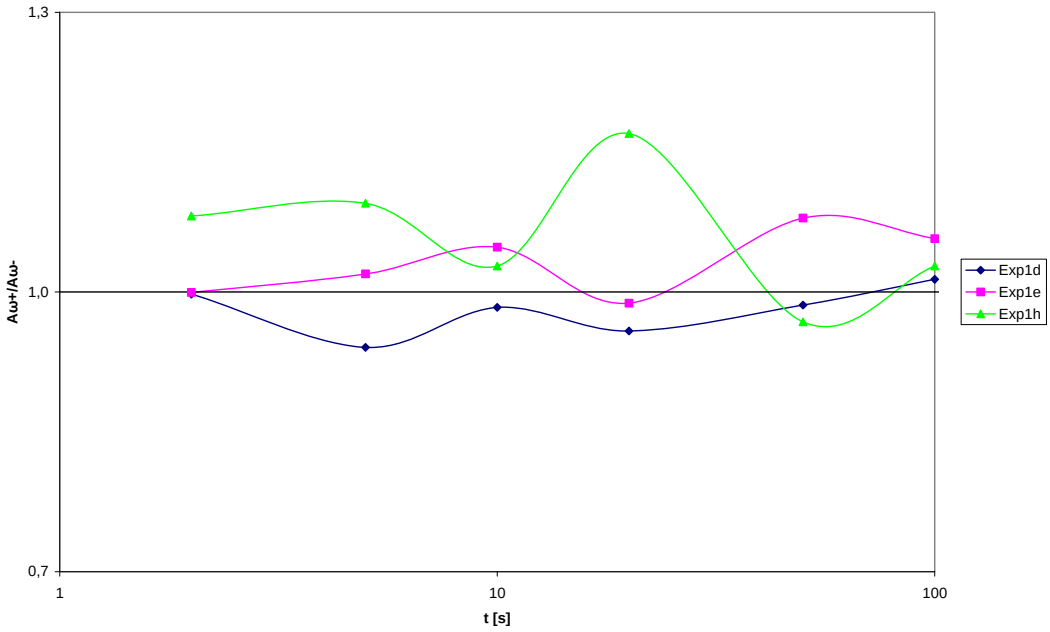

Figure 7.24: The ratio of positive to negative vorticity dominated areas in time for experiments 1d, 1e and 1h with different Richardson numbers.

What is also clearly noticed in all plots is that the period of vorticity area oscillation increase in time. This behaviour has to be compared with the evolution of the mean vorticity in time as well as on the detailed behaviours at the number and size at the individual vortices.

In the discussion, some theoretical arguments will lead to use the WKB method to predict vorticity evolution. (see appendix 6)

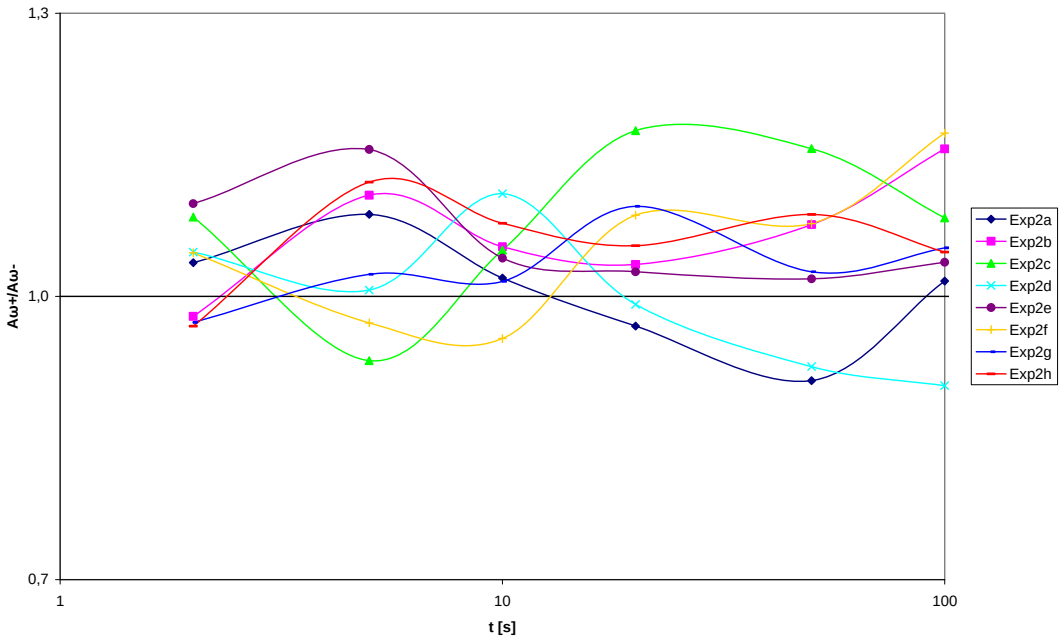

Figure 7.25: The ratio of positive to negative vorticity dominated areas in time for experiments from 2a to 2i with different Richardson numbers.

7.3.2. The evolution of vorticity and enstrophy in one line for different experiments

In this section we present about the evolution of vorticity and enstrophy in one line for different experiments following the numerical research of Dubos & Babiano (2003) and Dubos (2001). In figure 7.26 we can see the evolution of vorticity for experiment 2a with high Richardson number $Rig = 7{,}756$ in different times. We can observe that in time 2 seconds the peaks of vorticity were bigger, stronger that for peaks in time 100 seconds that have decreased considerably and are almost plane.

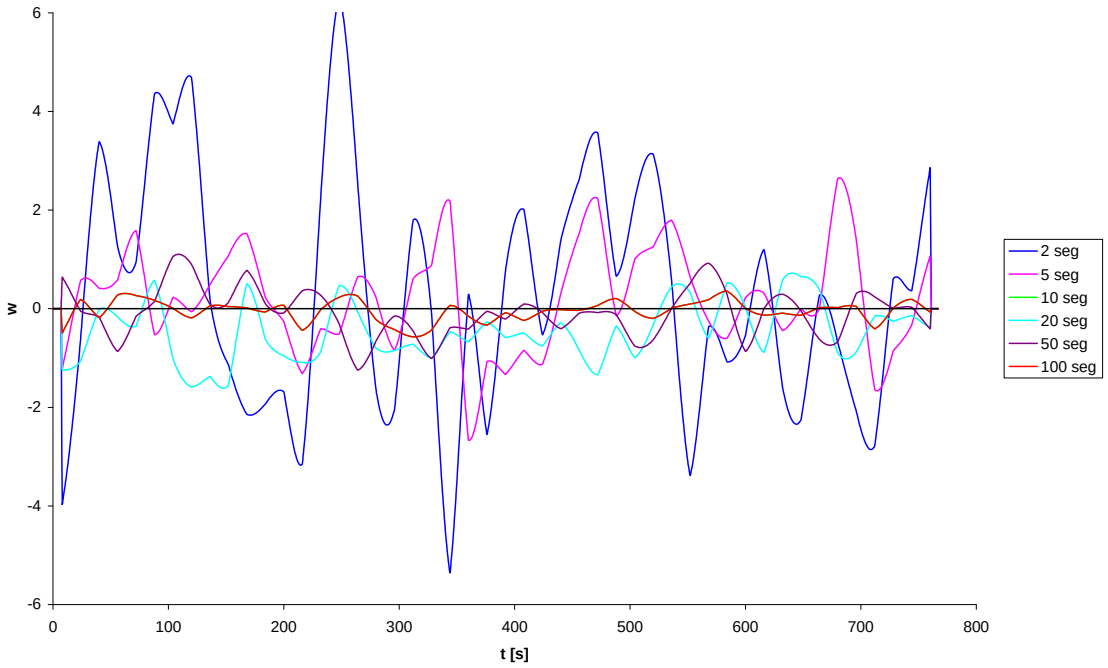

Figure 7.26: The evolution of vorticity in time for experiment 2a in one line with high Richardson number $Rig = 7{,}756$ for different times.

In figure 7.27 is presented the evolution of vorticity in time for the experiment 1c with average Richardson number $Rig = 1{,}84$ in different times and in figure 7.28 we can see the same evolution but for case with low Richardson number $Rig = 0{,}64$. In case of small Richardson number experiments it is not so clear to detect the difference between peaks of the vorticity at different times. The vorticity at 2 seconds is not as strong as in the cases at high Richardson numbers.

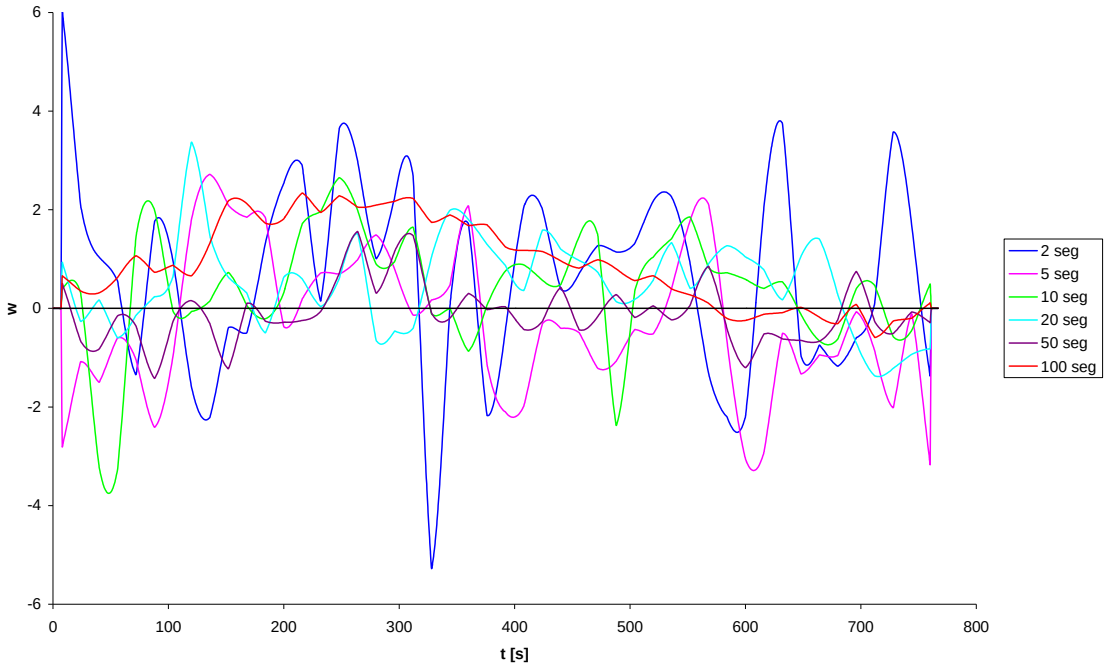

Figure 7.27: The evolution of vorticity in time for experiment 1c in one line with medium Richardson number $Rig = 1{,}84$ for different times.

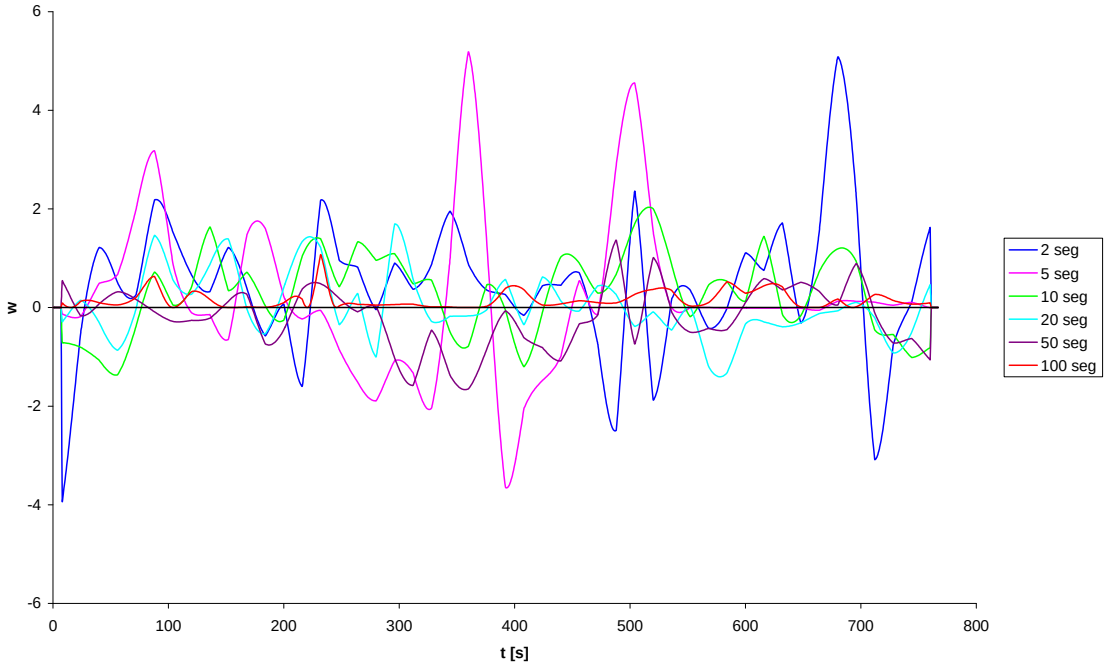

Figure 7.28: The evolution of vorticity in time for experiment 2f in one line with low Richardson number $Rig = 0{,}64$ for different times.

In figure 7.29 we show an example of the enstrophy spatial distribution in time for experiment 2a with high Richardson number. We can observe like in the case of the

vorticity evolution that at earlier times, the peaks of vorticity are large, and easy to count, but closer to the end of the experiments the vortices are only marginally larger than the noise, so it is not possible to keep the accuracy of the count. A detailed study on the number of vortices in decaying stratified turbulence will be presented and discussed below, comparing our stratified situation with a theoretical perfect 2D situation.

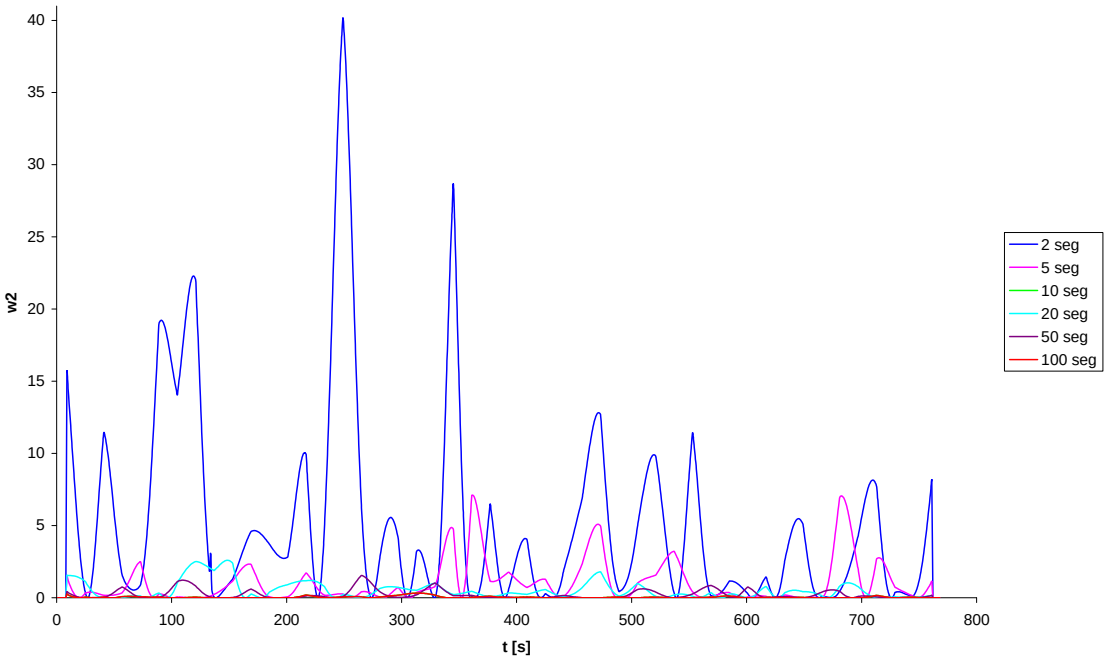

Figure 7.29: The Enstrophy spectra in time for experiment 2a in one line with high Richardson number $Rig = 7{,}756$ for different times.

In comparison to the previous case with high Richardson number we can see in figures 7.30 and 7.31 with medium and low Richardson number that the difference between the 2 seconds and 100 seconds is not so obvious. We can observe in figure 7.30 that the enstrophy is visible in 2 and 5 seconds, but during the experiments it is decreasing and it is not possible to see clearly the difference between 50 and 100 seconds. And in the case with low Richardson number in figure 7.31, we can see only clear enstrophy peaks in 2 and 5 seconds, and it is difficult to distinguish the peaks after 10 seconds till the end of the experiment.

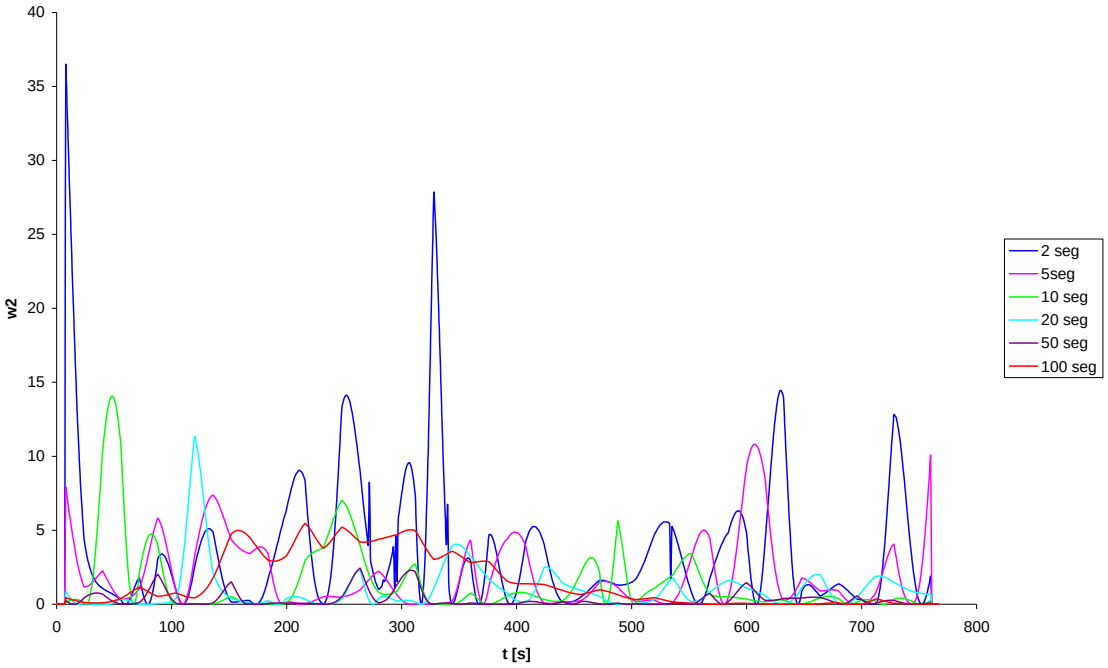

Figure 7.30: The Enstrophy spectra in time for experiment 1c in one line with medium Richardson number $Rig = 1{,}84$ for different times.

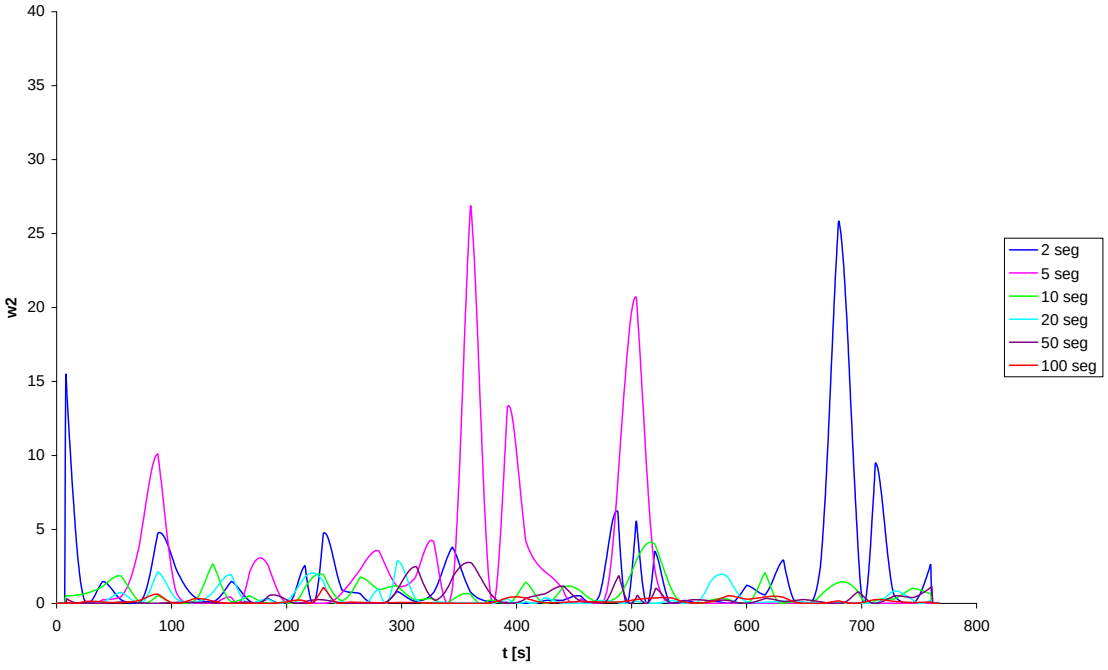

Figure 7.31: The Enstrophy spectra in time for experiment 1c in one line with low Richardson number $Rig = 0{,}64$ for different times.

It is also noticed that most of the largest vortices formed still remain some traces of the vortices that were merged and have also an inner structure; this is seen looking at the enstrophy oscillations within the largest size vortices.

Taking into account the number of vortices measured in experiments 1c, 2a and 2f we can find a more convenient dimensionless expression $N_o(t)/N_o(t_o)$ for their comparison. In figure 7.32 we can compare the evolution of this non-dimensional vortex number in time for different Richardson numbers (in a single line), with an error of 5%. The tendency line is exponential, such that

$$N_o(t)/N_o(t_o)=C\,e^{-\beta t} \tag{7.1}$$

where C is a constant or variable that might depend on buoyancy. The decay factor β is a new line decay exponent, which should be half of the plane exponent. We can observe

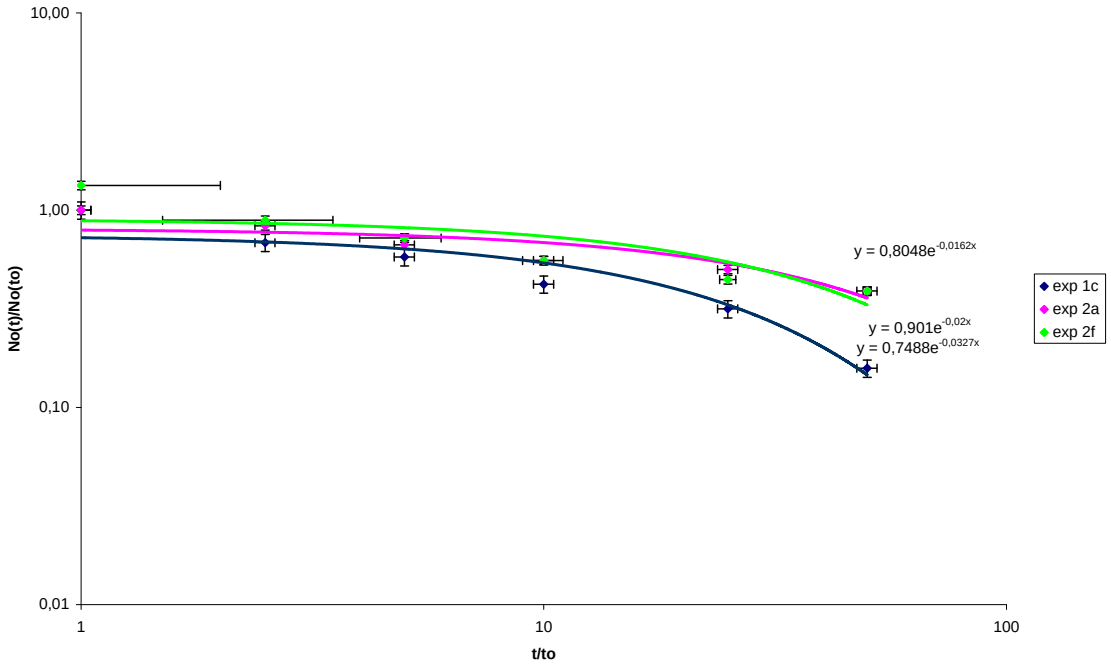

Figure 7.32: Dimensionless expression of the vortex number evolution in time for experiments 2a, 1c and 2f of $N_o(t)/N_o(t_o)$ and t/t_o with high, medium and low Richardson numbers $Rig=7{,}756$ (experiment 2a), $Rig=1{,}84$ (experiment 1c) and $Rig=0{,}64$ (experiment 2f) in single line, with an evaluation of r.m.s. error of 5%.

that this exponent varies from 0.0327 for 1c (high Richardson number), 0.02 for 2a (medium Richardson number) and 0.0162 for 2f (low Richardson number). The advantage of this line indicator is that it is much easier to calculate than the one described below, and that it also allows us to investigate directional anisotropy.

In figure 7.33 we show the evolution of positive vortex number in non dimensional way for experiments 1c, 2a and 2f of $N_o(t)^+ / N_o(t_o)^+$ with an error of 5%. We can observe here the tendency line as exponential with exponent for 1c 0.0402, for 2a 0.097 and for 2f 0.0285.

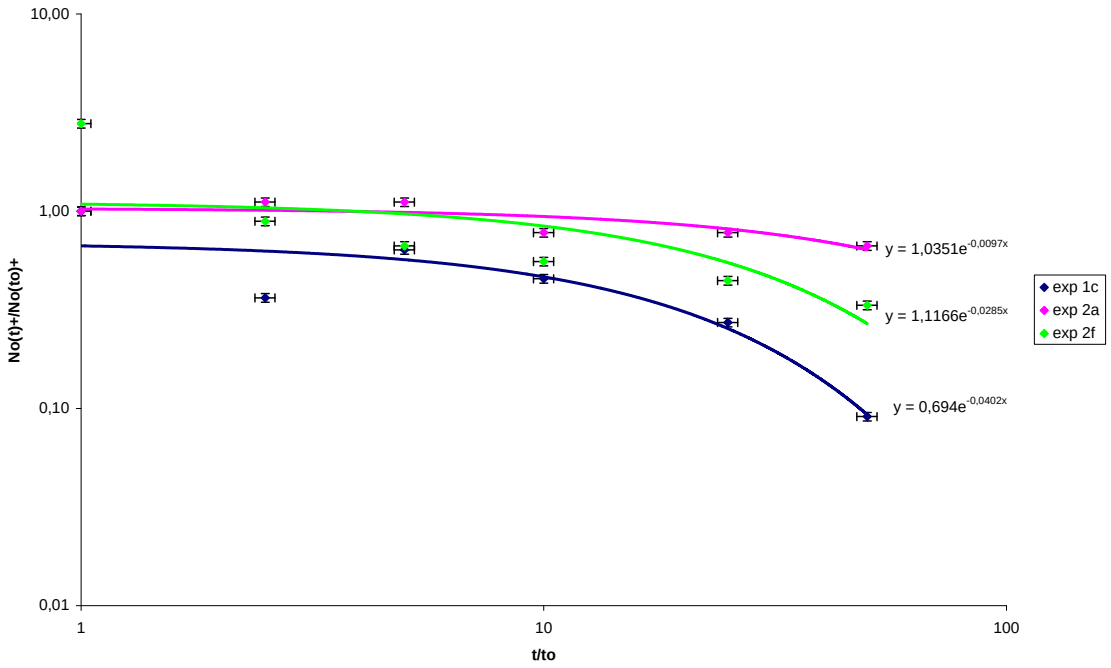

Figure 7.33: The evolution of positive vortices in time for experiments 2a, 1c and 2f of $N_o(t)^+ / N_o(t_o)^+$ and t/t_o with high, medium and low Richardson numbers $Rig = 7{,}756$, $Rig = 1{,}84$ and $Rig = 0{,}64$ in one line, with an evaluation of r.m.s. error of 5%.

In figure 7.34 we present the evolution of the negative vortex number for experiments 1c, 2a and 2f of $N_o(t)^- / N_o(t_o)^-$ with an error of 5%. The tendency line is as in previous cases is exponential with the exponential rate for 1c as 0.0254, for 2a as 0.0078 and for 2f as 0.0285.

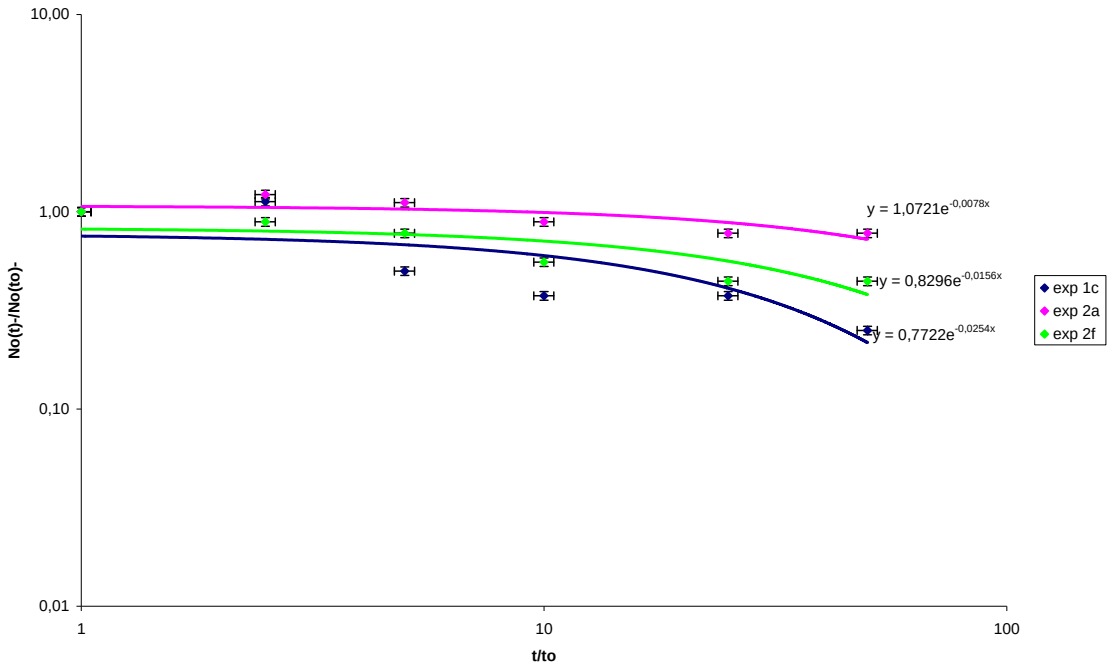

Figure 7.34: The evolution of negative vortices in time for experiments 2a, 1c and 2f of $N_o(t)^- / N_o(t_o)^-$ and t/t_o with high, medium and low Richardson numbers $Rig = 7{,}756$, $Rig = 1{,}84$ and $Rig = 0{,}64$ in one line, with an evaluation of r.m.s. error of 5%.

In figure 7.35 is observed the evolution of the enstrophy in time for three different experiments 1c, 2a and 2f with low, medium and high Richardson number of $N^2{}_o(t)/N^2{}_o(t_o)$ with an error of 5%. The tendency line is exponential with rate for 1c 0.043, for 2a 0.0029 and for 0.027.

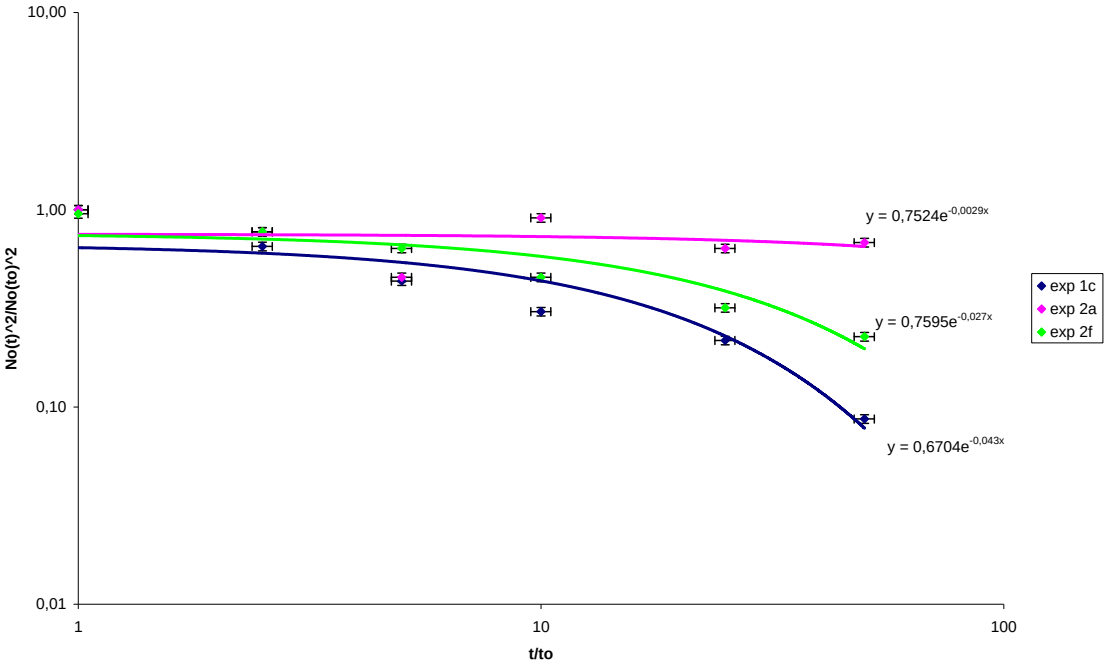

Figure 7.35: The enstrophy in time for experiments 2a, 1c and 2f of $N^2{}_o(t)/N^2{}_o(t_o)$ and t/t_o with high, medium and low Richardson numbers $Rig = 7{,}756$, $Rig = 1{,}84$ and $Rig = 0{,}64$ in one line, with an evaluation of r.m.s. error of 5%.

We can see that there is a complex non-linear and non-monotonic relationship between the stratification parameterize by Richardson number and the vortex decay. The decay rate of the number of vortices does not vary much in the highest Richardson number experiment. On the other hand for intermediate Richardson numbers the decay of the vortex number reaches maximum and for small Richardson number there is again a decrease in the vortex number rate. In all cases the difference between the tendency rates for different Richardson numbers does not vary much, indicating the importance of the grid forcing, in time the differences are more and more important. When *Rig* was 7.756 the exponential rate β was between 0.0029 and 0.016, when *Rig* was 1.84 then β 0.043 to 0.0254 and finally when the Richardson number was quite small $Rig = 0.64$ then β was between 0.0156 and 0.0285.

At the begging is much better for all vortices, because taking separately positive and negative vortices, the dispersion of data is much higher. In all cases it is clear that the highest decay of the number of vortices takes place with intermediate *Rig*, this means that stratification produces a highest vortex decay, probably through internal

wave interaction, which produces an additional dissipation, in the situation of maximum mixing efficiency (as described by Redondo 1990 and Fraunie et al. 2008). This effect will be modelled in several ways in chapter 9, due to its complexity.

7.3.3. The evolution of integral scale in time

As the stratification produces a complex interaction between the vertical vorticity produced by the collapse of the eddies and the horizontal vorticity produced by breaking internal waves with strong local vertical displacements at the density interface the homogeneous 2D turbulence decay power law is not going to followed, even in the strongly stratified situations. For the very weakly stratified flows we expect that the integral scale, or length scale where most kinetic energy resides, will not decay as fast and follow a 3D decay. We have to choose between different forcing and internal parameters to construct the dimensionless number that we are looking for, so we may distinguish different scaling effects during the whole mixing process. For example, we may compare similar behaviours under different conditions, characterized by different scales that may be useful in order to compare between natural large-scale and experimental (small-scale laboratory) flows. In chapter 8 we will compare the characteristic sizes for well defined vortices in the ocean surface.

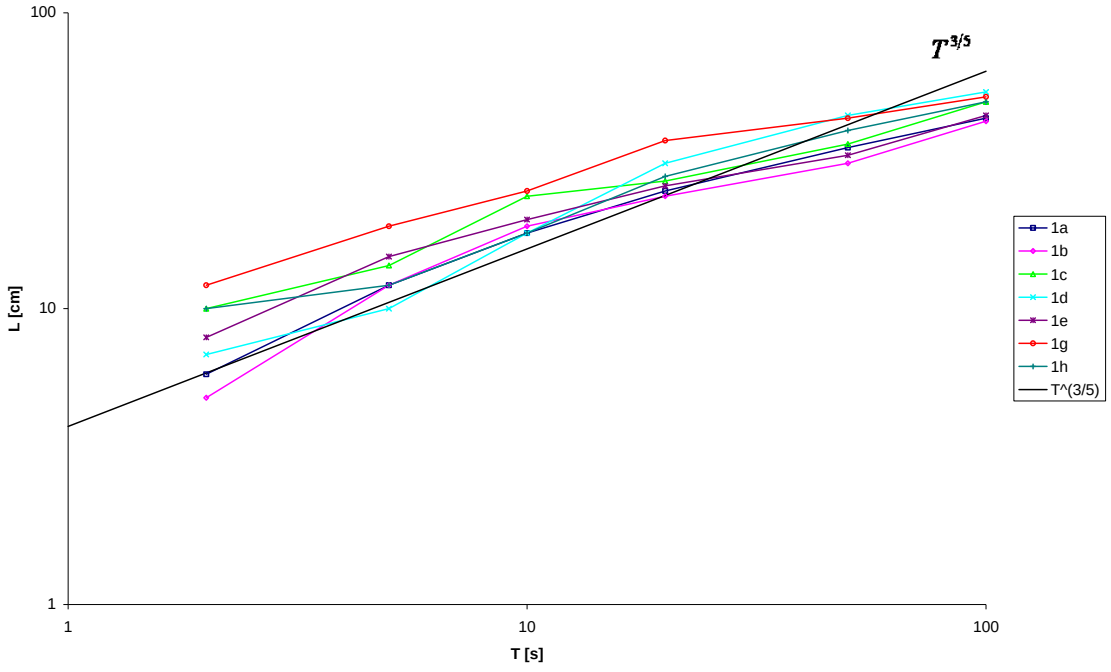

Figure 7.36: Evolution of the integral scale for experiments 1a to 1h with different Richardson numbers and different characteristic scales L[cm] according to the time T [s].

Here we will explore the relationship Time (T) – Integral length scale (L), scaled both with the grid forcing time scale and with the internal wave frequency time scale $1/N$. On the one hand, figures 7.36 and 7.37 present a dimensionless relationship only for the size using the mesh size and time as: $T - L/M$, where M is the characteristic grid scale equal to 10 cm. These figures show the evolution of integral scale of the plane flow in time for experiments 1a, 1b to 1h and 2a, 2b to 2i. Note that in this case T may be adimensionalised in two ways: 1) T times the Brunt -Väisälä frequency (N) and 2) T times the characteristic velocity u divided by M. In both cases the dominant relationship is proportional to $T^{3/5}$. But the kink in the growth law is a clear sign of the interactions between the dominant vortices and the internal waves. Note also that because the motions can also be vertical faster flowing crests of the internal waves are detected in the flow visualizations. The velocity at the plane intersecting several times a set halocline does not have to comply with the continuity equation.

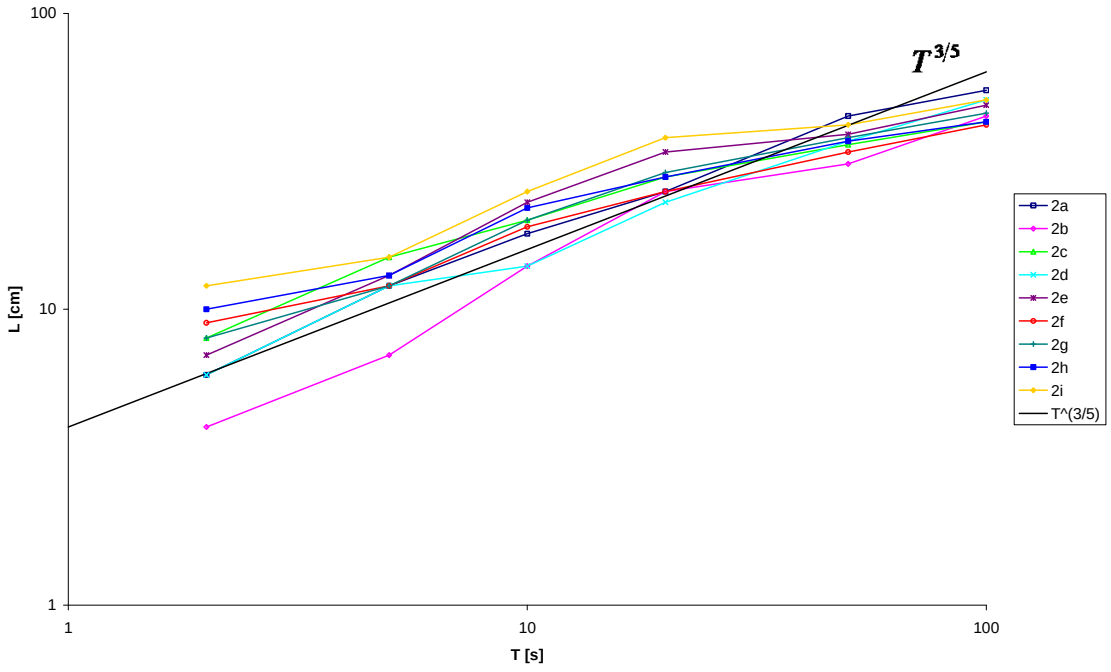

Figure 7.37: Evolution of the integral scale for experiments 2a to 2i with different Richardson numbers and the different characteristic scales L[cm] according to the time T [s].

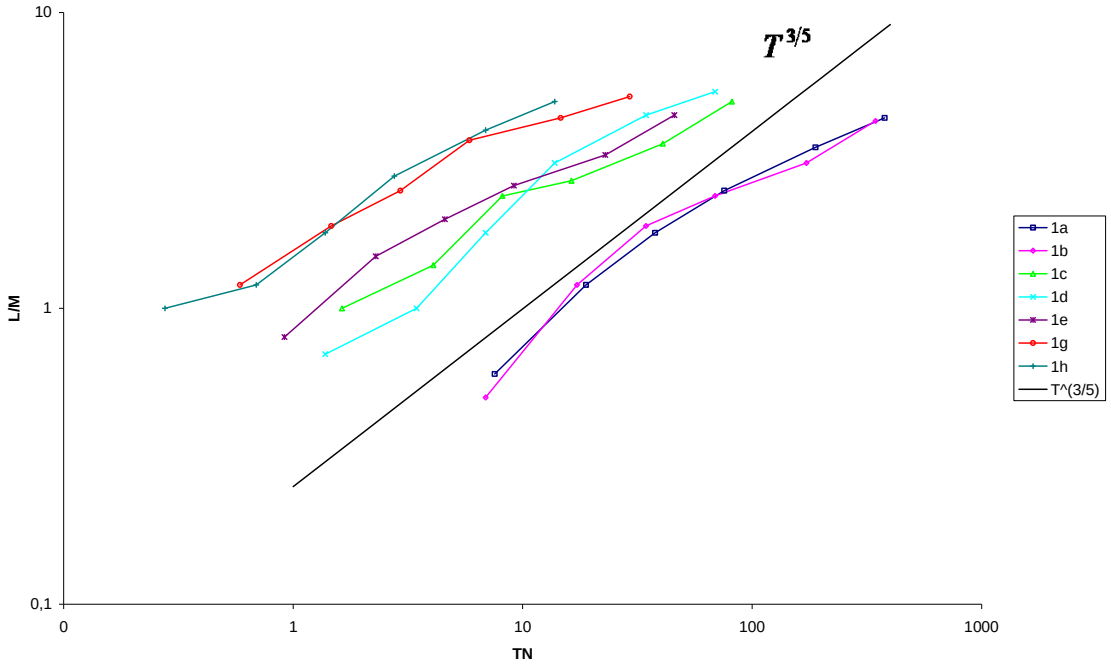

Figure 7.38: Evolution of the integral scale in non dimensional form for experiments 1a to 1h with different Richardson numbers, the dimensionless expression of L/M and $T\,N$ where *M* is the characteristic grid length scale (*10 cm*).

Figures 7.38 and 7.39 show the evolution in time of the integral scale of the plane flow in a dimensionless form of L/M and $T\,N$ where *M* is the characteristic grid length scale (10 cm) and *N* the Brunt - Väisälä frequency. These two figures are for two different experiments from 1a, 1b to 1h and from 2a, 2b to 2i.

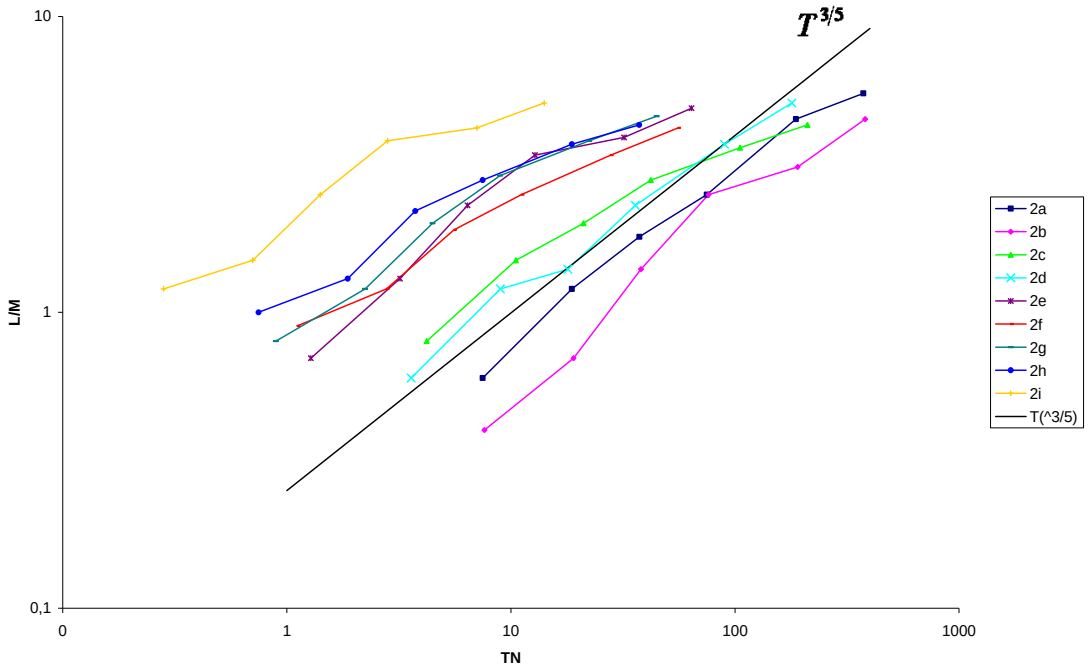

Figure 7.39: Evolution of the integral scale for experiments 2a to 2i with different Richardson numbers, the dimensionless expression of L/M and $T\ N$ where *M* is the characteristic grid length scale (*10 cm*).

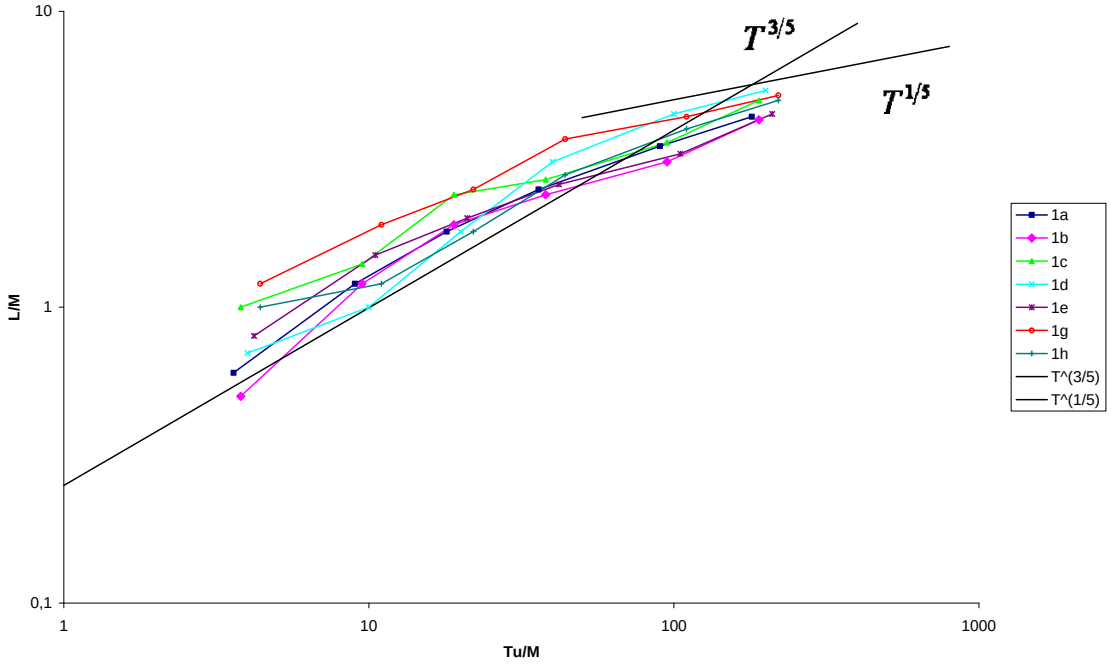

Figure 7.40: Evolution of the integral scale for experiments 1a to 1h with different Richardson numbers, the dimensionless expression of L/M and Tu/M where *M* and *u* are the characteristic grid length scale (*10 cm*) and velocity respectively.

In figures 7.40 and 7.41 we can see the evolution in time of the integral scale of the plane flow in a dimensionless form for experiments from 1a to 1h and from 2a to 2i in the way as L/M and Tu/M where M and u are the characteristic grid length and the velocity respectively.

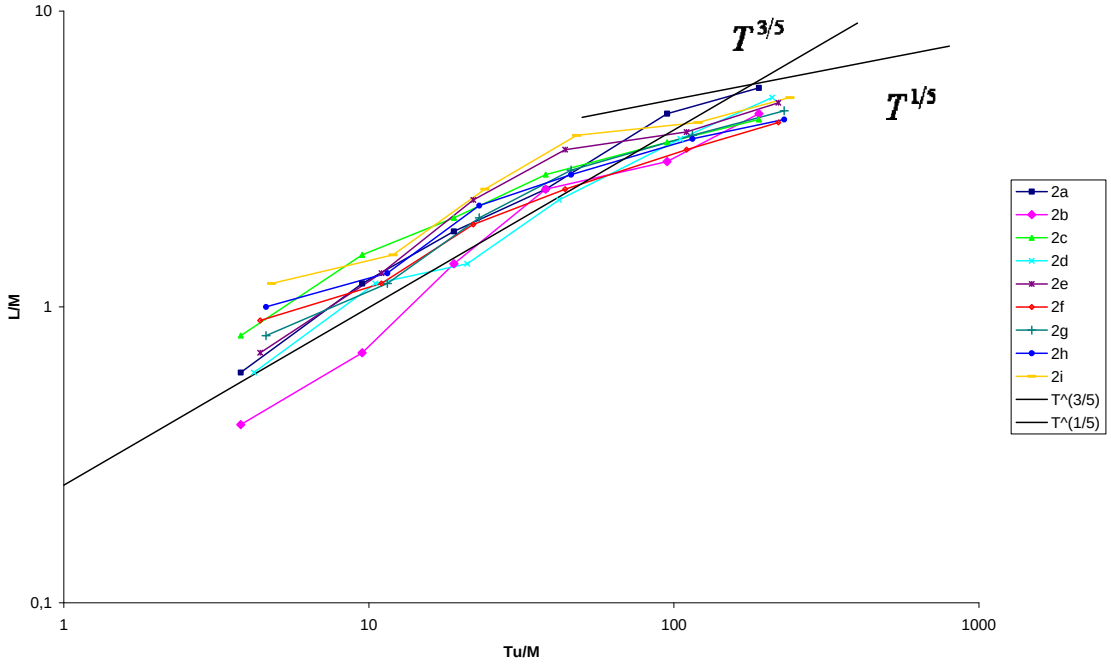

Figure 7.41: Evolution of the integral scale for experiments 2a to 2i with different Richardson numbers, the dimensionless expression of L/M and Tu/M where *M* and *u* are the characteristic grid length scale (*10 cm*) and velocity respectively.

It is easy to see that there is a strong influence at the internal waves between $NT \sim 3-8$, specially for the highest *Rig* experiments $T^{1/5}$.

From the much better scaling with the forcing time, it is evident that this effect is responsible for the initial growth of the eddies, only after 50 to 100 mesh sizes at the grid speed the flow really is dominated by buoyancy. This interval is shorter for the highest Richardson numbers.

7.3.4. The histograms of local vorticity measured by PIV

A detailed analysis of the PDF and histograms of the different vorticity fields in time are presented in this section. We observed that the vorticity field is different in all experiments, and depends also on the grid velocity besides of its role as part of the Richardson number, so at least a 2D parameter space will be needed. Following figures 7.42 to 7.46 show the evolution of the vorticity PDF's in time for different experiments during 100 seconds (every line correspond to different point in time as 2, 5, 10, 20, 50 and 100 sec).

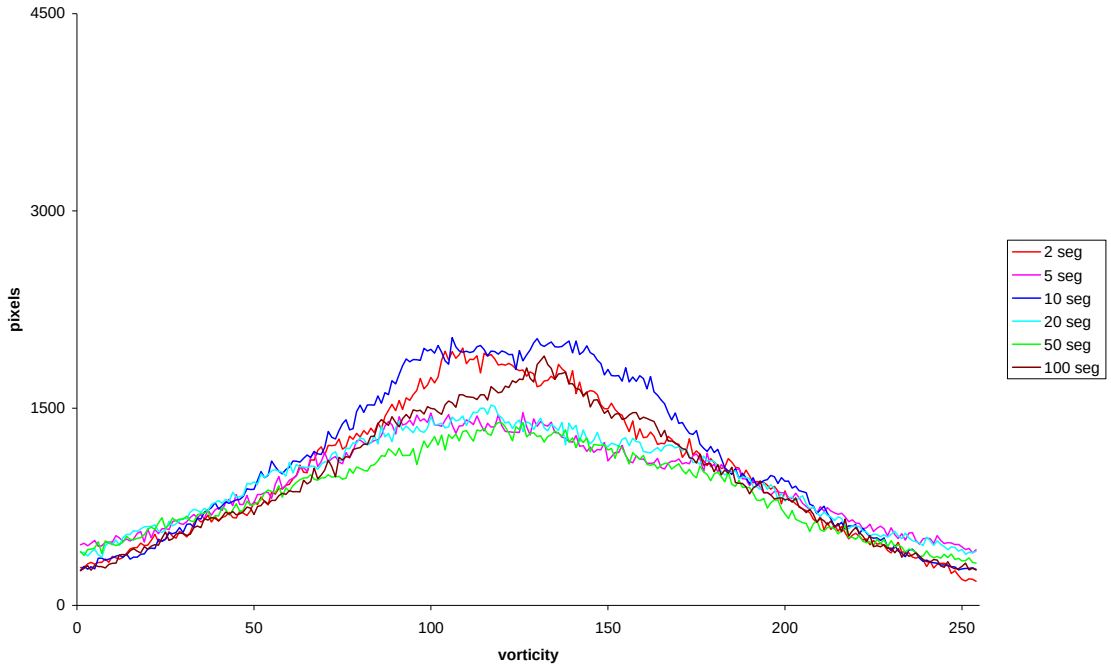

Figure 7.42: The histogram of local vorticity measured by PIV in experiment 1d with $Rig = 1.19$ for different times.

It can be observed that in experiment 2a the vorticity field histogram is increasing with time and it is mean that the area of vortices at the beginning is bigger that in the final part of the experiment. In figure 7.45 we can see how is decreasing the area of vortices from 2 seconds that occupy almost all grey level and in 100 seconds only 50 % or less. In other cases this is not so obvious because histograms are not so clear that in experiment 2a. In experiment 2b the histogram is decreasing and in 1d and 1e is almost the same during all experiment.

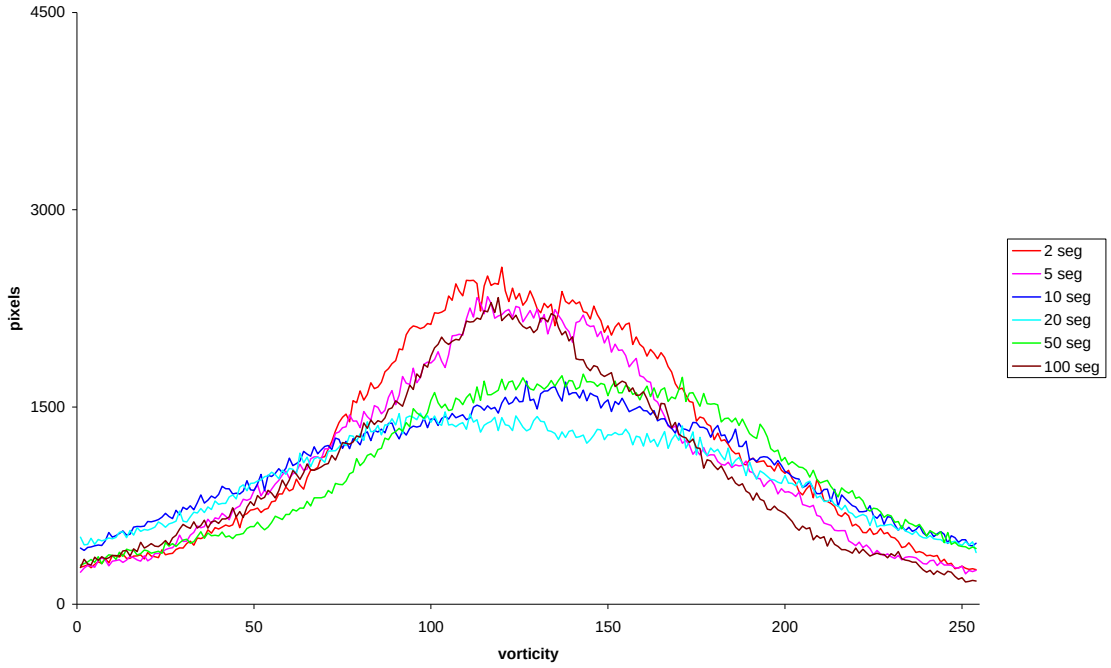

Figure 7.43: The histogram of local vorticity measured by PIV in experiment 1e with $Rig = 0.83$ for different times.

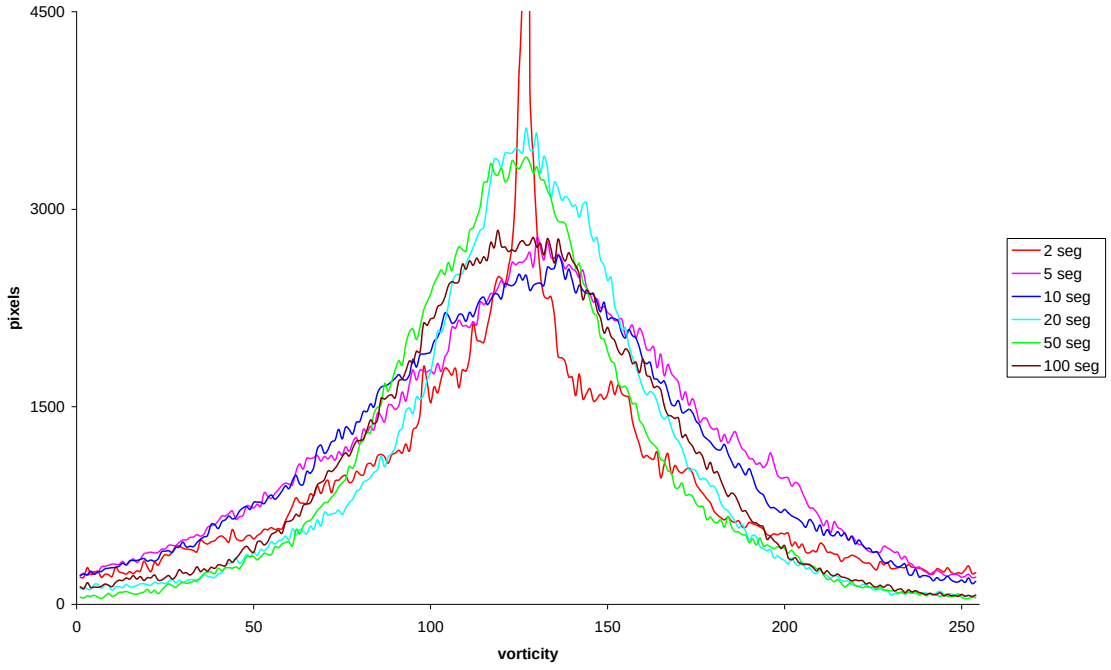

Figure 7.44: The histogram of local vorticity measured by PIV in experiment 1h with $Rig = 0.039$ for different times.

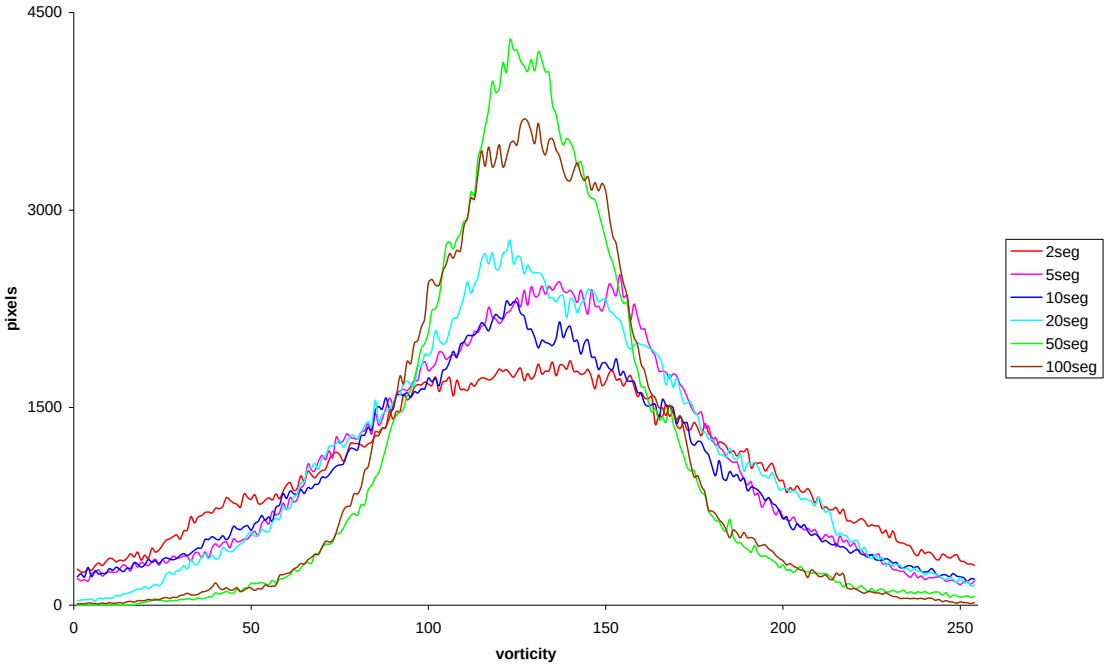

Figure 7.45: The histogram of local vorticity measured by PIV in experiment 2a with $Rig = 7.756$ for different times.

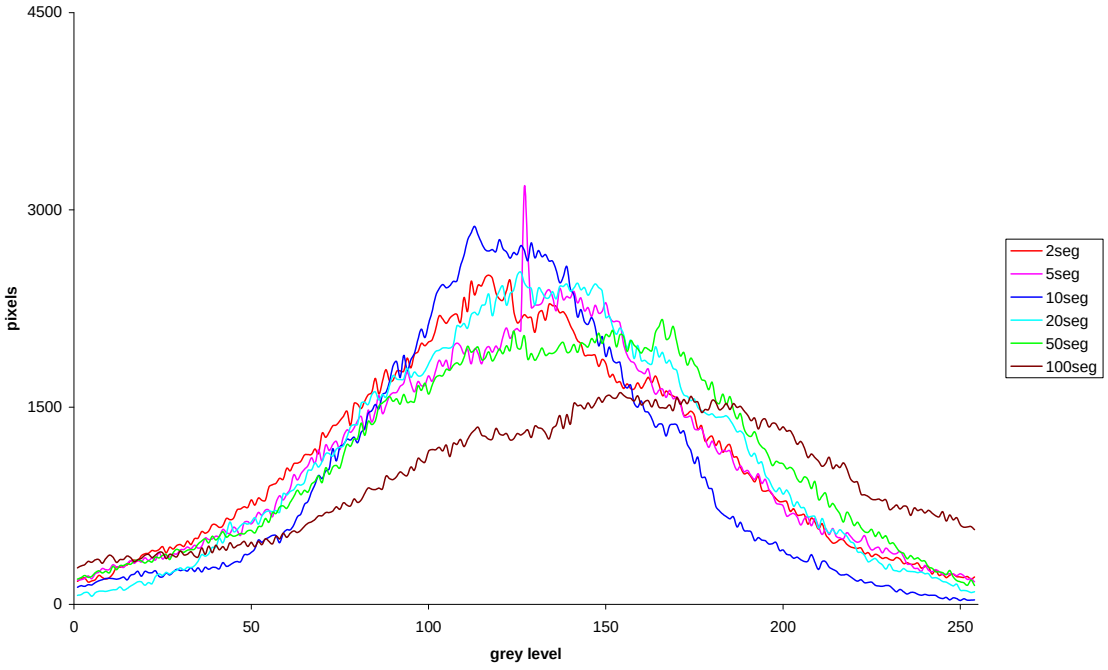

Figure 7.46: The histogram of local vorticity measured by PIV in experiment 2b with $Rig = 8.033$ for different times.

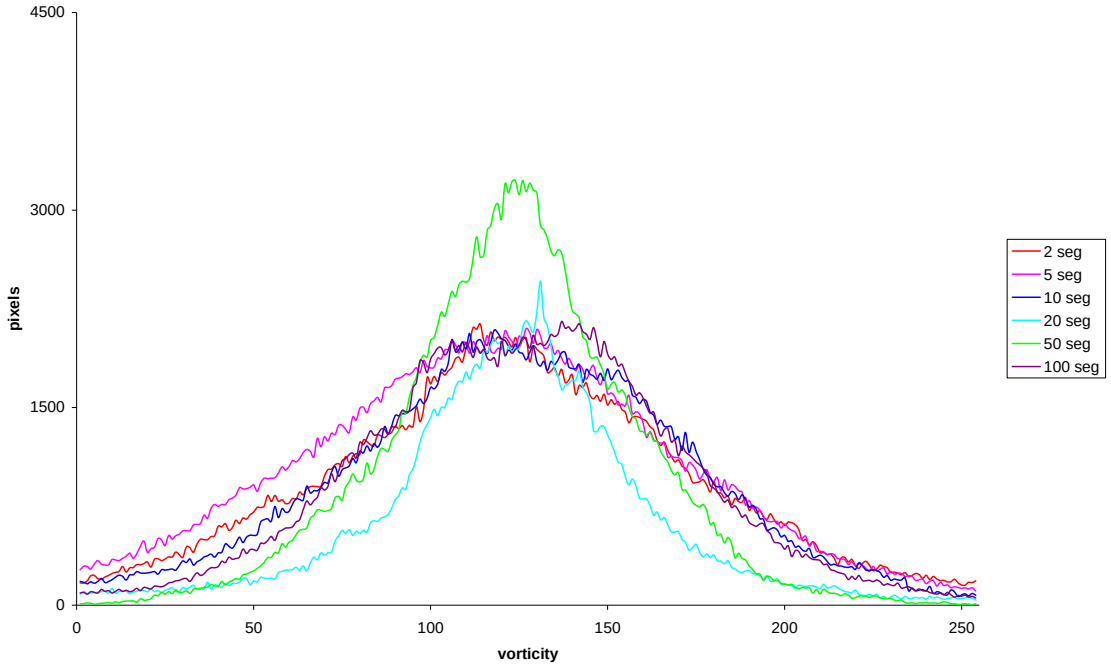

Figure 7.47: The histogram of local vorticity measured by PIV in experiment 2g with $Rig = 0.378$ for different times.

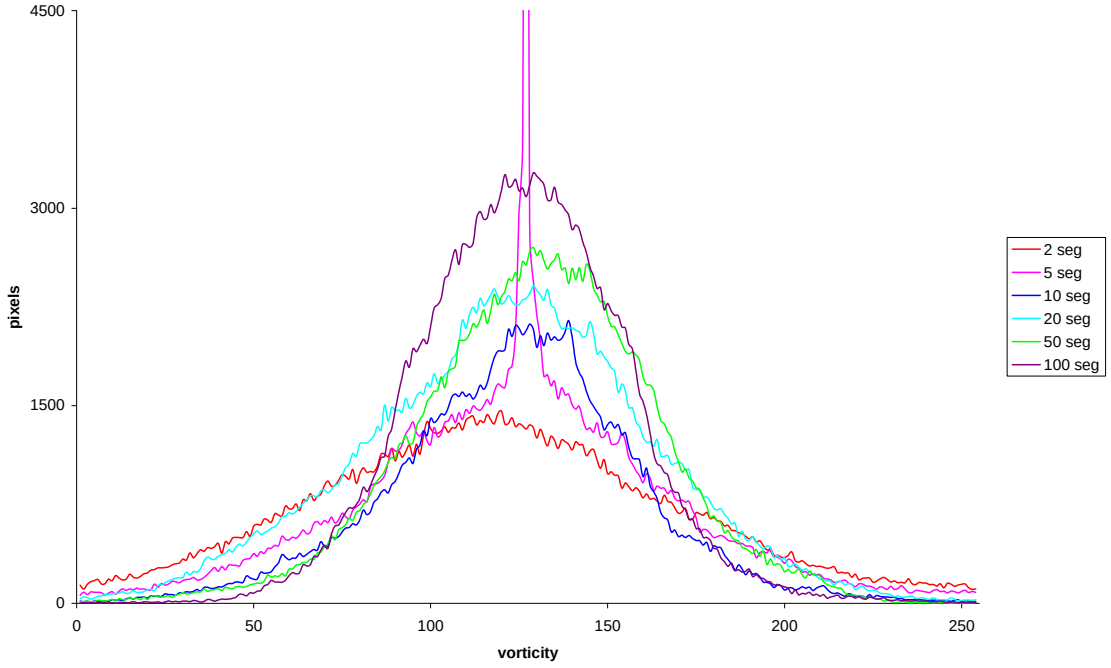

Figure 7.48: The histogram of local vorticity measured by PIV in experiment 2h with $Rig = 0.264$ for different times.

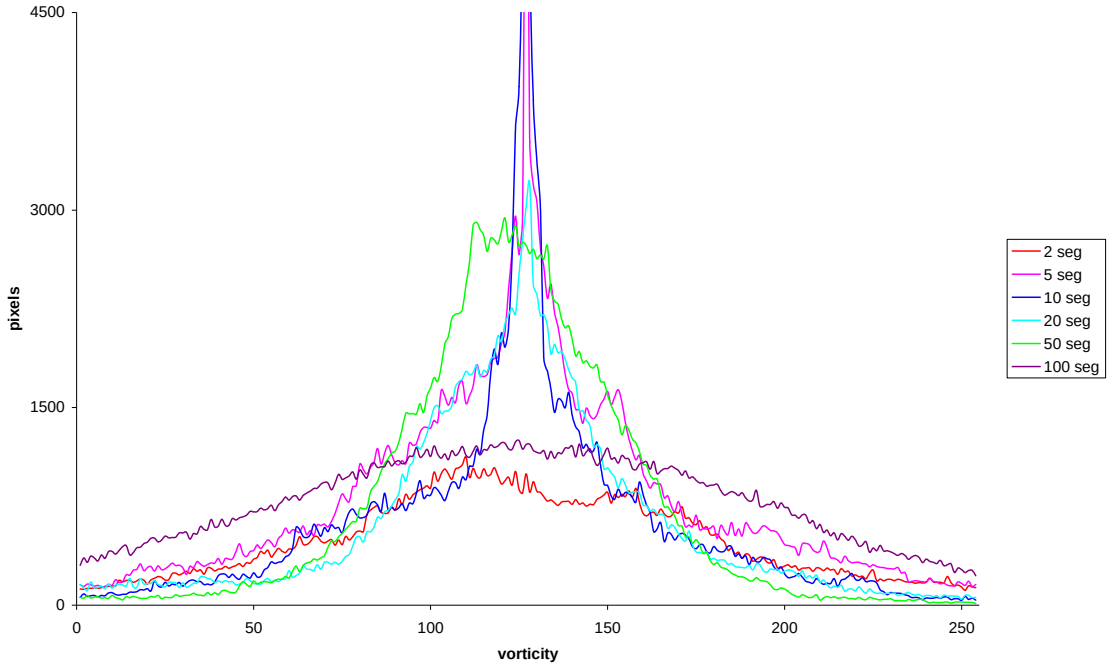

Figure 7.49: The histogram of local vorticity measured by PIV in experiment 2i with $Rig = 0.347$ for different times.

Taking maximum value from histograms we can construct other graph and we can see the difference between all experiments, figure 7.50. Here is too easy to notice that the line for experiment 2a is increasing in time with exponential tendency. For experiment 2b is in the other way, is decreasing in time also with exponential tendency. For experiments 1d and 1e we are not able to see the tendency, it is almost constant.

It is apparent that in most cases there is a slight increase in vorticity (note that we only measure vertical vorticity) and this is more evident in the highest Richardson number experiments. This is probably due to the fact that the strong internal waves are really tilting the isopycnal surface and the sidewise components of the vorticity are much larger initially. After 5-10 seconds the plane and isopycnal surfaces tend to align, and the vorticity decay at all positive and negative levels is apparent. Because only the central section of the tank, away from the walls is analysed, in some cases the final large dipole is shifted away from the observation region, and as shown in figure 7.46 a skewness of the measured PDF is produced. There is no apparent cyclonic or anti-cyclonic asymmetry.

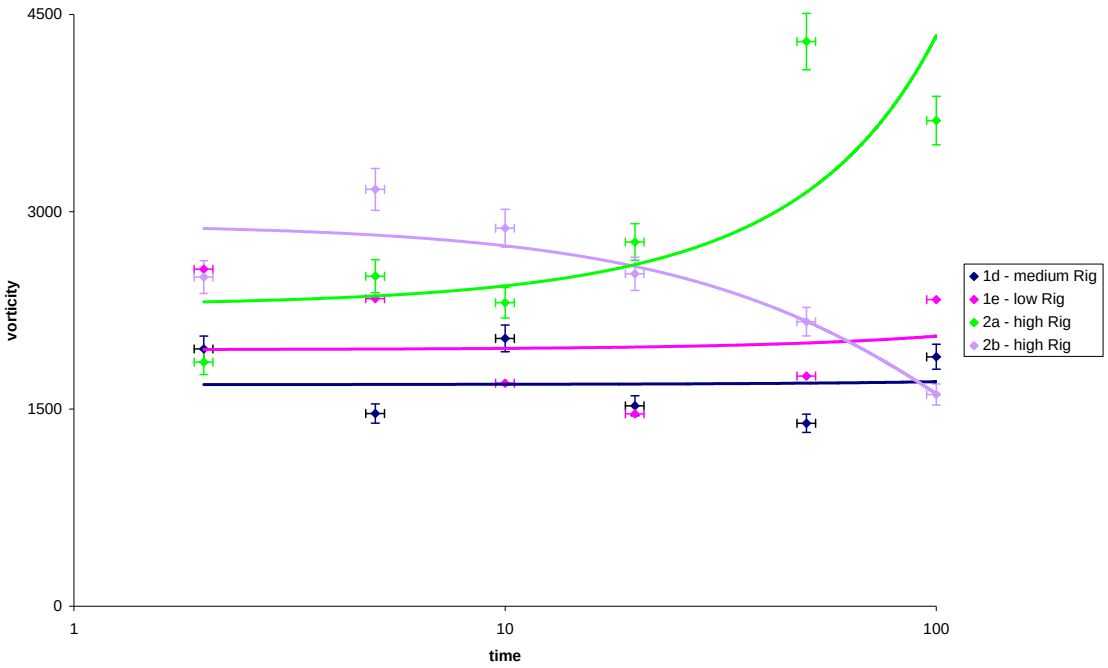

Figure 7.50: The presentation of maximum vorticity level for experiments 1d ($Rig = 1.19$), 1e ($Rig = 0.83$), 2a ($Rig = 7.756$) and 2b ($Rig = 8.033$) in time for different Richardson number.

7.4. Decay and merging of vortices with stratification

The next step was the vorticity evolution analysis in decaying turbulence. Here we present in some detail the study of the laws that dominate coherent structures created in the stratified turbulent flow. This behaviour of isolated vortices has been amply studied in a pure two dimensional flow (Tabeling 2002) but in these experiments we may focus on the role of buoyancy on the flow. As was commented above effect of the stratification most evident, stronger the buoyancy, higher the effective confinement in the vertical scale. Under standard theories of the evolution of vortices (Kraichnan 1975) in a bidimensional state (2D) we have specific energy and enstrophy conservation laws. Under stratified turbulence a simple energy argument shows that no vertical motions larger than the Ozmidov length scale L_o may hold where $L_o = \sqrt{\frac{\varepsilon}{N^3}}$ being ε the dissipation and *N* is the Brunt - Väisälä frequency. This overall behaviour is similar to what happens in a topological two dimensional flow (2D). We analyse the behaviour of vertical structures through time and specific study the vortex number and changes of new vortices that merge. In the pure bidimensional state an interesting effect in the energy exchange between scales, allows the energy flow towards large scales to allow the effective small cascade scale of the enstrophy. In this case, we can observe two types of inverse energy cascade defined in § 2.1 and § 4.3.1 the effect of decay that affects more the dissipation scales and the proper topological 2D effects.

The experimental analysis performed was the careful measuring of bidimensional and a computer generated threedimensional vorticity images (ω, x, y). The measurement process consisted in the visual identification of vortices in the vorticity field, defined by a layer sheet at the interface centre. Measures at their range in the study area, and the compilation of a vortex number as the relative area to total that they occupy, everything in percentage. In figure 7.51 we can see the threedimensional vorticity field with a multicoloured scale from experiment 1h with low Richardson number, and we can count peaks of vortices. The figure shows a snapshot of the evolution of the vertical vorticity scalar field as the turbulence decays after passage of the grid in this case in a weakly stratified interface.

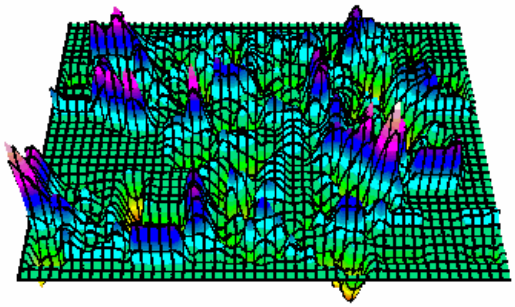

Figure 7.51: The vorticity 3D field with multicoloured scale in time t=2seg for experiment 1h and small Richardson number $Rig = 0.039$.

This process was done for six chosen measurement times in every experiment with stratification, in a logarithmic way. How we can see later the laws are potentials, therefore it seems interesting, in view of complexity of this visual analysis, to reduce measurements, maintaining the objectivity of analysis, it was checked that there times were enough to deduce the decay law.

Besides, here we make an analysis for two different levels of enstrophy of vortices, this is the power of the vorticity that they have. It seems suitable to make it in this way, as we can compare separately tendencies, and check if the decay is similar for all vortex strengths. The procedure guarantees the best precision at least in the vortices of high energy. It is easy to see that, when the vorticity limit is smaller, then we force to count many more vortices. Then a greater error will committed for lesser vortices. It results more difficult to distinguish vortices in the turbulent area where there are a greater number of them. Accordingly, we will count vortices for the high and mean energy as we can detail in figure 7.52 as an example where we show the high and mean enstrophy vorticity limits and the turbulent area or the background level of vorticity called sometimes the turbulent swamp (Dubos and Babiano 2002).

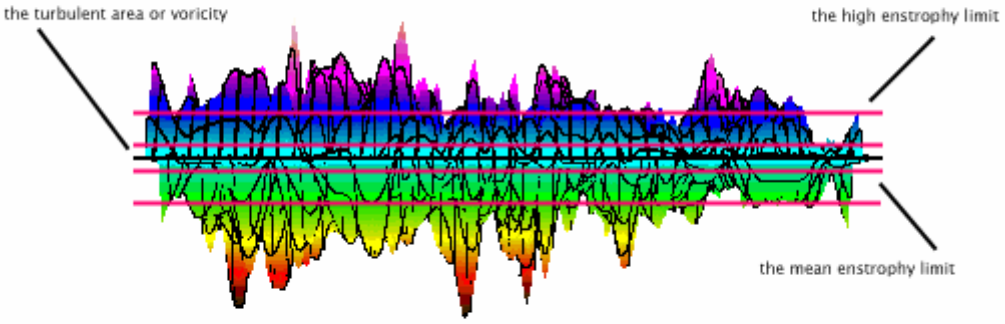

Figure 7.52: Vision limits of high and mean enstrophy.

The obtain data after visual inspection analysis, identification of vortices, their counting and area estimation (means calculation as area etc.) is presented in the following table 7.7 for 1a, 1c, 2a and 2f experiments with weak, moderate and strong stratification.

From the vortex number and the percentage area in every moment (from the frame pair PIV analysis), we can determine the new fundamental data for our analysis, the mean area of vortices in one certain moment of time. This value is received dividing the relative area of vortices by the counted vortex number as we can see below:

$$A_m = \frac{A_{rel}}{N_o} \tag{7.2}$$

where A_m is the mean area, A_{rel} the relative area and N_o the vortex number. With this method it is easy to obtain the values exposed in tables 7.8. These values can be analysed and compare with different theories and other experiment results.

Table 7.7: Visual data with high (8,8 – 7,756) and moderate (1,84) Richardson number obtained from experiments 1a, 1c and 2a.

Enstrophy Levels				
Exp 1a	High	Mean	High	Mean
sec.	Area %		Vortex number	
2	50	30	31	36
5	45	25	26	30
10	37	20	15	24
20	30	20	11	19
50	25	15	7	12
100	20	15	5	8

Enstrophy Levels				
Exp 1c	High	Mean	High	Mean
Sec.	Area %		Vortex number	
2	45	35	32	37
5	40	30	26	31
10	28	24	20	25
20	25	20	16	21
50	15	15	8	14
100	10	15	5	9

Enstrophy				
Exp 2a	High	Mean	High	Mean
Sec.	Area %		Vortex number	
2	50	40	40	43
5	45	35	28	35
10	30	30	26	32
20	25	30	20	24
50	15	20	17	20
100	10	15	13	16

Enstrophy				
Exp 2f	High	Mean	High	Mean
Sec.	Area %		Vortex number	
2	30	25	24	34
5	23	25	18	27
10	17	25	12	20
20	13	20	8	15
50	10	15	6	12
100	7	15	4	8

Table 7.8: The mean area data calculated for different levels of enstrophy (high, mean and total) for experiments 1a, 1c, 2a and 2f.

Experiment 1a with high Richardson number

Mean Area		Total		
High	Mean	A_{rel}	N_o	A_m
1,61	0,83	80	67	1,19
1,73	0,83	70	56	1,25
2,47	0,83	57	39	1,46
2,73	1,05	50	30	1,67
3,57	1,25	40	19	2,11
4,00	1,88	35	13	2,69

Experiment 1c with moderate Richardson number

Mean Area		Total		
High	Mean	A_{rel}	N_o	A_m
1,41	0,95	80	69	1,16
1,54	0,97	70	57	1,23
1,40	0,96	52	45	1,16
1,56	0,95	45	37	1,22
1,88	1,07	30	22	1,36
2,00	1,67	25	14	1,79

Experiment 2a with high Richardson number

Mean Area		Total		
High	Mean	A_{rel}	N_o	A_m
1,2500	0,9302	90	83	1,0843
1,6071	1,0000	80	63	1,2698
1,1538	0,9375	60	58	1,0345
1,2500	1,2500	55	44	1,2500
0,8824	1,0000	35	37	0,9459
0,7692	0,9375	25	29	0,8621

Experiment 2f with low Richardson number

Mean Area		Total		
High	Mean	A_{rel}	N_o	A_m
1,2500	0,7353	55	58	0,9483
1,2778	0,9259	48	45	1,0667
1,4167	1,2500	42	32	1,3125
1,6250	1,3333	33	23	1,4348
1,6667	1,2500	25	18	1,3889
1,7500	1,8750	22	12	1,8333

The basic theory about Kolmogorov scale and his extension to the problem of vortices structure (Tabeling 2002, Platonov et al. 2009), starts from some suggested hypothesis applied to the dynamics of process observed experimentally. Here we exhibit some power law dependencies (Babiano 2002):

1. The vorticity in the turbulent area that shows low vorticity or background does not have any influence in the analyzed processes; it means that the background

vorticity is essentially passive. The present data shows certain turbulence with a low intensity into which there are located well formed vortices with more intensity. This turbulence background can be avoided but a decision has to be taken about the levels of the mean and high energy to analyse the dominant vortices.

2. The energy and enstrophy are dominated by vorticity. The previous point and the absence of existence of energy interfaces of other type permit to analyse vortices as the only factor in equations.
3. The merging process of vorticity is assumed initially not to destroy energy, to check this we can apply the law of energy conservation.

If we apply laws of energy conservation to the set of vortices (i.e. merges conserve energy and also conserves peak vorticity), knowing that these are the principal and only factors with influences in vorticity and energy in an homogenous flow, we can start from the law of conservation and from the theory of Kolmogorov enforcing a local scale L_o transport (as we know that the energy only travel to the superior scales) and from expression of the kinetic energy that refer the decay energy with the vortex number and mean area of vortices (Γ).

$$E = \sum_i e_i \propto N_o \, \Gamma^2 \tag{7.3}$$

with the definition Γ as $\Gamma = \oint \omega \, dl$ and where the total energy of vortices is proportional to the square mean area that we calculated. If we consider that the vortex number is decreasing with the law of type $N_o \propto t^{-\chi}$ then we have:

$$A_m \propto t^{\chi/2} \tag{7.4}$$

where $\chi/2 = \beta$ and therefore the mean area has to increase with $t^{\chi/2}$, where χ is the vortex decay exponent, rate of vortex number of decadency in the logarithmic space. Many authors tried to find out this rate from different analytics theories, as Pomeau et al. 1966, Sire and Chavanis 2000 and Ywayama et al 1997 from theory about vortices in the mean field, Carnevale et al. 1990, Trizac and Hansen 1996 and Trizac 1998 from the

ballistic aggregation and Huber and Astrom et al. 1993 based on the Coulomb gas, and their obtained different values of decay exponent with limit from 0.67 (Ywayoma et al. 1997) to 1 (Carnavale et al. 1990 and Sire and Chavanis 2000). Sire and Chavanis 2000 introduced a numerical procedure which allows very long-time simulations of the Kirchhoff vortex dynamics in a two dimensional decaying fluid and they found a long-time asymptotic decay with $\chi \approx 1$. Trizac et al. 1998 proposed a ballistic coalescence model mimicking the fusion of vortices in freely decaying bidimensional turbulence. A temporal scaling behaviour was reached where the vortex density evolves like $t^{-\chi}$. A mean analytical argument was shown to overestimate the decay exponent χ whereas give $\chi = 0.71 \pm 0.01$, in agreement with laboratory experiments and simulations of Navier-Stokes equation (Tabeling 2002).

Some other approximations are presented from different laboratories experiments and numerical models, although with a wide range of values of the decay exponent between 0.44 ± 0.1 to 1. Benzi et al. (1992) showed that after a transient period, the number of vortices $N_o(t)$ is decreasing in time as t^{χ} with $\chi = -0.6 \pm 0.05$. By direct numerical simulation of two dimensional Navier-Stokes equations, Mc Williams et al. 1990 found $N_o(t) \approx t^{-0.7}$ in a case where vortices with the same where presented in the initial condition. The results obtained by Mc Williams confirmed that the peak vorticity inside vortex cores is roughly conserved and that the number of vortices as a function of time decreases as a power law, as Bracco et al. (2000) discussed. They studied the behaviour of two-dimensional turbulence due to the interest as a simple conceptual model of vortex-dominated large-scale planetary flows. The evolution of vortex statistics in freely decaying bidimensional turbulence at very large Reynolds number has also practical application. After the vortices have been generated and the system has become dominated by vortex dynamics the situation changes and at least square fit estimate of vortex decay rate gives $\chi = 0.76 \pm 0.03$. Weiss & Mc William 1993 analysed the temporal scaling behaviour of the flow using scaling theory, a long-time integration of the fluid equations, and a dissipative, modified point-vortex model that represents the turbulences as a system of interacting coherent structures. Their presented results from both systems and it shows excellent agreement in a number of aspects, both with each other and with the mean-vortex scaling theory: the evolution of average vortex properties and low-order moments displays self-similar evolution with the same scaling form. Furthermore, the two systems gave the same value of the scaling exponent

$\chi = 0.72$. Cardoso et al. (1994) on the other hand, compared their results to the theoretical predictions and did not observed the predicted exponents by Batchelor theory, where t is supposed to be t^{-2} and whereas their found $t^{-0.44\pm0.1}$.

It can be observed the big variety of exponents. Nevertheless, nowadays exists a general theory that predicts the behaviour in experiments with pure bidimensional (2D) topology and, under some hypothesis determine realistic values for χ. The new hypothesis is that merger rate depends on the dispersion rate with diffusivity D defined as:

$$D = \frac{1}{2}\frac{d}{dt}X^2 \tag{7.5}$$

where X^2 is dispersion $X^2 = \left\langle \left(\vec{x} - \overrightarrow{x_0}\right)^2 \right\rangle$ (same dispersion rate in all experiments). Dimensionally, could correspond to the velocity by the longitude scale, units of L^2/T, in the way that $D \propto ul$. From the definition of kinetic energy and considering hypothesis of the vortex theory applied in this chapter, we have:

$$E_c = \frac{1}{2}\iint u^2\, dA \approx \sum e_i \propto N_o\, \Gamma^2 \tag{7.6}$$

and from here, we can define u in a proportional way so that the model implies:

$$u \propto \left(\frac{N_o}{A_{rel}}\right)^{1/2} \Gamma = \rho^{1/2}\,\Gamma \tag{7.7}$$

where ρ is a parameter defined the vortex number density as $N_o/A_{rel} = A_m^{-1}$ (diffusivity exponent) is defined and with scale $l \propto \rho^{-1/2} = A_m^{1/2}$ we obtain:

$$D \propto ul \propto \left(\rho^{1/2}\,\Gamma\right) A_m^{1/2} = \Gamma \tag{7.8}$$

We can see that the diffusivity then depends on the internal vorticity over a lengthscale i.e. the circulation Γ. Experimentally it was determined that the diffusivity, in any case, has this type of law:

$$D \propto t^{1/3} \tag{7.9}$$

If energy is conserved, then $N_o \Gamma^2 = const$ so:

$$N_o \propto \Gamma^{-2} \propto D^{-2} \propto t^{-2/3} \tag{7.10}$$

We have one theoretical value based on the experimental ratio that set the χ the decay exponent in approximately 0.67. This theory is incomplete, because still we do not know why it seems that the dispersion is proportional to the mean vertical area. No attempt has been made here to include the effect of internal or inertial waves as energy sinks or as vorticity generators through the Baroclinic torque.

Here we present results with high Richardson number, with strong stratification, and we can observe that results have indeed a potential fit in the logarithmic plots 7.44, 7.45, and 7.46. We can see the good line fits showing precisely the number of vortices in a plane by means of the decay exponent χ. Comparing the decay factor χ to the β factor of equation 7.4 we immediately deduce that

$$\chi = 2\overline{\beta} \tag{7.11}$$

All directional influence of β is lost when the entire plane is considered.

It interesting to notice, that we have, initially, the expected tendencies theoretically. The vortex number adjusts well in the logarithmic space and downward slope as seen in figures 7.53, 7.54 and 7.55. Also, as expected from 2D theory, the mean area of the vortices increases with time, adjusting also to a straight line in logarithmic space. These results show how the merging of vortices is the basic physical process, in which the basic vortex number tends to decrease and generate vortices of large scales.

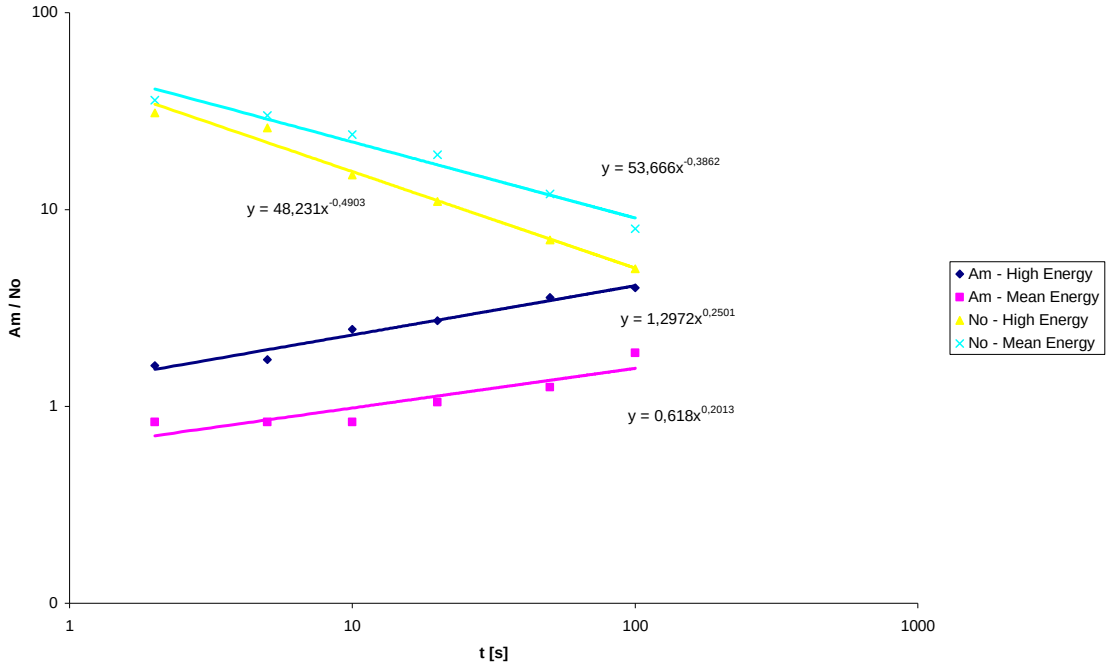

Figure 7.53: The evolution of vortex number and mean area for experiment 1a with high Richardson number $Rig = 8{,}8$.

As we want to investigate the role of stratification on the vortex decay process, we start the analysis with a very strong stratification case, with the highest Richardson number for all experiments 1a $Rig = 8.8$ and for 2a also, almost as large, $Rig = 7.756$, because these cases should be more similar to pure (2D) bidimensional theories which we described previously. Checking the value of the slopes in figure 7.53, we see that the value of decay exponent χ according to the number vortex slope for high energy is 0.49. According to the low energy vortices, is 0.38, even further away from the pure 2D values. The values of mean area are in accordance with the value of high energy vortices. If we notice, 0.25 in the first case and 0.20 in second, approximately $\frac{\chi}{3}$. So the proposed theoretical pure 2D flow law is not clearly upheld. It is clear that the results of decay of the vortices number are not explained by the theory for pure 2D experiments. With strong stratification values 0.25 and 0.20 are too small compared with the expected 2D values. It is possible that experimental errors due to the difficulty that involves counting and the estimation of the vortices areas are 5% to 10%. The numbers of vortices with high energy give us better results, with an easier count because of their high energy and easier determination of area. Those with an average energy result more complicated to separate from the turbulent background and it can lead to a

larger error. This is one of causes why the separation of high energy vortices is recommended, as it presents the decay laws clearly.

The same happens in results from experiments 2a, shown in figure 7.54 where the value of the decay exponent χ according to the number vortex slope for high energy is 0.27 and for the mean energy 0.25. In the both cases the values are much lower. The values for the mean area are in accordance with the vortices value of high energy: 0.15 in the first case and 0.01 in the second.

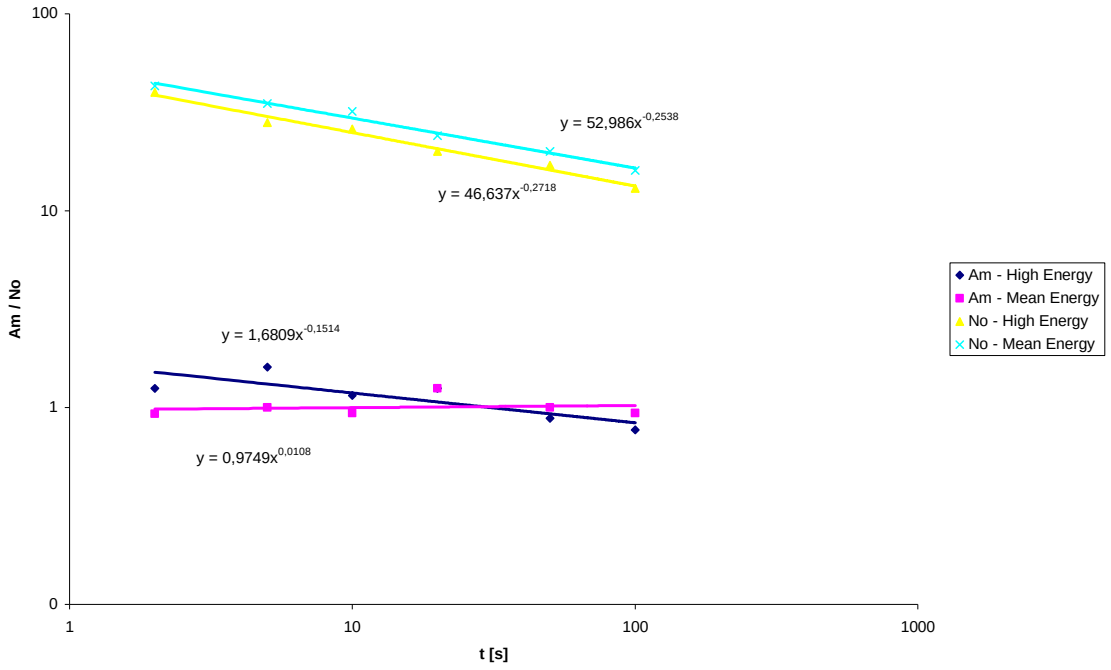

Figure 7.54: The evolution of vortex number and mean area for experiment 2a with high Richardson number $Rig = 7{,}756$.

Nevertheless, the show fits are good and it is not insignificant that we observe the slope change. Despite that we can have a certain error. We must mention of the smoother tendency that shows decay of the vortices, and the slope of the evolution of the mean area, reaches up to $\frac{4\chi}{5}$. It seems that different hypothesis area needed to explain the vortex decay of the mean energy and a different one for the every strong vortices. For these vortices, according to this tendency, their number could decrease slowly, and their mean area could increase faster. This area increase could come from some interaction between the associated area to the vortices with the average energy and the internal wave field. The relative area decays very slowly and, added to the slow

decadency of vortex number; it causes a fast increase of the mean energy. It seems very clear that the cause of the difference of the real stratified flow that we have analysed with respect to a pure 2D bidimensional theory which we applied to predict their behaviour. Given that there exist in reality processes associated to the vertical scale; it is quite possible that we have an energy transition from the largest scales towards the smallest scales in a 3D fashion. The high energy vortices could behave slightly more in a pure 2D environment, but with an additional 3D energy cascade towards the smallest scales that feed firmly from the vorticity at mean scale, and change their behaviour.

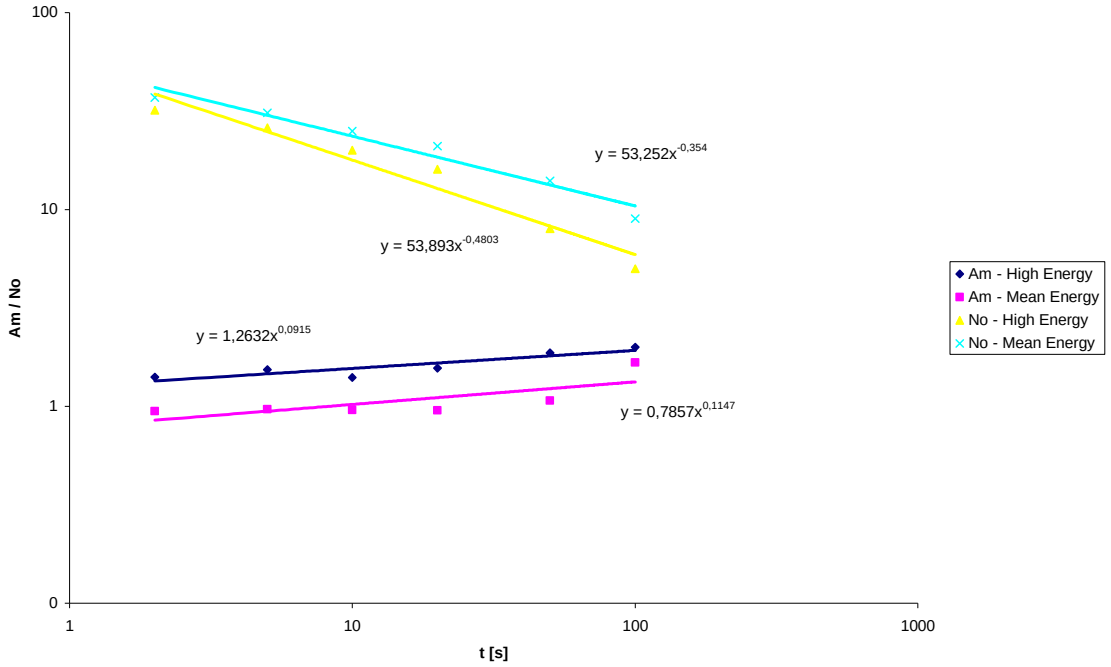

Figure 7.55: The evolution of vortex number and mean area for experiment 1c with medium Richardson number $Rig = 1{,}84$.

For the experiment 1c with mean stratification (figure 7.55), and Richardson number $Rig = 1{,}84$ we observe again the same behaviour as in previous cases. In this case, the slopes are higher: 0.48 for vortices of high energy and 0.35 for mean energy. Both cases are not well explained with the theory, and do not upheld the described laws. The values of the mean are increase, again, for the high energy is 0.09, and different that awaited for these with mean energy, 0.11. It is interesting to notice that this relation repeats itself in this experiment; again we can add some reinforcement to the hypothesis of a real tendency change, eliminating the possibility of systematic error in the counting method and or of the area estimation.

The calculation of the turbulent integral scale, presented above confirms independently the importance of the buoyancy on the vortex decay, especially after a few Brunt - Väisälä periods. From the previous analysis we could extract one important detail in the calculation of non dimensional numbers, the horizontal scale of vortices. For this, we use the total sum of vortices and areas, considering that the sum is of all significant vortices, and therefore is more adequate for the extraction of the average horizontal scale. We want to check, anyway, that this scale follows a power increase in time, generating one graph and extracting one rate of lineal increase, for each experiment.

Based on the vortex number and relevant area, we have the global study for every experiment. In the following figures: 7.56, 7.57 and 7.58 we present the total number of horizontal vortices in time for experiments 1a, 1c and 2a with high and medium Richardson number.

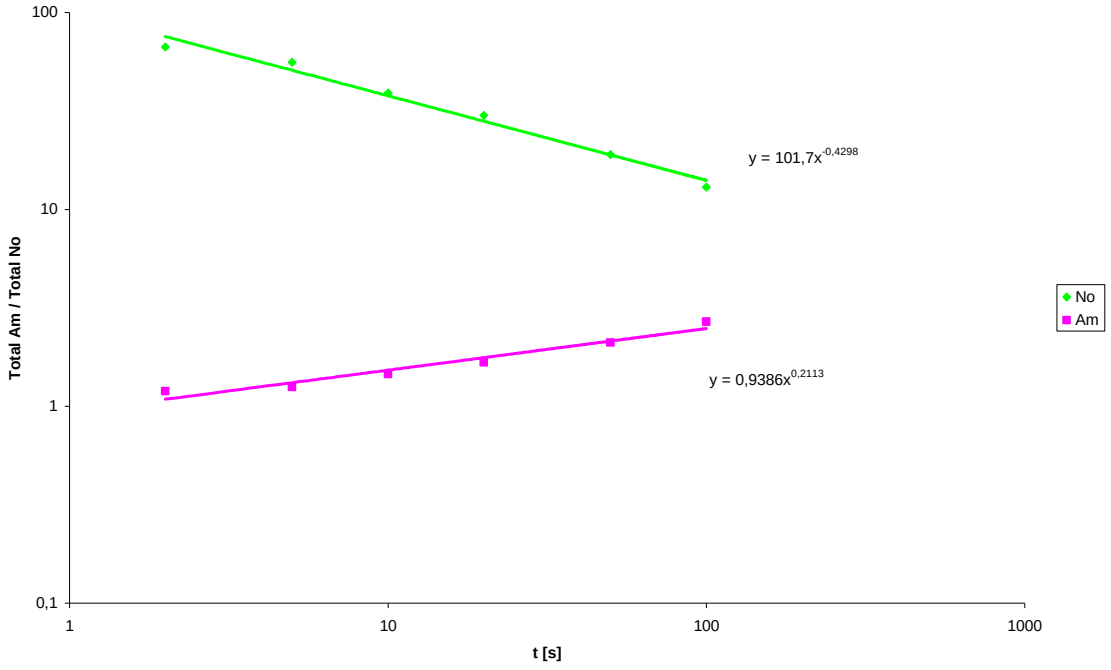

Figure 7.56: The evolution of total vortex number and total mean area for experiment 1a with high Richardson number $Rig = 8{,}8$.

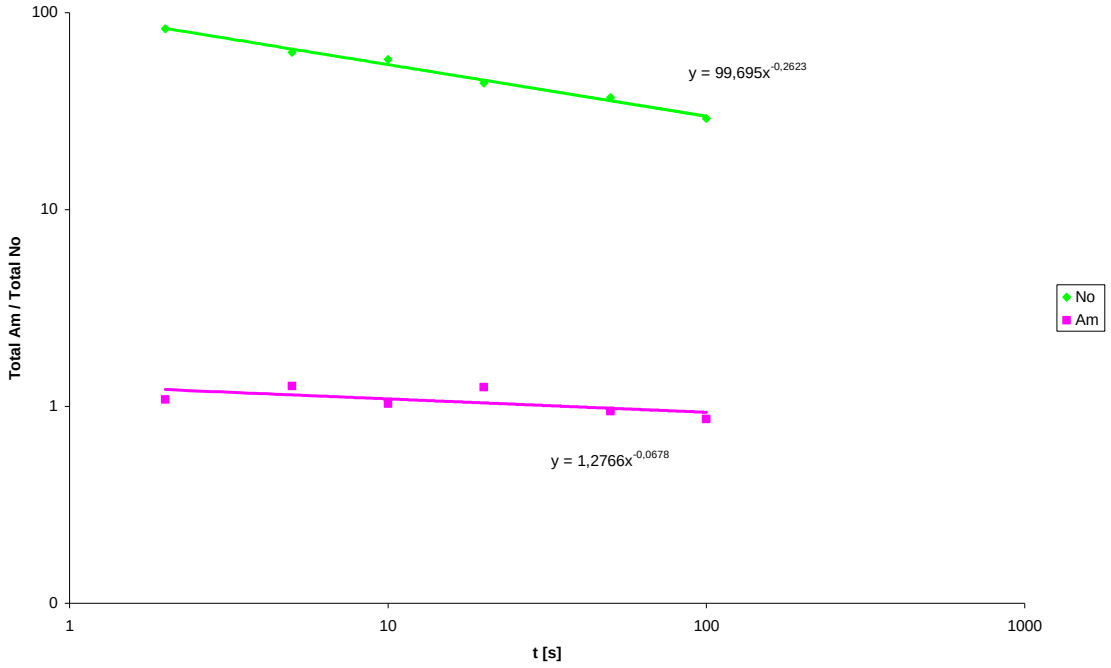

Figure 7.57: The evolution of total vortex number and total mean area for experiment 2a with high Richardson number $Rig = 7{,}756$.

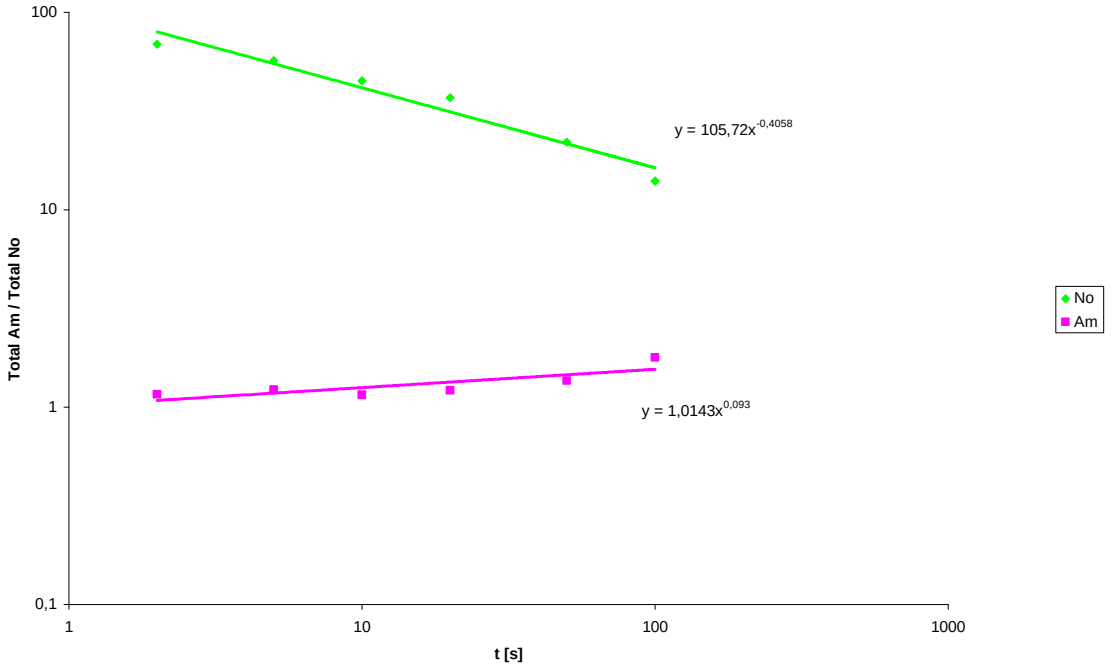

Figure 7.58: The evolution of total vortex number and total mean area for experiment 1c with medium Richardson number $Rig = 1{,}84$.

With this data, and considering the area of a perfect circular vortex, it is possible to obtain the characteristic scale of vortices at every moment in time and it helps to

evaluate independently how the horizontal scale increases as well as other useful information such as the vortex density or the packing ratio and several other geometrical and topological descriptors used by other authors (Bracco et al. 2004, LaCasce 2008). In figure 7.59 we can see the representation of this horizontal scale for experiment 1 with different rates for all measurements, from 0.0005 to 0.0016. Than in figure 7.61 are presented results from experiment 2, and the horizontal scale is increasing with rates from $0.9E-0.5$ to 0.0012. It confirms a power increase.

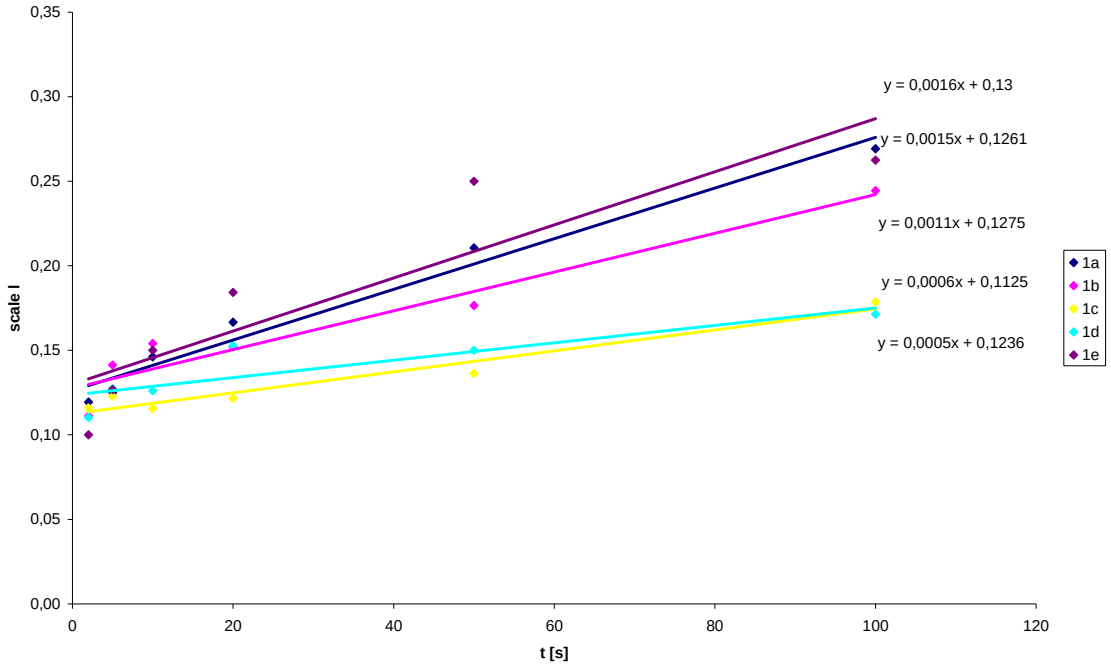

Figure 7.59: Integral scale *l* in time for experiments 1a, 1b to 1e with different Richardson numbers.

In figures 7.60 and 7.62 we can see the evolution of integral scale for the first and second experiment with a potential approximation. In figure 7.60 we can see that the horizontal scale is increasing with rates from 0.09 to 0.26 and in figure 7.62 the increasing rate vary between 0.03 and 0.15. For experiment 2a we observe decreasing rate which is -0.06.

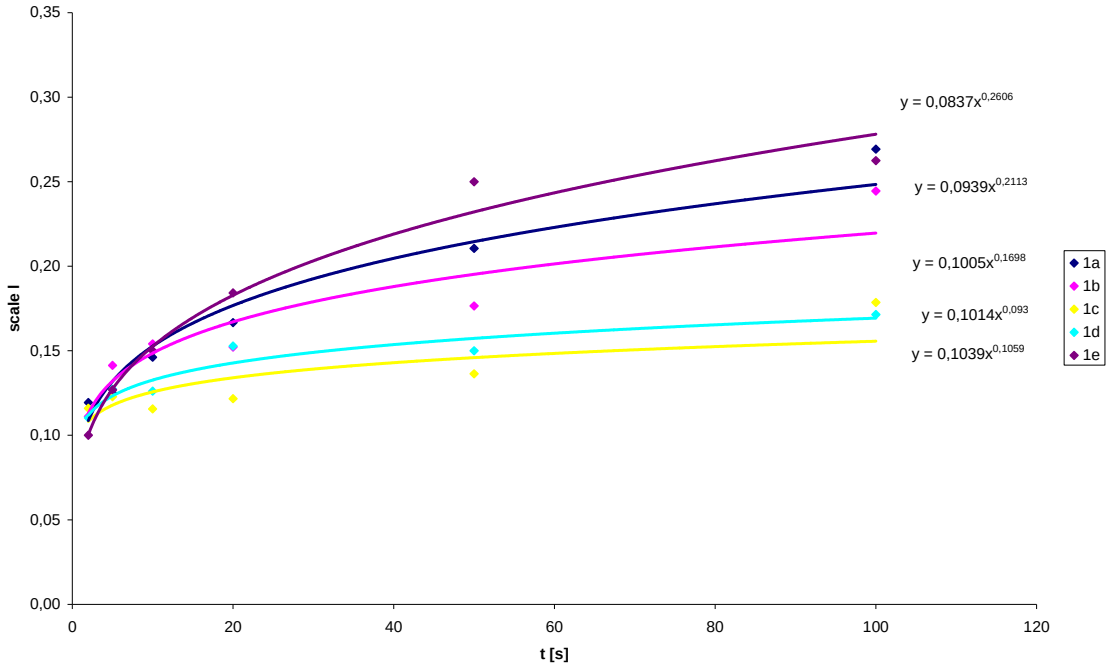

Figure 7.60: Integral scale *l* in time for experiments 1a, 1b to 1e with different Richardson numbers and with potential fits.

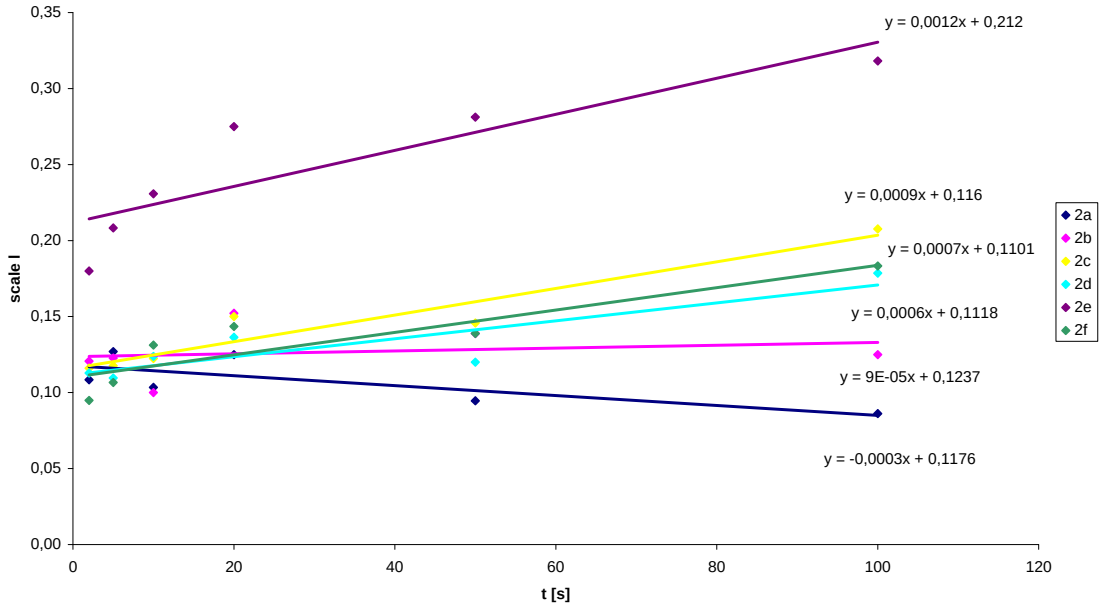

Figure 7.61: Integral scale *l* in time for experiments 2a, 2b to 2f with different Richardson numbers and linear fits.

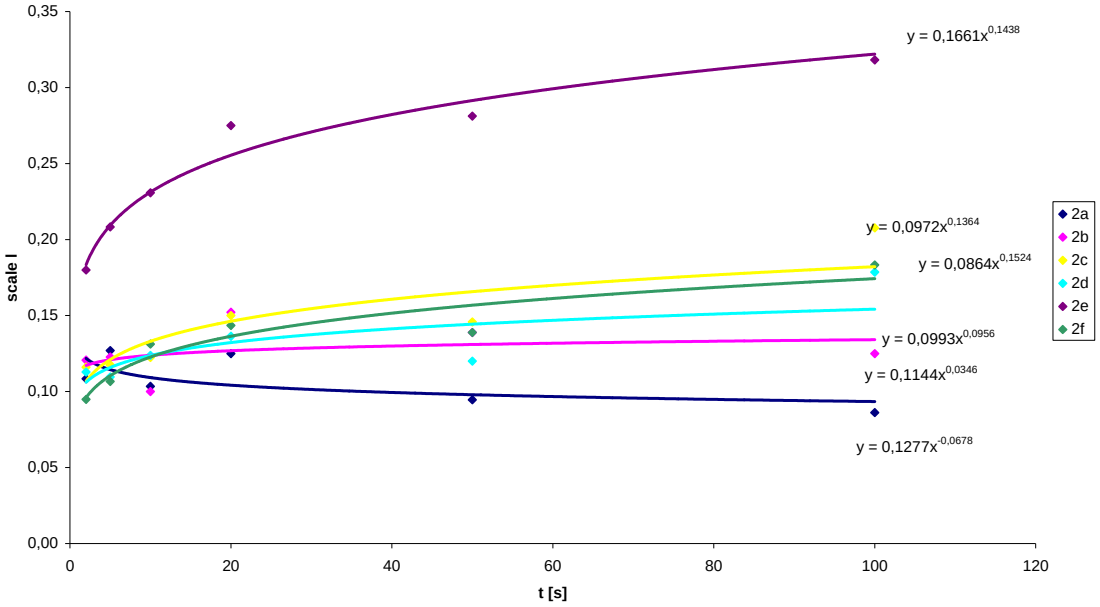

Figure 7.62: Integral scale *l* in time for experiments 2a, 2b to 2f with different Richardson numbers and with potential approximation.

The scaling theory by Carnevale et al. 1990 provides predictions on the evolution of the mean vortex properties and the lower statistical moments of the vorticity field, assuming that vorticity is concentrated inside coherent structures. The vortex number N_o term describes the statistical properties of the vortex population. The time evolution of the vortex number is assumed to have a power law form

$$N_o(t) = N_o(t_o)\left(\frac{t}{t_o}\right)^{\chi} \tag{7.12}$$

where N_o is the vortex number and χ is a certain exponent. As a hypothesis, it is assumed that the time evolution of the vortex number properties is self-similar.

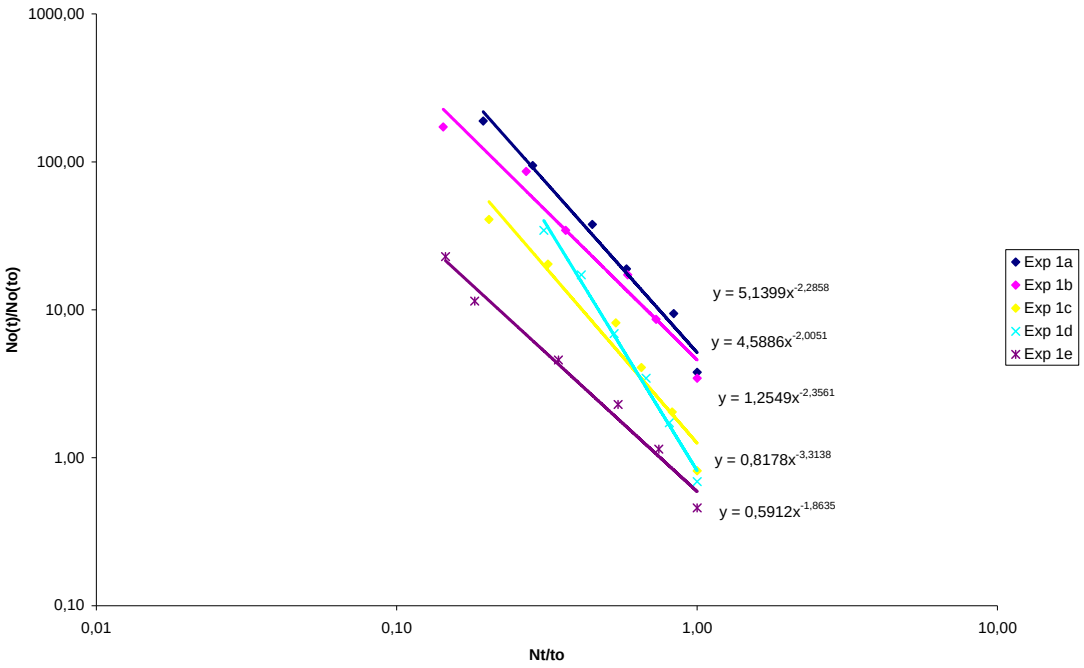

Figure 7.63: Dimensionless expression for experiments 1a to 1e of $N_o(t)/N_o(t_o)$ and Nt/t_o where N_o is the vortex number and N is the Brunt - Väisälä frequency.

In figure 7.63 we present the dimensionless expression for experiments 1a to 1e for the vortex number. The tendency line in every experiments is potential, and with this we can find the rate χ. We can observe the variety of this rate, which varies between -1.86 and -2.35. The same for experiments 2a, 2b, 2c etc, the exponent χ is between -1.19 and .3.76, shown in figure 7.64.

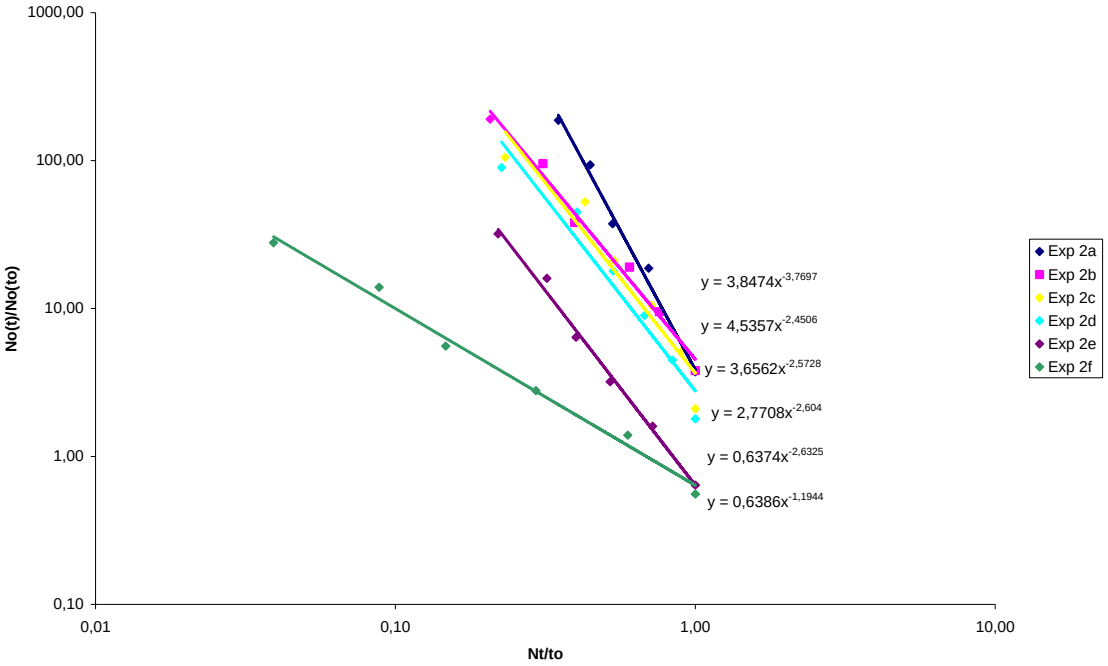

Figure 7.64: Dimensionless expression for experiments 2a to 2f of $N_o(t)/N_o(t_o)$ and Nt/t_o where N_o is the vortex number and N is the Brunt - Väisälä frequency.

7.5. Decay and merging of vortices without significant stratification (with low Richardson number)

In this section some results of the decay and merging of vortices in an experiment with very weak stratification and low Richardson number are presented.

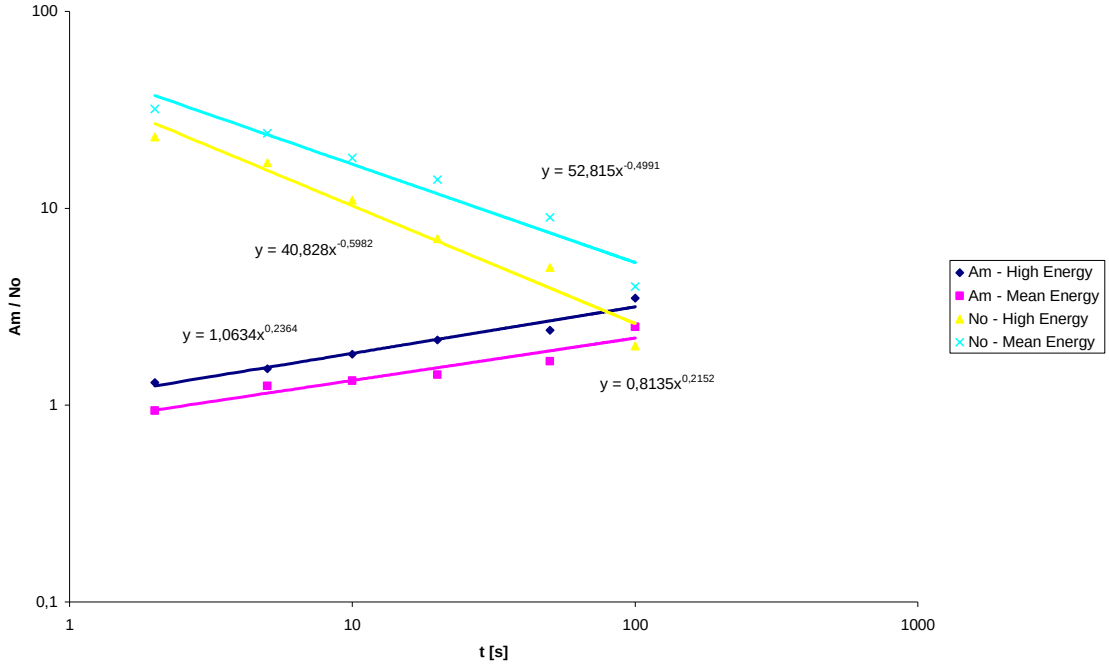

Figure 7.65: The evolution of vortex number and mean area for experiment 1h with low Richardson number $Rig = 0.039$.

In these cases values of the rate χ are acceptable, with experimental values of the decay parameters 0.59 and 0.49 in figure 7.65. The values are close to the $\chi = 2/3$ 2D theoretical value for the vortex number decay law in the case of high energy coherent structures but slightly lower that we expect for lower energy. Still, it can be noticed in this case a certain rapprochement between both behaviours. The weak stratification does not affect so much the high energy vortices, putting in time at the same level the vortex decay behaviour in both high and low energy structures.

Taking everything into a consideration, we can say that the study and analysis of the number of the vortices and the structure of the quasi 2D flow in our experiments does give a limit to the rate χ around the value 0.67, $\chi \approx 2/3$ and for the limit $Rig \approx 0$.

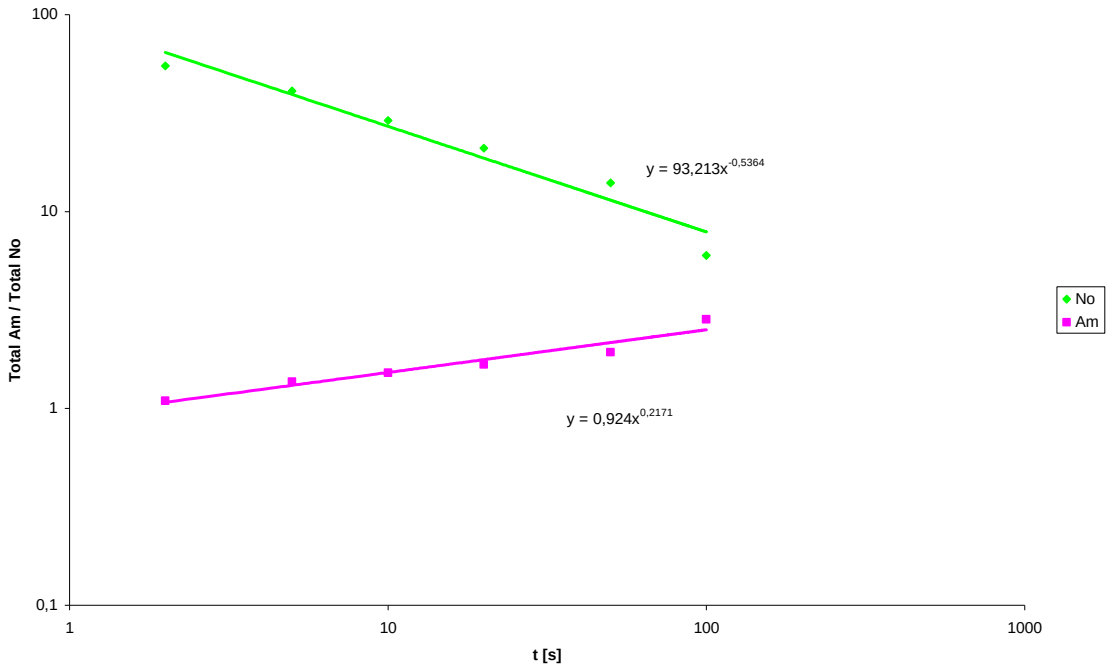

Figure 7.66: The evolution of total vortex number and total mean area for experiment 1h with low Richardson number $Rig = 0.039$.

From the previous analysis, we can extract one important fact; the horizontal scale of vortices grows in time until the size of the container is reached. We want to confirm, besides, that this follows lineal increase in time after an initial period, creating one graph and extracting a rate of the lineal increase of the average vortex size. In figure 7.66 we can see the evolution of the total vortex number until the vortices are indistinguishable from the background level and total mean area for weak stratification and low Richardson number. With this data, and considering the area of vortices as the perfect circular, it is obtain the characteristic scale of vortices in every moment in time.

In figure 7.67 we can observe the horizontal scale with rate of 0.217 for experiment 1h and 0.221 for 2h. The Richardson number of experiment 1h is much smaller than 2h, and we can see that for Richardson number $Rig = 0.039$ the stratification almost does not exist or is very weak. It is confirms the behaviour of a smooth lineal increase after an initial power law.

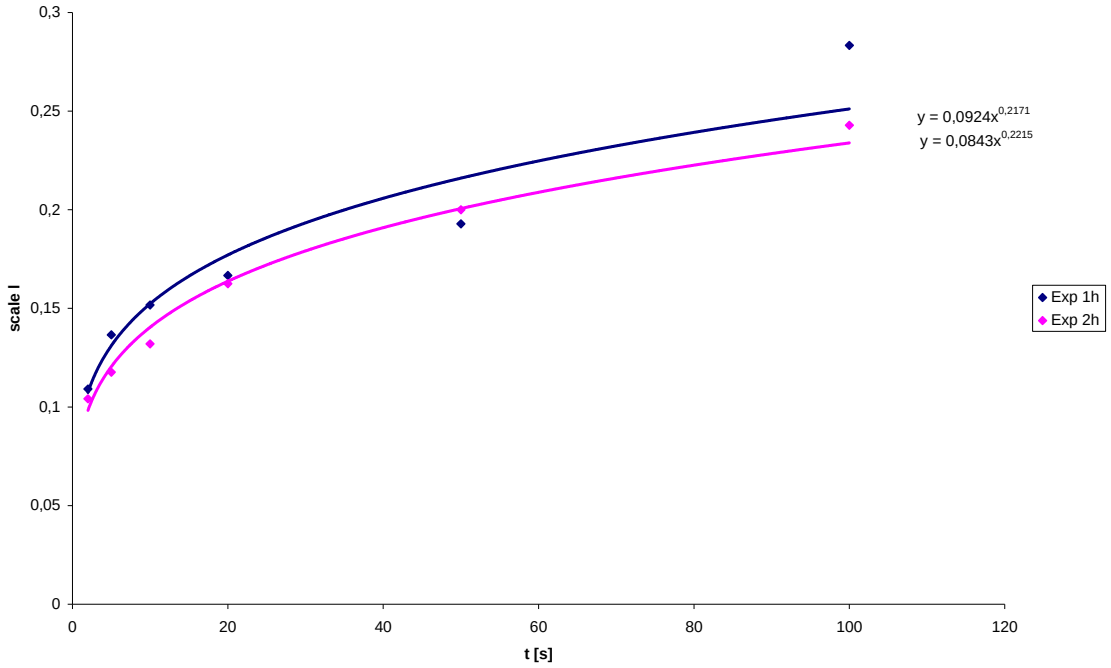

Figure 7.67: Integral scale in time for experiments 1h and 2h with low Richardson number $Rig = 0.039$ and $Rig = 0.264$.

In figure 7.68 we show a dimensionless expression for experiments 1h and 2h for the vortex number and for the weak stratification. The tendency line in every experiment is potential, and with this we can find the rate χ. We can observe that this rate for experiment 1h is 0.46 and for experiment 2h is 0.50. We can notice that the rate is similar in both of cases it is due to low Richardson number.

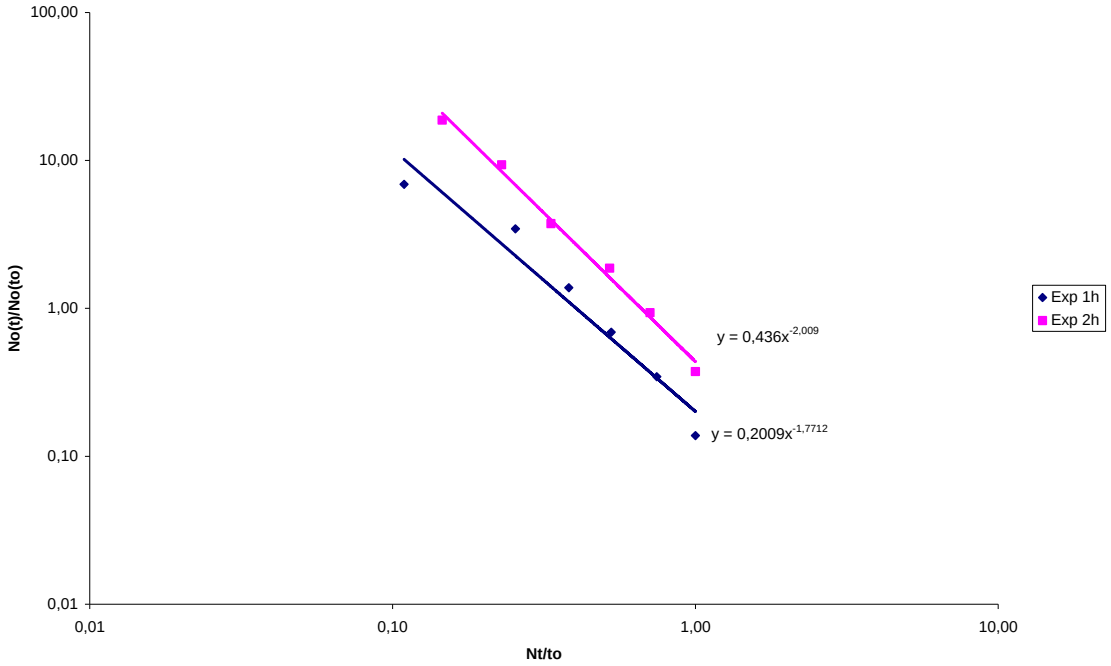

Figure 7.68: Dimensionless expression of $N_o(t)/N_o(t_o)$ and Nt/t_o where N_o is the vortex number and N is the Brunt - Väisälä frequency for experiments 1h with $Rig = 0.039$ and 2h with $Rig = 0.264$.

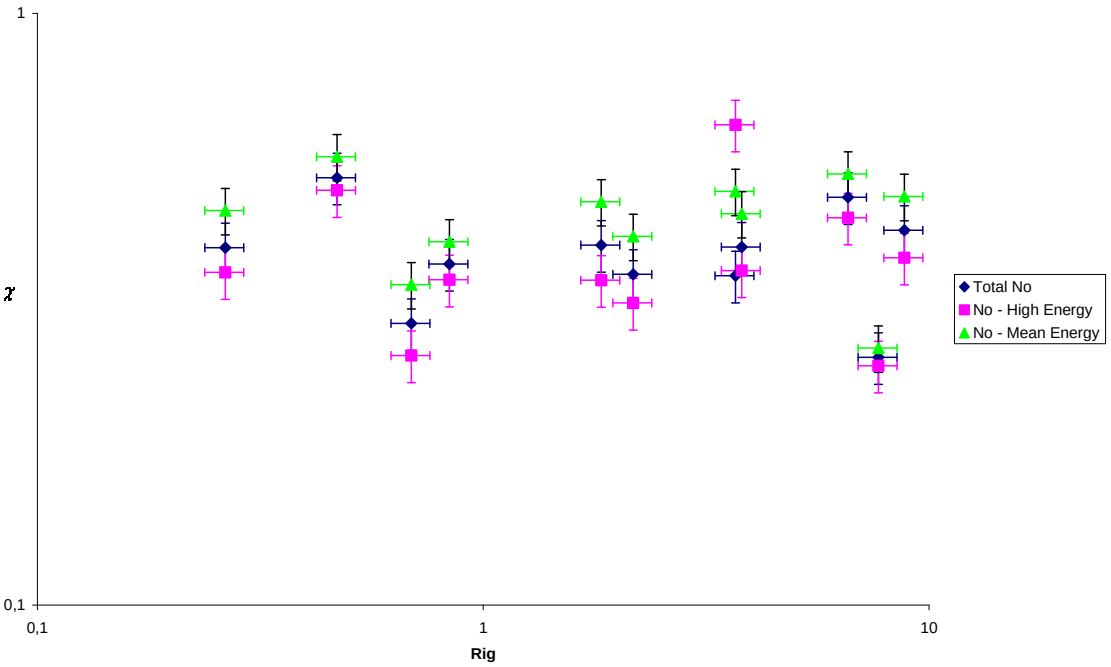

Figure 7.69: Exponent χ in function of Richardson number for different experiments in high and mean energy.

In plots 7.69 and 7.70 we show the relationship $\chi(Rig)$ and $\beta(Rig)$ for all available experiments.

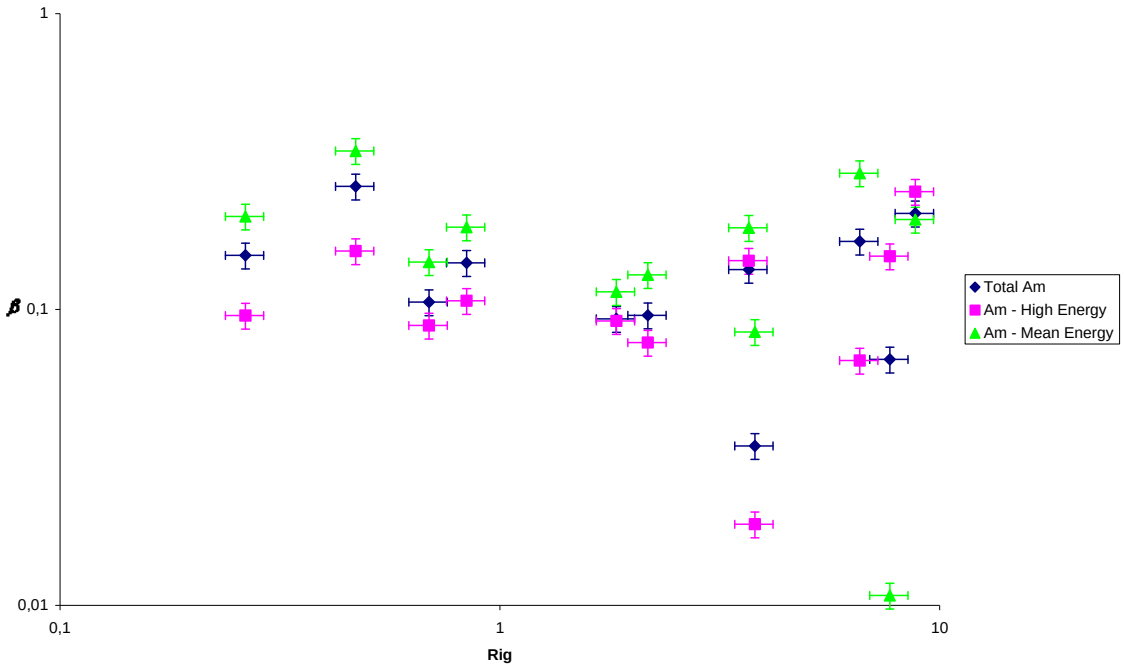

Figure 7.70: Exponent β in function of Richardson number for different experiments in high and mean energy.

We may see that the increased dispersion of β is due to the directional anisotropy, probable due to the internal wave number influence.

In figure 7.71 we can observe de dependence of exponents χ and β in the logarithmic plot for total vortex number, high and mean energy for different experiments.

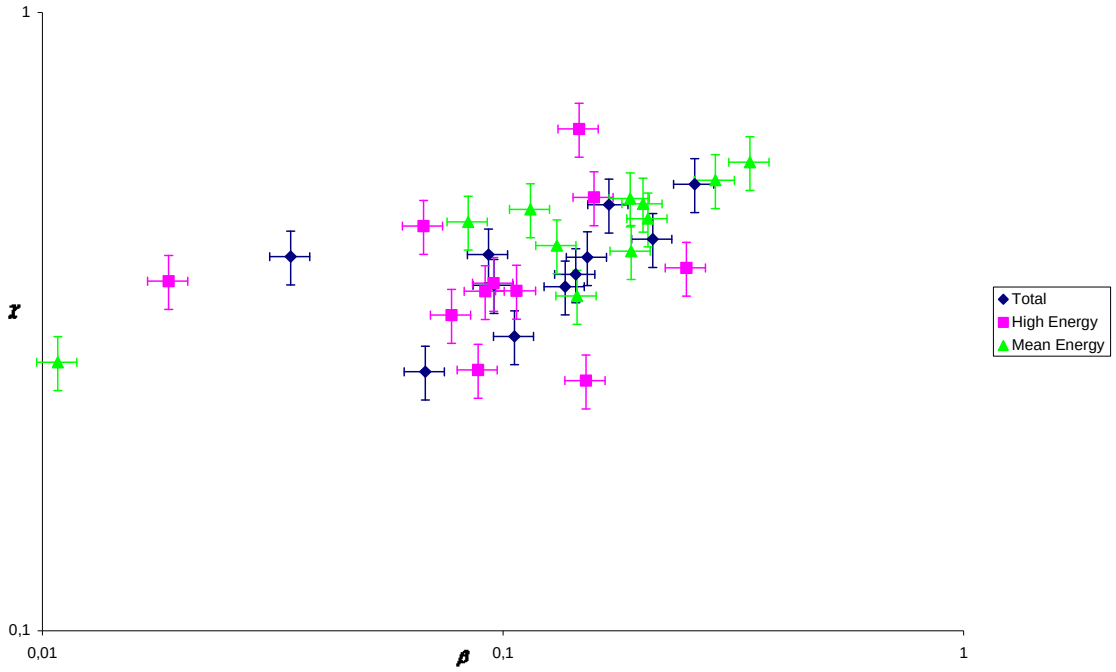

Figure 7.71: Exponent β in function of exponent χ for different experiments in high and mean energy and for total vortex number.

7.6. Mixing Efficiency – Entrainment

The mixing efficiency was measured between passages and related with the increase of potential energy and the decay process considering how long and how many grid passages were necessary for these two layers to be totally mixed. To consider individual turbulent decay processes, in order to study the mixing process, the grid was driven through the interface with the bars parallel to the interface and then we waited until all motions stopped. After this, densities were measured in seven points. We repeated the whole procedure again until the density in the entire tank was the same, thus the two layers were totally mixed. We use the definition on entrainment and mixing efficiency described in § 3.3. Here in figures 7.72 and 7.73 we present results of mixing efficiency in function of time for experiments 1 and 2 in a logarithmic plot. It is noticed that the mixing efficiency decreases with time as expected.

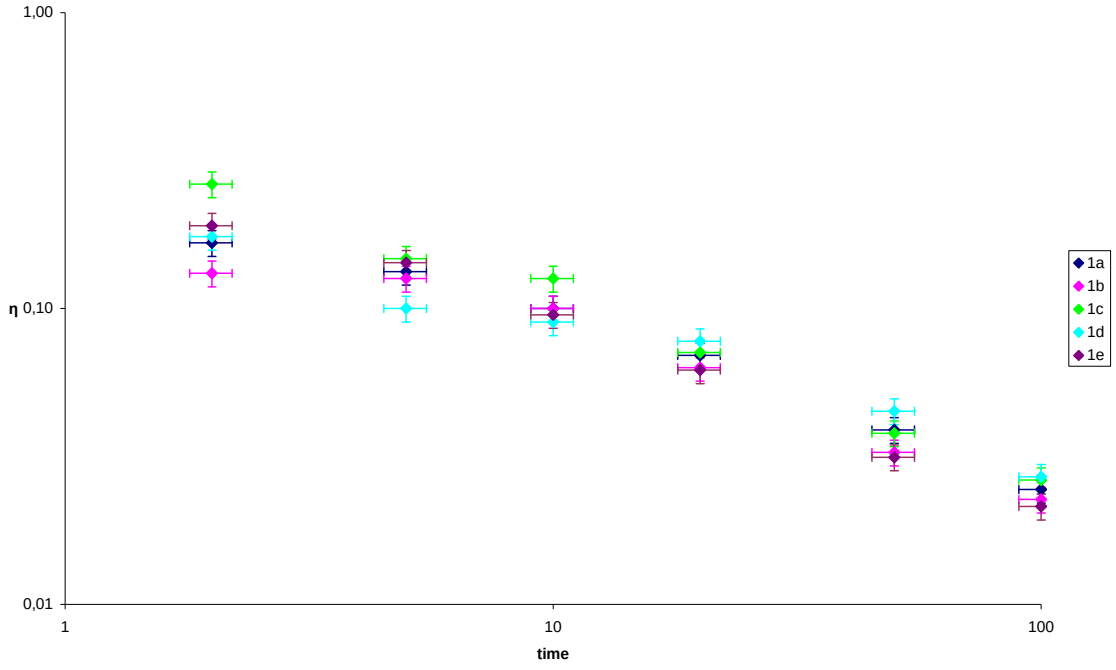

Figure 7.72: The mixing efficiency in function of time in logarithmic scale for experiments 1a – 1e.

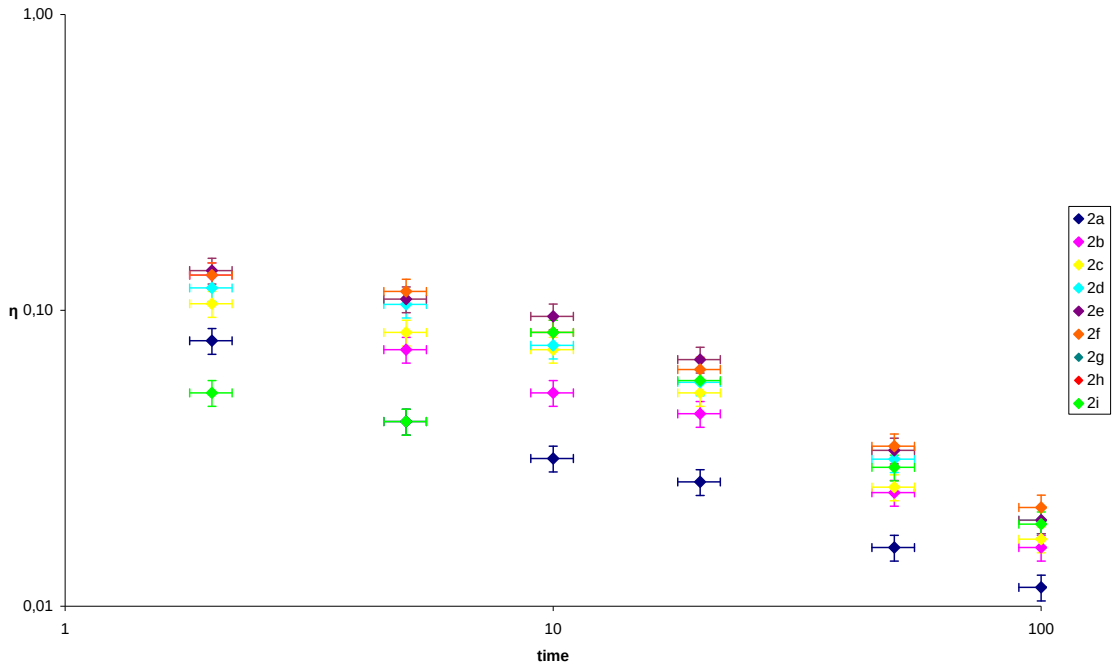

Figure 7.73: The mixing efficiency in function of time in logarithmic scale for experiments 2a – 2i.

In figure 7.74 we can see the mixing efficiency in function of Richardson number in logarithmic scale for all experiments 1a–1e and 2a–2i, showing a wide range of stabilities. The behaviour is clearly non-linear and very similar to that at a vertical grid drop at Linden (1980) and Redondo (2002). The critical Richardson number showing maximum η is $Rig \approx 2$.

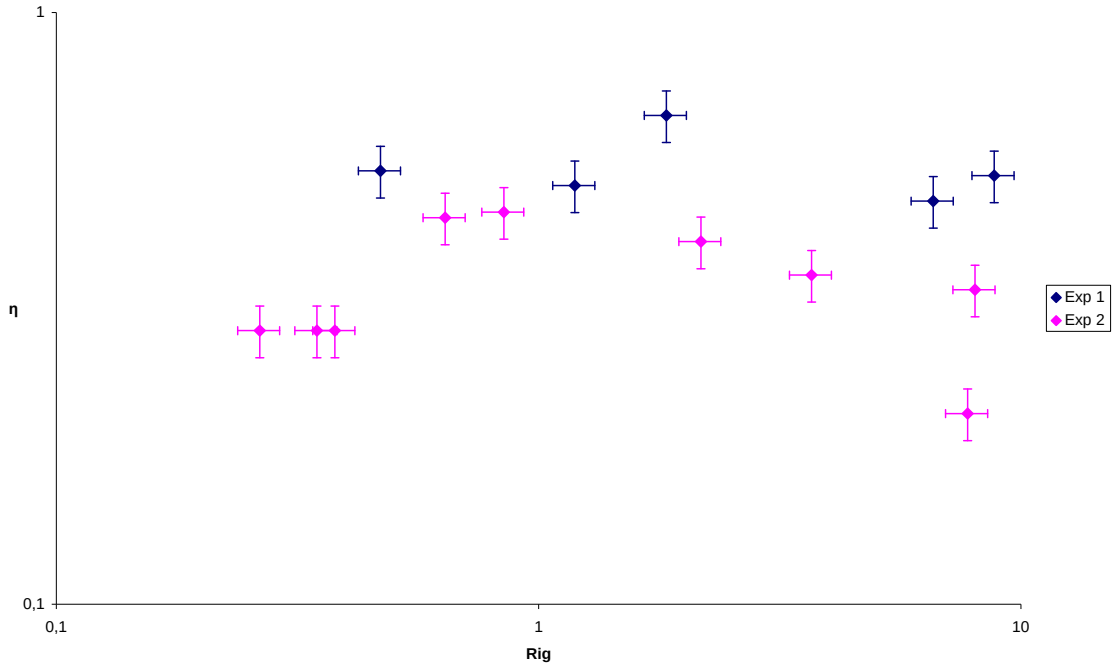

Figure 7.74: The mixing efficiency $\eta(Rig)$ in function of Richardson number in a logarithmic plot for experiment sets 1 and 2.

7.7. General parameterization of stratified non rotating flows

The experimental domain related to dimensionless numbers is very important to relate experimental results with natural and numerical models. Richardson and Reynolds numbers are summarized in table 7.6. Dimensionless numbers are related to the balance of the different forces implicated in the flows.

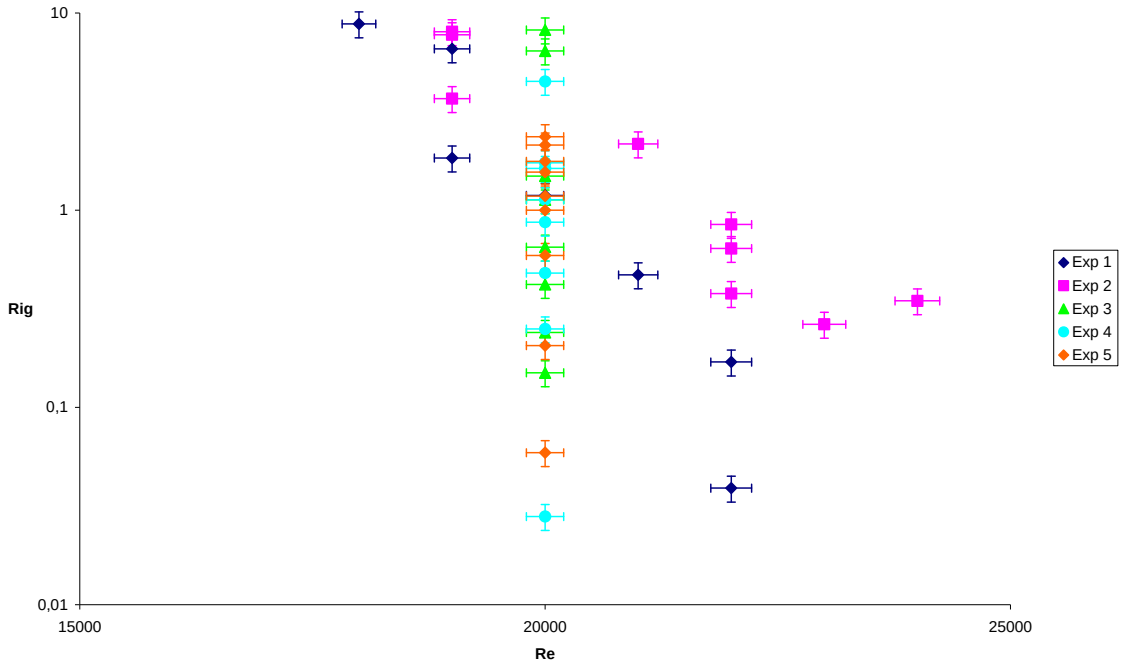

Figure 7.75: Parametric domain in stratified decaying 2D turbulence experiments performed in the tank with dimensions $1m \times 1m$. $Rig - \mathrm{Re}$

Results from all experiments are shown in figure 7.75 in the plane $Rig - \mathrm{Re}$. The set of stratified experiments presented dependence between both *Re* and *Rig*, where if Richardson number is decreasing then Reynolds number is increasing. For experiments 3, 4 and 5 the Reynolds number is constant, so it is impossible to observe the decrease of the Richardson number.

Taking values of exponents χ and β from figures 7.63 and 7.64 we obtain following graphs, where we can see the χ rate in function of Richardson and Reynolds numbers and the β rate in function of Reynolds number. In figure 7.76 we can observe the dependence of exponent in dimensional Richardson number and in 7.77, 7.78 and 7.79 the dependence in Reynolds number.

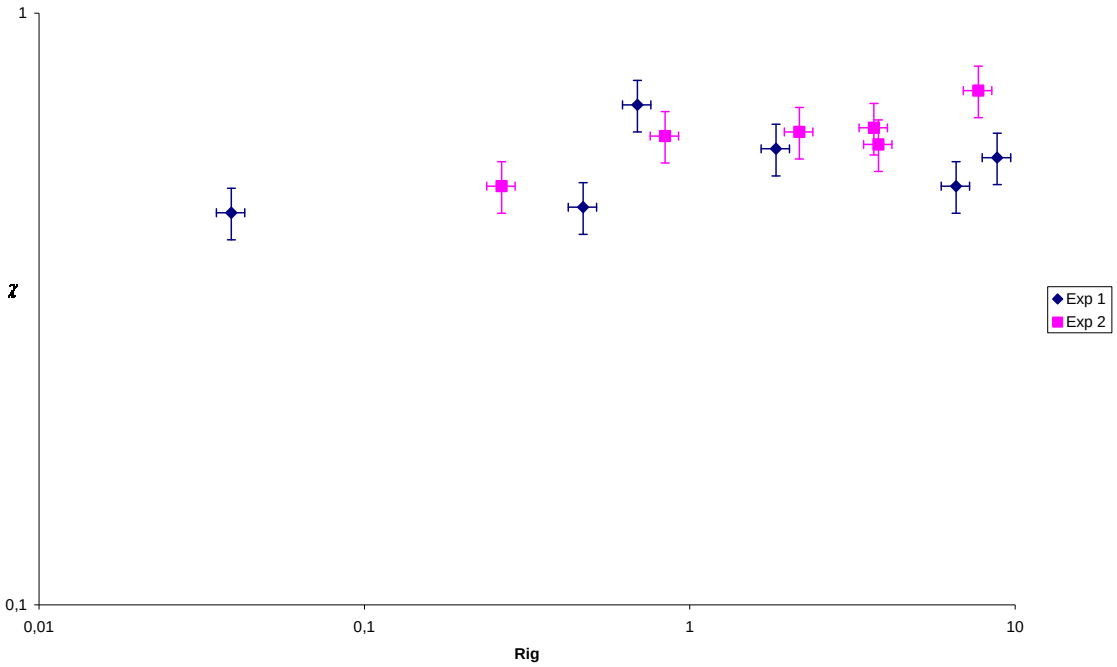

Figure 7.76: Exponent χ in function of Richardson number for experiments 1 and 2.

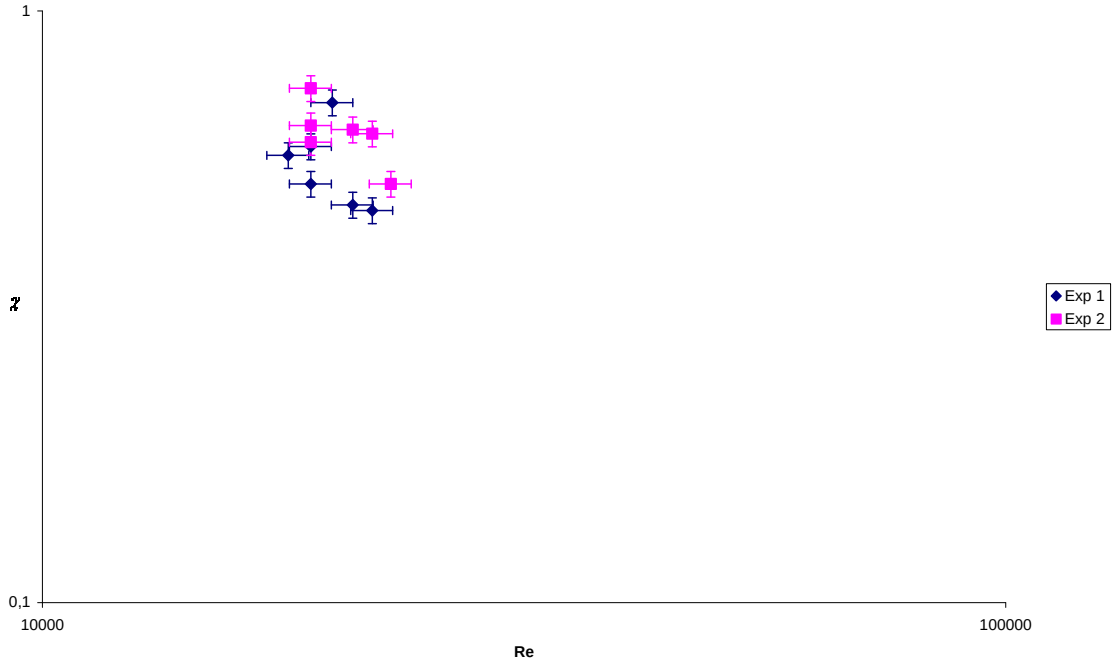

Figure 7.77: Exponent χ in function of Reynolds number for experiments 1 and 2.

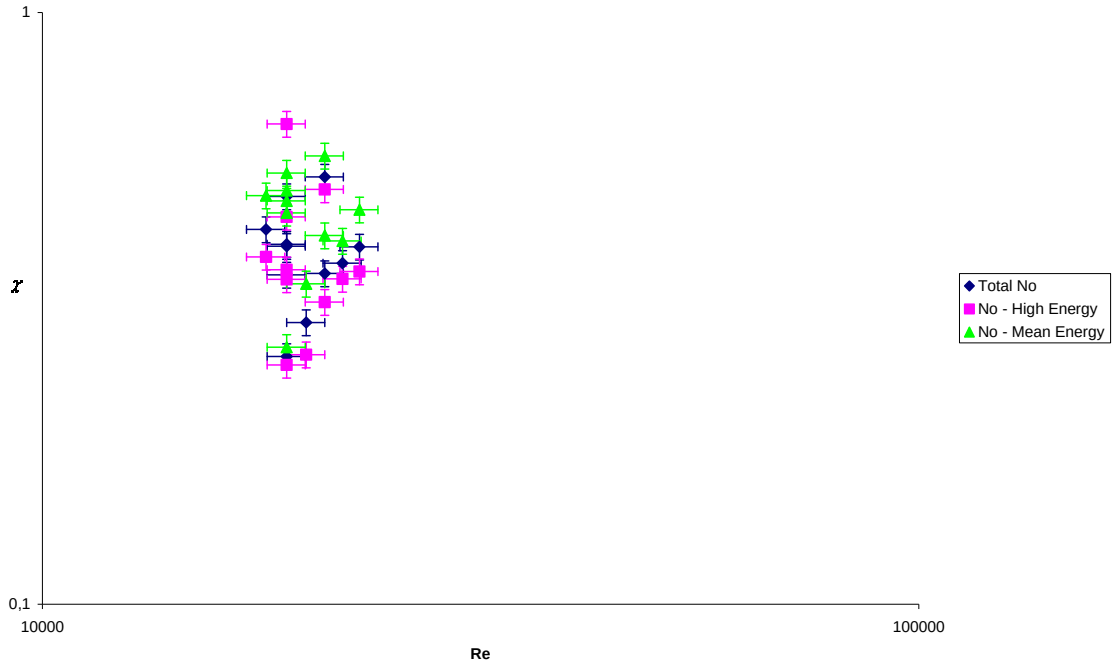

Figure 7.78: Exponent χ in function of Reynolds number for different experiments in high and mean energy and for total vortex number.

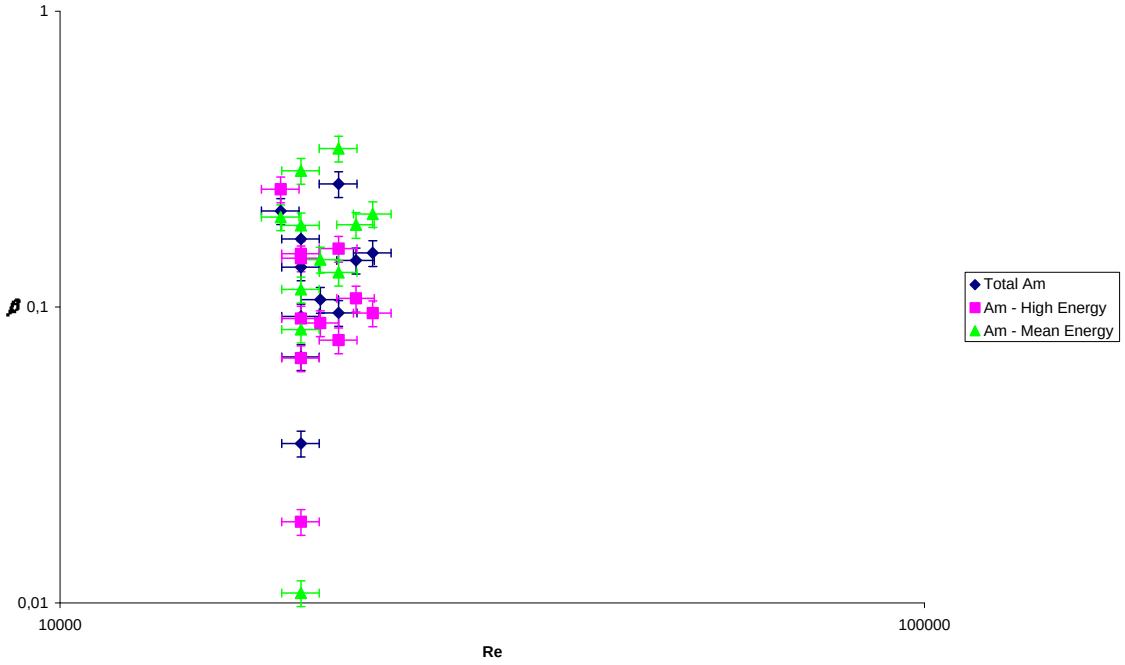

Figure 7.79: Exponent β in function of Reynolds number for different experiments in high and mean energy and for total vortex number.

In figures 7.80 and 7.81 we show the exponent B, which indicated the vortex decay as an exponential fit measured in a line within the 2D interface, different fits from

positive $\omega+$, negative $\omega-$, total vorticity ω and enstrophy ω^2 are presented as a function of both Richardson and Reynolds numbers from experiment 1c, 2a and 2f (with low, medium and high Richardson numbers). The exponent B is obtained directly from the fits of figures 7.32, 7.33, 7.34 and 7.35. We can see in figure 7.74 that the exponent B is quite similar in all cases with low, medium and high Richardson number. Figure 7.81 presents the relation between the Reynolds number and the exponents B for positive, negative and total vorticity and enstrophy in logarithmic terms. We can see that for experiments 1c and 2a the Reynolds number is the same, but there is certain difference between B exponents for both cases reinforcing the role of the buoyancy on the decay process, unfortunately, the Reynolds number was not varied systematically and other processes related to the spectral gap between the forcing and the dissipation may be relevant, In order to investigate at a totally different range of larger scales, we investigate the detection and role of surface vortices in the ocean using image analysis from satellite observations.

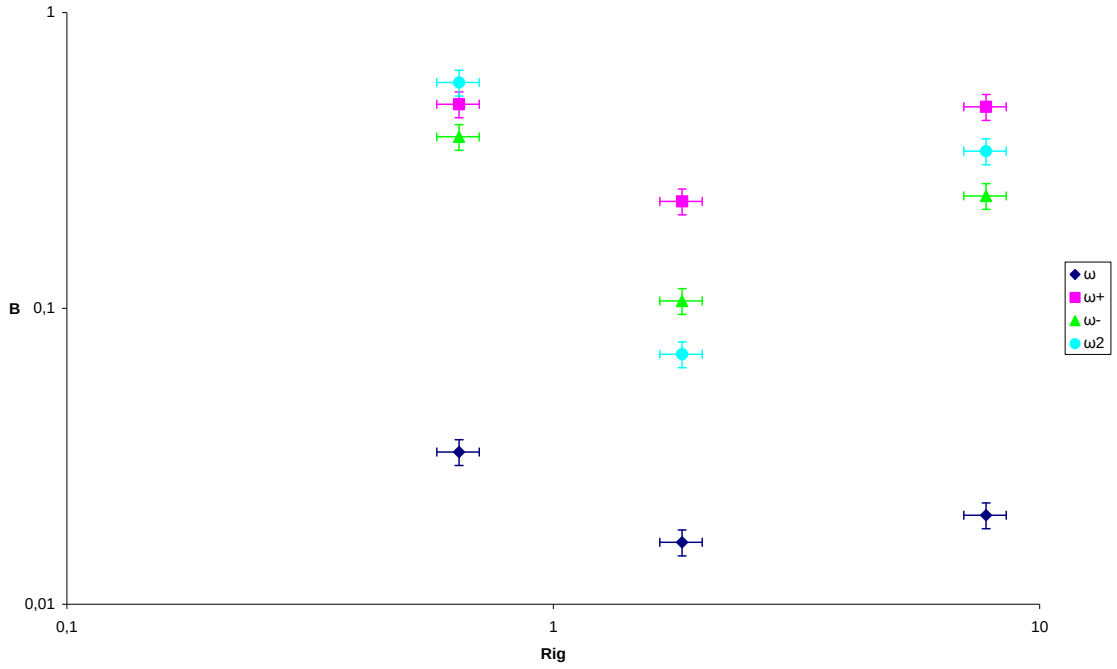

Figure 7.80: The exponent B from ω, $\omega+$, $\omega-$ and ω^2 in function of Richardson number, in logarithmic term, for experiments with low, medium and high Richardson number, $Rig=0{,}64$, $Rig=1{,}84$ and $Rig=7{,}756$.

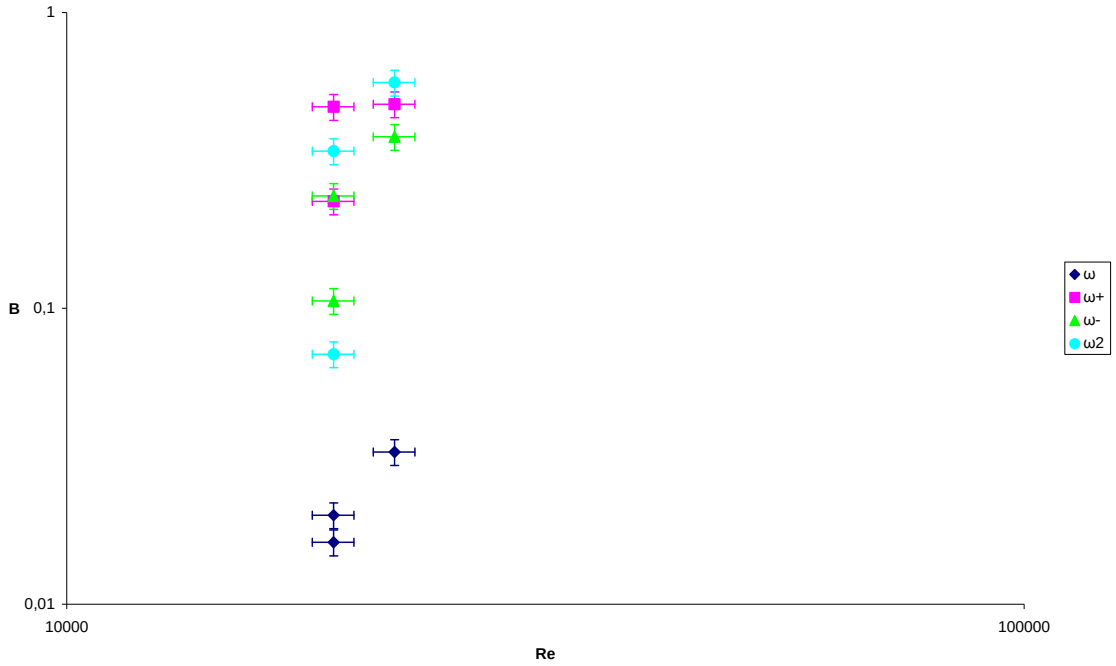

Figure 7.81: The exponent B from ω, $\omega+$, $\omega-$ and ω^2 in function of Reynolds number, in logarithmic term, for experiments with low, medium and high Richardson number, $Rig = 0{,}64$, $Rig = 1{,}84$ and $Rig = 7{,}756$.

Figure 7.82 shows the complex relationship between the Richardson number and the overall decay exponent of the number of vortices, so being evident that for the non-stratified experiments the three dimensional effects dominate and produce an extra dissipation effect on the vorticity by shifting vertical vorticity to horizontal three dimensional vorticity. It can also be observed that there is a non linear relationship between vortex decay and highest Richardson numbers. The hint of a maximum, meaning more dissipation, or more mixing at intermediate Richardson numbers agrees with the detected maximum in mixing efficiency for intermediate Richardson numbers detected first by Linden 1980, in grid decaying experiments.

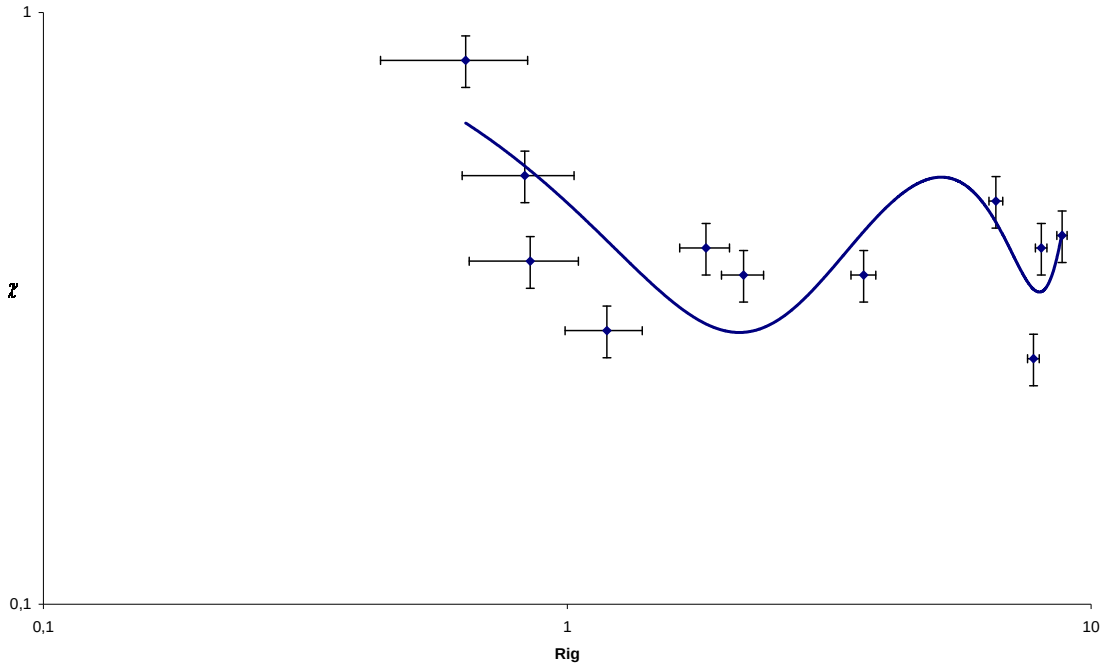

Figure 7.82: Decay exponents as a function of Richardson number.

CHAPTER 8

Satellite observations of vortices in the Ocean

8.1. Use of SAR images in ocean studies

The Synthetic Aperture Radar (SAR) is a useful tool that may be used to study both marine water dynamics and its pollution. Oil spills and natural slicks may be detected and processed with advanced computer techniques to reveal vortex dynamics and turbulence spectral characteristics of the complex eddy and current interaction in the ocean surface. In the framework of the European Union contract Clean Seas, more than 300 SAR images of the North-west Mediterranean Sea area taken between December 1996 and December 1998 were analyzed. 255 eddies can be detected under certain conditions and we analyzed statistically the appearance, size and position of vortices in the test area. It is shown that the maximum size of the eddies detected near the coast is limited by the Rossby deformation radius and that there is a decrease in size in the coastal waters in the direction of the Liguro-Provenzal current with the largest eddies occurring near the cape of Rosas. The role of submarine canyons in the vortex generation is indicated by the asymmetry of their distribution with respect to the thalwegs. It is demonstrated that useful information of a geometrical nature obtained by SAR satellite images may be used to estimate relevant dynamical parameters of coastal flows. Natural and man made distributions of tensioactive substance concentrations in the sea surface features exhibit self-similarity at all radar reflectivity levels when illuminated by SAR. This allows the investigation of the traces produced by vortices and other features in the ocean surface. The man-made oil spills besides often presenting some linear axis of the pollutant concentration produced by moving ships also show their artificial production in the sea surface by the reduced range of scales, which widens as time measured in terms of the local eddy diffusivity, distorts the shape of the oil spills. Thanks to this, multi-fractal analysis of the different backscattered intensity levels in SAR imagery can be used to distinguish between natural and man-made sea surface features due to their distinct self-similar properties. The differences are detected using the multi-fractal box counting algorithm on different sets of SAR images giving also information on the age of the spills. Different multifractal algorithms are compared presenting the differences in scaling as a function of some physical generating process such as the locality or the spectral energy cascade.

8.2. Introduction

The Synthetic Aperture Radar SAR its active radar which emits its energy in the centimetre frequencies range during a very short time period and it is able to receive the echoes. Due to the large orbital velocity of the satellite (7,5 km/s) approximately, its SAR antenna itself may be converted as a virtual antenna of a much larger size. The SAR instrument may be installed on a plane, on a helicopter or on board a satellite. The SAR emits short EM waves in the range of centimetres. The radar backscattering depends on the roughness of the small scale surface. When the surface is rougher (mostly due to capillary waves in the ocean surface) the intensity of the receiving signal is stronger due to Bragg resonant dispersion (Gade and Alpers 1999). In consequence a white zone is observed in the image when the surface is very rough. The dark areas are visible when there is a concentration of tensioactive products such as oil. Other phenomenon which has a strong significance in the use of the SAR images to monitor the sea surface is the Langmuir circulation (Sole at el. 2000). It is related to the surface particle concentration on the convergence zone between two vertical cells at sea. Algae, zoo-plankton, products of the marine life or waste from industries, spillage from tankers, hazardous waters, dregs at suspension, etc. accumulate on the convergence surface strips between two cells as seen in figure 8.1. It is precisely there that they form the high concentration tensioactive wakes or strips which we can observe clearly in the SAR images. Due to this phenomenon, the SAR images may detect many different oceanic dynamic meso-scale processes, such as internal waves, marine surface currents, hydrographic fronts, vortices and bathymetric characteristics of the sea bottom at coastal areas (Gade and Redondo 1999). The meteorological phenomena as cyclones, atmospheric fronts, surface wind, atmospheric internal waves and rains are also detected by the SAR images due to their effect on the sea surface roughness.

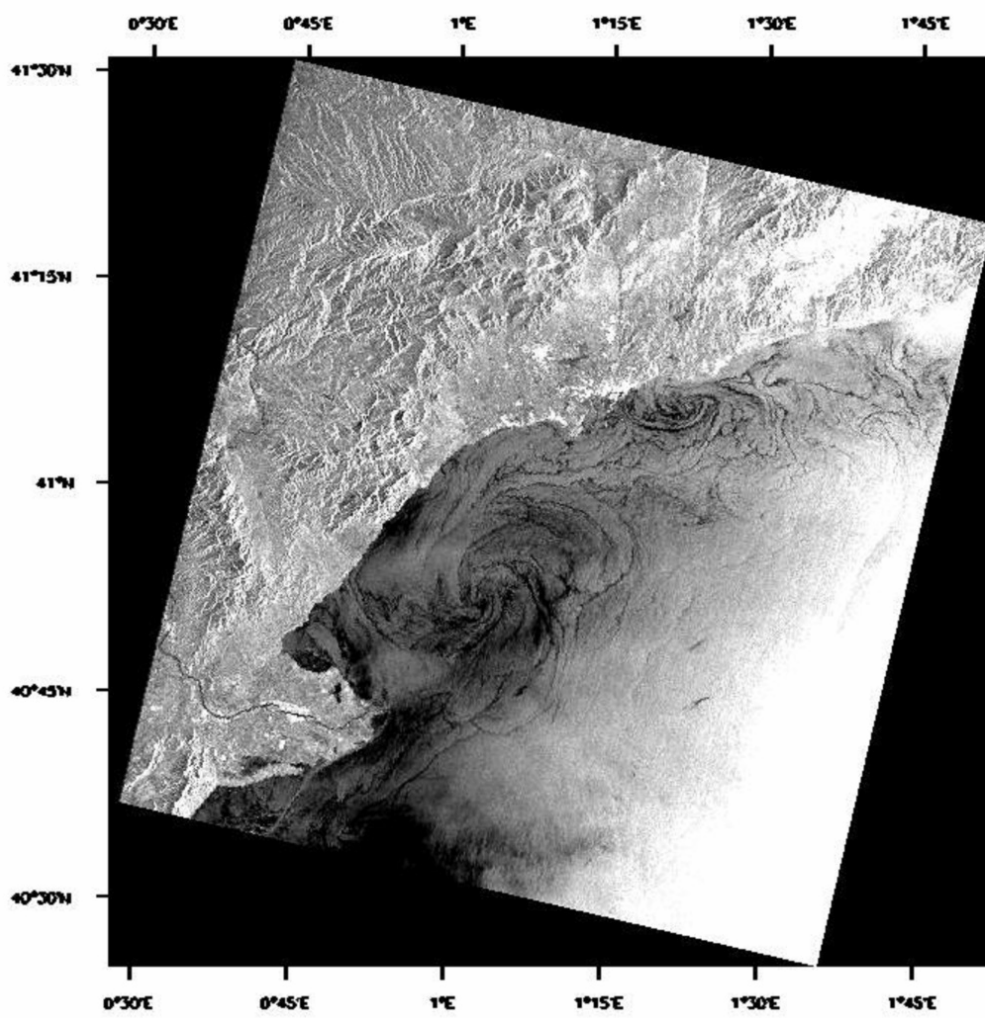

Figure 8.1: Dynamic features on sea surface near the Ebro delta. ERS-2 SAR 100Km x 100Km image on 27.08.97 at 10:30 UTC.

8.3. Image analysis and descriptions

Figure 8.2 shows the position, the shape and the spatial direction of the 255 elliptical vortices clearly detected in the different SAR images during two years of observations. In order to better visualize the bathymetrical structure of the marine bottom, the "thalwegs" of the submarine canyons have been marked with lines.

Most of the vortices are located in a relatively nearby maritime band near to the continental shelf. It is worthwhile to note the correlation between the spatial positions of the vortices and the submarine canyons: most of the vortices are located towards the left side of the submarine canyons. The spatial direction of the ellipses adjusted to the vortices was determined through the angle between the North direction and the direction of their mayor axis. The other region of concentration of the vortices is situated in the centre of the marine test area. There seem to be two main sources of the big eddies in the Gulf of Leon, as discussed by Redondo & Platonov (2001).

The analysis of the direction of rotation of the vortices shows that 76 have an anticyclonic character and 179 correspond to cyclonic (anticlockwise).

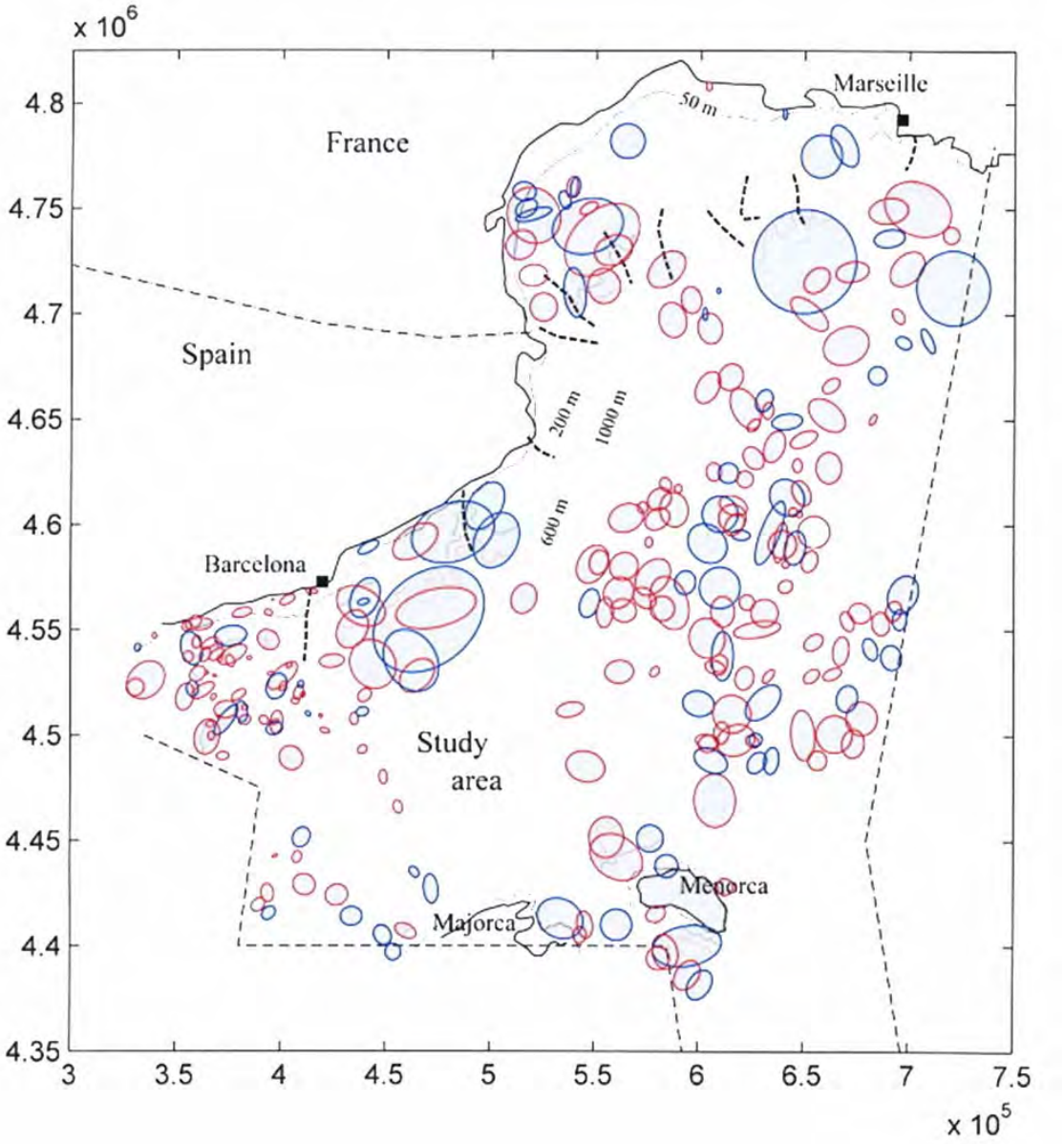

Figure 8.2: Submarine canyons and the detected vortices in the period between 1996 and 1998 in the NW Mediterranean

8.4. Statistical analysis of vortices

The extension of most of the SAR detected vortices (63 %) is less than 100 Km^2. 33% of vortices occupy an area between 100 to 500 Km^2 and only 4% of the vortices possess a large area between 500 and 1200 Km^2 (figure 8.3). About a 93% of vortices have a diameter less than 20 Km. The greatest part of the vortices (79%) have an elipliticity (relation between big and little diameter) near 1.125 – 1.625 that shows that this form is more stable (figure 8.4), in agreement with Saffman (1995).

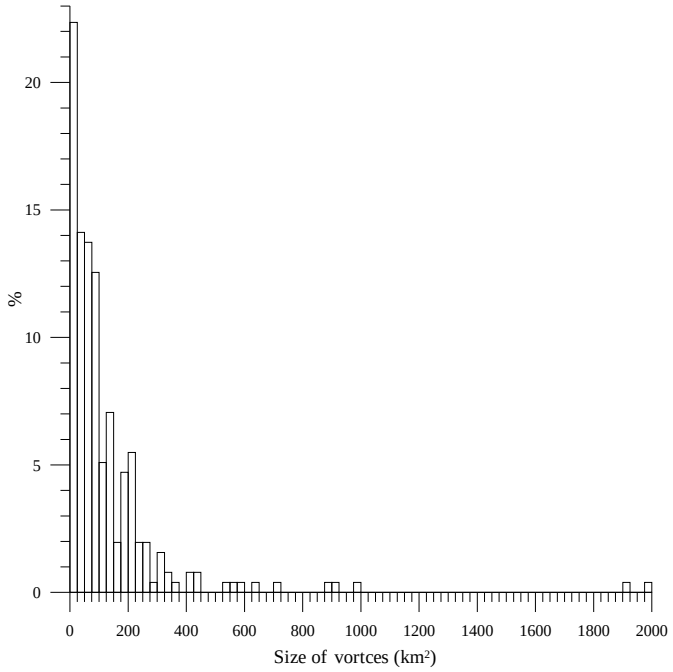

Figure 8.3: Histogram of the detected vortices in function of their areas

As mentioned above, the vortices near the Barcelona marine area (Redondo and Platonov, 2001) are due to a bi-normal distribution of the vortices and they considered that there exist two main types of mechanisms, detected by an angular dependence, related to their orientation:

- Dynamical, due to the influence of the Liguro-Provenzal current (about 50% of the detected vortices have direction angles between 25^0 and 75^0, figure 8.5).
- Bathymetrical, due to the influence of the submarine canyons situated mostly perpendicularly to the coast line (25% of the cases the detected vortices have azimuth angles between 125^0 and 145^0).

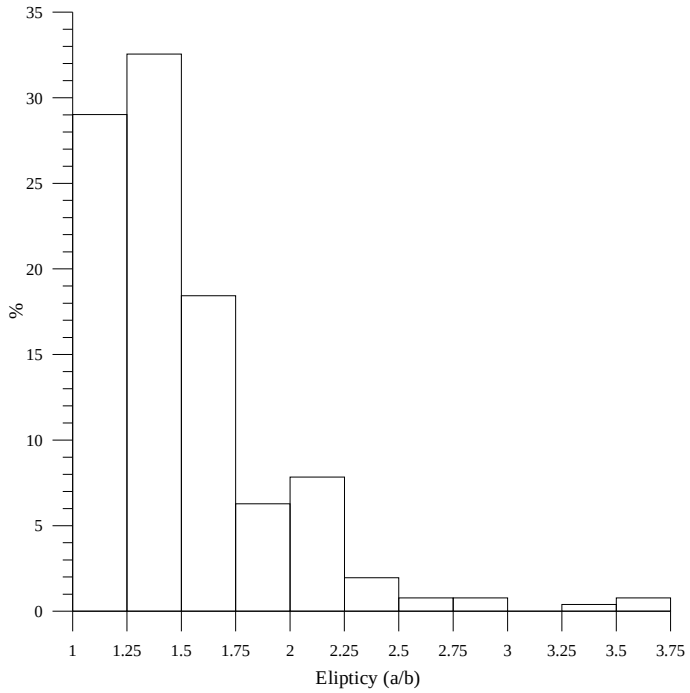

Figure 8.4: Histogram of the elipcity of the detected vortices (a/b)

In the present analysis of the 255 detected vortices, the figure 8.5 shows that the general orientation of the vortices is direction between NW and NE.

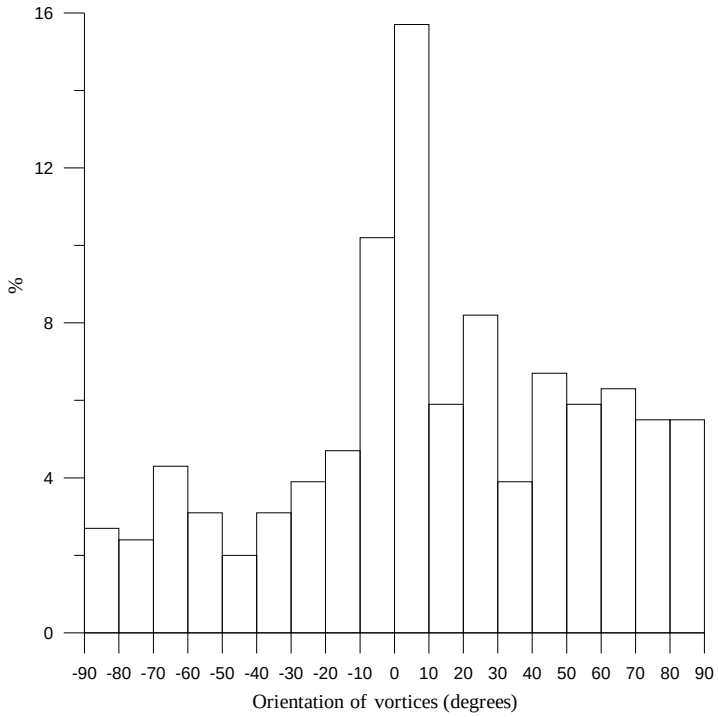

Figure 8.5: Histogram of the vortices function of the angles (between the North and the direction of their greater axis; clockwise direction is positive).

Figure 8.6 shows an enhanced SAR image with two marked typical examples of regular and irregular surface flows. A combination of oil spills and natural slicks are present, in figure 8.7 the same information given by the spatial distribution of SAR intensity pixels (about 4 x 10^4 m^2 per pixel) in a 3D representation, with the third coordinate indicating the actual local value of the reflected SAR intensity, which is a measure of ocean surface rugosity.

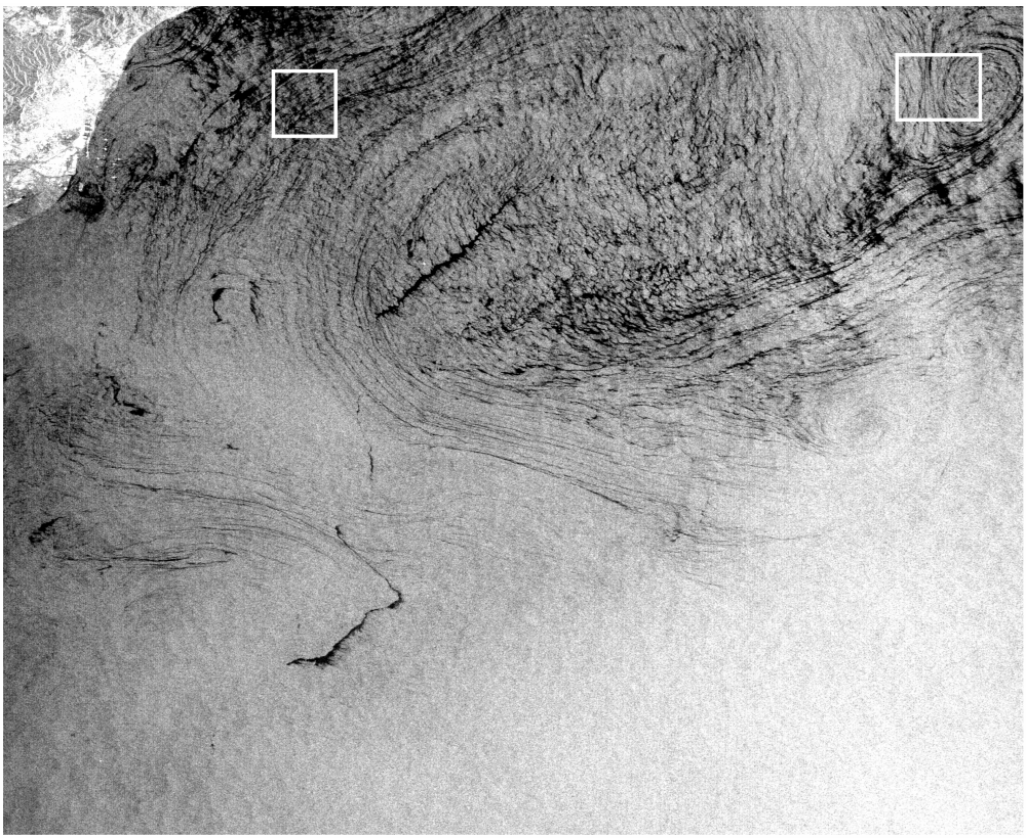

Figure 8.6: SAR ERS-2 images of the area near Barcelona 24.08.97, marked squares show the regions of image enhancement (oil spill (left) and self-similar vertical surface feature (right)).

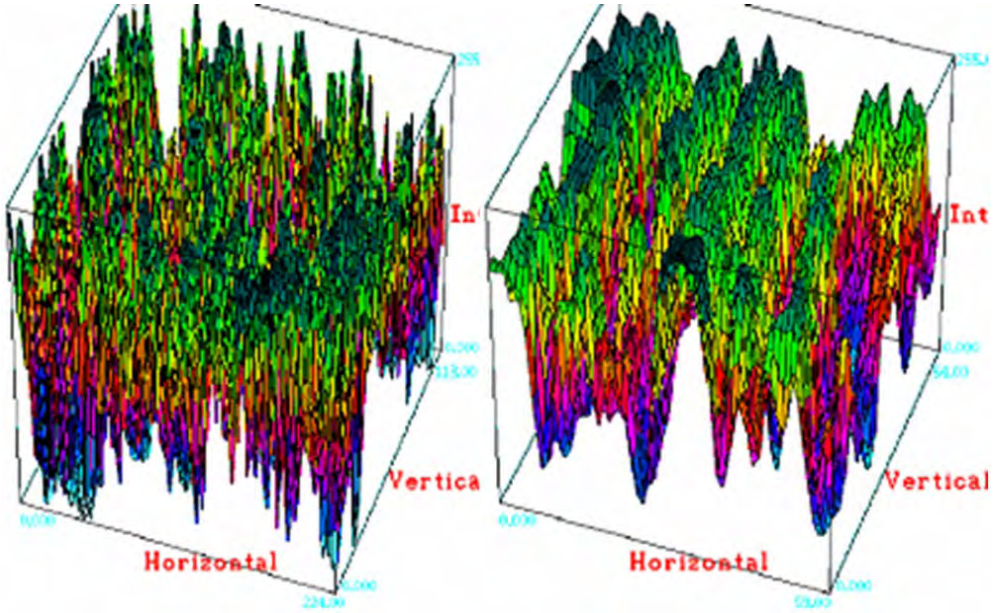

Figure 8.7: Analyzed by DigImage the results in a 3D view of the structure of the false colour derived from intensity of SAR signals that reflect surface roughness: oil spill and slicks (left) and self-similar vertical surface feature (right).

To calculate the fractal dimension of the images, as discussed in chapter 5, the Box-Counting method used produces coverage of the object. For the plane these boxes will be square and for an object in space they will be cubes. The distribution of the boxes is accomplished systematically, the intersection of these with the object produces a systematic measure that we have N boxes with a non void intersection, but as they are not exactly the result of the best coverage possible if a single scale is used, so we apply the concept of self-similarity and the basic covering is accomplished repeating the process for many different possible diminishing observation scales, and presenting the best power fit for all scales.

When we work with real images they do not have generally some perfectly defined contours, but we have some quite wide ranges of scalar intensity values to process. If we group the available data and describe them by a single larger set and calculate the fractal dimension we then lose the corresponding single intensity value information due to the intensity variation.

It is also possible to accomplish a segmentation in many intervals that contains each one a very well defined intensity range. For each one of these ranges we applied the usual fractal dimension calculation with the box-counting method and we obtain the corresponding fractal dimension for each intensity level. The result of the process is a

set of dimension values, function of the intensity, and this measure will not need to rely on the evaluation of a limit neither to the smallest nor to the largest scales. An advantage of this straight-forward method is that the best fit to calculate D may be performed choosing freely the scale, the scale interval and the number of pixel values that will be used, this multi-fractal method has some advantages with respect of the $f(\alpha)$ spectra described in chapter 5.

The fractal dimension $D(\rho)$ is then a function of pixel intensity, (we may relate μ to ρ) and may be calculated using

$$D(\rho) = -\frac{\log N(\rho)}{\log \lambda} \tag{8.1}$$

where $N(\rho)$ *i*s the number of boxes of size λ needed to cover the SAR contour of intensity ρ.

The box - counting algorithm divides the embedding Euclidean plane in smaller and smaller boxes (e.g., by dividing the initial length λ_0 by *n*, which is the recurrence level of the iteration). For each box of size λ_0/n it is then decided if the convoluted line, which is analyzed, is intersecting that box. Finally, is plotted *N* versus λ_0 /*n* (i.e., the size of the box *e*) in a log-log plot, and the slope of that curve, within reasonable experimental limits, gives the fractal dimension. This method of box-counting is used in ImaCalc software (Grau et al. 2005) that we applied to detect the self-similar characteristics for different SAR image grey intensity levels ρ and to identify different sea surface dynamic processes. Each of the intensity values may reflect different physical processes and lead to a different value of its fractal dimension; this whole entity can be either fractal or not fractal but exhibits a range of values 0-2 for all intensity.

The program ImaCalc (Grau et al. 2005, Platonov et al. 2008, and Redondo et al. 3008) performs interactively most of the multi-fractal box counting methods as well as the spectral ones. Different regions may be equalized depending on their intensity histogram distribution.

Using the traditional energy spectra used in turbulence studies characterized by a single power law within the inertial sub-range (defined as the range of scales where production and dissipation of energy, ε are in local balance) we use a theoretical

relationship between the turbulence spectral slope and the fractal dimension, we are now able to apply it to a spatial spectrum as described in chapter 5, and define a global fractal dimension using directly the spectral analysis on the radial distribution of intensity values of a SAR image

With this methodology a unique value is obtained that characterizes the overall spatial fractal dimension of the system. The steps are described as follows (Vassilicos et al. 1991): make an image segmentation to obtain the interest region (ρ_{mn} , *m* and *n* are the *x*-*y* discrete coordinates). Compute the FT (Fourier Transform) to obtain the frequency spectrum representation. (l_{uv} , *u* and *v* are the frequency discrete coordinates). Compute the square of the signal intensity or energy S_{uv} with: $S_{uv} = |\upsilon_{uv}|^2$. Obtain the *radial* representation, as the radial distribution of S_{uv} and finally find the exponent *p* from $S_r = r^{-p}$. Using the radius as an isotropic length scale λ.

With a linear fit from a log-log representation of S_r we may obtain the spatial spectral value of the set of all SAR image intensities, which we assume is also *p* and using as the Euclidean dimension $E_u = 3$ and the fractal dimension relationship we have:

$$D = \frac{7 - p}{2} \tag{8.2}$$

And thus we also have a global, indirect measure of the average fractal dimension from the radial spectral energy, note that only if the scalar used corresponds to velocity component energy will have the correct physical dimension; otherwise the energy spectrum will just indicate the square of the physical signal used.

8.5. Results on vortex multifractal measurements of the ocean

The measurement of multi-fractals is mainly the measurement of a statistic distribution which is why the results yield useful information even if the underlying structure does not show a clear self-similar or self-affine behaviour. For a monofractal object, the number *n* of features of a certain size λ varies as can be measured by counting the number *n* of boxes needed to cover the object under investigation for increasing box sizes λ and estimating the slope of a log–log plot. For multifractal measurements, a probability distribution is measured. In practice, using the box counting method, for every box *i* the probability of "containing the object", or in this application, the values of a certain SAR reflectivity, is also called the partition function, which may be obtained for different moments *q* which can vary from -8 to +8 . Both methods described above may be used to extract useful information about the age of the oil spills as well as about other mixing processes in the ocean surface.

Thus it is possible to define D_i as described above. The well known multifractal function $f(\alpha)$ may be seen as the fractal dimension of the set of intervals that corresponds to a singularity a, and a graph of *a* vs. $f(\alpha)$ is called the multifractal spectrum of the measure. A measure is multifractal when its multifractal spectrum exists and has the shape of an inverted parabola. A generally equivalent way to describe a multifractal scaling is by considering the scaling laws of the moments of the measure.
In practice, the object density is taken to the respective power of *q*, summed for all *i*, and plotted versus the box size in a log–log coordinate system. From the slope, which is also called the mass exponent t, the generalized dimensions are estimated as $D(q) = t(q)/(1-q)$.

Images can be pre-processed using any image processor, e.g. to convert from colour/grey images to black-and-white using different types of algorithms, to invert background and foreground, to extract boundaries. With SAR images from the ocean surface we cannot rely strictly on theoretically limit for the calculation of the fractal, non- fractal or multifractal behaviour, because they have a finite size, and we have assigned a fixed range of values to the different SAR reflectivity intensity. The range of scale boundaries are defined by the image resolution, and we use numerical log/log fits (which tend to straighten any curve) to obtain the Rényi dimensions. Generalized dimensions $D(q)$ can be obtained with the method of moments for any image and box

size described. In order to compare the two multifractal analysis procedures involving either a single fractal measure for each of the intensity levels (or grouped in sets) with the moment calculation for the generalized dimensions, we checked the numerical values at each algorithm step. Outside of this scale range, the theoretical values of $D(q)$ are calculated as the limit when λ approaches zero and the numerical values of $D(q)$ are calculated from the regression fits. They are still very close if we select the range of scale and a grid matching the theoretical generation pattern. We applied this for a range of oil spill images.

The study of the structured distribution in the space such that at any resolution the set is the union of similar subsets to the whole will indicate the same fractal dimension for every intensity value. But the scale factor at different parts of the set is not the same for most SAR images. If more than one dimension is needed, then the measure considered is characterized by the union of fractal sets, each one with a different fractal dimension.

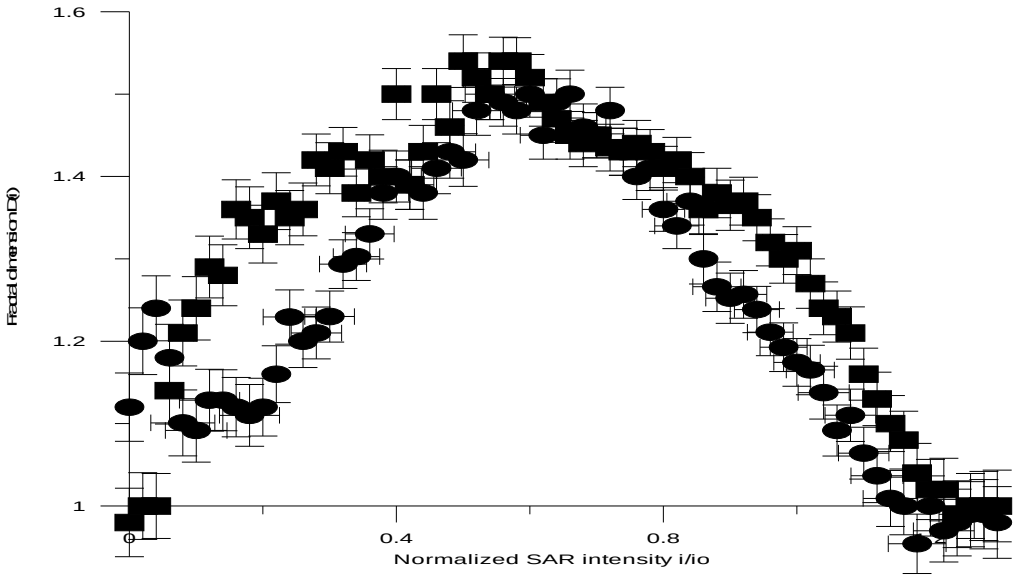

Figure 8.8:Multi-fractal set of Dimensions $D(q)$ obtained for a recent oil spill (dots), showing the low values between 0.1 and 0.4 of the normalized SAR intensity. A natural spill is more convoluted (squares) and shows a more uniform parabolic type of $D(q)$ functions.

Figure 8.8 shows the comparison of the function $D(q)$ for a natural slick, that shows a smoother parabolic shape (squares) and a recent oil spill (dots) against a

normalized SAR intensity, calculated by averaging over the background intensity values.

The SAR images exhibited a large variation of natural features produced by winds, internal waves, the bathymetric distribution, by thermal or solute convection by rain, etc as all of these produce variations in the sea surface roughness.

If we suppose that the surface currents are responsible (at least partly) for the spatial distribution of the ocean roughness for two main reasons, first the slope at both sides of an eddy is very different at producing radar backscatter from a side (as happens with ERS-1/2 and also ENVISAT) the other reason is that the surface tensioactives natural or man produced will be advected by the current lines relating the scalar and the vorticity distribution within the complex mesoscale ocean surface topology. Figure 8.9 shows an example of detected vortices using SAR. From the observations of four year period it is possible to improve on the data from figure 8.2 and map the positions, sizes orientations and shapes of a certain area as shown in figure 8.10 for the NW Mediterranean.

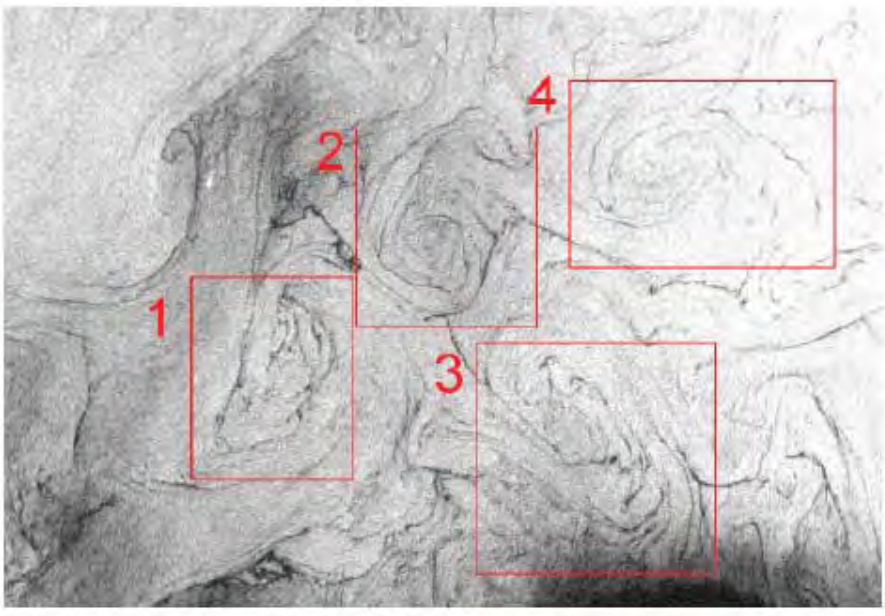

Figure 8.9: Examples of 4 vortices detected by SAR in the ocean surface

The satellite-borne SAR seems to be a good system to detect man-made oil spills and oil slicks, the dynamic feature detection gives information over the surface motions at different scales. It is also a convenient tool to investigate the eddy structures of a

certain area, such as the cases where the effect of bathymetry and local currents are important in describing the ocean surface behaviour.

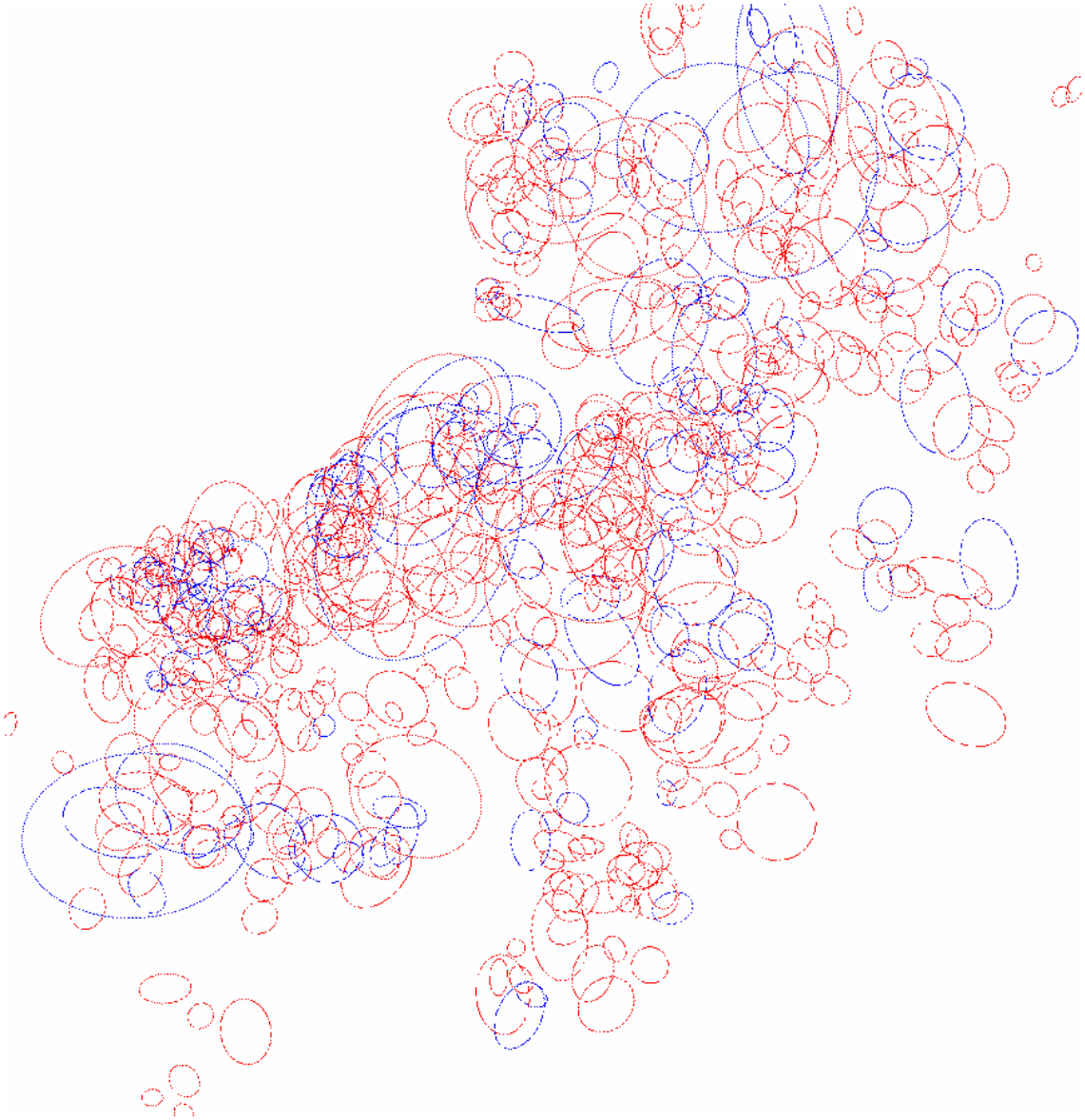

Figure 8.10: The example of the observation of four year period of size orientation and shapes of a certain area for the Gulf of Lyon region.

In this example presented near Barcelona and Marselle, the maximum eddy size agrees remarkably well with the limit imposed by the local Rossby deformation radius using the usual thermocline induced stratification. With the measured data, the average Rossby deformation radius of the area, *Rd* is about 20 Km. It is interesting to use this information to define the coastal flows (Matulka et al. 2009).

8.6. Other Geometrical and Topological Fractal measurements

Fractals are geometric entities that present self-similarity and they are often the result of iterative processes such as turbulence. The self-similarity implies that if we have observations from different scales the results are similar, although in natural systems it is enough to have only a certain statistical similarity. These natural entities have usually anisotropic nature and then there may be different scaling laws for the different directions. Examples of these are the surface topography and the clouds, where the vertical coordinate has a smaller magnitude that horizontal coordinates due to stratification Grau (2003) and Redondo (2008). Fractal analysis is a very useful tool to characterize these objects in which an additional possibility is the calculation of the corresponding fractal dimension along the different coordinates so it may also reflect the anisotropic scaling. The eddies can also be detected from SAR as well as from infrared or colour images the local self-similarity (Snaith…).

Figure 8.11: Complex eddy patterns detected by SAR in the NW Mediterranean sea and example of oil spills and river plumes a) affected by a local vortex south of Barcelona SAR ENVISAT frame, b) detail at higher resolution, c) eddy structure.

Figure 8.11 show the type of measurements that allow comparing the local topology of the flows with Direct Numerical simulations (Castilla et al. 2007) such as that shown in figure 8.12. The laboratory experiments and field simulations may be used to estimate the evolution of the fractal dimension of a spill model in non-dimensional time discussed in next section.

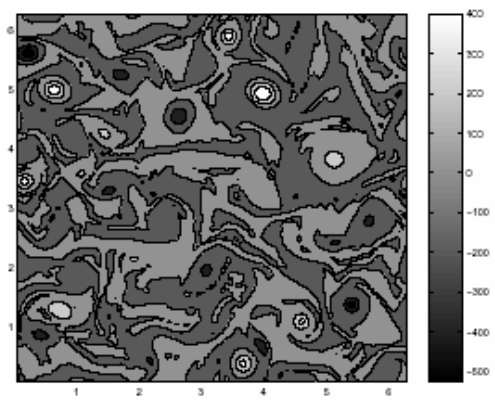

Figure 8.12: D.N.S. of a 2D equilibrium vorticity pattern, where the structure of the flow is revealed.

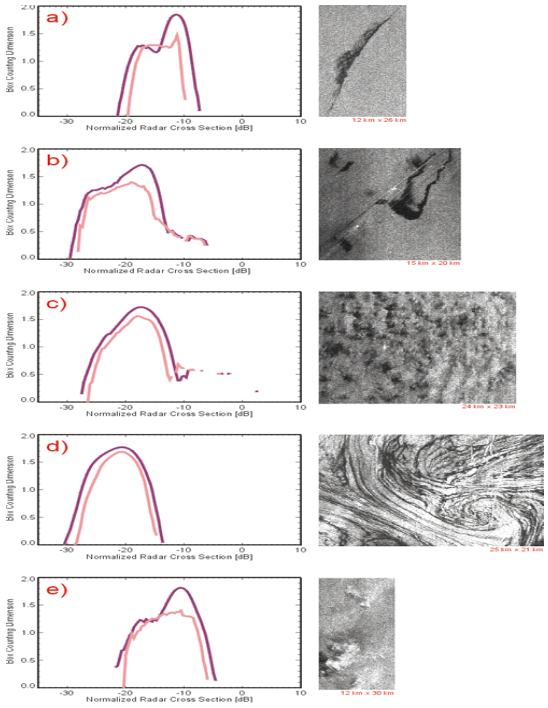

Figure 8.13: Multifractal $D(q)$ curves for different features in SAR images a) and b) spills, c) convection, d) eddy, e) rain.

In figure 8.13, we may observe the very different topological characteristics of natural slicks and oil spills and advanced flow visualization techniques aid the identification of vortices or of Langmuir cells. The different causes of the slicks as shown in figure 8.13 are also reflected in the $D(q)$ plots discussed above and used first by Gade and Redondo (1998). Other multifractal measurements can also be related to

physical mechanisms that affect in a different fashion the different scalar intensities used to identify the flows, as in Platonov et al. (2008) and Redondo et al. (2007) where stratification is shown to affect clearly the maximum fractal dimension.

The correlations of intensity values and the radial integral of these, indicates the spatial scale *l* where the SAR intensities are well correlated. If we suppose that the surface currents are responsible (at least partly) for the spatial distribution of the ocean roughness for two main reasons, first the slope at both sides of an eddy is very different at producing radar backscatter from a side (as happens with ERS-1/2 and also ENVISAT and RADARSAT)

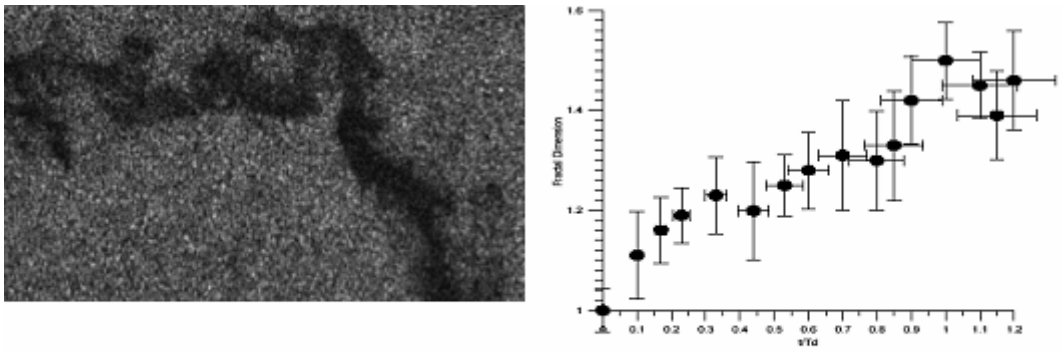

a) b)

Figure 8.14: a) ASAR higher resolution image of a wethered oil spill; b) evolution of $D(q)$ in time.

For example, the oil spill shown in figure 8.14 a), at a higher resolution using ASAR would correspond to a range of non- dimensional times T_{oil} between 0.7 and 0.8 matching the fractal dimension of 1.3-1.4 evolution seen in 8.14 b). There are other indications that may be useful from the SAR observations, such as the low local wind at the time the image was taken. There is a consistent pattern that distinguishes the recent oil spills and the natural slicks that have adapted to the multi-scale turbulent flow of the ocean surface. Figure 8.15 shows some of the differences between recent, characterized by the low fractal dimension of low SAR reflectivity values, and weathered oil spills or slicks, which exhibit parabolic behaviour of the curve $D(q)$.

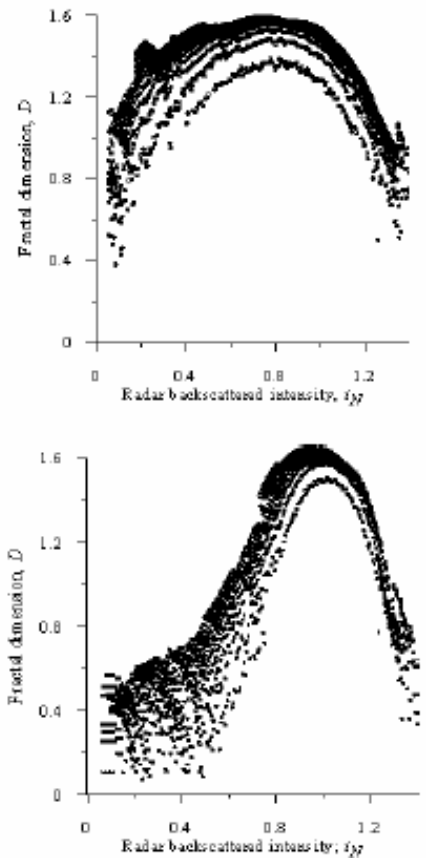

Figure 8.15: Normalized multifractal patterns exhibited by natural slicks (above) and oil spills (below), Redondo & Platanov (2009).

Several uses of these new techniques are proposed taking advantage of Zipf's Law, both for anthropogenic oil spills and other features, it is possible to predict the likely probability of oil spill accidents of different sizes, as well as the local eddy characteristics that strongly influence the turbulent horizontal diffusivity, *K(x,y).*As an example from Jolly et al (2000), figure 8.16 shows a map of local average diffusivities derived from SAR observations near Barcelona, of course Richardson's law has to be applied and different sizes of spills will comply with the 4/3 law. Both numerical simulations as see in 8.13 and laboratory experiments confirm the conditions for hyperdiffusion ($D^2 = c\,t^{n(f,N)}$ with $n(f,N) \rangle 3$ to exist, as well as the trapping associated with coherent structures and vortices in the ocean, which are well detected under the Weilburn distribution of prevailing winds in the NW Mediterranean Sea..

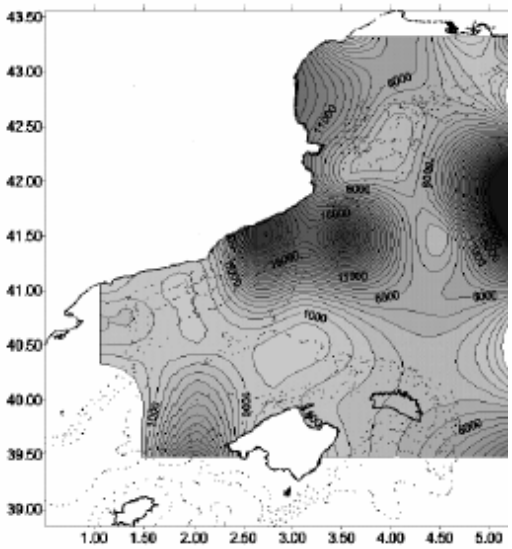

Figure 8.16: 2D map of Eddy diffusivity values derived from local estimates of the integral scale from SAR images.

8.8. Summary and conclusions

This scenario is an appropriate model for geophysical flows which are known to contain very energetic vortices mesoscale oceanic eddies and atmospheric highs and lows. This upscale transfer of energy is inhibited at the Rossby deformation radius: The energy limitation is caused by baroclinic instability at larger scales, which accounts for the dominant observed size of geophysical vortices. Laboratory experiments on annulus flow, where the flow is driven in a rotating annulus by differential heating of the lateral walls of the annulus, or by internal heating of the fluid. A horizontal temperature gradient is established which drives a zonal flow via the 'thermal wind' balance. For certain values of the parameters this flow is unstable to baroclinic modes that feed on the energy in the temperature or density fields.

Many features have been identified with structures and phenomena observed in several experiments, and understanding of atmospheric and ocean dynamics has been significantly advanced. The experiments have provided new insights about the dynamics and have revealed a wide range of nonlinear behaviour.

Experiments performed by Linden et al. 1996 showed the effect of mixing from the edge on a rotating stratified system. When the instability is caused by differential heating or by buoyancy there seems to be a range of very different dynamic regimes, including as in many experiments. Work by Carrillo et al. 2001 has revealed the complex interactions possible between lateral (or coastal) stirring and the rotating-stratified flow dynamics.

The investigation of such strongly non-homogeneous flow, which leads to intermittent two dimensional turbulence, is believed very important if correct parameterizations of pollutant dispersion (such as Oil spills) in coastal areas are to be made. The availability of a large scale flow allows both to measure Eulerian velocities with precision as well as Lagrangian flows using particle tracking as well as local measurements of diffusivity by video recording the dispersion of neutral tracers. A possible oil spill prediction technique, involves the releasing of hundreds of small and inexpensive tracer (GPS) Lagrangian buoys near an accident to aid the predictions of coastal currents.

Recent man-made oil spills in the sea surface are characterized by the low fractal dimension values ($D_2 \langle 1.2$) over the region of low reflectivity in SAR images; on the

other hand natural oil slicks show a typical parabolic shape with maximum of $D_2 \langle 1.5$. Most of the SAR images analyzed were obtained during 1996-1998 (near 900 images with 300 in the North-western Mediterranean Sea area) but SAR and ASAR images from ENVISAR have also been used. One of the problems in order to identify oil spills is the possibility of confusion with natural tensioactive spills, which may be due to plankton, algae or even wind pattern reflections on the ocean surface, one of the possibilities is to use the scaling properties of the turbulence that adverts and diffuses the tracers.

By using the multifractal "Box counting Algorithm" as a function of the SAR intensity and a suitable non dimensional Damkholer time, based on the local dissipation in the ocean surface, it is possible to distinguish between recent oil spills and natural slicks and to relate certain patterns to physical processes on the ocean surface. The routine observations also help to identify pollution patterns and to predict possible accidents. It is also possible to estimate the local values of horizontal eddy diffusivity and to deduce the persistence of oil spills and slicks in the ocean. The eddy structure and local characteristics are invaluable when a prediction of tracer or surfactant path has to be made. In current numerical models that do not account for the strong spectral content at $R= N\ h/f$, with N the Brunt-Väisälä frequency and f the Coriolis parameter, only Gaussian order predictions are available, on the other hand intermittency and higher order dose and persistency predictions are needed for practical remedial situations.

CHAPTER 9

Discussion

9.1. General Discussion

As was mentioned before, one of the most important role of stratification and rotation in environmental turbulence, and in general of all body forces, including magnetic fields; is to modify the slope of the spectral energy cascade.

Another experimental and numerical observation is that while the anisotropy of the Reynolds stresses is obviously linked with the non-homogeneity taking the vertical axis (in stratified flows) and the rotation axis (in rotating flows). Scalar behaviour in such flows has non-linear mixing properties Redondo (2002). There are similar effects that depart from Kolmogorov's K41 and also for K62 theories, not just in second order structure functions (and related spectra) for spatial non-homogeneity, for anisotropy and for spatial and temporal intermittency.

The directions of gravity, rotation axis and magnetic field act as principal axes and play dominant roles in the two dimensional due to body forces. These forces are dominant of the entropy cascade over the direct energy cascade, but it is important to realize that both direct and inverse cascades may not be in equilibrium at the same time. The intermittency coupled with the non-homogeneity and anisotropy act indistinguishably to modify the dispersion within the flow; here the role of coherent structures is also relevant as described in Babiano (2002).

The results of this thesis and then discussion are based mostly on the role of buoyancy but also show the extent of the available data within the HIDRALAB II project analysed with new methods of PIV and conditional sampling in stratified and rotating flows published in Matulka et al. (2009) and Redondo et al. (2004), that have been developed and are available for further exploration of the different parametric regions. For instance, processing velocity data of the grid experiments both the decaying grid wakes and quasi steady oscillating grid experiments also gives spectral information.

In the cases where the experimental initial conditions were spread out across all the parametric fields they obeyed to the fact that we specifically looked for the largest possible variability in the range of parameters. In other cases, such as the non-rotating experiments from chapter 7, the range of experimental initial conditions was also performed for a wide parametric range. The Richardson number varied mostly when the density difference was changed.

The set of rotating stratified experiments may be classified in regions dominated by one or several dominant instabilities such as those appearing in the non-rotating case internal waves, Holmobe instability, Kelvin-Helmholtz billows, non-linear pairing and fully developed turbulence, described first by Redondo (1989, 1990). In the case of rotating stratified flows, instead of using the Burger number, because the equilibrium between rotation and stratification is attained when $Ri\,Ro = 1$, we may use the diagonal to conditionally sample the different scales of the Rossby deformation radius $R_D = Nh/f$ when R_D are stable. A new parameter map to be used as a general frame of reference with Rig, $1/Ro$ and Re presents important advantages when comparing different experiments and field data, and simplifies the complicated relationship between these dimensionless numbers.

The analyzed non-rotating experiments were performed under the initial conditions from $\mathrm{Re} = 24\times10^3$ and 22×10^3; $Rig = 0.03$ and 8.8; and $N = 0.13$ and 5.73. The relationships $T-L$, $TN-L/M$ and $Tu/M-L/M$ were proportional to $T^{3/5}$ in the non-rotating experiments. In the rotating experiments (Appendix 3), analysis within a 3D parametric space show dependence between Re and Rig proportional to $\mathrm{Re}^{3/4}$ different from that reported from natural conditions without rotation where the values were proportional to $\mathrm{Re}^{3/2}$. The parameter analysis showed non-dependence between the rest of the dimensionless numbers and its values spread out across the values of Re from 2500 to 1.6×10^6 and Rig from 0 to 1.6×10^5.

The expected sample dependence between Rig and Re is found eliminating the velocity. Between Ri and Re, cannot be applied because of the modification of the vertical length scale due to both stratification and rotation. This stresses the need of measuring the relevant length scale during the experiments.

As seen in the non-rotating experiments, there is a clear interaction between the internal wave field and the domain size of the horizontal vortices for non-dimensional times $NT\langle 5$. The final growth of the size of the decaying stratified vortices is controlled by the size of the experimental domain. When there is an external imposed length scale, it can be shown, applying a simple equilibrium model as described in Matulka et al. (2008), that showed that the energy decays as $K(t) = ct^{-2}$, but the role of the initial conditions and the influence of the stratification, which would include an extra buoyancy term with a dependence of t^{-1}, this modifies the decay of kinetic energy as

well as the evolution of the ratio of turbulence kinetic energy to potential energy, as well as the vorticity.

The role of Coriolis-induced inertial waves as well as the buoyancy-induced internal waves is expected to influence most the inertial decay phase of the flow. So in order to modify global parameters as the mixing efficiency, the control of the initial conditions seems much more important than previously thought. The changes in local mixing efficiency in rotating and stratified affects the global behaviour of a whole estuary as shown by Munk (2001), Kraichnan (1967) and Platonov (2002), knowing the basic instabilities as a function of the position in parametric space ($\mathrm{Re}, Rig, 1/Ro$) is important for environmental applications.

9.2. New aspect of the research

Previous studies have focussed on the simplest cases, attempting from steady and spatially homogeneous flows to generate parameterizations of mixing that can then be applied more generally. However, real processes are both time and space-dependent, and it is an unsubstantiated assumption that steady parameterizations are useful in such situations.

New tools are available to investigate the significance of spatial and temporal variations, theoretical, numerical and experimental techniques can all be brought to bear. The thesis also aims to identify how important temporal and spatial intermittency is for both the absolute and relative efficiency of mixing. The laboratory experiments in stratified (chapter 7) and rotating flows such as grid driven turbulence with periodic or non-monotonic forcing, and periodic or non-monotonic shear layers.

One of the core ideas will be to identify when intermittency can be ignored, and when it must be retained at the core of the modelling. As there is a suspicion that a time-scale and length-scale driven are important and we expect that the insightful ideas of "fossil" turbulence may play a valuable role.

The eddy diffusivities in the ocean exhibit a large variation and show a marked anisotropy, not only horizontal values are much larger than vertical ones but there is a strong dependence on the spatial extent of the tracer dye or pollutant and at larger scales the topology of the basic flow is very important. In the case of oil spills, these are strongly influenced by the buoyancy and horizontal diffusion depends on ambient factors such as wave activity, wind and currents (These ocean surface analyses are presented in chapter 8).

Several methods of deriving eddy diffusivity maps from image information should give more realistic estimates of the spatial/temporal non-homogeneities (and intermittencies in the Kolmogorov K62 sense obtained as spatial correlations of the turbulent dissipation, or from structure functions) and these values may be used to parameterise either sea surface turbulence or atmospheric turbulence at a variety of scales. It is possible that different fractal dimensions may be due to different levels of intermittency (and thus different spectra, which are not necessarily inertial nor in equilibrium). These techniques are helpful in providing more realistic estimates of spatial and temporal variations of the horizontal dispersion in the environment; which

reflect the influence of spectral energy distribution on local diffusivity in terms of a Generalized Richardson's Law by Castilla (2001). From a practical point of view, we consider that a fractal and multi-fractal analysis is useful as a link between laboratory experiments visualization and Satellite Remote sensing observations of the Earth.

A complex Parameter Space Using Ri, Ro, Re has been used to fit experimental and numerical observations on the Structure (and Topology) of the Stratified Rotating Flows. The Spectra change appreciable with slopes from 1.1 to 4, but relevant to dispersion, not only the Spectral slope is important (Generalised Richardson's Law) but the initial topology of the initial release (in Elliptical, Vortex core or Hyperbolic Regions dominated by shear). Using fractal geometry as well, we can establish now a theoretical baseline pattern for the turbulence behaviour that is reflected in the different descriptors (volume fraction, velocity and vorticity we can thus obtain a certain classification relating D_3 and the sum (integral) of the different fractal dimensions D_2 for different levels of scalar (volume fraction intensity or temperature). Vorticity evolution is smooth and quite different than that of volume fraction or density. The correlation between the local Ri and the fractal dimension detected from volume fraction, energy or entropy is good. Using multi-fractal geometry we can also establish certain regions of higher local activity used to establish the geometry of the turbulence mixing.

A taxonomy of changes in the equilibrium (or not) cascade may lead to more physically realistic (and understandable) models to parameterize the sub-grid scaling that has a important role be taken when interpreting the direct 3D Kolmogorov cascade and the Inverse 2D Kraichnan Cascade.

9.3. Discussion on energy decay in stratified flows

Previous studies have only assumed pure 2D turbulence and vortex conservation measuring the number of vortices as well as the area increase only on the simplest hypothesis; here we extend the arguments and results to spatially non-homogeneous flows with varying buoyancy. The parameterization of mixing is assumed also to affect the dominant vortex distribution, more information may be found in Peco (2009).

Using the spectral relationship from (Kolmogorov 1941) we have:

$$E(k) \approx C\,\varepsilon^{2/3}\,k^{-5/3} \tag{9.1}$$

We may relate kinetic energy and dissipation as:

$$k \approx C\,\varepsilon^{2/3} \tag{9.2}$$

So integrating the equation we obtain:

$$\frac{dk}{dt} = c(\varepsilon)\,k^{3/2} \tag{9.3}$$

which gives decay with both linear and quadratic terms that strongly depends on initial conditions, in particular with k_o.

On the one hand, from the stable stratification case; the aim is to explain and model the flat structure dynamics by the zigzag instabilities as precursors of quasi 2D or under the horizontal and vertical shear conservation arguments. This field is open to an anisotropy and non-linear statistic theory of ‘wave-vortex’, supported by the direct numerical simulations. Recent results of Lagrangian dispersion by passive tracers (couples) showed that diffusion looks dominated by the linear modes of movement, essentially anisotropic dispersive waves and the quasi-geostrophic modes. While the organized eddies from non-linear interactions play a minor role in the tracer trapping. Those results are found into other domains in the environment. Paradoxically the measurement of eddy structures is easy to visualize than the more elusive wave manifestations. A possible new research (for high Reynolds, low initial pair separation)

must allow to quantify the portion of organized eddies into the dispersion. Those studies would also give information on the force and time scales of the organized eddy structures and the specific promoter instabilities.

The values of the mixing efficiency are comparable with other experiments, but further work is needed to investigate the effect of intermittency on the mixing process. This is still in progress (Zouari and Babiano 1994, Linden et al. 1996, Carrillo et al. 2001 and Chen et al. 1996).

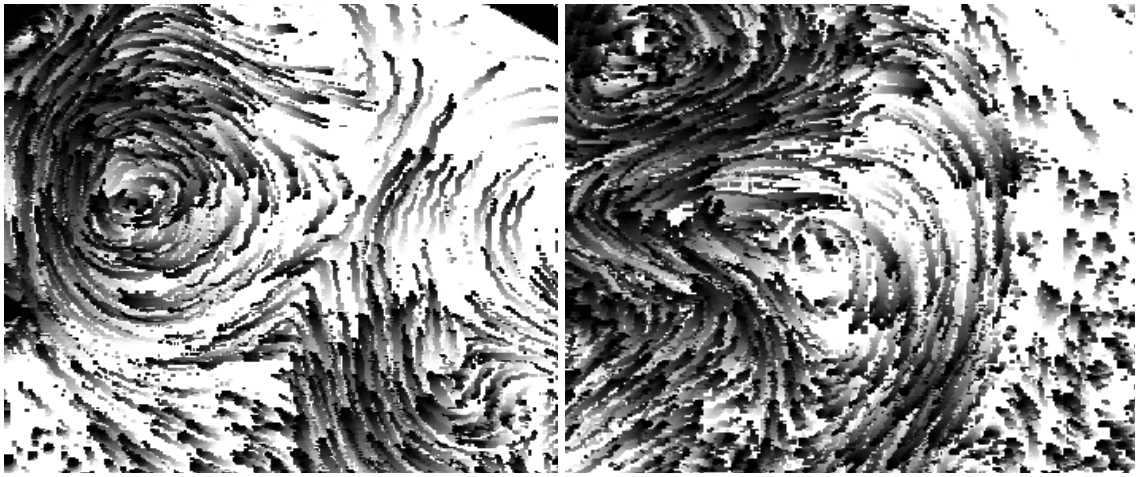

Figure 9.1: Example of particle tracking, following the pliolite tracers.

Here we want to understand and describe key aspects of the structure of the non-homogeneous turbulence affected by stratification and rotation, in particular to study the evolution of the background vorticity and their interaction with the dominant coherent structures such as the dominant vortices. Other effects connected with non-homogeneity (for example boundary layer - vortex interactions) are also studied. Figures 9.1 shows particle traces detected at the density interface from above. There are several techniques that are used to track the pliolite particles and produce the velocity and vorticity plots used to calculate spatial correlations and spectra (Zouari and Babiano 1994). Figure 9.2 shows the evolution of the vorticity scalar field as the turbulence decays after the passage of the grid in the strongly stratified interface. The dominant vortices can be studied as they interact, merge or break up.

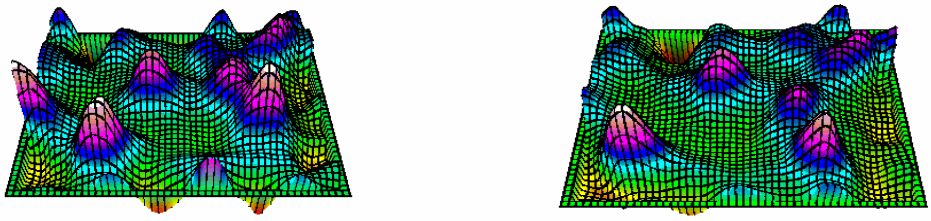

Figure 9.2: Example of 3D vorticity maps in false colour, the behaviour of the dominant vortices, seems much more complex than previously thought, showing non-local interactions.

As seen in non rotating experiments (Chapter 7), there is a clear interaction between the internal wave field and the domain size of the horizontal vortices for non dimensional times $NT\langle 5$. The growth in size of the decaying stratified vortices is controlled by the size of the experimental domain. When there is an external imposed length scale, it can be shown applying a simple equilibrium model with constant dissipation such as equation 9.2. That the energy decays as $K(t) = ct^{-2}$, but the role of the initial conditions and the influence of the stratification, which would include an extra buoyancy term, which modifies the evolution of both, the turbulence kinetic energy and the domain scales.

The role of coriolis induced inertial waves, as well as the buoyancy induced internal waves, are expected to influence most the inertial decay phase of the flow. So in order to modify global parameters as the mixing efficiency, the control of the inertial conditions seems much more important than the previous thought (Turner 1973).

The energy spectrum for two-dimensional N-point vortex systems is also estimated. The system in an infinite plane is considered. We focus our attention on the energy spectrum of the system “in equilibrium” in the grid oscillating experiments and “in a transient state” in the stratified decay of turbulence at a sharp density interface. For like-sign point vortex systems in a plane determined by the PIV system, we have succeeded in deriving a scaling law of the energy spectrum $E(k) \sim k^{-p}$ for the intermediate k regime, via the 2-point correlation function $R_2(r)$. However, the

applicability of the derived scaling law is limited by the validity of the asymptotic expansion used. By a direct numerical simulation, we have obtained (Liechtenstein et al 2006, Redondo et al. 2009) various powers $p = 2.11 - 3.19$ for transient states. With the quasi-equilibrium state hypothesis we find that the energy spectrum in the intermediate regime does not obey a power law. It is concluded that for point vortex systems in a plane, the scaling law of the energy spectrum in equilibrium and in the transient state depends on the system parameters, and does not seem universal.

The stated features are seen in the simple non-rotating uniform experiments, and further work will investigate multifractal and scaling behaviour of the vortices in stratified flows with and without rotation as well as implementing more realistic boundary conditions in the experiments.

There is a relationship between the length scales l as the integral length of the turbulence at the stirred side of the tank or its thickness and the local Ri and the vertical extent of the interface λ_I as:

$$\lambda_I = c\, l\, Ri^{3/2} \tag{9.4}$$

with c being a constant of order unity (Redondo 1987).

Even when there is no rotation, the collapse of turbulence due to buoyancy forces generates horizontal vortices (for more information see Hopfinger and van Heijst 1993 and Fernando 1991) for discussions on rotating and stratified flows. We present results on experiments where stirring in a stratified fluid takes place non-uniformly and vortices are formed as a result of a transfer of horizontal to vertical vorticity.

The eddy diffusivities in geophysical flows exhibit a large variation and show a marked anisotropy, not only horizontal values are much larger than vertical ones but there is a strong dependence on the spatial extent of the tracer dye or pollutant and at larger scales the topology of the basic flow is very important.

Those features are seen in the simple non-rotating uniform experiments, and further work will investigate multifractal and scaling behaviour of the vortices in stratified flows with and without rotation as well as to implement more realistic boundary conditions in the experiments like grid and jet stirring from the sides.

A sequence of pliolite particles showing tracks after the horizontal traverse of the grid across the sharp density interface is seen in figure 9.1. Several parameters may be

calculated, such as the turbulent energy dissipation ε, that also depends on the length scale, introducing the notion of intermittency μ, as it varies from approximately 0.2 to 0.7, even in different homogeneous and stationary experiments. The new energy spectra $E(k)$, needs a correction term in its power of $k: -5/3$ becomes $-5/3-\mu/9$, thus, the global form of the spectra is $E(k) \sim k^{-p}$. An interesting approach, relating the Fractal dimension, the intermittency and the spectral exponent is to find relationships that may be used to parameterise the sub-grid turbulence in terms of generalized diffusivities that take into account the topology and the self-similarity of the mixing and dispersive flows. Relationships between the diffusivity, the spectral exponent *p*, the intermittency μ, and $D(q)$, may be found for the volume fraction or the concentration, at the same time other locally measured parameters such as the Enstrophy or the gradient alignment as well as their multi-fractal structures seem to be physically relevant indicators of the local turbulence and the mixing.

The structure of non-homogeneous turbulence affected by stratification and rotation is investigated both by means of laboratory and numerical experiments. The experiments are used to quantify the different types of dominant instability and the topological aspects of the turbulent cascades detected both horizontally and vertically. Grid turbulence in a rotating stratified two layer system is measured with PIV and sonic anemometry. Observations of the horizontal velocity energy spectra as well as structure functions are used to estimate local intermittency and tracer dispersion. Numerical experiments using both Direct Numerical Simulations (DNS) and Kinematic Simulations (KS) are used to interpret some results in the context of a generalised Richardson's Law affected both by intermittency and by coherent structures (see figure 9.3), which in the experiments scale with the Rossby deformation Radius.

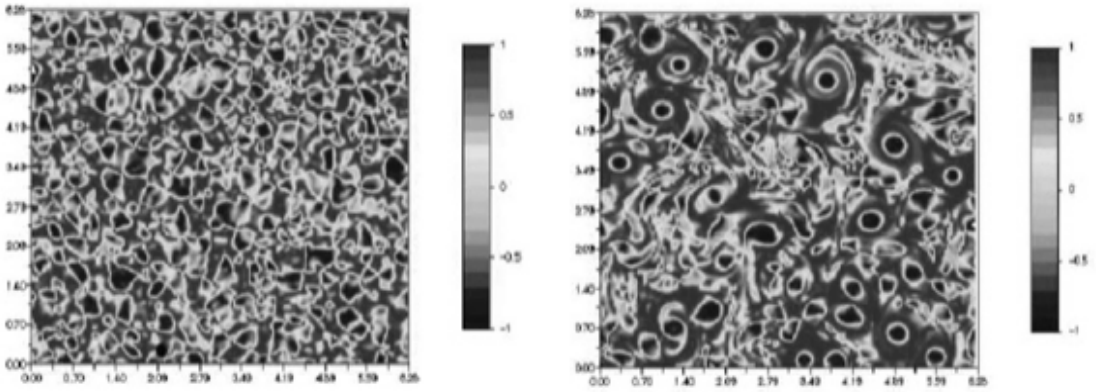

Figure 9.3: Comparison of a KS and a DNS with similar spectra (Castilla et al. 2007)

The decay and interaction of grid wakes affected by stratification (and rotation) generates a combination of eddies and straining regions that grow in time and with distance from the turbulence source, but a change in decay law is observed when internal (or inertial) waves set in at $Nt = 3-4$ which reach maximum complexity and local mixing efficiency before the front reaches the end walls. There are much possible instability that may modify the cascade process and the energy redistribution among different eddy sizes. Normally both inverse and direct energy and enstrophy cascades take place at the same time, with a dominant inverse cascade in 2D flows. Both cases are studied analyzing mixedness, as well as the third order structure functions, that indicate strong inverse cascades towards the large scales producing spectral variations. The mixing processes are compared by mapping the different intermittency and the multifractal scaling in the vortex and tendril arrays.

New interest has emerged concerning the scaling properties of non-homogeneous turbulence flows and their relation to mixing and dispersion. They are reflected in the scale invariance of Navier-Stokes equations, both in two dimensions (2D) and three dimensions (3D).The statistical behaviour of two-dimensional and three-dimensional fully developed turbulence has been intensively investigated in the homogeneous cases. A common way to approach the study of energy scale to scale transfer is through the velocity structure functions. Usually studies the scaling properties of moments of velocity differences at the scale r, if $L \rangle r \rangle\rangle \eta$, where the L is the integral scale, η is the dissipative (Kolmogorov K41) scale, with the dissipation calculated in the usual way.

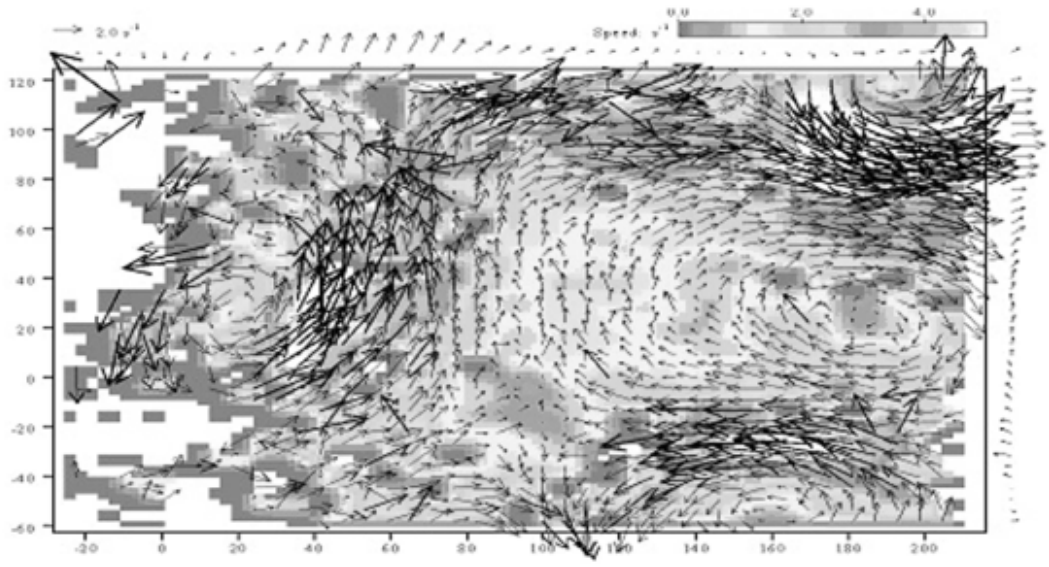

Figure 9.4: Particle tracking revealing the structure of the flow

In general, one can define the scaling exponents of the structure functions in the inertial range as seen above, that predicts that the statistical properties of the velocity depend only on ε and *the local scale*, it then follows by dimensional analysis that the scaling exponents are linear $\xi/q = q/3$, but in many experimental and numerical simulation at very high Re, has show that Kolmogorov scaling is violated and that the scaling exponents are nonlinear function of *q*. From a practical point of view, the inertial range is defined by the range of scales where the third-order structure function follows the K41 law, It is precisely in this region where a fractal behaviour or either the velocity or of any adverted scalar should be detected clearly.

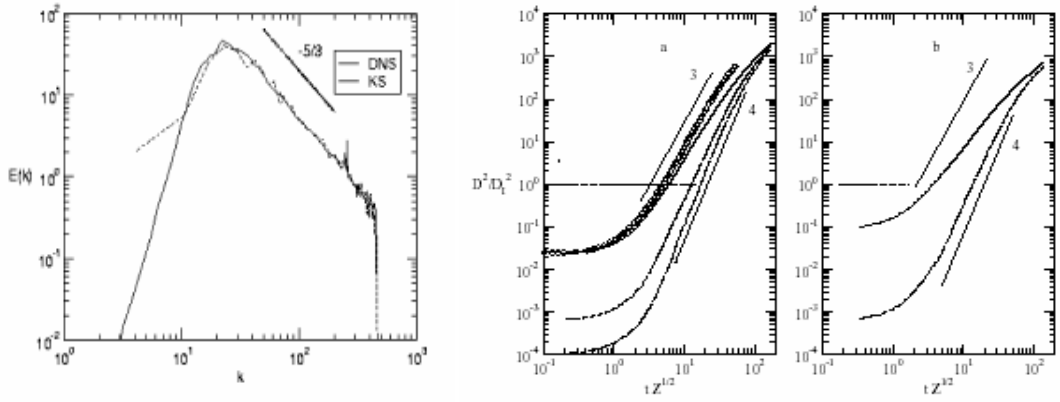

Figure 9.5: (left) Energy spectra of the simulations. (right) Particle tracer separation in time showed as the slope of the Richardson time exponent. (Castilla and Babiano 2007)

9.4. Topology of the Vortex Interaction

When the Reynolds number is larger, the inertial range is broader but for the low to moderate Reynolds numbers accessible to direct numerical resolution, this range is often very narrow. In these cases we may apply The Extended Self- Similarity ESS as a property of velocity structure functions in turbulence (Benzi et al. (1992, 1995) and Mahjoub et al 1989). It states that when the moments are plotted against another, then the scaling is much more pronounced. In the other words, the ratio of two scaling exponents stays constant for a wider range of scales than each of them does when taken separately. The ESS scaling comprises not only the inertial range, but also reaches as far down as few Kolmogorov scales, so we may compute the scaling exponents with much higher accuracy even at relatively moderate Reynolds numbers. It is important to compute higher order moments of the flow velocity because spectra do not reflect structure. Figure 9.6 shows vorticity and shear 2D turbulence maps obtained by KS and DNS, and have similar spectra shown in figure 9.5 (left) and although the structures have similar sizes they are very different. It can be numerically shown that the spectral slope strongly affects Richardson's dispersion Law (Richardson (1926) and Castilla et al. (2009)).

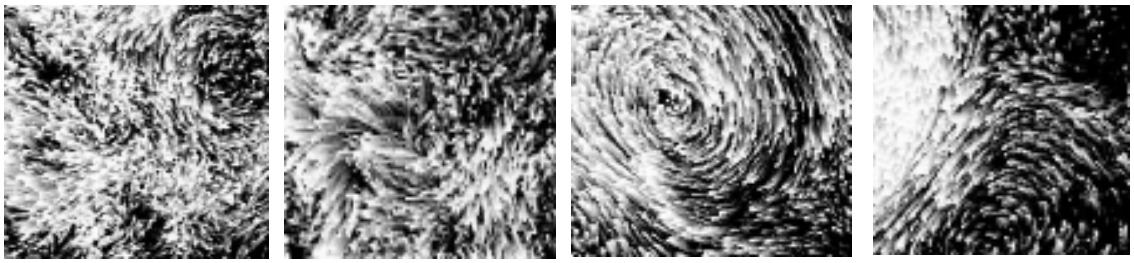

Figure 9.6: Different topological structures that characterize dispersion (left to right) Quadripole structure, Wave-Vortex interaction, Isolated Eddy. And Dipolar shear front. (See Appendix 3)

Another important feature of ESS is that it provides information in terms of the relative scaling exponents, which are more universal in that they remain valid also in a 2D case. But this kind of scaling universality often disappears if the flow is non-homogeneous, The scaling exponents of up to 6th order are calculated, details on the procedure is shown for different experiments in Mahjoub et al.(1998). In this case, for vertical flows under non-homogeneous conditions, we are able to obtain a better

quantification of the intermittency using ESS in a 2D section of the flow. The relationship between intermittency and the fractal dimension of the structures is obtained using the sixth order structure function using: $\mu(i) = 2\xi_3 - \xi_6$ even if $\xi_3 \neq 1$, in a similar way, the fourth order structure function may also be used ($\mu = 2/3 - \xi_4$). The Anomalous dispersion detected in figure 9.5 (right) numerically is often associated to coherent structures as those particle tracking in figure 9.6. Fractal measurements of the vorticity and scalar tracers can also be used to map intermittency in a simpler way and also relate these spectral measures to the maximum fractal dimension as shown in chapter 5.

9.5. Models of Vortex Evolution

If we use a diffusion-reaction equation with two terms indicating the diffusion of the number of vortices and theirs destruction due to merging, annihilation as other causes related to internal or inertial wave interaction as:

$$\frac{\partial N_o}{\partial t} = \frac{\partial}{\partial x}\left(\nu_\omega \frac{\partial N_o}{\partial x} \right) - c\left(Ri, R_o\right) N_o{}^2 \tag{9.5}$$

with $\nu_\omega(\mathrm{Re})$ a vortex diffusivity and $c\left(Ri, R_o\right)$ as term indicating the "catalytic" effect of body forces on vortex-vortex merging. It is easy to see that we may apply this equation to either isolated vortices or to vortex dipoles at point zero circulation Γ. For a single vortex, even a point one. Γ May be expressed as $\Gamma = \pi r^2 \omega$ (Baumert 2009) with r the size and ω the vorticity. A special family of vortices which comply with $u^2 = r^2 \omega^2$ are called vorticons so that their energy is finite and $\omega = \pm \frac{u}{r}$. With three conditions we can define the total energy k and enstrophy ω^2 as:

$$k = \sum_i^{N_o} \frac{1}{2} r_i^2 \, \omega_i^2 = N_o \, \overline{k} \tag{9.6}$$

and

$$\omega^2 = \sum_i^{N_o} \frac{1}{2} \, \omega_i^2 = N_o \, \overline{\omega}^2 \tag{9.7}$$

The average or effective radius R_ω is defined as:

$$R_\omega{}^2 = \frac{2k}{\omega^2} = \frac{2\overline{k}}{\overline{\omega}^2} \tag{9.8}$$

It is interesting to introduce the Van Karman constant $\kappa \approx \frac{1}{\sqrt{2\pi}}$ relating vortices ω and angular period or turn over time T as $\omega = \frac{1}{\kappa^2 T}$ and then the dissipation can be estimated as

$$\varepsilon = \frac{k}{T} = \bar{k}\,\bar{\omega}\,N_o^{\,2} \tag{9.9}$$

If we use a mean free path for the vortex motion: λ_ω, and a time between vortex mergers or destruction, z, then the vortex eddy diffusivity us $\nu_\omega = \frac{\lambda_\omega}{2\tau}$ with $\tau = \frac{\lambda_\omega}{u}$ and the speed is $u = \sqrt{2k}$.

We now assume that the mean free path of the vortices before interacting is proportional to their radius initially but will also depend on the Brunt – Väisälä frequency (as the Richardson number) as time evolves and λ_ω is larger as N_o decreases as $N_o \propto t^{-\chi}$ as shown in § 7.4 then $\lambda_\omega = R_\omega$ so:

$$\lambda_\omega = \sqrt{Rig\,N_o} = Ri^{1/2}\left(\frac{t}{t_o}\right)^{\chi/2} \tag{9.10}$$

The number of vortices will evolve in time but will both help to converse energy and vorticity so

$$N_o = \frac{k}{\bar{k}} = \frac{\omega}{\bar{\omega}} \tag{9.11}$$

if $c(Ri, R_o)$ is constant both for energy and vorticity (i.e. no interaction between waves and vortices), then

$$\frac{dk}{dt} + c'(Ri, R_o)k^2 = 0 \tag{9.12}$$

and

$$\frac{d\omega}{dt} + c^{"}\left(Ri, R_o\right)\omega^2 = 0 \tag{9.13}$$

with solutions $k(t) \propto t^{-1}$. This is not realistic because we have seen that

$$k(t) = \frac{1}{t^2 + t} \tag{9.14}$$

even in an homogenous flow so at least it is necessary to keep both kinetic energy diffusion and vorticity/enstrophy diffusion. This effective diffusion, following Baumert (2009) will be considered to be the same for the energy k and for enstrophy ω^2 so

$$\nu_k = \nu_\omega = KT \tag{9.15}$$

leading to a set of equations similar to the $k-\omega$ model of Wilcox (et al. 2006)

$$\begin{aligned} &\frac{\partial k}{\partial t} - \frac{\partial}{\partial x}\left(\nu_k \frac{\partial k}{\partial x}\right) = \nu_k\left(s^2 - \omega^2\right) \\ &\frac{\partial \omega}{\partial t} - \frac{\partial}{\partial x}\left(\nu_\omega \frac{\partial \omega}{\partial x}\right) = \frac{1}{2\pi}\left(s^2 - 2\omega^2\right) \end{aligned} \tag{9.16}$$

being s the local shear $s = \left|\frac{du}{dx}\right| = \frac{\overline{u_i^{'} u_j^{'}}}{\nu_k}$ for N_o, k and ω the above equations lead to power laws which would have a complex spatial dependence on the flow topology $s(x.y)$, $\omega(x,y)$ and also on the levels of buoyancy (Ri) and on Rotation (R_o). It is clear that an inverse cascade exists as the energy decay and the vortex length scales increase as both the energy and the vorticity decrease.

Comparing the simple quadratic homogenous model:

$$\frac{dk}{dt} + c^{'}\left(Ri, R_o, t\right)k^2 = 0 \tag{9.17}$$

with

$$\frac{dk}{dt} + c\,k^{3/2} = 0 \tag{9.18}$$

described in Matulka et al. (2008) and above, having used that $\varepsilon = \frac{k^{3/2}}{L}$.

Using variable separation and integrating

$$\int_{k_o}^{k(t)} \frac{dk}{k^2} = \int_{t_o}^{t} c^{'}\left(Ri, R_o, t\right)dt \tag{9.19}$$

We may model in a simple way the effect of internal waves on the vortex and energy decay. Probably function $c^{'}\left(Ri, R_o, t\right)$ will have a non-linear dependence in time, especially after $Nt \geq 5$, when grid turbulence begins to collapse (Fraunie et al. 2008). But let as consider two cases:

a) indicating that the decay increase in time due only to internal waves

$$c^{'}\left(Ri, R_o, t\right) = Ri\,t \tag{9.20}$$

and

b) indicating that internal waves dye out and stop affecting energy

$$c^{'}\left(Ri, R_o, t\right) = \frac{Ri}{t} \tag{9.21}$$

case a) leads to

$$k(t) = \frac{1}{\frac{1}{k_o} - \frac{Ri}{2}\left(t - t_o\right)^2} \tag{9.22}$$

while assumption b) leads to

$$k(t) = \frac{1}{\frac{1}{k_o} - Ri \ln \frac{t}{t_o}} \tag{9.23}$$

Both of these functions fit the strong decay of the number of vortices presented in chapter 7, but care is needed with the values of the initial energy and a virtual time to avoid the singularities when the denominator is zero.

The behaviour of the number of vortices can be modelled using an Onsager type (Onsager 1949, Redondo 2003) equation such as

$$\frac{\partial N_o}{\partial t} + c(Ri, R_o, t) N_o{}^2 - \nu_\omega \nabla^2 N_o = 0 \tag{9.24}$$

If we use the wave equation on the vortex number assuming a strong interaction between the point-like vortices and the internal waves moving along the density interface as

$$\frac{\partial^2 N_o}{\partial t^2} = V_o{}^2 \nabla^2 N_o \tag{9.25}$$

we can solve a non-linear damped oscillation type of equation such as

$$\frac{\partial^2 N_o}{\partial t} + 2\beta \frac{\partial N_o}{\partial t} + o N_o = 0 \tag{9.26}$$

where

$$\beta = -\frac{V_o{}^2}{2\nu_\omega} \tag{9.27}$$

and

$$o = -\frac{c(Ri, R_o, t)V_o^{\,2}}{\nu_\omega} \tag{9.28}$$

The above equation solution will depend on the relative values of β and o. We will discuss some of the possible types of solution using an analogy with a damped oscillation with a variable natural frequency $\omega_o^{\,2} = o\,N_o(t)$. The three basic types of solution are:

a) If $\beta^2 = c\,N_o(t)$ there will be a critical experiential decay such that

$$N_o(t) = N_o(t)e^{-\left(\frac{c(Ri,R_o,t)V_o^{\,2}N_o(t)}{\nu_\omega}\right)^{1/2}t}(t-1) \tag{9.29}$$

b) When $o\,N_o(t) \rangle \beta^2$ then a damped oscillation could occur providing the oscillation takes place around the average number of vortices $N_o(t)$ such that

$$N_o(t) = N_o(t)e^{-\beta t}\cos\omega' t \tag{9.30}$$

With

$$\omega' = \left(c(Ri, R_o, t)N_o(t) - \frac{V_o^{\,4}}{4\nu_\omega}\right)^{\frac{1}{2}} \tag{9.31}$$

This type of solution is sketched in figure 9.7.

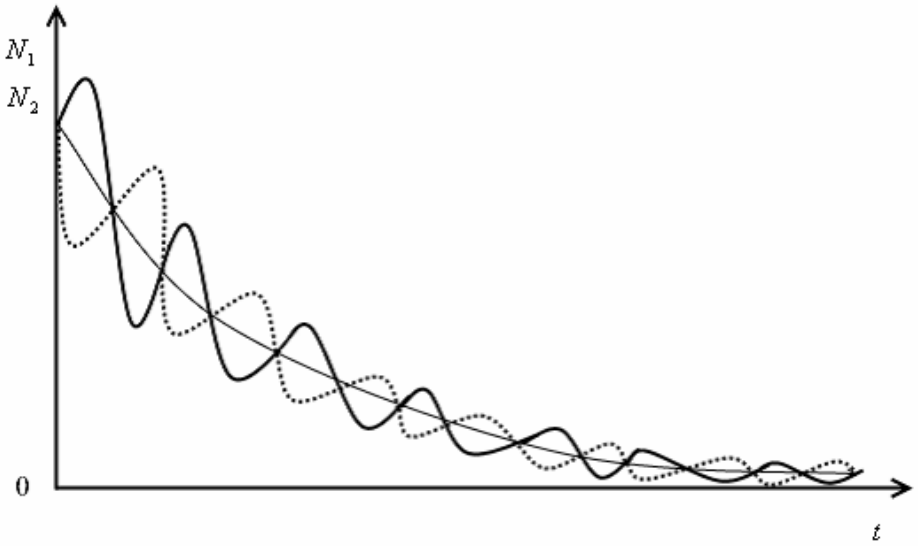

Figure 9.7: Possible type of oscillatory decaying solution for the number of vortices

In the final stages of the decay when $N_o(t)$ is very low, t then the only possible solution is a strong exponential decay.

c) When $o\, N_o(t) \langle \beta^2$ the solution is

$$N_o(t) = N_o(t) e^{(\beta^2 - \omega_o{}^2)^{1/2} t} + b\, e^{-(\beta^2 - \omega_o{}^2)^{1/2} t} \tag{9.32}$$

with b dependent on initial conditions.

It is also interesting to investigate the separate behaviour of the larger and smaller vortices within the decaying flow. If we consider only the interval where the total number of vortices is very large and we denote $N_1(t)$ the t large vortices and $N_2(t)$ the smaller vortices we have $N_o(t) = N_1(t) + N_2(t)$ and assuming that vortex viscosity is small then

$$\frac{\partial N_o}{\partial t} = c(Ri, R_o, t) N_o{}^2 \tag{9.33}$$

we can again consider a W.K.B. type of approximation, like assuming $\omega_o^{\,2} = c\,N_o$ in the oscillating case and use a generalised Volterra-Lotke equation (Volterra et al. 1931) given by Kolmogorov (et al. 1936) as

$$\begin{aligned} \frac{dN_1}{dt} &= c\,N_o(t)K_1(N_1,N_2)N_1 \\ \frac{dN_2}{dt} &= c\,N_o(t)K_2(N_1,N_2)N_2 \end{aligned} \tag{9.34}$$

where $K_1(N_1,N_2)$ and $K_2(N_1,N_2)$ are empirical functions based on the topological interactions between large and small vortices which are modulated or coupled in a non-local fashion by the internal wave field. More detailed observation and analysis is needed on the taxonomy of the different vortex-wave interaction, a possible solution is sketched in figure 9.8, with different coefficients indicating that vortices of different sizes merge in very different ways, for example if a big vortex interacts with several small closeby vortices much more enegetically (i.e. faster) than a small vortex with several large vortices. It seems from the detail analysis of the experimental evolutions of the stratified non rotating flows of chapter 7 (as well as in the rotating stratified experiments) that it is easier for a large vortex to absorb a small one that the other way round. Just like in the bio-taxonomical interactions where *"A big fish eats the smaller ones"*.

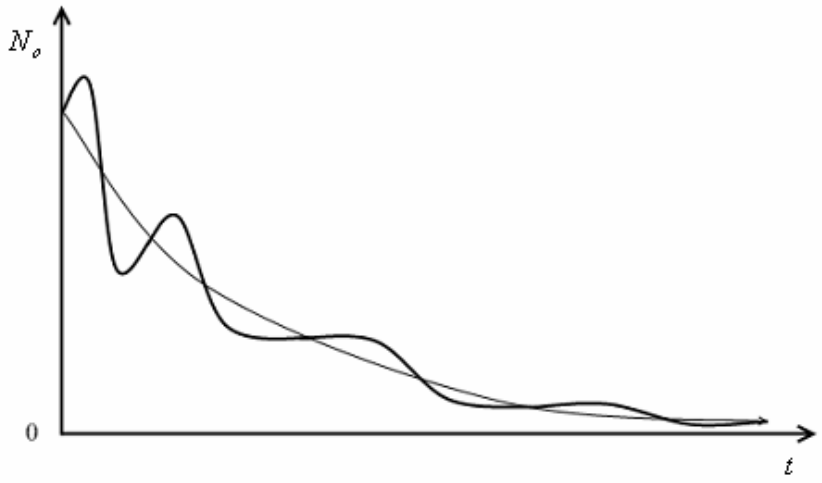

Figure 9.8: Oscillations in the numbers of big and small vortices as they follow a general oscillatory decay in a stratified and/or rotating flow.

CHAPTER 10

Conclusions

10.1. General Conclusions

Laboratory experiments on mixing in a rotating stratified fluid are essential for the development of computer models of geophysical phenomena, because, if better predictions are to be made, the distributions of potential and kinetic energy have to be correctly assessed for each process under study. Oceanic and atmospheric flows due to their high Reynolds numbers, may be considered as turbulent motions under the constraints of geometry, stratification and rotation. At large scales these flows tend to be along isopycnal surfaces due to the combined effects of the very low aspect ratio of the flows (the motion is mostly confined to thin layers of fluid) and the existence of stable density stratification. The effect of the Earth's rotation is to reduce the vertical shear in these almost planar flows. The combined effects of these constraints produces approximately two-dimensional turbulent flows termed also as geophysical turbulence.

In a strictly two-dimensional flow with weak dissipation, energy input at a given scale is transferred to larger scales, because these constraints stop vortex lines being stretched or twisted. Physically this upscale energy transfer occurs by merging of vortices and leads to the production of coherent structures in the flow that contain most of the energy. This process seems to lead to the appearance of order from chaos. This scenario is an attractive model for geophysical flows which are known to contain very energetic vortices; these are often the source of helical instabilities that lead to tornados and hurricanes. The mesoscale oceanic eddies and atmospheric highs and lows typical of the weather patterns show an accumulation of energy at the dominant length scale given by their equilibrium Rossby deformation Radius. This scale marks where and when the rotation induced Coriolis forces are in equilibrium with the effect of buoyancy. The upscale transfer of energy is inhibited at the Rossby deformation scale by baroclynic instability at larger scales, which accounts for the dominant observed size of geophysical vortices. Different regions of the parameter space based on the local versions of the Reynolds number, the Richardson number and the Rossby number are used to compare both laboratory observations and field data.

The main goal of the presented work was to show the differences in topology due to buoyancy (and also to rotation) in the structure of complex realistic flows in the laboratory and in the environment such as those presented in chapter 8 detected by SAR satellite images in the ocean. The experimental results and the theory presented

about 2D turbulence needs to be modified because we shoe clearly that the experiments in chapter 7 do not agree with “pure” 2D flows. Different new theories are as discussed in chapter 9. We detect also clear differences between the decay process in stratified fluids and rotating fluids.

In a rotating fluid the frequency 2Ω and in a stratified fluids the buoyancy frequency N, play analogous roles. Both can be shown by a crude argument to be the angular frequency with which a displaced particle oscillates; and both are the upper limit of the angular frequency range for which waves can occur. The relationship between the role of the Rossby number in a rotating fluid and that of the Froude number in a stratified fluid is known if we write the latter in the form (Froude number, which is defined in chapter 2)

$$Fr = U/LN$$

When both stratification and rotation are present, their relative importance is indicated by the parameter

$$S = N/2\Omega = 1/\alpha$$

A value of *S* around 1 indicates that stratification and rotation have comparable influences; when *S* is small, one is dealing with a rotating flow modified by stratification, and when *S* is large it is the other way round.

It is very interesting that the spectral measurements in both stratified and rotating flows are close to the 3D value p= 5/3 but as either stratification or rotation dominates, then in both cases the flow becomes more non-local, in the sense that the flow in a plane horizontal flow becomes more and more dominated by either “blini” or “pancake” shapes in the case of stratification and ¨columnar vortices¨ in the case of strong rotation.

We show in figures 10.1, 10.2 and 10.3 numerical results of the evolution of a decaying stratified and rotating flow as a function of the parameter described above α results from the thesis of Liechenstein (2006) and Cambon et al. (2004).

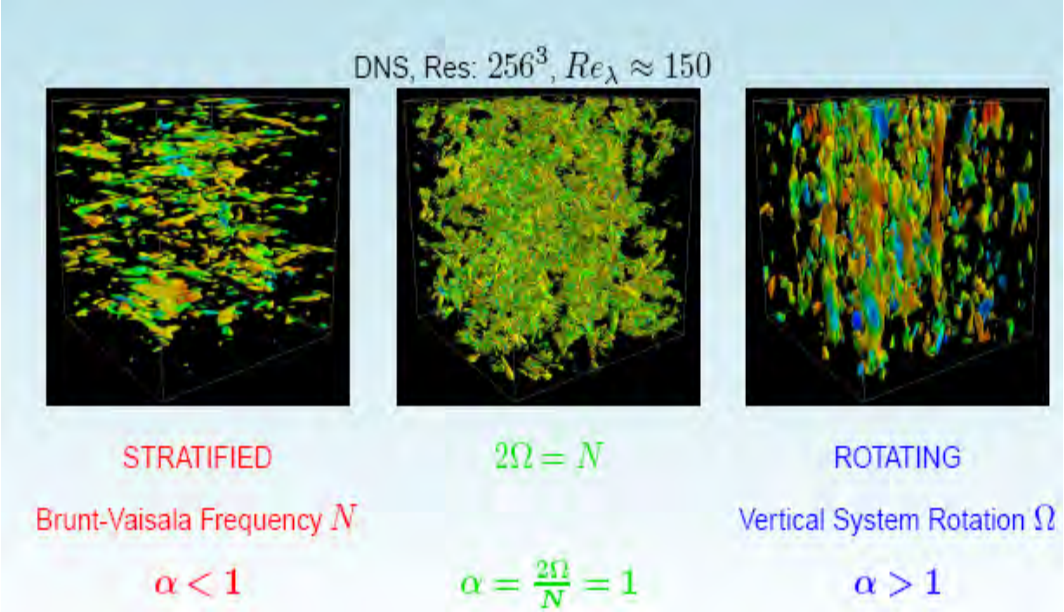

Fig. 10.1: final structure of the decay of a rotating-stratified flow in a box for different values of α .

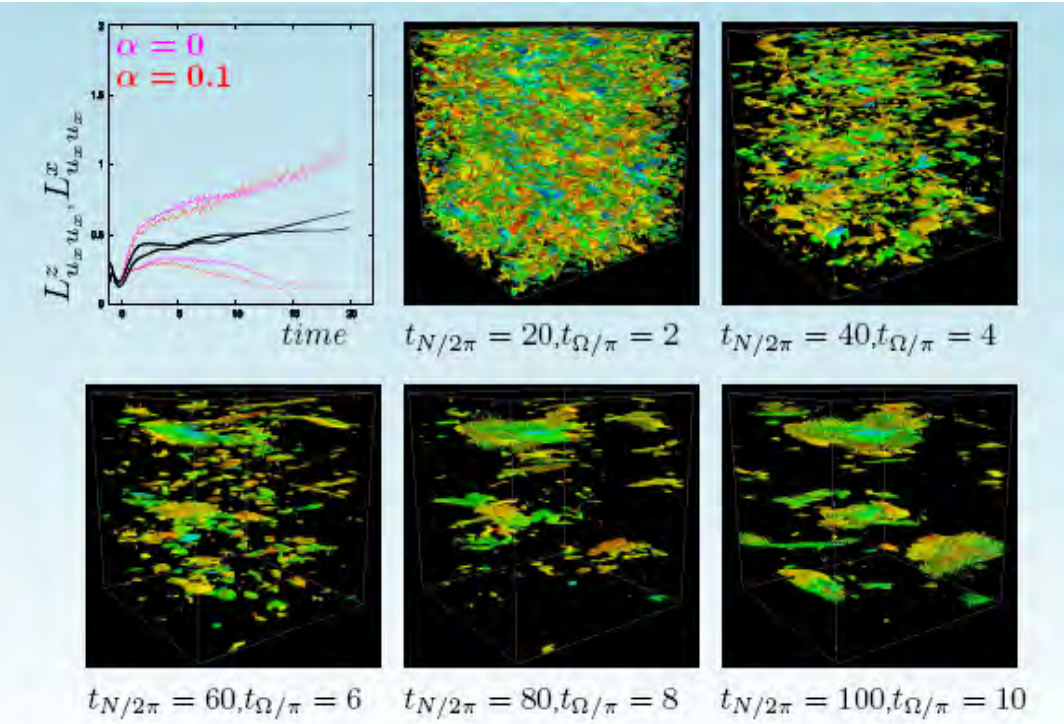

Fig. 10.2: Evolution of the structure of the decay of a stratified flow for different values of α .

Figures 10.2 and 10.3 show the evolution of the integral length scales in vertical and horizontal planes and the structure of the flow for different non-dimensional times.

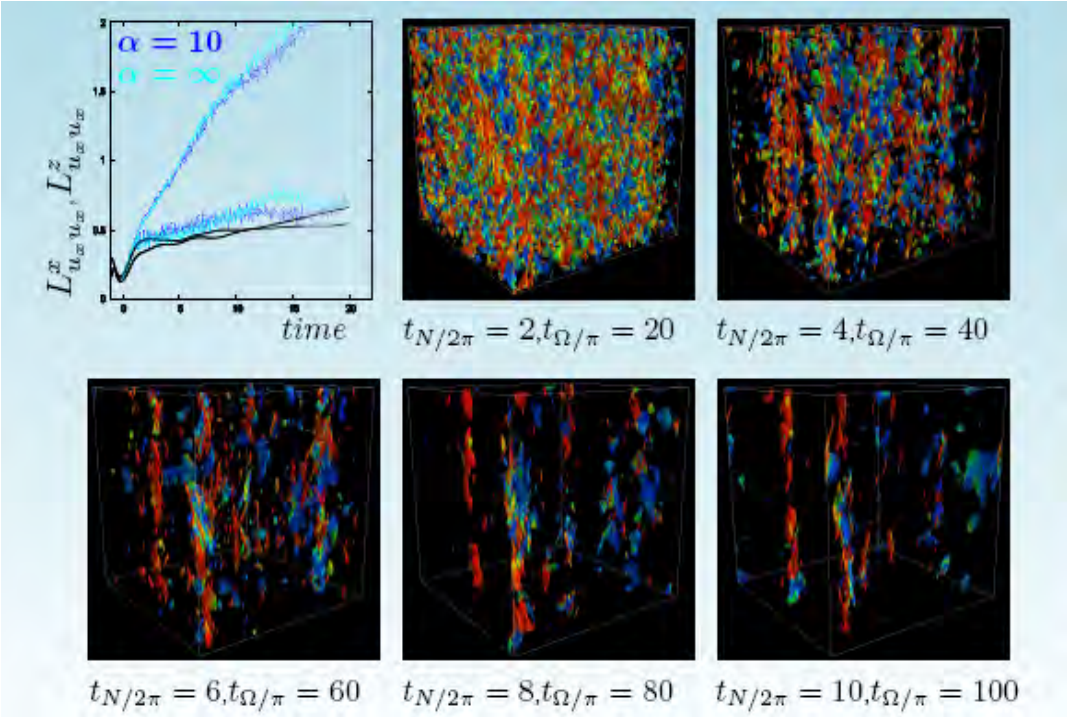

Fig. 10.3: final structure of the decay of a rotating-stratified flow for different values of α .

We have also seen in the experiments made without rotation the dramatic effect that a strong density interface has both on vertical and horizontal mixing. The effect of density interfaces also tends to spread further the non-homogeneous lateral mixing akin to that taking place near the coastline. An intrusion spreading along the initially sharp interface generates strong vertical vorticity. Matulka (2003)

The evolution of such non-homogeneous mixing has been discussed in Redondo et al. (1995). Even when there is an overall large scale coastal type of current as in the experiments of Carrillo et al. (2001), the front grows in time as shown in chapter 7 and in appendix 6 and may even destroy the overall large scale circulation creating a new pattern of eddies of multiple sizes.

Several methods of deriving eddy diffusivity maps from image information should give more realistic estimates of the spatial/temporal non-homogeneities (and intermittencies in the Kolmogorov 62 sense obtained as spatial correlations of the turbulent dissipation, or from structure functions) and these values may be used to parameterize either sea surface turbulence or atmospheric turbulence at a variety of scales. It is possible that different fractal dimensions may be due to different levels of intermittency (and thus different spectra, which are not necessarily inertial nor in equilibrium). These techniques of visual evolution of the structure functions of velocity

differences and of fractal dimension evaluation, are helpful in providing more realistic estimates of spatial and temporal variations of the horizontal dispersion in the environment; which reflect the influence of spectral energy distribution on local diffusivity in terms of a Generalized Richardson's Law.

A complex Parameter Space using Ri, Ro, Re may be used to fit experimental and numerical observations on the Structure (and Topology) of the Stratified Rotating Flows (Matulka et al. 2009). The Spectra change appreciable with slopes from 1.1 to 4, but relevant to dispersion, not only the Spectral slope is important (Generalized Richardson's Law) but the initial topology of the initial release (in Elliptical, Vortex core or Hyperbolic Regions dominated by shear). Using fractal geometry as well, we can establish now a theoretical baseline pattern for the turbulence behavior that is reflected in the different descriptors (volume fraction, velocity and vorticity we can thus obtain a certain classification relating D3 and the sum (integral) of the different fractal dimensions D2 for different levels of scalar (volume fraction intensity or temperature). Vorticity evolution is smooth and quite different than that of volume fraction or density. The correlation between the local Ri and the fractal dimension detected from volume fraction, energy or entropy is good. Using multi-fractal geometry we can also establish certain regions of higher local activity used to establish the geometry of the turbulence mixing.

In figure 10.4 we plot in a log-log parameter space of $\left(Ro^{-1}, Ri\right)$ some of the experiments performed at the Trondheim Rotating table, the size of the cross is proportional to the measured Rossby deformation Radius.

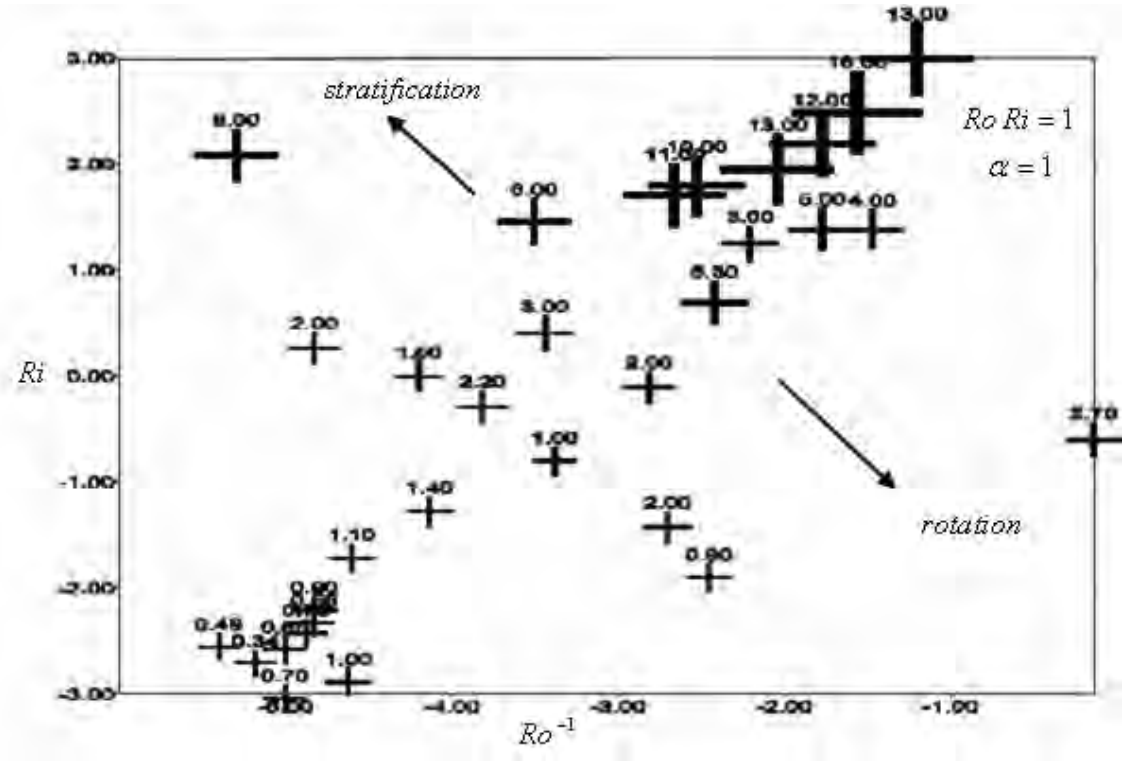

Figure 10.4: Parameter map of the experiments done in the Trondheim Rotating Table. The crosses are proportional to the Rossby Deformation Radius, when $R_o Ri = 1$ than buoyancy and Coriolis forces are in equilibrium.

To incorporate most of the previous experiments performed in sheared and zero-mean flow turbulence Redondo (1990) and Redondo (2004), we plot in a 3D parameter space the different regions with their most common instabilities (figure 10.5). For different Reynolds numbers the diagonal of the Richardson and inverse Rossby number indicates when stratification and rotation are in equilibrium. This has been seen in small scale experiments and the results of chapter 8 of large vortices in the ocean surface indicate that similar behavior could be extrapolated in the three dimensional plot towards largest Reynolds number, on the other hand the behavior on non-rotating mixing experiments shows an intermediate parameter range which is dominated by Holmboe type of instabilities, while for smaller Richardson number Kelvin Helmoltz billows dominate with a higher mixing efficiency. For very high Richardson number internal waves dominate the flow. There is a large unexplored region in this parameter space when both Richardson and Reynolds numbers are large but the Rossby number is small.

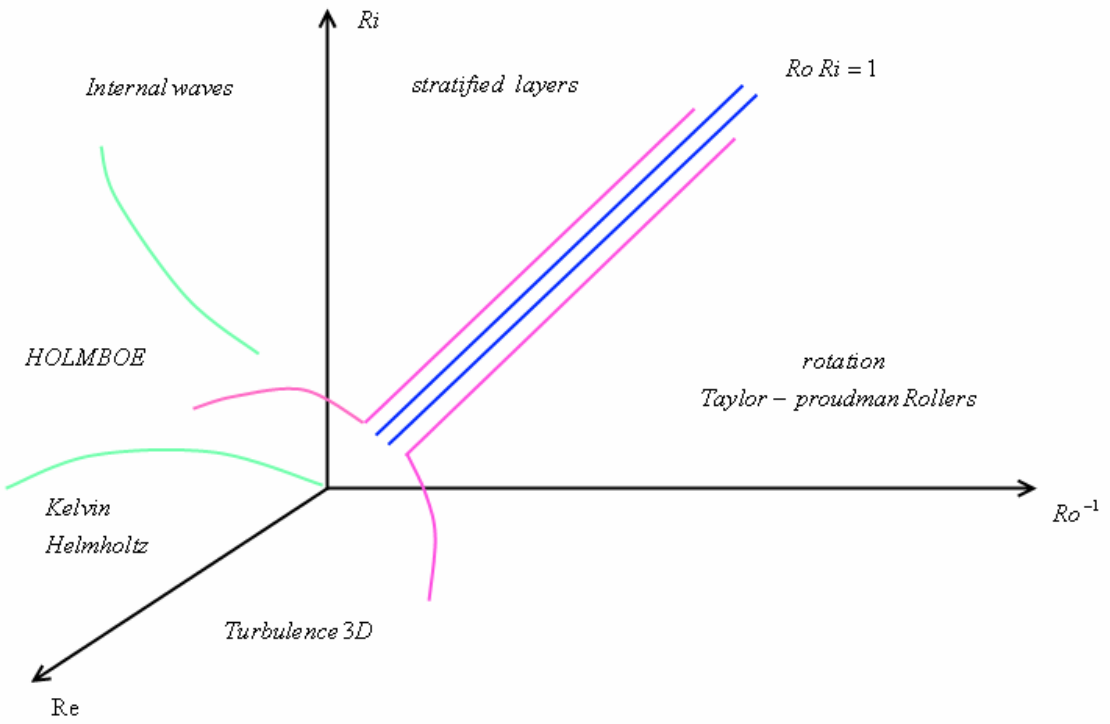

Figure 10.5: Three dimensional, complex parameter space of the appearance of the dominant instabilities that lead to mixing for rotating-stratified flows at different scales, the non-rotating parameter space (Re, Ri) is described in Fraunie et al. (2008).

A taxonomy of changes in the equilibrium (or not) cascade may lead to more physically realistic (and understandable) models to parameterize the sub-grid scaling that has a important role be taken when interpreting the direct 3D Kolmogorov cascade and the Inverse 2D Kraichnan Cascade.

The experiments, whose results are shown in chapter 7, are mostly non-rotating, the rotating experiments discussed in the publications and annexes and the observations of vortices and other features in the ocean surface have in common their non-homogeneous and non steady behavior (decay) and we describe and highlight some of the experimental and theoretical results of this thesis and the conclusions in the several specific issues investigated. More information is available in annexes and in the published and submitted papers.

10.2. Conclusions on the vortex structure and evolution

As described in chapter 7 and 9 the decay of vortices in a stratified media is quite different to that of a pure 2D flow. The decay of vorticity PDF's and the oscillations in the area covered by either positive or negative vorticity show clearly that the frequency increases in time. Another important new observation is that the decay process is different for vortices with different levels of maximum vorticity. For very stratified flows identified by their high Richardson number, the decrease in peak vorticity decreases much faster than in the non stratified flows.

By comparing both the evolution of the vorticity and enstrophy PDF's in time, we have noticed that the period of the oscillations caused by buoyancy increases in time as it also exhibits decay. This decay has been shown to be much more complex in flows affected by body forces than in pure, theoretical 2D flows. It has been observed, and validated recently by Lacasce (2008) that the number of vortices and their areas are related, but that the conditions depends strongly on the type of dissipation in the vortex number equation. The vorticity decay, in a similar way as the energy decay has a modified KWB type of damped oscillator equation.

We derive two types of simple models, to predict the vorticity decay and the observed oscillations, both agree with certain aspects of the experimental observations. Depending on the role of the decay constant that depends strongly on the body forces, and the particularity of the internal frequency for stratified flows (or on the inertial frequency for rotating flows), the behaviour of the decay may be either over damped, critical or under damped, oscillating flow. There are clear instances of resonances between the inertial frequency and the oscillating behaviour observed.

The dominant power law decay in time is quadratic, but the initial conditions, and in particular the initial kinetic energy reinforces a linear term.

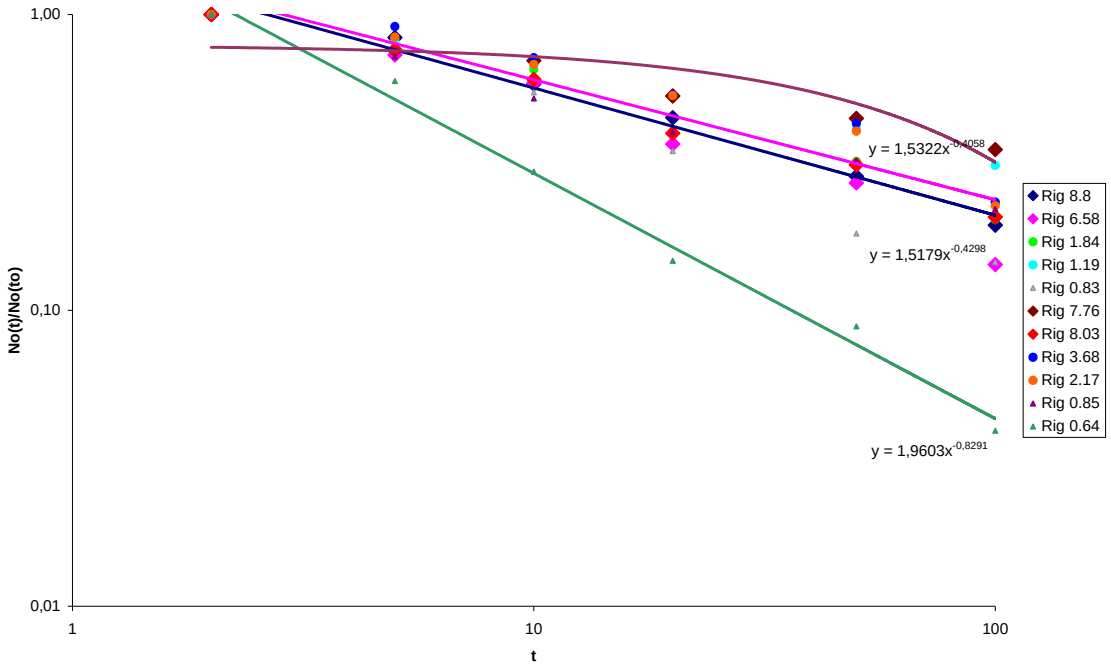

Figure 10.6: Relationship between non-dimensional number of vortices and time.

The decay of vortices in stratified turbulence is much complex than previously thought because although greater stratifications produce a quasi 2D behaviour, the reduction in buoyancy produces a topologically very different decay process, which is much more three dimensional. This can be seen in figures 10.6 and 10.7, where in general the highest decay rates correspond to the least stratified situations. The relationship agrees with a power low, and not with an exponential decay as seen in the lack of fit of the exponential curve for $Rig = 7.76$.

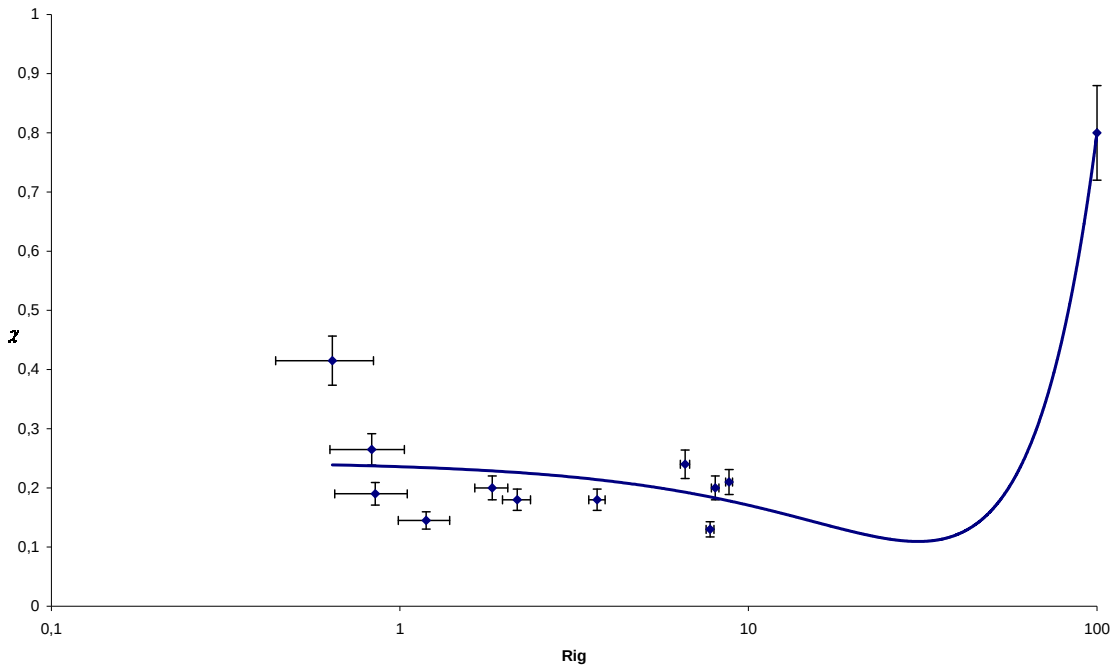

Figure 10.7: Power decay exponents versus gradient Richardson number.

Figure 10.7 shows the complex behaviour of the interaction between vortex decay and buoyancy. The possible minimum at intermediate numbers would be consistent with a maximum in mixing efficiency at intermediate Richardson number, the value at $Rig = 100$ just indicates the theoretical value for a pure 2D decay flow. The role of the rotation in the stratified rotating situation would also produce a complex reduction in the decay rate indicating the non linear effect of coupled internal and inertial waves.

10.3. Conclusions on the Kinetic Energy decay

We have shown the important role of the initial conditions on the decay of even pure 2D flows; more so, the effects of buoyancy and rotation modify the simple quadratic decay law. We also show the oscillations due to the exchange between kinetic and potential energy, this has profound influence on the mixing efficiency of these flows as discussed in appendix 6.

As with the vorticity behaviour, the dominant decay term is quadratic, but the linear decay may be important, by comparing two different sets of experiments at different Reynolds numbers, we show that for medium-low Re the type of behaviour is the same.

The role of the initial kinetic energy has been shown to be much more important than previously thought.

This also affects the conversion of kinetic to potential energy and controls mixing efficiency, thus finding a possible explanation to the long memory exhibited in some mixing flows (Gonzalez-Nieto et al. 2008). The discussion on mixing efficiency of appendix 6 also leads the way to confirm the higher mixing efficiencies, probably due to parameter resonances, of intermediate Richardson numbers, see also 10.5.

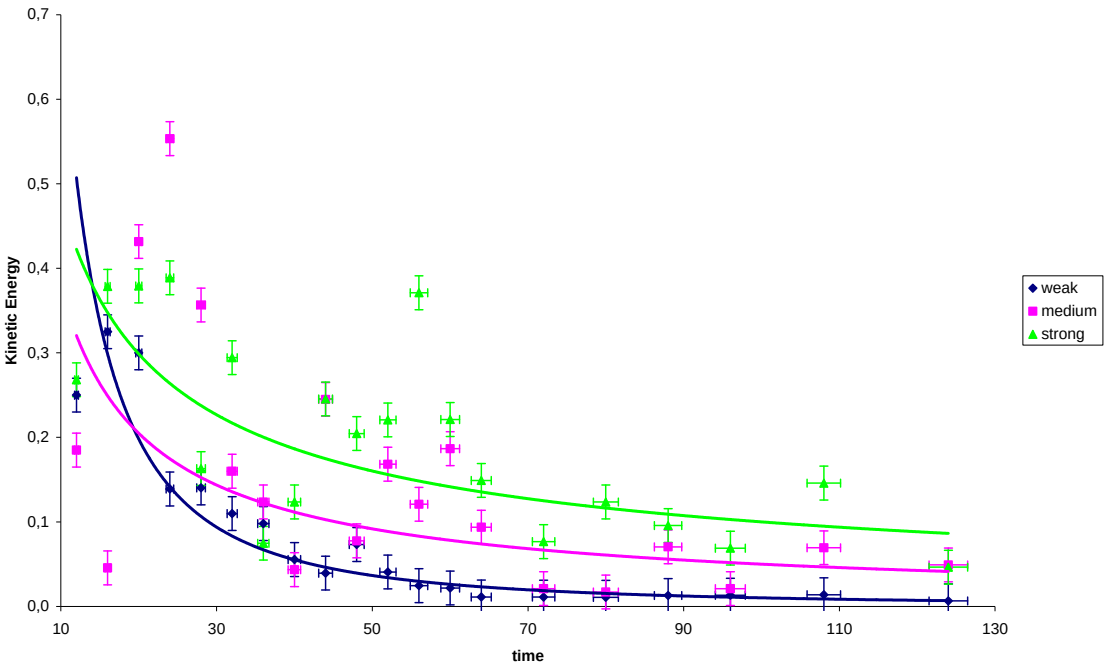

Figure 10.8: Horizontal Energy decay in a stratified interface turbulent decay experiment for low Reynolds number experiments (Peco 2009).

In section 9.3 we use simple energy decay model to interpret the experimental research such as those in figures 10.8 and 10.9.

We have used two different homogenous models such as:

$$\frac{dk}{dt} + c'(Ri, Ro, t)k^2 = 0 \qquad \text{and} \qquad \frac{dk}{dt} + c(Ri, Ro, t)k^{3/2} = 0$$

described in chapter 9.

Modelling in a simple way the effect of internal and inertial waves on the energy decay with a non-linear dependence in time of the wave-vortex interaction, especially after $Nt \geq 5$, when grid turbulence begins to collapse (Fraunie et al. 2008). The type of solution depends on the time dependence of the coefficients c' and c such as:

$$k(t) = \frac{1}{\frac{1}{k_o} - \frac{Ri}{2}(t - t_o)^2} \qquad \text{and} \qquad k(t) = \frac{1}{\frac{1}{k_o} - Ri \ln\frac{t}{t_o}}$$

depending on the assumption on time dependence of coefficients c' and c.

In figure 10.8 we see that for the least stratified case we have almost an exponential decay while for intermediate and strong stratification the presence of oscillations is detected in a similar way as for vorticity oscillation. These experiments were performed by Peco (2009) in a small size version on the experiments described in chapter 7. The larger Reynolds number experiments show similar behaviour in figure 10.9 with the oscillatory behaviour corresponding to the largest Richardson number experiments. We confirmed also the importance of the initial conditions and the complex relationship between kinetic energy, vorticity and mixing efficiency (see appendix 6).

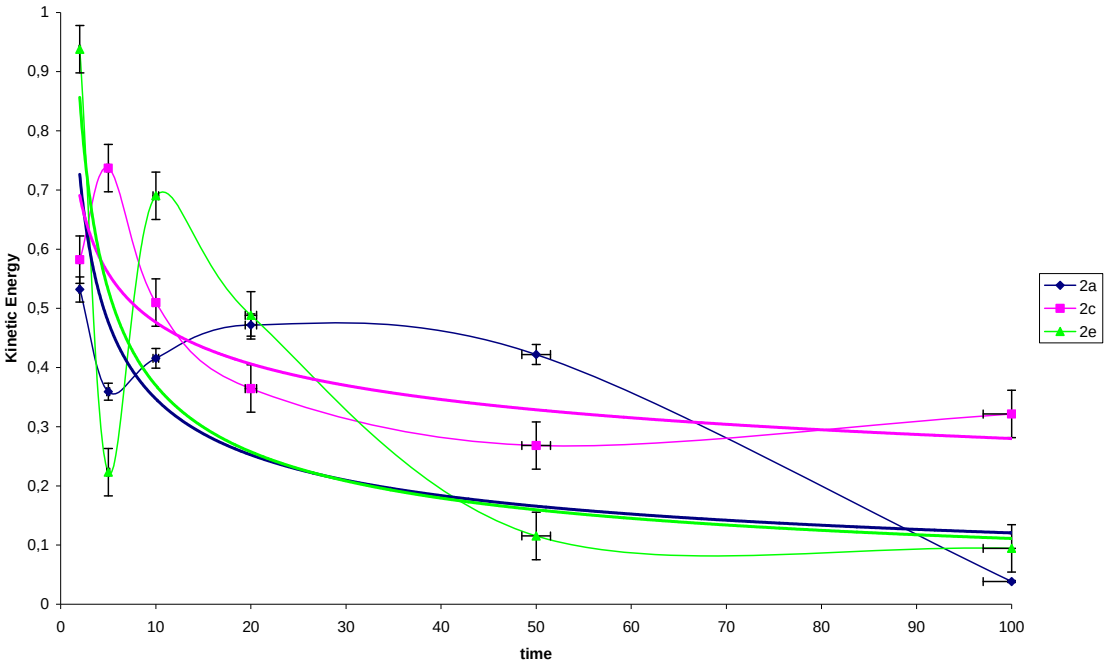

Figure 10.9: Horizontal Energy decay in a stratified interface turbulent decay experiment for high Reynolds number experiments.

10.4. Conclusions on the Number of Vortices and their interactions

The results of Chapter 7 and the theoretical derivations in chapter 9 show clearly a oscillatory behaviour of the number of vortices in selected parameter ranges. It is also possible to trace the behaviour of vortices of different level of enstrophy and in many cases a non-local behaviour is detected, in the sense that the topology of vortex interactions is very wide. To name a few; these possibilities occur:

a) Rupture of a vortex in two
b) Merge of two vortices in a single one
c) Rupture of a vortex dipole in four vortices
d) Merge of two vortex dipoles into a larger one
e) Sudden break of a large vortex into many smaller ones
f) Merge of several small vortices in a complex large vortex
g) Interaction of a single vortex and a internal wave
h) Interaction of several vortices and several internal waves

The measurements of the decay rate of the vortex number in time has been very revealing, and the relationship between the exponent of decay χ with the exponent of area increase β.

The vortex number N_o term describes the statistical properties of the vortex population. The time evolution of the vortex number is assumed to have a power law form as $N_o(t)=N_o(t_o)\left(\frac{t}{t_o}\right)^{-\chi}$ and the area corresponding to the vortices will have like $A_m(t)=A_m(t_o)\left(\frac{t}{t_o}\right)^{\beta}$ where N_o is the vortex number, A_m is area occupied by the vortices, χ is a certain exponent of the vortex decay and β is the time increase in vortex area. The relationship between χ and β has been explained in chapter nine, so that in a pure 2D flow it only depends on the type of vortex dissipation as described by Lacasce (2008). In figure 10.10 we compare the stratified experimental decay of the stratified experiments with the different types of dissipation. This confirms the complex non-linear interaction between the vorticity, the area and the mixing efficiency.

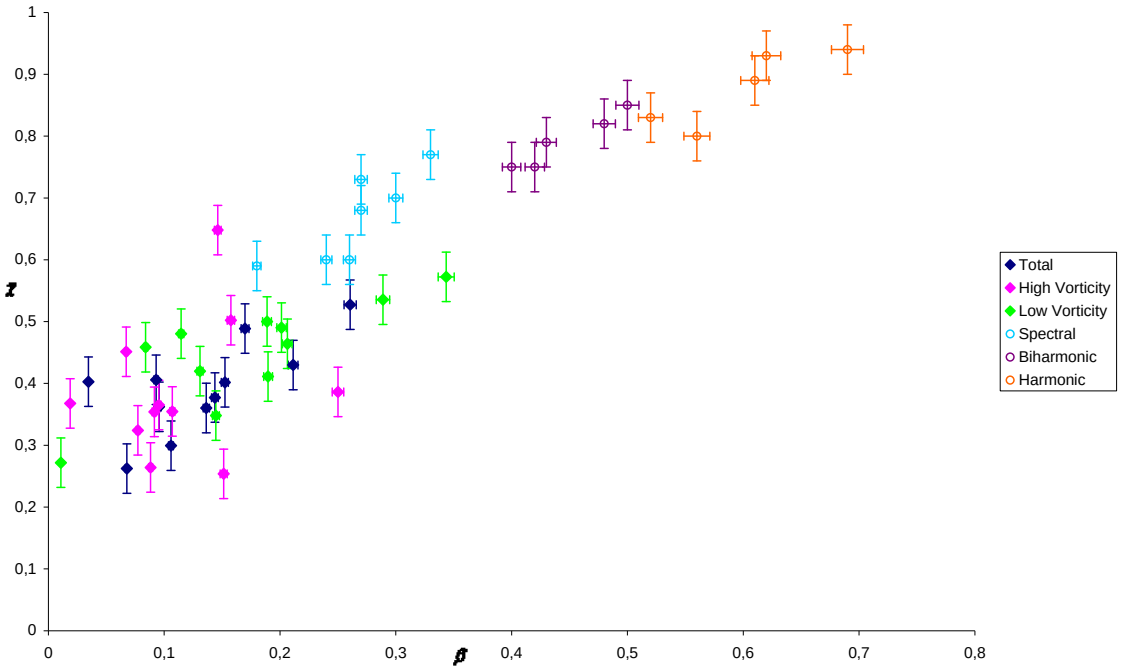

Figure 10.10: Relationship between the vortex decay rate and the vortex area decrease. The open symbols correspond to the numerical simulation of Lacasce (2008) for different types of dissipation (Spectral, Bilharmonic or Harmonic). The filled symbols correspond to vortices of high and low vorticity and the total number of vortices which were discussed in figure 10.7.

10.5. Conclusions on Mixing in Stratified Flows

There is strong asymmetry in the distribution of the vortices sizes as shown in Matulka (2003) which were caused by the interaction of a mixing front and a coastal current. Those features are seen in the non-rotating decay experiments in Chapter 7 at the passage of a vertical bar grid that moves horizontally, in these experiments the non-homogeneity can be related to the non-homogeneity relating the distance from the grid to the time times the grid velocity. These experiments agree with the previous observations showing an increase in vortex size as the grid wake grows. The effect of buoyancy is twofold, first it produces a collapse in the turbulence and further work is in progress to implement more realistic boundary conditions in the experiments.

We can see that after totally mixing the two initial layers the flow becomes fully 3D and then the results are very different of the theoretical 2D predictions. Only for surface flows, where an equivalent Richardson number at the density difference between air and water of several thousand, the coefficients of vortex decay, and area increase give values of 2/3 and 1/3. Mixing efficiency is maximum for intermediate Richardson numbers. This effect is possibly due to wave-vortex resonances of the type described by Cano et al. 2008.

10.6. Conclusions on Satellite observation of the environment

The use of routine satellite information by SAR or other sensor types may be of great interest to build a seasonal database of the dynamic conditions of the mesoscale turbulence in the ocean, after several years of observations the dominant patterns and the causes for different topological characterizations might be understood better. In the simplified conditions described above the maximum size of stable vortices can be characterized directly by the Rossby deformation radio RD depending on the square root on the depth on the local thermocline h. There is self-similar scaling at a very large range of scales and a linear dependence between the RD and the frequency of Brunt-Väisälä in the condition of a fixed h, this may be used to forecast and to check from satellite routine observations many of the dynamic characteristics of a certain area. The strong vertical stratification of the surface water aids the development of the largest vortices. As the frequency N strongly depends on the seasonal thermal balance, the wave mixing activity and other local bathymetry induced processes that affect the water column, the range and spatial distribution of detected vortices is very useful in the predictive behavior of a marine zone. In such a manner, more sophisticated data analysis such as the evaluation of integral length scales or local fractal dimensions of the sea surface appearance, together with the detailed information of the position and sizes of the mesoscale dominant eddies of size about R_D provides useful information on the mesoscale ocean turbulence.

A large collection of more than 900 SAR images obtained from three European coastal areas (Baltic Sea, North Sea and NW Mediterranean) by the ERS-1 and ERS-2 were analyzed and compared with other Satellite images. The research was done in the frame work of the CLEAN SEAS European Union project and more information is available in Platonov et al (2008)

The use of routine satellite information by SAR or other sensor types may be of great interest to build a seasonal database of the dynamic conditions of the mesoscale turbulence in the ocean, after several years of observations the dominant patterns and the causes for different topological characterizations might be understood. It is important to characterize the types and structure of the main vortices detected as well as the spectral cascade processes that take place, these may be investigated by using fractal methods on images of the area as well as with models of the turbulent cascade and field

measurements of diffusion.

The different multifractal formalisms can be used to discriminate between different physical processes that, despite being similar, have different transport mechanisms for the different scales, or in time. From the comparison of the multifractal plots of the well defined SAR detected vortices with those of convective cells, vortices show a maximum complexity for the low reflectivity values, while convection, probably because the basic instability happens everywhere at the same time, exhibits almost the same fractal dimension for a wide range of intermediate SAR reflectivity. The analysis of recent versus more convoluted oil spills is also interesting both in the formalisms presented for the fractal measures, which on the long run, they tend to be those of the turbulent environment, and initially for low SAR reflectivity the generalized dimensions are low but in time they increase to a limit of 1.5–1.6.

10.7. Further Work

Further comparison and analysis of the effects of stratification and rotation are possible, and to extend the experiments in the parameter space (Ri, Ro, Re) seems very important. In order to fill the parameter space a new set of experiments in a larger rotating table should be done (Coriolis platform in Grenoble of 13 m in diameter). The study of the different topological regions, following the Okubo-Weiss parameter and distinguishing the energy, enstrophy and palinstrophy in shear dominated regions (hyperbolic) and vertical (elliptical) regions would also be important to describe the effect of buoyancy and rotation on the flow structure. In the same way future work should include the study of the structure functions of several orders. It has been speculated Tabeling (2002) that many different conservation laws of weaker effect are present for higher order velocity (energy) and vorticity (enstrophy), but probably the role of internal waves of frequency N and inertial waves of frequency $f=2\Omega$, would affect different order structures in a different way. Fractal analysis would be also useful in the study of the different spatial fillingness of different q values. It would be interesting to perform the same vortex number analysis for the rotating stratified experiments. The fractal tool used in SAR ocean images may also be used in the laboratory experiments (Matulka et al. 2009). In the same way intermittency and higher order structure function of the velocity and vorticity flows should be investigates as a function of Richardson and Rossby numbers.

References

AFANASYEV, Y.D. (2003), MCC Analysis of velocity field in the Easter Black Sea during the "Black Sea'99" experiment. *Department of Physics and Physical Oceanography*, Newfoundland, Canada.

ALSTROM, P., G. HUBER (1993), Universal decay of vortex density in two dimensions. *Physica Atm.* **195**, 448.

BABIANO, A. (2002), On particle dispersion processes in two-dimensional turbulence. In Turbulent mixing in geophysical flows. *Eds. Linden P.F. and Redondo J.M.*, 2-33.

BARRY, M.E., G.N. IVEY, K.B. WINTERS & J. IMBERGER (2001), Measurements of diapycnal diffusivities in stratifed fuids. *J. Fluid Mech.* **442**, 267-291.

BAUMERT, H.Z. (2009), Primitive turbulence: kinetics, Prandtl's mixing length, and von Kármán's constant. *Physics Fluid Dynamics*. In Press.

BENZI, R., M. COLELLA, M. BRISCOLINI and P. SANTANGELO (1992), A simple vortex model for two-dimensional decaying turbulence. *Phys. Fluids A* **4**(5), 1036-1039.

BENZI, R., S. CILIBERTO, C. BAUDET and G. RUIZ CHAVERRIA (1994), On the Scaling of Three-dimensional Homogenous and Isotropic Turbulence. *Elsevier Physica D* **80**, 385-398.

BERRIZI, F., DALLE MESE E. and MARTORELLA M. (2004), A sea surface fractal model for ocean remote sensing. *International Journal of Remote Sensing* **25**(7-8), 1265-1270.

BEZERRA, M.O., DIEZ M., MEDEIROS C., RODRIGUEZ A., BAHIA E., SANCHEZ-ARCILLA A. and REDONDO J.M. (1998), Study on the influence of waves on coastal diffusion using image analysis. *Jour. Flow Turbulence and Combustion* **59**, 191-204.

BOFFETTA, G., A. CELANI and M. VERGASSOLA (2000), Inverse energy cascade in two-dimensional turbulence: Deviations from Gaussian behaviour. *Physical Review E* **61**(1), 29-32.

BOUBNOV, B.M., DALZIEL S.B. & LINDEN P.F. (1994), Source-sink turbulence in a stratified fluid, *J. Fluid Mech.* **261**, 273-303.

BOURUET-AUBERTOT, P., J. SOMMERIA & C. STAQUET (1996), Stratified turbulence produced by internal wave breaking: two-dimensional numerical experiments. *Dyn. Atm. Oceans* **23**, 357-369.

BRACCO, A., J.C. MCWILLIAMS, G. MURANTE, A. PROVENZALE, J.B. WEISS (2000), Revisting freely decaying two-dimensional turbulence at millennial resolution. *Physics of Fluids* **12**(11), 2931-2941.

BRACCO, A., J. VON HARDENBER, A. PROVENZALE, J.B. WEISS and J.C. MCWILLIAMS (2004), Dispersion and mixing in quasi-geostrophic Turbulence. *Physical Review Letters*, **92** (4 pages).

BROWN, M.R. (1997), Experimental evidence of rapid relaxation to large-scale structures in turbulent fluids: selective decay and maximal entropy. *J. Plasma Physics* **57**, 203-229.

CAMBON, C. (2000), Turbulence and vortex structures in rotating and stratified flows, *Eur. J. Mech.* **20**, 489-510.

CAMBON, C., R RUBINSTEIN and F.S. GODEFERD (2004), Advances in wave turbulence: rapidly rotating flows. *New Journal of Physics* **6**, 1-29.

CANO, D., J.L. CANO and A.M. MATULKA (2008), Three-dimensional turbulence vorticity: Numerical and experimental modelling. *IL NUEVO CIMENTO C* **31**, 791-811.

CARDOSO, O., D. MARTEAU and P. TABELING (1994), Quantitative experimental study of the three decay of quasi-two-dimensional turbulence. *Physical Review E* **49**(1), 454-461.

CARNEVALE, G.F., Y. POMEAU and W.R. YOUNG (1990), Statistic of ballistic agglomeration. *Physical Review Letters* **64**(24).

CARNEVALE, G.F., J.C. MCWILLIAMS, Y. POMEAU, J.B. WEISS and W.R. YOUNG (1991), Evolution of vortex statistic in two-dimensional turbulence, *Physical Review Letters* **66**(21).

CARRILLO, J.A., REDONDO, J.M., SZANCHEZ, M.A., and PLATONOV, A. (2001), Coastal and interfacial mixing laboratory experiments and satellite observation, *Physics and chemistry of the Earth* **26**(4), 305-311.

CARRILLO, J. A. (2002), *Influencia de la Turbulencia y de la Dinámica de Interfases de Densidad Sobre Organismos* Planctónicos*: Aplicación al estuario del Ebro,* Ph.D. Thesis, UPC, Barcelona, Spain.

CARRILLO, A., HUQ P., PÉREZ M.C. and REDONDO J.M. (2008), Spatial and temporal variation of picoplanktic cyanobacteria population in a density stratified estuary, and the introduction of a cellular gradient number. *Estuarine, Coastal and Shelf Sci*. **76**, 153-162.

CASTILLA, R. (2001), S*imulación Cinemática de Flujo Turbulento.* Ph.D. Thesis, UPC, Barcelona, Spain.

CASTILLA, R., REDONDO J.M., GAMEZ P.J. BABIANO A. (2007), Coherent vortices and Lagrangian dynamics in 2D turbulence. *Non-Linear Processes in Geophysics* **14**, 139-151.

CASTILLA, R., J.M. REDONDO and A. BABIANO (2009), Intermittency in K.S. and D.N.S. models. *EROFTAC SERIES*, In Press.

CAULFIELD, C.P. & W.R. PELTIER (2000), The anatomy of the mixing transition in homogeneous and stratified free shear layers. *J. Fluid Mech.* **413**, 1-47.

CHASSAING, P., R.A. ANTONIA, F. ANSOLMET, L. JOLY and S. SARKAR (2002), *Variable density fluid turbulence. Fluids Mechanics and its applications. Kluwer Academics Publisher*.

CHAVANIS, P.H. (2000), Quasilinear theory of the 2D Euler equation. *Phys. Rev. Lett.* **84**, 5512-5515.

CHAVANIS, P.H. and C. SIRE (2000), Statistics of velocity fluctuations arising from a random distribution of point vortices: The speed pf fluctuations and the diffusion coefficient. *Physical Review E* **62**, 490-506.

CHEN, X., ALLEN S.E. (1996), The influence of canyon on shelf currents: A theoretical study. *Journal of Geophysical Research.* **101**(8), 18.043-18059.

CLERCX, H.J.H. and A.H. Nielsen (2000), Vortex statistics for turbulence in a container with rigid boundaries. *Physical Review Letters* **85**(4), 752-755.

DALZIEL, S.B. (1992), Decay of rotating turbulence: some particle tracking experiments, *Appl. Scien. Res*. **49**, 217-244.

DALZIEL, S.B. (1993), Decay of rotating turbulence: some particle tracking experiments: *In Flow Visualization and Image Analysis*. *Ed. Nieuwstadt,* Kluwer, Dordrecht, 27-54.

DALZIEL, S.B. (1993), Rayleigh-Taylor instability: experiments with image analysis, *Dyn. Atmos. Oceans* **20**, 127-153.

DALZIEL, S.B., LINDEN P.F. & BOUBNOV B.M. (1995), Experiments on turbulence in stratified rotating flows: *In Mixing in Geophysical Flows, Ed. Redondo & Metais; CIMNE*, Barcelona, 195-208.

DALZIEL, S.B. (1998), Rayleigh-Taylor instability: experiments with image analysis. *Dynamics of Atmospheres and Oceans* **20**,127-153.

DALZIEL, S.B. and J.M. REDONDO (2007), New visualization methods and self-similar analysis in experimental turbulence studies. *CIMNE*, Barcelona, Spain.

DALZIEL, S.B., M.D. PATTERSON, C.P. CAULFIELD, & I.A. COOMARASWAMY (2008), Mixing efficiency in high-aspect-ratio Rayleigh-Taylor experiments. *Phys. Fluids* **20**, 65-106.

DERBYSHIRE, S.H. and J.M. REDONDO (1990), Fractals and waves, some geometrical approaches to stably-stratified turbulence. *Anales de Física, Serie A* **86**.

DUBOS, T. (2001), *Cascade bidimensionnelle d'un traceur: Diagnostic dans l'espace physique et modélisation*. PhD Thesis. Paris, France.

DUBOS, T. and BABIANO A. (2002), Two-dimensional cascades and mixing: a physical space approach. *J. Fluid Mech.* **467**, 81-100.

DUBOS, T. and BABIANO A. (2003), Comparing the two-dimensional cascades of vorticity and a passive scalar. *J. Fluid Mech.* **492**, 131-145.

DUBUCM, B., ZUCKER S.W., TRICOT C., QUINIOU J.F. and WEHBI D. (1989), Evaluating the fractal dimension of surfaces. *Phys. Rev.* **425**, 113 - 127.

ELDEVIK, T. and K.B. DYSTHE (2002), Spiral Eddies. *Journal of Physical Oceanography* **32**, 851-869.

EVERTSZ, C.J.G., MANDELBROT B.B. (1992), Multifractal measures (Appendix B). *In: Peitgen et al H.-O., ed. Chaos and fractals. New York: Springer-Verlag* **1992**, 922-953.

EYINK, G. (2006), A turbulent constitutive law for the two-dimensional inverse energy cascade. *Journal of fluid Mechanics* **549**, 191-214.

EYINK, G.L. and K. R. SREENIVASAN (2006), Onsager and the theory of hydrodynamic turbulence. *Reviews of Modern Physics* **78**(1), 87-135.

FEDER, J. (1988), *Fractals in physics. Cambridge Univ. Press*.

FERNANDO, H.J.S. (1991), Turbulent mixing in stratified fluids. *Annu. Rev. Fluid Mech*. **23**, 455-493.

FINCHAM, A.M., MAXWORTHY T. and SPEDDING G.R. (1996), Energy dissipation and vortex structure in freely decaying stratified grid turbulence. *Dyn. Atm. and Oceans* **23**, 155-169.

FLOHR, P. and VASSILICOS J. C**.** (2000), A scalar subgrid model with flow structure for large-eddy simulations of scalar variances. *J. Fluid Mech*. **407**, 315-349.

FLOR, J. B. and HEIJST G. J. F. (1996), Stable and unstable monopolar vortices in a stratified fluid. *J. Fluid Mech.* **311**, 257-288.

FONT, J., C. MILLOT, J. SALAS, A. JULIA and 0. CHIC (1998), The drift of Modified Atlantic Water from the Alboran Sea to the caster Mediterranean. *Sci. Mar*, **6**(3), 211-216.

FRAUNIE, P., S. BERREBA, Y.D. CHASHECHKIN, D. VELASCO and J.M. REDONDO (2008), Large eddy simulation and laboratory experiments on the decay of grid wakes in strongly stratified flows. *IL NUOVO CIMENTO C* **31**, 909-930

FRISCH, U. (1995), *Turbulence. Cambridge University Press*.

FULTZ, D., LONG R.R., OWENS G.U., BOHAN W., KAYLOR R and WEIL J. (1958), Studies of thermal convection in a rotating cylinder with some implications for large-scale atmospheric motions. *Meteor. Monog*. **4**, 104.

FUNG, J.C.H., HUNT J.C.R., MALIK N.A. and PERKINS R.J. (1992), Kinematic simulation of homogeneous turbulence by unsteady random Fourier modes. *J. Fluid Mech.* **236**, 281-318.

GADE, M and ALPERS W. (1999), Using ERS-2 SAR images for routine observation of marine pollution in European coastal waters. *The Science of the Total Environment.* **237/238**, 441-448.

GADE, M., REDONDO J.M. (1999), Marine pollution in European coastal waters monitored by the ERS-2 SAR: a comprehensive statistical analysis. I*GARSS 99. Hamburg* **III**, 1637-1639.

GOLDSTEIN, S. (1931), On the stability of superposed streams of fluids of different densities. *Proc. R. Soc. Lond.* **132**, 524-548.

GONZÁLEZ-NIETO, P.L., J.M. REDONDO, J.L. CANO and C. YAGÜE (2004), The role of initial conditions on Rayleigh-Taylor mixing efficiency, *International Workshop on The Physics of Compressible Turbulent Mixing,* Ed. Dalziel S., DAMTP, Cambridge University, U.K.

GONZALEZ-NIETO, P.L., J.L. CANO and J.M. Redondo (2008), An experimental model of mixing processes generated by an array of top-heavy turbulent plumes. *IL NUOVO CIMENTO C*, **31** 679-698.

GRAU, J. (2005), *Analysis of the Meteosat images sequences using the digital processing method*. PhD Thesis, UPC, Barcelona.

GREGG, M.C. (1987), Diapycnal mixing in the thermocline: a review. *J. Geophys. Res.* **92**(C5), 5249-5286.

HELMHOLTZ, H. VON (1887), On discontinuous movements of fluids, translation of "Uber discontinuirliche Flussigkeits-bewegunden". *Monats. Konigl. Preuss. Acad. Wiss Berlin* **23**, 215-228.

HIDE, R. (1959), An experimental study of thermal convection in a rotating liquid. *Phil. Trans. Roy Soc. London* A **250**, 441-478.

HOLLIDAY, D. & M.E. MCINTYRE (1981), On potential energy density in an incompressible stratified fluid. *J. Fluid Mech*. **107**, 221-225.

HOLLOWAY, G. (1986), Considerations on the theory of temperature spectra in stably stratified turbulence. *J. Phys. Oceanogr*. **16**, 2179-2183.

HOPFINGER, E.J. and VAN HEIJST G.J.F. (1993), Vortices in rotating fluids. *Annu. Rev Fluid Mech.* **25**, 241-289.

HUBER, G. and P. ALSTROM (1993), Universal decay of vortex density in two dimensions. *Physica A* **195**, 448.

ISERN-FONTANETA, J., J. FONTA, E. GARCÍA-LADONAA, M. EMELIANOVA, C. MILLOTB and I. TAUPIER-LETAGEB (2004), Spatial structure of anticyclonic eddies in the Algerian basin (Mediterranean Sea) analyzed using the Okubo–Weiss parameter. *Deep-Sea Research II* **51**, 3009–3028.

JOLLY, G.W., A. MANGIN, F. CAUNEAU, M. CALATAYUD, V. BARALE, H.M. SNAITH, O. RUD, I. MIHO, M. GADE, J.M. REDONDO & A. PLATONOV (2000), The Clean Seas Project - Final Report. E.U. Brussels.

KANG, H.S. & C. MENEVEAU (2001), Passive scalar anisotropy in a heated turbulent wake: new observations and implications for large-eddy simulations. *J. Fluid Mech.* **442**, 161-170.

KELVIN, L. (1898), On the stability of steady and of periodic fluid motion. *Phil. Mag*. **23**, 459-459 & *Mathematical and physical papers* (1910).

KEVLAHAN, N.K.R. and M. FARGE (1997), Vorticity filaments in two-dimensional turbulence: creation, stability and effect. *J. Fluid Mech.* **346**, 49-76.

KIM, J., P. MOIN and R. MOSER (1987), Turbulence statistics in fully developed channel flow at low Reynolds number. *J. Fluid Mech.* **177**, 133-166.

KOLMOGOROV, A. N. (1936), The basic notion of probability theory. *Giorni dell Instituto Italiano degli Attuari.*

KOLMOGOROV, A. N. (1941), The local structure of turbulence in incompressible viscous fluid at very large Reynolds numbers. *C. R. Acad. Sci URSS* **30**, 301.

KOLMOGOROV, A.N. (1962), A refinement of previous hypotheses concerning the local structure of turbulence in a viscous incompressible fluid at high Reynolds number. *J. of Fluid Mechanics*. **13**, 82 - 85.

KRAICHNAN, R. (1967), Inertial ranges in two-dimensional turbulence. *Phys. Fluids* **10**, 1417-1422.

KRAICHNAN, R. (1975), Statistical dynamics of two dimensional flow, *J. Fluid Mech.* **67**, 155-175.

KUNDU P. K. (1990), *Fluid Mechanics*. *Academic Press*, Orlando, Florida.

LACASCE, J.H. (2008), The Vortex merger rate in the freely decaying, two-dimensional turbulence. *Physics of Fluids* **20**, 1-14.

LIECHESTEIN, L. (2006), *Rotating stratified flows*, PhD Thesis, Ecole Central Lyon.

LIECHTENSTEIN, L., F.S. GODEFERD and C. CAMBON (2006), The role of nonlinearity in turbulent diffusion models for stably stratified and rotating turbulence. *International Journal of Heat and Fluid Flow* **27**, 644–652.

LINDBORG, E. (2006), The energy cascade in a strongly stratified fluid. *J. Fluid Mech*. **550**, 207-242.

LINDEN, P.F. (1980), Mixing across a density interface produced by grid turbulence. *Journal of Fluid Mechanics* **100**, 3–29.

LINDEN, P.F. (1979), Mixing in stratified fluids. *Geophys. Astrophys. Fluid Dynamics.* **13**, 3-23.

LINDEN, P.F. and J.M. REDONDO (1991), Molecular mixing in Rayleigh-Taylor instability. Part I: Global mixing, *Phys. Fluids.* A**3** (5), 1269-1277.

LINDEN, P.F., J.M. REDONDO and D.L. YOUNGS (1994), Molecular mixing in Rayleigh-Taylor instability, *J. Fluid Mech.* **265**, 97-124.

LINDEN, P.F., BOUBNOV B.M. and DALZIEL S.B. (1996), Source-sink turbulence in a rotating, stratified fluid. *J. Fluid Mech.* **298**, 81-112.

MAHJOUB, O., A. BABIANO and J.M. REDONDO (1998), Velocity structure and extended self similarity in non-homogeneous turbulent jets and wakes. *Journal of Flow Turbulence and Combustion* **59**, 299-313.

MAHJOUB, O., J.M. REDONDO and R. ALAMI (1998), Structure functions in geophysical flows. *Rapp. Comm. Int. Mer. Medit*., **35**, 136-127.

MAHJOUB, O.B., REDONDO J.M. and BABIANO A. (2000), Structure functions in complex flows, *Journal of Flow Turbulence and Combustion* **59**, 299.

MAHJOUB, O.B., GRANATA T. and REDONDO J.M. (2001), Scaling laws in geophysical flows. *Phys. Chem. Earth* 2**6**, 281-285.

MANDELBROT, B. (1977), *The Fractal Geometry of Nature. Ed. W.H. Freeman and Company*, New York.

MANDELBROT, B.B. (1985), Self-affine fractals and fractal dimension. *Physica Scripta* **32**, 257.

MARTINEZ BENJAMIN, J. J., J.M. REDONDO; J. JORGE; A. PLATONOV (2000), Applications of SAR images in the western Mediterranean Sea 1999. *EARSeL symposium on remote sensing in the 21st century* (Vallodolid, Spain) **19**, 461-465

MATULKA, A. (2003), *Environmental Turbulence. Effects of Rotation and Stratification on Diffusion and Mixing in Geophysical Flows*. Master of Science. Warsaw, Poland.

MATULKA, A., J.M. REDONDO and J.A. CARRILLO (2008), Experiments in stratified and rotating decaying 2D flows, *IL NUOVO CIMENTO C* **31**, 757-770.

MATULKA, A., J.A. CARILLO & J.M. REDONDO (2009), Synthetic turbulence models. ERCOFTAC SERIES. *Eds. (F. Nicolleu, C. Cambon, J.M. Redondo & J.C. Vassilicov.* In Press.

MARTINEZ BENJAMIN, J.J., J.M. REDONDO, J. JORGE & A. PLATONOV (2000), Applications of SAR images in the western Mediterranean Sea. Remote Sensing in the 21st Century: *Economic and Environmental Applications, Casanova (ed.),* 461-465

MCEWAN, A.D. (1983), Internal mixing in stratified fluids. *Journal of Fluid Mechanics* **128**, 59–80.

MCEWAN, A.D. (1983a), The kinematics of stratified mixing through internal wavebreaking. *J. Fluid Mech*. **128,** 47-57.

MCWILLIAMS, J.C. (1984), The emergence of isolated coherent vortices in turbulent flow. *J. Fluid Mech.* **146**, 21-43.

MOLEMAKER, M.J. & J.C. MCWILLIAMS (2009), A complete energy budget using a local available potential energy density. *J. Fluid Mech*., In Press.

MOROZOV, E.G., K. TRULSEN, M.G. VELARDE and V.I. VLASENKO (2002), Internal Tides in the Strait of Gibraltar. *Journal of Physical Oceanography* **32**, 3193-3206.

MUNK, W. (2001), Spirals on the Sea, *Sciencia Marina* **65**, 193-198.

NGAN, K., D.N. STRAUB and P. BARTELLO (2004), Three-dimensionalization of freely-decaying two-dimensional turbulence. *Physics of Fluids* **16**(8), 2918-2932.

OKUBO, A. (1971), Oceanic diffusion diagrams. *Deep-Sea Res.* **18**, 789–802.

OKUBO, A. and Ozmidov R.V. (1980), An empirical relationship between the horizontal eddy diffusivity in the ocean and the scale of the phenomenon. *Atmos. Ocean. Phys.* **6**, 534–6 (in Russian).

ONSAGER, L. (1949), Statistical hydrodynamics. *Suppl. Nuovo Cim*. **6**, 279-287.

OSBORN, T.R. & C.S. COX (1972), Oceanic structure. *Geophys. Astr. Fluid Dyn.* **3**, 321-345.

OZMIDOV R.V. (1990), Diffusion of Contaminants in the Ocean. *Oceanographyc Sciences Library*.

PECO REGALES, C. (2009), *Mezcla turbulenta en la termoclina haloclina*, Tesina. UPC, ETSEIB, Barcelona, Spain.

PLATONOV, A. and REDONDO J.M. (1999), Observations of coastal Induced eddies in the NW Mediterranean Sea.

PLATONOV, A.K. (2002), *SAR satellite images applications to both sea contamination and dynamic studies in the NW Mediterranean*. Ph.D. Thesis, UPC Barcelona.

PLATONOV, A., J.J. MARTINEZ-BENJAMIN y J.M. REDONDO (2005), Observaciones mediante RADARSAT y ERS de las condiciones medioambientales en el Estrecho de Gibraltar. *XI Congreso nacional de Teledetección*, 21 -23 septiembre 2005. Puerto de la Cruz. Tenerife.

PLATONOV, A., A. CARRILLO, A. MATULKA, E. SEKULA, J. GRAU, J.M. REDONDO and A.M. TARQUIS (2008), Multifractal observations of eddies, oils spills and natural slicks in the ocean surface. *IL NUOVO CIMENTO C,* **31**, 861-880.

PLATONOV, A., A. TARQUIS, E. SEKULA and J.M. REDONDO (2009), SAR Observations of vertical structures and turbulence in the ocean. *R. Castilla, E. Oñate and J.M. Redondo (Eds.).* In Press.

PLOTNICK, R.E., GARDNER R.H., HARGROVE W.W., PRESTEGAARD K., PERLMUTTER M. (1996), Lacunarity analysis: A general technique for the analysis of spatial patterns. *Physical Review* **53**(5), 5461-5468.

POMEAU, Y. (1966), *Transport theory for a two-dimensional dense gas,* PhD Thesis, Univeristy of Orsay, France.

REDONDO, J.M. (1987) *Difusión turbulenta en fluidos estratificados*. Ph.D. Thesis, Univ. Barcelona.

REDONDO, J.M. (1990), *The structure of density interfaces*, PhD Thesis, Cambridge University.

REDONDO, J.M. and CANTALAPIEDRA I.R. (1993), Mixing in horizontally heterogeneous flows. *Applied Scientific Research* **51**, 217–222.

REDONDO, J.M. and METAIS O. (1995), *Mixing in geophysical flows*. *Ed. CIMNE,* Barcelona.

REDONDO, J.M., SÁNCHEZ M.A. & CANTALPIEDRA I.R. (1996), Turbulent mechanisms in stratified fluids, *Dyn. of Atmospheres and Oceans* **24**, 107-715.

REDONDO, J.M. (1988), Difusión turbulenta por rejilla oscilante. *Revista de Geofísica* **44**, 163-174.

REDONDO, J.M. & P.F. LINDEN (1993), Mixing produced by Rayleigh-Taylor instabilities. In: S.B. Mobbs and J.C. King: *Waves and turbulence in stably stratified flows. IMA* **40**, 395-422.

REDONDO, J.M., and PLATONOV A. (2001), Aplicación de las imágenes SAR en el estudio de la dinámica de las aguas y de la polución del mar Mediterráneo cerca de Barcelona. *Ing. Agua* **8**, 15–23

REDONDO; J. M. (2002), Mixing efficiencies of different kinds of turbulent processes and instabilities: Applications *to the environment in turbulent mixing in geophysical flows*. *Eds. Linden P.F. and Redondo J.M.*, 131-157.

REDONDO, J. M. (2003), Fractal aspects at magnet-thermoelectricity: Towards generalised Onsager relations. IEEE proceedings: Thermoelectric **22** ICT, 439-442.

REDONDO, J.M. (2004), The topology of stratified rotating flows in topics in fluid mechanics. *Prihoda & K.Kozel, CAS*, 129-135.

REDONDO J.M. and GARZON G. (2004), Multifractal structure and intermittency in Rayleigh-Taylor Driven Fronts. *Ed. S. Dalziel.* DAMTP, Cambridge. Web page: http://www.damtp.cam.ac.uk/iwpctm9/proceedings/IWPCTM9/Papers/Redondo_Garzon/Paper.pdf

REDONDO, J.M. and PLATONOV A.K. (2006), Oil Spill Detection and Prediction in the Northwest Mediterranean Sea. *SEASAR06 Conf.* ESA.

REDONDO, J.M., R. CASTILLA and E. OÑATE (2007), *Models, experiments and computation in turbulence. CIMNE*, Barcelona, Spain.

REDONDO, J.M., J. GRAU, A. MATULKA and A. PLATONOV (2008), Multifractal analysis of SAR of the ocean surface, currents, eddy structure, oil slicks and diffusivity analysis. *Instrumentation Viewpoint*, **13**, 107-108.

REDONDO, J.M., J. GRAU, A. PLATONOV and G. GARZÓN (2008), Análisis multifractal de procesos autosimilares: imágenes de satélite e inestabilidades baroclinas. *Rev. Int. Mét. Num. Cálc. Dis. Ing*. **24**(1), 25-48.

REDONDO, J.M. and A.K. PLATONOV (2009), Self-similar distribution of oil spills in European coastal waters. *Environ. Res. Lett*. **4**. In Press.

REDONDO, J.M., DIAZ and BEZERRA (2009), Sintethic Turbulence. *ERCOFTAC SERIES*, In Press.

RÉNYI, A. (1955), On a new axiomatic theory of probability. *Acta Mathematica Hungarian* **VI**(3-4): 285-335.

REYNOLDS, 0. (1883), An Experimental investigation of the circumstances which determine the motion of water shall be direct or sinuous, and of the law of resistance in parallel channels. *Philosophical Transactions of the Royal Society* **174**, 935-982.

RICHARDSON, L.F. (1922), *Weather prediction by numerical process*, Cambridge: *Cambridge University Press.*

RICHARDSON, L.F. (1926), Atmospheric diffusion shown on a distance-neighbour graph. *Proc. R. Soc. London*. **110**, 709.

RICHARDSON, L. F. (1929), A search for the law of atmospheric diffusion. *Beitr. Phys. frei. Atmos.* **15**, 24.

RODRIGUEZ, A., SANCHEZ-ARCILLA A., REDONDO J.M., BAHIA E. and SIERRA J.P. (1995), Pollutant dispersion in the near shore region, modelling and measurements. *Water Science and Technology* **32**, 169–178.

ROOIJ, F. DE, P.F. LINDEN and S. B. DALZIEL (1999), Experimental investigations of quasi-two-dimensional vortices in a stratified fluid with source-sink forcing. *J. Fluid Mech*. **383**, 249-283.

ROULLET, G. & P. KLEIN (2009), Available potential energy diagnosis in a direct numerical simulation of rotating stratified turbulence. *Journal of Fluid Mechanics* **624**, 45-55

SAFFMAN, P.G. (1995), *Vortex Dynamics*. *Cambridge University Press.*

SEURONT, L., SCHMITT F., LAGADEUC Y., SCHERTZER D. and LOVEJOY S. (1999), Universal multi- fractal analysis as a tool to characterize multiscale intermittent patterns: example of phytoplankton distribution in turbulent coastal waters. *Journal of Plankton Research* **21**(5), 877-922.

SIRE, C. and P.H. CHAVANIS (2000), Numerical renormalization group of vortex aggregation in two-dimensional decaying turbulence: The role of three-body interactions. *Physical Review E* **61**(6), 6644-6653.

SNAITH, H.M., M. GADE, G. W. JOLLY, A. MANGIN, V. BARALE, O. RUD, M. ISHII (2000), CLEAN SEAS: A north Sea Test Site. Report, E.U. Brussels.

SOLE, J., CUESTA I., GARCIA-LADONA E., GRAU X. (2000), Effect of Langmuir circulations in particle dispersion. Turbulent diffusion in the environment. *J.M. Redondo & A. Babiano*. UPC, Barcelona. 53-60.

STANLEY, H., MEAKIN P. (1988), Multifractal phenomena in physics and chemistry. *Nature* **335**, 405–409.

STAQUET, C. (2000), Mixing in a stably stratified shear layer: two-and three-dimensional numerical experiments. *Fluid Dyn. Res.* **27**, 367–404.

TABELING, P. (2002), Two-dimensional turbulence: a physicist approach. *Physics reports* **362**, 1-62.

TAILLEUX, R. (2009), On the energetics of stratified turbulent mixing, irreversible thermodynamics, Boussinesq models, and the ocean heat engine controversy. *J. Fluid Mech*, Accepted.

TAMPIERI, F. and A. MAURIZI (2008), A re-evaluation of surface layer turbulence from Antarctic data. *IL NUOVO CIMENTO C* **31**, 711-743.

TARQUIS, A.M., M.C. MORATÓ, M.T. CASTELLANOS and A. PERDIGONES (2008), Comparison of structure function and dentrended fluctuation analysis of wind time series. *IL NUOVO CIMENTO C* **31**, 633-651.

TARQUIS, A.M., E. SEKULA, A. MATULKA, J. GRAU, A. PLATONOV and J.M. REDONDO (2009), I.O.P. (Proceedings in Earth Sciences), In Press.

TAYLOR, G.I. (1932), The transport of vorticity and heat through fluids in turbulent motion. *Proc. Roy. Soc.* A **135**, 685-705.

TENNEKES, H. and LUMLEY L. (1972), A first course in turbulence, *MIT Press*.

TRITTON, D.J. (1999), *Physical Fluid Dynamics*. *Oxford University Press*, Oxford.

TRIZAC, E. (1998), A Coalescence model for freely decaying two-dimensional turbulence. *Europhysics Letters*, **43**, 671-676.

TRIZAC, E. and HANSEN J.P. (1996), Free energy of electric double layers around finite particles. *J. Phys.: Condens. Matter* **8**, 9191-9199.

TURCOTTE, D.L. (1988), Fractals in fluid mechanics. *Ann. Rev. Fluid Mech.* **20**, 5-16.

TURNER, J.S. (1968), The influence of molecular diffusivity on turbulent entrainment across a density interface. *J. Fluid Mech.* **33**, 639-656.

TURNER, J.S. (1973), *Buoyancy Effects in Fluids. Cambridge University Press*, Cambridge.

VASSILICOS, J.C. and HUNT J.C.R. (1991), Fractal dimensions and spectra of interfaces with application to turbulence. *Proc R. So. Lond*. A **435**, 505-534.

VOLTERRA, V. (1931), *La Théorie Mathématique de la Lutte pour la Vie*, *Gauthier-Villars*, Paris, 214.

VOSS, R.F. (1985), "Random fractal forgeries", *in fundamental algorithms for computer graphics*. *R.A. Eamshaw, ed. (Springer-Verlag*, Berlin), 805-835.

VOSS, R.F. (1988), Fractals in nature: from characterization to simulation. *The science of Fractal Images*, **1**, 21-70.

WEISS, J.B. and J.C. MCWILLIAMS (1993), Temporal scaling behaviour of decaying two-dimensional turbulence. *Phys. Fluids* A **5**, 608-621.

WINTERS, K.B., P.N. LOMBARD, J.J. RILEY & E.A. D'ASARO (1995), Available potential energy and mixing in density-stratified fluids. *Journal of Fluid Mechanics* **289**, 115-128.

WOLANSKI, E.J. and BRUSH L.M. (1975), Turbulent entrainment across stable density step structures. *Tellus* **27**, 259.

YAGÜE, C. (1992), *Estudio de la mezcla turbulenta a través de experimentos de laboratorio y datos micrometeorológicos.* Ph. D. Thesis. Complutense University of Madrid.

YWAYAMA, T. and H. FUJISAKA (1997), Dynamical scaling law in the development of drift wave turbulence. *Physical Review*, 55(5).

ZILITINKEVICHA, S.S., T. ELPERIND, N. KLEEORIND, I. ROGACHEVSKIID, I. ESAUC, T. MAURITSENE, and M.W. MILESF (2008) Turbulence energetics in stably stratified geophysical flows: strong and weak mixing regimes. *Quarterly Journal of the Royal Meteorological Society.*

ZOUARI, N. and A. BABIANO (1994), Derivation of the relative dispersion law in the inverse energy cascade of two-dimensional turbulence. *Elsevier, Amsterdam. Physica D*, **76**, 318-328.

APPENDIX 1

Basic Review of Remote Sensing

A1.1. The digital processing of the satellite images

We can define remote sensing as technique that allows us to retrieve the information about objects situated at the Earth's surface from a distance. In order to make remote observation possible there has to be some kind of interaction between the object and a sensor. The principal elements from any system of remote sensing are sensor, observed object and energy flow (reflection, emission or emission-reflection) that permit to put both in the relation. Remote sensing techniques constitute one instrument to obtain atmospheric and meteorological variables which are based on a satellite image analysis.

A1.1.1. Satellite type

For obtaining the atmospheric and meteorological relevant variables from remote sensing, meteorological satellites are used. A meteorological satellite is one space platform of remote sensing, that carries on board four collections of highly sensible instruments. These satellites are equipped with a sensor which retrieved reflected (visual) and emitted (infrared) radiation from the electromagnetic spectrum.

Regarding the satellite type, there exist in general: the geostationary satellites and the synchronous satellites. The geostationary satellites normally provide, in accordance with the satellite type used, the information in three bands, one in the visible (VIS), one in the mid infrared and one in the thermal infrared (IR). They have in general low space resolution (5 km) and high temporal resolution (one image, every 30 min.). Besides owing to their large distance from the Earth, one geostationary satellite can provide images from most of Earth's disk (both hemispheres). For this reason they are mainly directed to the research of large scale and planetary phenomena. Rossby Waves, Weather fronts, Stream Jets, etc.

The Meteosat satellite is one of the geostationary satellite series controlled by the European Organisation for the Exploitation of Meteorological Satellites (EUMETSAT). The first Meteosat was launched on November of 1977, and the last one on September of 1997 as a satellite to be called Meteosat 7. The Meteosat system is able to take the images every half an hour which is a good temporal resolution for the monitoring of the meteorological phenomena, as for example the distribution and deviation of clouds. Is possible to obtain three images each one designated in visible (VIS), thermal infrared (IR) and water vapour infrared (VA) corresponds to three sensors that are on board of the satellite. Every sensor collects the electromagnetic radiation in the rank of the wavelength different for each one, which permits to interpret images in the function of various characteristics of the observed objects. Their space resolution range is from 2.5 km in visible to 5 km in infrared. The function of Meteosat is to collect the information for to deduce the sea surface temperature, direction of the motion clouds, temperature and the maxim altitude of clouds, the top atmosphere humidity.

The Meteosat Second Generation (MSG) is the most advanced satellite from the group of Meteosat and was launched on August of 2002. The MSG space resolution is from 1 km in visible spectrum and obtain images every 15 min, and in the thermal infrared to 3 km. Its observation system has 12 channels (not like Meteosat which has

only three) and is available to obtain information about winds, surface temperatures and atmospheric humidity.

Contribute the Geostationary Earth Radiation Budget (GERB) instrument which observes the balance between the solar radiations which come to the Earth and is reflected by her to the space.

Nowadays EUMETSAT is considering thinking about the Meteosat Third Generation (MTG), which will be launched between years 2015-2025. The MTG will have five different observation missions at the Earth: The High Resolution Fast Imagery (HRFI), The Full Disk High Spectral Resolution Imagery (FDHSI), The Lightning Imagery (LI), The Infrared Sounding (IRS) and The UV/Visible Sounding (UVS) and will have the temporal resolution to 5 min and space resolution to 0.5-1.0 km.

The synchronous satellites provide the information in the major number of the bands. They have normally at least one band in visible and the other in the near, mid, thermal and far infrared. They have one high space resolution to 1 km (NOAA) and one low temporal resolution, between 6 hours (NOAA) to 16 days (LANDSAT).

The Television Infra-Red Observation Satellite (TIROS), which is named as The National Oceanic and Atmospheric Administration (NOAA), is the North America's polar orbit operated by NOAA. It also forms one part of the Polar Operational Environment Satellite program (POES) developed by the National Aeronautics and Space Administration (NASA) in the cooperation with the NOAA agency. The measure object of these satellites is the temperature and atmospheric humidity, the land surface temperature, the sea surface temperature, identify snow and ice.

The other synchronous satellite is the Environmental Satellite (ENVISAT), a land surface observation satellite constructed by the European Space Agency (ESA) and launched on 1st of March 2002. The ENVISAT mission involves a major contribution for the ESA and is equipped with 10 instruments designed for retrieve data about the atmosphere, oceans, terrestrial areas and polar regions. The ENVISAT satellite is present at the synchronous orbit. It offers the global cover of the Earth with one period of 35 days, however for the majority of the instruments this period is only 2 or 3 days.

The European Remote Sensing Satellites (ERS-1 and ERS-2) under the management of the ESA were constructed by the European industry. These satellites were launched in 1991 and 1995 respectively. They provide by one active microwave system that can retrieve data crossing the thick cloudy mass and during the night. One of the instruments measures the wind direction and speed over the oceans, the other

sensor, the altimeter can measure the waves altitude. In the ERS-2 is installed one passive traditional scanner A long-Track scanning Radiometer (ATSR) with seven canals in the visible range, near and thermal infrared. The ERS-2 is also equipped with the global cartography of the ozone layer.

The Quick Scatterometer (QuikSCAT) operated by NASA was launched on 19 June 1999. The QuikSCAT mission is used the radar that was designed to measure the wind velocity and direction over the ocean surface. This instrument helps to improve the knowledge about the mechanism of the climate change.

In this way, studies about geostationary and synchronous satellites for extracting the information of the meteorological and atmospheric data as aerosols, CO_2, NO_2, ozone etc. were realized. In case of the geostationary satellites we have: Meteosat (Paronis et al., 1998; Hamanou et al., 1998; Dulac et al., 2001, Ourtirane et al., 2002). In case of the synchronous we have exclusively the NOAA (Dammann et al., 2002; Flores et al., 2002; Wang et al., 2002; Morales et al., 2002; Iino et al., 2004, Ginzburg et al., 2004).

A1.1.2. Sensor type

There are many and various sensors available for the satellites, but actually, sensors with visible and no visible radiations that record the radiometric information digitally are used. More usual sensors are The Multi Spectral Scanner (MSS), The Advanced Very High Resolution Radiometer (AVHRR), The Visible Infrared Spin Scan Radiometer (VISSR), respectively they are installed at the satellites LANDSAT, NOAA, METEOSAT. The sensors in the accordance of the spectra region where they operate they can be qualifying like microwaves, visible and infrared sensors.

A1.1.2.1. Microwaves sensors

Many microwaves sensors exist. Often used is the scatterometer in the high frequency of microwave. This radar is designed to measure the wind velocity and direction over the ocean surface. The impulse of the short pulse is transmitted and the power of the reflected echo from the surface at the variety of the incidence angle is measured. Principally answers to surface bumpy texture, but in the minor measure are influence by the foam and spray, which put the superior limit level of resolution at the high wind velocities. This instrument explores the row from 1800 km of wide and his space resolution is 25 km. These sensors were launched on board of the ERS-2 and QuikSCAT.

A1.1.2.2. Visible and Infrared sensors

The remote perception of the ocean with visible and infrared sensors has the inheritance quite old. For example the NOAA satellite from 1978 uses the Advanced Very High Resolution Radiometer (AVHRR). Following, we have the visible and infrared sensors which are installed on board of satellites:

- The AVHRR sensor launched on board of the NOAA satellite detects the radiation in the visible, near, mid and far infrared, with a very high resolution to 1.1. km. (Dammann et al., 2002; Flores et al., 2002; Wang et al., 2002; Morales et al., 2002; Takeuchi et al., 2003; Iino et al., 2004, Ginzburg et al., 2004)
- The Spinning Enhanced Visible and Infrared Imager (SEVIRI) provides the images in 12 channels (4 in visible and near infrared and 8 in thermal infrared) every 15 minutes (high temporal resolution). Has the space resolution of 3 km in infrared and 1 km in one of the visible band. The future program of Meteosat comes as the introduction of this new tool, for observe the ozone on board of the MSG satellite. The new channel of the SEVIRI in the wave longitude close to 9.7 microns gives the opportunity to observe ozone without precedents in the time and in the space resolution, from the geostationary orbit. (Dash et al., 2003)
- The European Meteosat satellite owns the visible and Infrared Spin Scan Radiometer (VISSR) sensor, which registers visible disk over the Earth every 30 min, offered images in the visible spectrum and thermal infrared. This sensor offers the information about three spectrum bands: 0.4 to 1.1 μm (visible), 5.7 to 7.1 μm (water vapour channel) and 10.5 to 12.5 μm (thermal infrared). In the visible channel. The space resolution is 1.25 km and in the infrared and water vapour channel is 5 km. (Iino et al., 2004)
- The Along Track Scanning Radiometer (ATSR), on board of two satellites ERS-1 and ERS-2, and advanced ATSR system, on board of the ENVISAT, are two sensors with the middle resolution which provide the information in the visible, near and thermal infrared of the short wave. The thermal infrared channel is especially useful to conduct cartography of the sea surface temperature. The visible, near to infrared channels can be used for make global maps of the vegetation with the space resolution of 1 km. (Noyes et al., 2002)

- The Advanced Along Track Scanning Radiometer (AATSR) is one radiometer of high quality of images in the visible and thermal infrared, this which measures Sea Surface Temperature (SST). AATSR is the third sensor of the ATSR series on board of the ENVISAT satellite of the ESA. The objective of AATSR is study of the Land and Sea Surface Temperature and the climate investigation.

Table A1.1. The Summary of the existing satellites with sensors, operators, objectives and operation period.

Satellite	Sensor	Operator	Objective	Launch Date
METEOSAT	MSS VISSR	ESA	to collect the information from the sea surface, the direction of the clouds motion, the temperature and the maximum altitude of the clouds, humidity at the top troposphere	November 1977 (first) October 1997 (last)
MSG	SEVIRI	ESA	winds, the land surface temperatures, atmospheric humidity	August 2002
MTG		ESA	atmospheric vectors of motion at high altitudes, troposphere humidity at the middle and high levels, the Atlantic surface temperature	2015 - 2025
TRIOS-NOAA (series 14-17)	AVHRR	NOAA	measurement of the temperature and atmospheric humidity, the Land Surface Temperature, the Sea Surface Temperature	May 1994 (first) June 2002 (last)
ENVISAT	ATSR AATSR GOMOS MIPAS SCIAMACH MERIS	ESA	measurement of the concentration of greenhouse gases like ozone, CO_2, N_2O, NO_2 etc.	March 2002
ERS-1/ERS-2	ATSR Scatterometer	ESA	measurement of the wind direction and velocity over the ocean, cartography o f the ozone layer	ERS-1 July 1999-2000 ERS-2 April 1995
QuikSCAT	Scatterometer	NASA	measurement of the wind velocity and direction over the ocean surface	June 1999

A1.1.3. Band type

If we consider that the region of the electromagnetic spectrum in which we work, the satellites and sensors can be put into three categories:

- techniques in visible and near infrared (embrace to the sensor that measure the intensity of the solar radiation reflected by the Earth in the interval of 0.4 to 2.5 μm)
- techniques in thermal infrared (sensors that register the emitted radiance by the radiant system in the interval of 3-5 μm and 8-14 μm)
- techniques in microwaves (measure the intensity and polarization of the centimetres waves, between 0.1 to 100 cm)

Table A1.2: The electromagnetic spectrum with wavelengths.

	Wavelength (m)
Visible	0.38 - 0.78 μm
Near Infrared	0.78 - 2.5 μm
Mid Infrared	2.5 - 50 μm
Thermal Infrared	50 - 1000 μm
Microwave	0.1- 30 cm

In case of the solar spectrum (visible) we have: Meteosat (Paronis et al., 1998; Hamanou et al., 1998; Dulac et al., 2001; Ourtirane et al., 2002), NOAA (Dammann et al., 2002; Flores et al., 2002; Takeuchi et al., 2003). In case of the infrared: Meteosat (Ourtirane et al., 2002; Noyes et al., 2002; Dash et al., 2003), NOAA (Göttsche et al., 2002; Wang et al., 2002; Morales et al., 2002; Iino et al., 2004). In the bibliography we can not find too much the information about the techniques in microwaves: NOAA-10 (Chedin et al., 2003).

A1.1.3.1. Techniques in the visible and near infrared

a) Aerosols

The aerosol term or particle, sometimes without distinction, is defined like dispersion of solid substance or liquids in the air. The properties of aerosols that affect more at the process of the atmospheric contamination are the particle size, the form and chemical composition. The particle size oscillate between 1 and 1000 micros, although there exist some different ones outside of theses limits. In the atmosphere, the particles of the lower size than 1 micro perform the movements to chance, producing collisions between them.

The particles with sizes between 1 and 10 micro form mechanically stable suspensions in the air. They are called the suspend particle matter (SPM), which can be transported at the big distances by the winds. The particles grater than 10 micros remain in the suspension in the air during the relatively shorts periods, they are called sediment able matter.

b) Greenhouse gases

The greenhouse gases absorb and reflect preferentially one fraction of the solar energy, in one specific range in accordance with wavelength received. For example the ozone absorbs radiant energy in the zone of the ultraviolet spectrum (between the ranges of 0 to 0.28) and the water vapour (between 0.7-7).

The ozone is one substance that has two roles totally different to make, depends where is fined in the stratosphere and troposphere.

The stratospheric ozone that exists in the stratosphere (from 10 to 50 km) is essential for maintaining the life of the planet surface because absorb the lethal radiations of ultraviolet that come to us from the Sun.

The troposphere ozone that exists in troposphere, together with the Earth surface, is very important secondary pollutant. It exists very close to the surface is formed by the solar light in which participate, principally, the nitric oxide and hydrocarbon presented in the air. This component is more harmful that the photochemical smog and causes important damages to health, when it is in high concentrations, and stopped growth plants and trees.

Recently, Paronis at el. (1998) present the Aerosol Optical Thickness (AOT) observation in the Mediterranean. The proposal work is to characterize the aerosol of the marine bottom and to improve the recovery of the dust over the Mediterranean with the Meteosat satellite. The algorithm for the AOT over the Atlantic and Mediterranean from the visible channel of Meteosat consider two models for different components of aerosols: the aerosol from the sea bottom and aerosol from the desert.

Hamanou et al. (1998) realize one observation of the vertical structure of the dust transport in Africa that occurred over the Mediterranean between the 1 of January and 30 of June of 1997. This development was identified with visible images of Meteosat. The vertical observation of aerosol was interpreted in the European project MEDUSE (Hamanou et al., 1997).

Dulac et al. (2001) utilize the visible channel of Meteosat for observe the space-temporal variation of the AOT. They documented for the first time the vertical distribution of the aerosols during one situation of a typical winter. They found that the highest extinction of the aerosol is happened between 600 and 1400 meters in the altitude of the layer in the dry air over the Atmospheric Marine Boundary Layer (MBL). The results show that more than 90% of the dust is transported over the MBL.

Dammann et al. (2002) present a study of the aerosol impact over the Heat Radiation Budget (ERB) with satellite data. They use the existed data of NOAA/AVHRR satellite without support of geostationary ERG experimented on board of MSG, to detect the parameter of the optical aerosol.

Flores et al. (2002) employ one statistic model for determination of the global solar radiation from the surface of the Balearic Islands from the images of NOAA/AVHRR, which present wide cover, with one adequate space resolution. This model was checked for 12 months of 1998 and received the determination coefficient upper than 0.98 in all cases, with a mean square error between 9.7% and 15.9%, and with a bias error that varied between -9.8% and 1.2%. The results retrieved by satellites are more precise that obtained by interpolation data at the surface if the measurements stations have the distance between them more than 30 km.

A1.1.3.2. Infrared

Noyes et al. (2002) compare the Meteosat-7 and (A)ATSR that use the Earth data. Meteosat is one geostationary satellite with one channel in thermal infrared, which is used to retrieve the Land Surface Temperature (LST). Consequently, data from the IR channel of Meteosat is very similar to the bands of (A)ATSR.

Wang et al. (2002) present the split-window algorithm to calculate the Land Surface Temperature (LST) from the NOAA/AVHRR in one big scale. The results indicate that (1) LST increased during 10 years (1982-1992), (2) the space variation of LST in China was constant, (3) from the beginning of the 1980 till principle of the 1990 different regions present different changes of the temperature, in some areas increased in others decreased. The article indicates that this is the viable way to study the change of LST using thermal infrared bands of NOAA/AVHRR.

Morales et al (2002) show one method to estimate the surface temperature of South America from images of NOAA/AVHRR. This was one project conducted together with the National Centres for Environmental Prediction (NCEP) and the National Centre for Atmospheric Research (NCAR). The proposed method was based on the images correction from the atmospheric effect and from the emissivity, in two thermal channels. The atmospheric profiles were obtained monthly from the climatologically data from the reanalysis. The proposed model was based on the radiative transference equation.

Dash et al. (2003) use data from the first SEVIRI launched on board of MSG over the major part of the Earth (Schmetz et al., 2002) to estimate the Land Surface Temperature (LST). The Thermal Infrared Spectral Indices method (TISI) was adapted to the SEVIRI channels. This method was resistant for the surface type and covered the wide range of the emissions. Also, it was applied to data of AVHRR for most of Central Europe, for this region was planned the LST estimation.

Iino et al. (2004) use the meteorological data of NOAA/AVHRR and GMS-5/VISSR satellites to investigate the dust intrusion from China towards the Pacific Ocean close to Japan during the period of 2000-2002. They analyse the dust events, focused on advection of the shown images from the satellites, which are classified in three types like: ‘dry slot’, ‘high-pressure wedge’ and ‘travelling high’. The results are compared with concentrations of suspend particle matter (SPM). The ‘high –pressure wedge’ type is seen more clear at the images than ‘travelling high’ type, but SPM

concentrations are similar in both, owing to the differences in the vertical distribution of dust and in the observed conditions.

Table A1.3: Summary of the Bibliographic Revision.

	Satellite	Sensor	Band	References
LST	Meteosat-7 NOAA MSG	ATSR AVHRR SEVIRI	IR	Mito et al. 2002 Wan et al. 2002 Gottsche et al. 2002 Noyes et al. 2002 Wang et al. 2002 Morales et al. 2002 Dash et al. 2002
SST	NOAA	AVHRR	IR	Ginzburg et al. 2004
RS	NOAA	AVHRR	VIS	Flores et al. 2002
Aerosols	ENVISAT METEOSAT NOAA MSG	AVHRR GOMOS	VIS, IR	Paronis et al. 1998 Dulac et al. 2001 Dammann et al. 2002 Ourtirane et al. 2002 Kyrola et al. 2004
Ozone	ENVISAT	GOMOS MIPAS	VIS	Verronen et al. 2005
Dust SPM	METEOSAT NOAA	AVHRR VISSR	VIS, IR	Hamanou et al. 1998 Iino et al. 2004

LST Land Surface Temperature
SST Sea Surface Temperature
RS Solar Radiation
SPM Particular Matter
IR Thermal Infrared
VIS Visible

Ginzburg et al. (2004) use the measurement of data from the night time weekly Multichannel Sea Surface Temperature (MCSST) based on NOAA/AVHRR, to investigate the seasonal and year-on-year variability of the Sea Surface Temperature (SST) on the Black Sea during the period of November of 1981 till December of 2000. Calculate and compare fields of SST for the central months of tour hydrological seasons (February, May, April and November) with fields of SST corresponding to in-situ

measurements. The minimum picks for summer of SST are observed in 1982, 1984 and 1985, and maximum values in 1991, 1992, 1998 y 1999.

Many Features are dominated by vertical structures such as the Jovian storm or a hurricane in the Atmosphere as shown in figure 10.1.

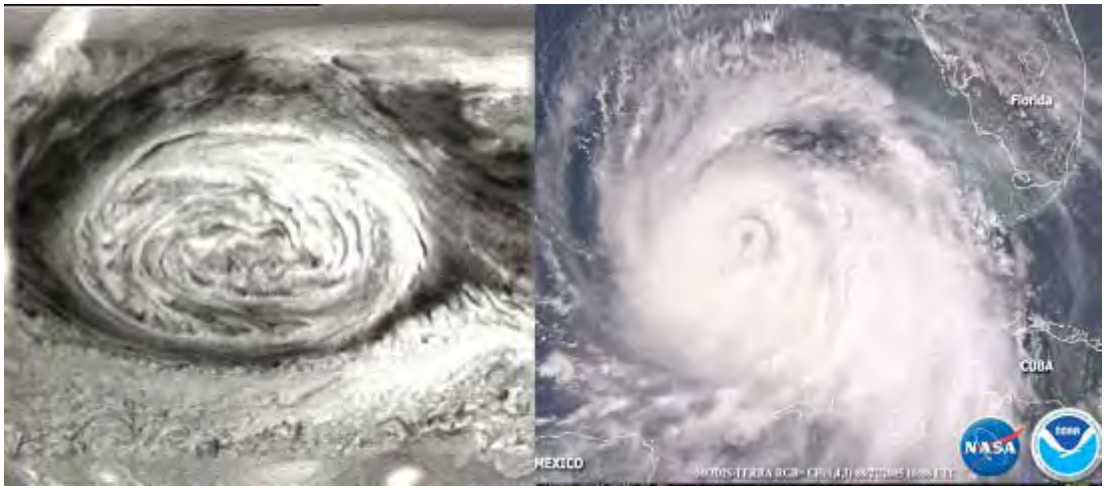

Figure A1.1: (left) Jupiter's Storm, (right) Katrina Hurricane.

A.1.2. References

BEEK, R., BUCHWITZ M., ROZANOW V.V., BURROWS J.P. (2004), Trace Gas Column Retrieval from IR Nadir Spectra – A Model Study for SCIAMACHY, *Advances in Space Research* **34**, 743-738.

BRACHER, A., BOVENSMANN H., BRAMSTEDT K., BURROWS J.P. (2005), Cross Comparison of O_3 and NO_2 Measured by the Atmospheric ENVISAT Instruments GOMOS, MIPAS and SCIAMACHY, *Advances in Space Research.*

CHEDIN, A., SERRAR S., HOLLINSWORTH A., ARMANTE R., SCOTT N.A. (2003), Detecting Annual and Seasonal Variations of CO_2, CO and N_2O from a Multi-year Collocated Satellite-radiosonde Data-set Using the New Rapid Radiance Reconstruction (3R-N) Model, *Journal of Quantitative Spectroscopy and Radiative Transfer* **77**, 285-299.

DAMMANN, K.W., HOLLMANN R., STUHLMANN R. (2002), Study of Aerosol Impact on the Earth Radiation Budget with Satellite Data, *Advances in Space Research* **29**(11), 1753-1757.

DASH, P., GOTTSCHE F.M., OLESEN F.S. (2003), Emissivity and Temperature Estimation from MSG SEVIRI Data; Method Validation with Simulated and NOAA-14 AVHRR Data, *Advances in Space Research* **32**(1), 2241-2246.

DULAC, F., CHAZETTE P., GOMES L., CHATANET B., BERGER H., VINICULA DOS SANTOS J.M (2001), A Method for Aerosol Profiling in the Lower Troposphere with Coupled Scatter and Meteorological Rawindsondes and First Data From the Tropical Atlantic of Sahara, *Journal of Aerosol Science* **32**, 1069-1086.

FLORES, H., BALDASANO J.M., VERA N., Nadal P. (2002), Radiación Solar en las Islas Baleares Mediante Imágenes de Satélites, *Recent Advances Quantitative Remote Sensing*, 261-267.

FONT, J., MILLOT C., SALAS J., JULIA A. and CHIC O. (1998), The drift of Modified Atlantic Water from the Alboran Sea to the easter Mediterranean. *Sci. Mar*, **62**(3), 211-216.

GINZBURG, A. J., KOSTIANOY A.G., SHEREMET N.A. (2004), Seasonal and Interannual Variability of the Black-Sea Surface Temperature as Revealed from Satellite data (1982-2000), *Journal of Marine Systems* **52**, 33-50.

GOTTSCHE, F. M., OLESEN F.S. (2002), Atmospheric Correction of IR Satellite Data Using Neural Networks, *Recent Advances in Quantitative Remote Sensing*, 651-655.

GRAU, J. (2005), *Processat digital d'imatges aplicat a l'anàlisi de sequències Meteosat*. Ph.D. Thesis, UPC.

HAMANOU, E., CHAZETTE P., PAPAYAMIS A., BALIS D., MARENCO F., SANTACESARIA A., ANCELLET G. (1997), Ground-based Measurements of Saharan Dust Optical Properties in the Frame of the European MEDUSE Project, *Journal of Aerosol Science* **26**(1), 695-696.

HAMANOU, E. and CHAZETTE P. (1998), Evidence of Saharan Mineral Aerosols Transport to the Mediterranean Inside Well-defined Layers, *Journal of Aerosol Science* **29**(1), 1263-1264.

IINO, N., KINOSHITA K., TUPPER A.C., YANO T. (2004), Detection of Asian Dust Aerosols Using Meteorological Satellite Data and Suspended Particulate Matter Concentrations, *Atmospheric Environment* **38**, 6999-7008.

KYRÖLÄ, E., TAMMINEN J., LEPPELMEIER G.W., SOFIEVA V. (2004), GOMOS on Envisat: an Overview, *Advances in Space Research* **33**, 1020-1028.

MITO, G.O., LANEVE G., CASTRONUOVO M.M. (2002), Derivation of Land Surface Temperatures from MODIS Data Using General Split-window Technique, *Recent Advances in Quantitative Remote Sensing*, 631-638.

MORALES, L.J., PARRA J.C., SOBRINO J.A. (2002), Estimating Land Surface Temperature in South America from NOAA-AVHRR Images and Reanalysis Data, *Recent Advances in Quantitative Remote Sensing*, 698-706.

NOYES, E.J., REMEDIOS J.J., LLEWELLYN-JONES D.T., EDWARDS M.C. (2002), Comparison of Meteosat-7 and (A)ATSR Data Over Land: A Sensitivity Analysis, *Recent Advances in Quantitative Remote Sensing*, 656-663.

ORIOL-PIBERNAL, E. (2002), Preparados para el lanzamiento del MSG-1, *Recent Advances in Quantitative Remote Sensing*, p. 871-873.

OURTIRANE, K, FAID A. (2002), Remote Sensing of Saharan Aerosol Over Land and Sea, *Recent Advances in Quantitative Remote Sensing*, 139-145.

PARONIS, D., DULAC F., CHAZETTE P., HAMANOU E. and LIBERTI G.L. (1998), Aerosol Optical Thickness Monitoring in the Mediterranean, *Journal of Aerosol Science* **29**(1), 671-672.

SALAS, J., MILLOT C., FONT J. and GARCÍA-LADONA E. (1999), *Analysis of mesoscale Phenomena in the Algerian Basin from Drifting Buoys and Infra-red Images*. Ph.D. Thesis, UPC, ICM.

SCHMETZ, J., PILLI P., TJEMKES S., RATIER A. (2002), An Introduction to Meteosat Second Generation (MSG), *Bulletin of the American Meteorological Society* **83**(7), 979-991.

STUHLMANN, R., RODRIGUES A., TJEMKES S., GRANDELL J. (2005), Plans for EUMETSAT's Third Generation Meteosat Geostationary Satellite Programme, *Advances Space Research*.

TAKEUCHI, W., TAMURA M., YASUOKA Y. (2003), Estimation of Methane Emission from West Siberian Wetland by Scaling Technique between NOAA AVHRR and SPOT HRV, *Remote Sensing of Environment* **85**, 21-29.

VERRONEN, P.T., KYRÖLÄ E., TAMMINEN J., FUNKE B., GIL-LÓPEZ S. (2005), A Comparison of Night-time GOMOS and MIPAS Ozone Profiles in the Stratosphere and Mesosphere, *Advances in Space Research*.

WAN, Z., ZHANG Y., ZHANG Q., LI Z. (2002), Quality Assessment and Validation of the MODIS Global Land-surface Temperature, *Recent Advances in Quantitative Remote Sensing*, 575-584.

WANG, Ch., YAN H., NIU Z. (2002), Change Analysis of Land Surface Temperature in China Using NOAA-AVHRR Data, *Recent Advances in Quantitative Remote Sensing*, 672-678.

APPENDIX 2

Descriptive plots of a High Richardson number experiment

We will present here as an example an evolution of several parameters in time obtained from the 2D vorticity maps estimated by PIV, the times will be chosen following an almost equally spaced logarithmic sequence as 1, 2, 5, 10, 20,50,100,200,500 some of the velocity, vorticity and different visualizations where the number and structure of the vortices are shown as a function of the initial Richardson numbers, the main results are presented in chapter 7 for all experiments but we will show here more details and different types of visualisation used, that would, if shown for all data add a couple of thousand pages to this thesis.

In figure A2.1 we present a typical medium resolution vorticity 2D plot in false colour used to investigate the structure of the flow, this was obtained by PIV (see appendix 3) of two frames separated 0.1 seconds of the experimental sequence. It was checked that provided that the interrogation region was small enough 6-10 pixels and the local velocities were not too high. The results were independent of the time and spatial resolution within the limits used. For consistency the same resolution was used in most of the results presented in chapter 7, but higher resolutions both in space and time are possible as shown below.

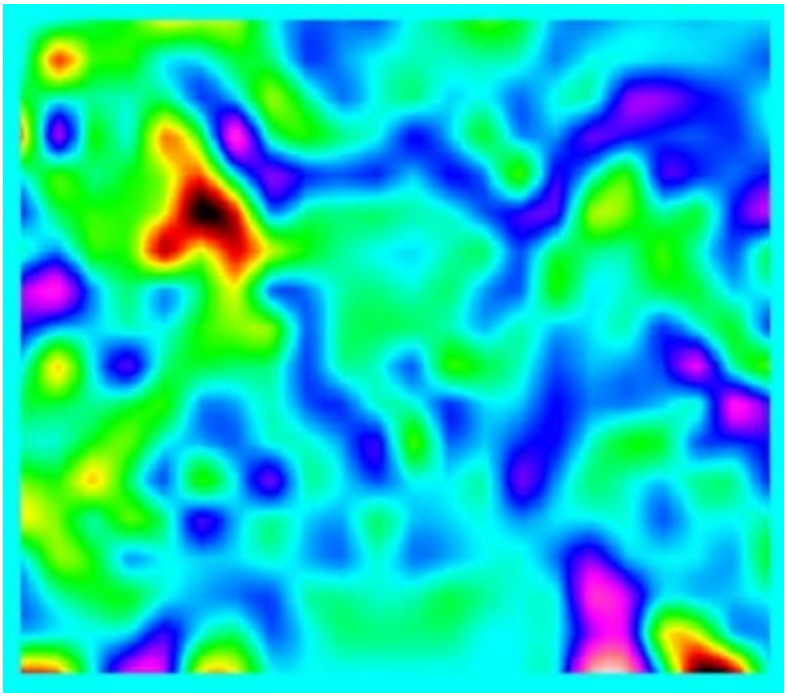

Figure A2.1: False colour vorticity map for high Richardson number $Ri = 8.8$ at time $t = 1$ sec or $3.8\,Nt$.

The same information can be depicted in different ways, and it was found to be very useful when examining the evolution of the flow and counting the different types of vortices (Positive, negative, large and small, etc.) to use a 3D rendering plot, the false colours are just a matter of choice. The vorticity coloured map is presented in figure A2.2 for time $t = 1$ sec and $Ri = 8.8$ just as in figure A2.1.

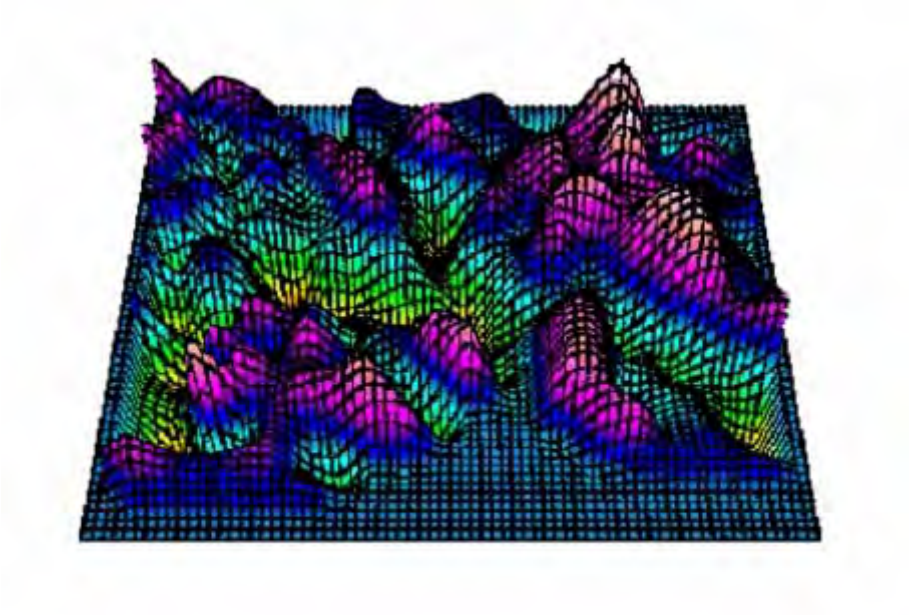

Figure A2.2: False colour 3D vorticity map for high Richardson number $Ri = 8.8$ at time $t = 1$ sec or $3.8\,Nt$.

The same information may be viewed from different angles, view points or resolution, this dynamical procedure was sometimes needed when counting the different levels of vorticity described in chapter 7.

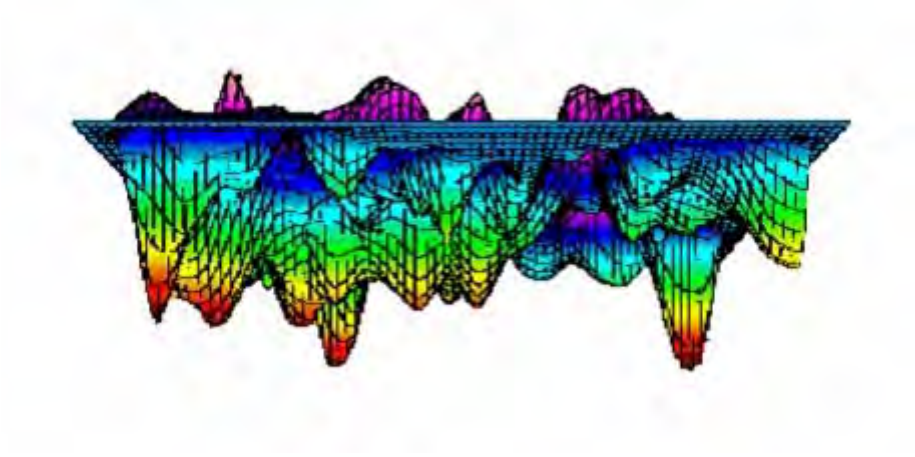

Figure A2.3: False colour 3D vorticity map viewed from the side for high Richardson number $Ri = 8.8$ at time $t = 1$ sec or $3.8\,Nt$.

An alternative plot for the vorticity, showing the region of low turbulence in white is presented in figures A2.3 and A2.4 viewed from different view points. (red is negative vorticity, while blue-violet indicates positive vorticity.

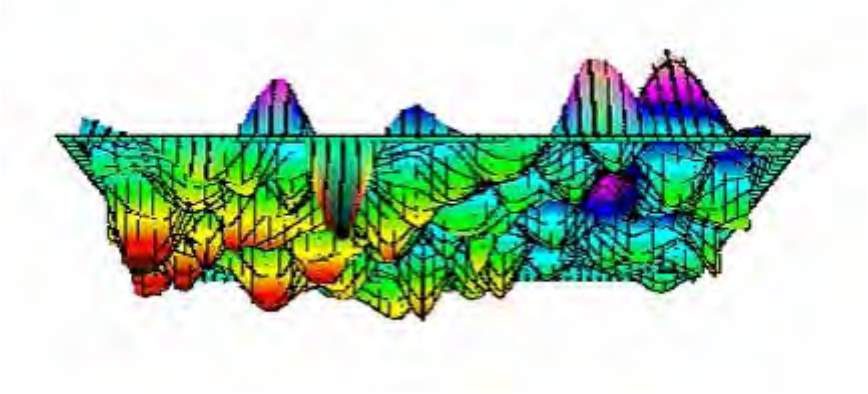

Figure A2.4: False colour 3D vorticity map for high Richardson number $Ri = 8.8$, viewed from below to identify better the negative (clockwise) vortices at time $t = 1$ sec or $3.8\,Nt$.

The values of vorticity for each of the points of the analysis plane, which was a region in the centre of the 1mx1m Perspex box of 90cm x 50cm at a resolution of 352 pixels in *x* and 288 pixels in *y*. so the average precision of the spatial coordinates were 1.7 mm in the vertical and 2.5 mm in the horizontal. All of the 103377 points are plotted with their interpolated vorticity values as a sequence line by line in figure A2.5.

The values of enstrophy for each of the points are plotted also as a sequence line by line in figure A2.6, these plots are very useful to check the range of values at each

time and to calculate the PDF`s and spectra of the different descriptors, i.e. velocity, velocity components, vorticity, shear, stream function, dissipation etc.

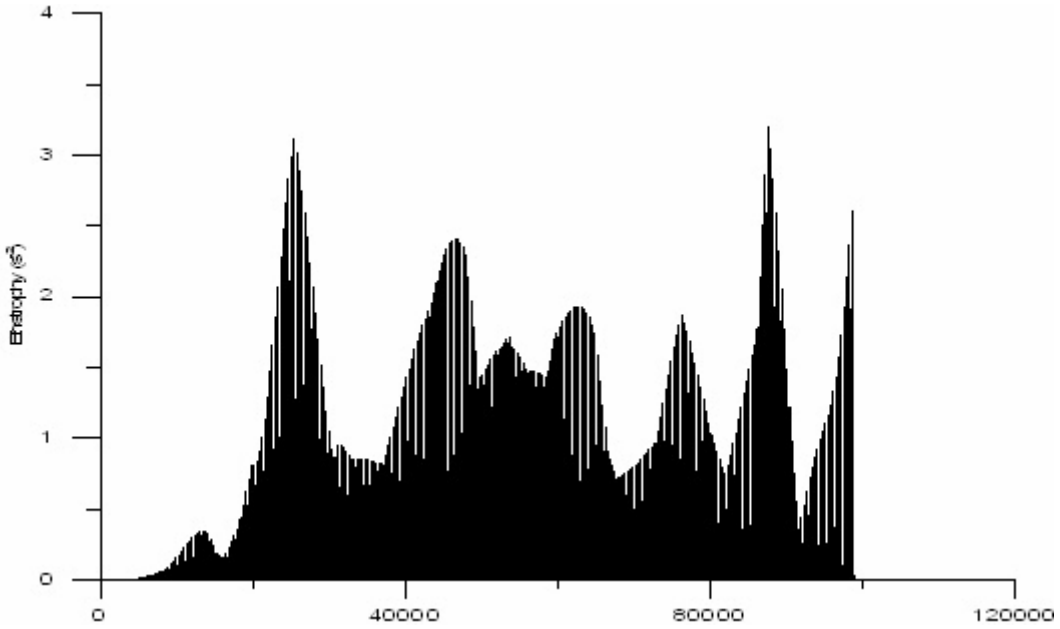

Figure A2.5: Line by line vorticity squared or enstrophy values from a 2D plot for high Richardson number $Ri = 8.8$ at time $t = 1$ sec or $3.8\,Nt$.

The values of an estimate of the local dissipation calculated as the square of the local derivatives of the vorticity for each of the points are plotted as a sequence line by line in figure A2.6.

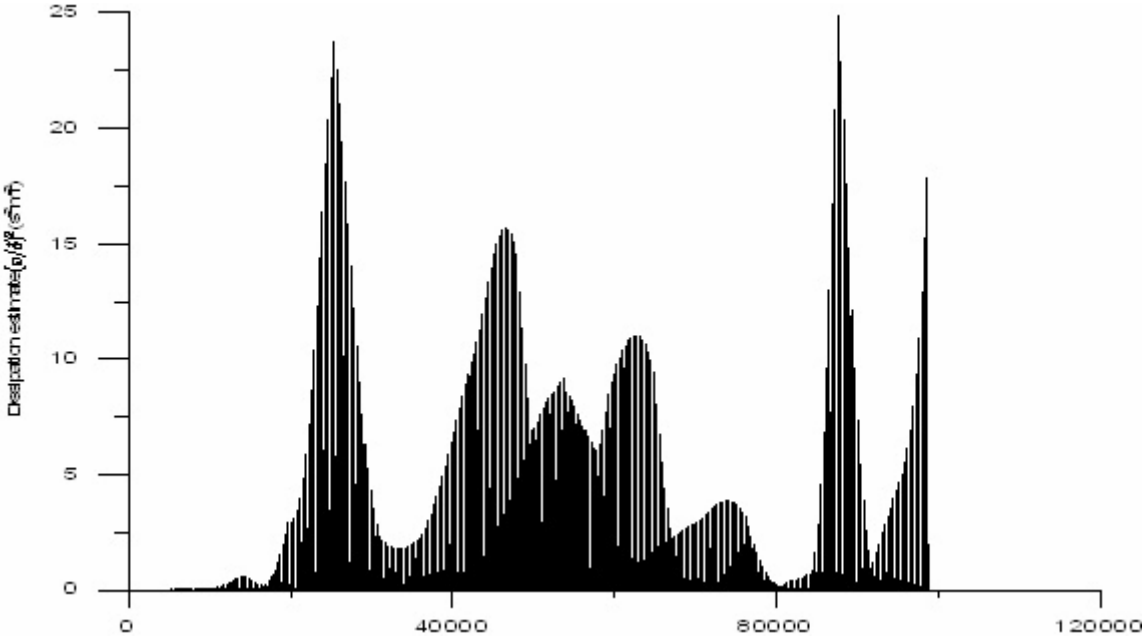

Figure A2.6: Line by line values of dissipation estimated from vorticity derivates squared for high Richardson number $Ri = 8.8$ at time $t = 1$ sec or $3.8\,Nt$.

The enstrophy was calculated directly squaring the vorticity point by point. A measure of dissipation could be easily calculated by finding for each point, except for the lower and right row and column of data the following expression:

$$\varepsilon = \left(\frac{\partial \omega}{\partial x} \right)^2 \qquad \text{(A2.1)}$$

In what follows a sequence of vorticity and velocity 2D plots for a high Richardson number, $Ri = 8.8$ will be shown, for different times $t = 2$, until 500 seconds. Different types of plots used will be shown as examples of the use of DigImage and DigiFlow fluid analysis programes.

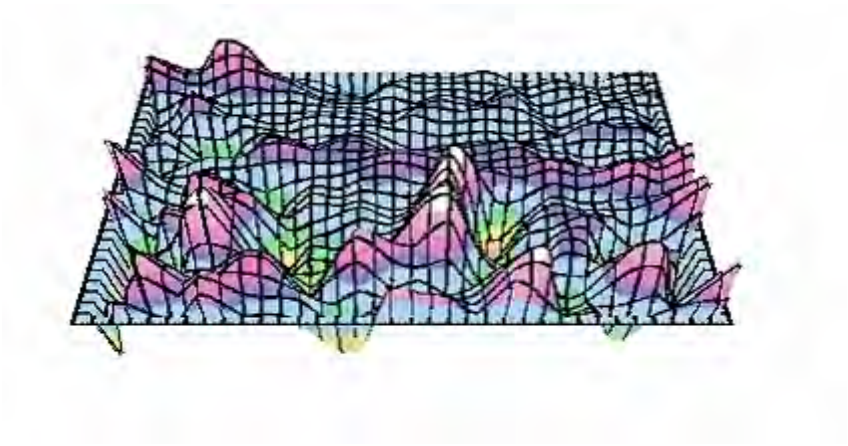

Figure A2.7: False colour 3D vorticity map for a high Richardson number $Ri = 8.8$, viewed from below to identify better the negative (clockwise) vortices at time $t = 1$ sec or $3.8\,Nt$.

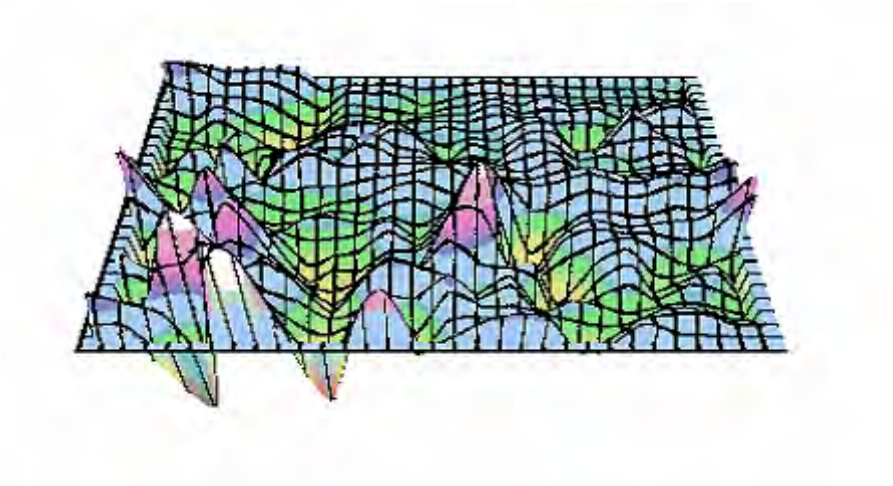

Figure A2.8: False colour 3D vorticity map for a high Richardson number $Ri = 8.8$, viewed from below to identify better the negative (clockwise) vortices at time $t = 1$ sec or $3.8\,Nt$.

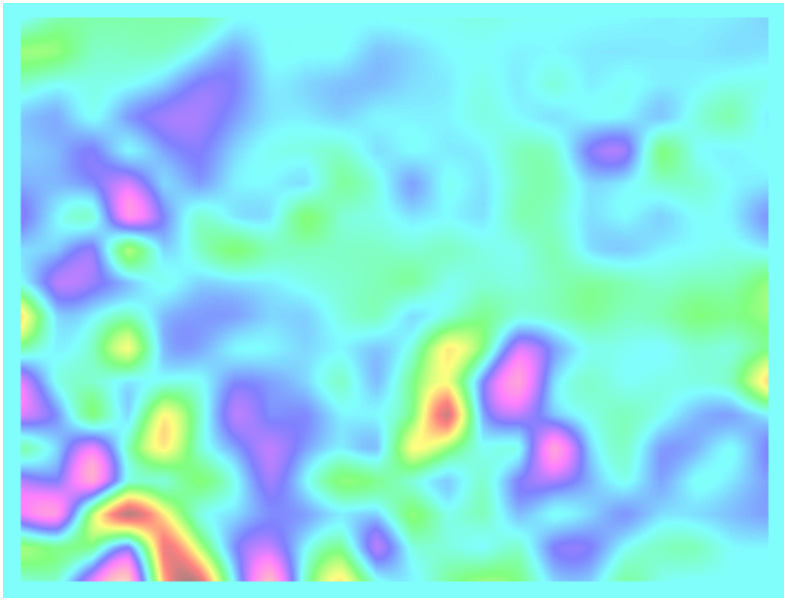

Figure A2.9: False colour vorticity map for a high Richardson number $Ri = 8.8$, for a side view of a density interface at time $t = 1$ sec or $3.8\,Nt$.

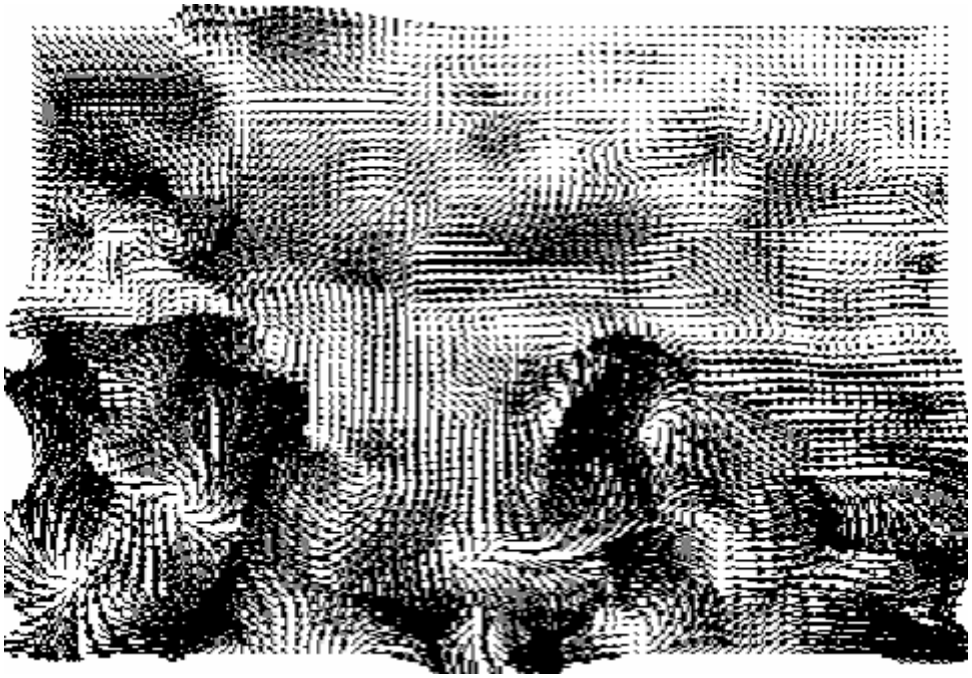

Figure A2.10: A side view of the velocity plot of a stratified density interface.

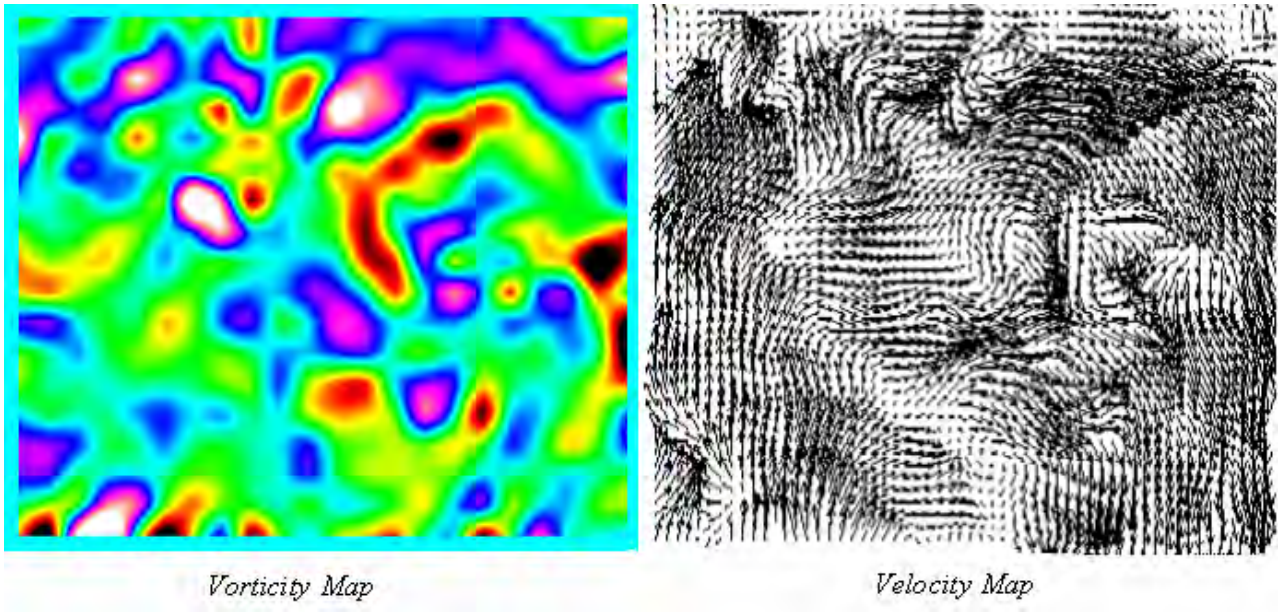

Figure A2.11: False colour vorticity and velocity plots.

APPENDIX 3

Examples of DigiFlow analysis

Here we show some alternative visualization and analysis tools used on the image processing used to map the centre-plane at the maximum Brunt-Väisällä frequency in the stratified rotating experiments described in this thesis. The video used was either a standard VHS or a Super VHS at a sampling rate of 50 Hz, the camera was a *Cohu* high resolution black and white CCD. Faster camera speeds in digital format up to 100 Hz did not improve the resolution.

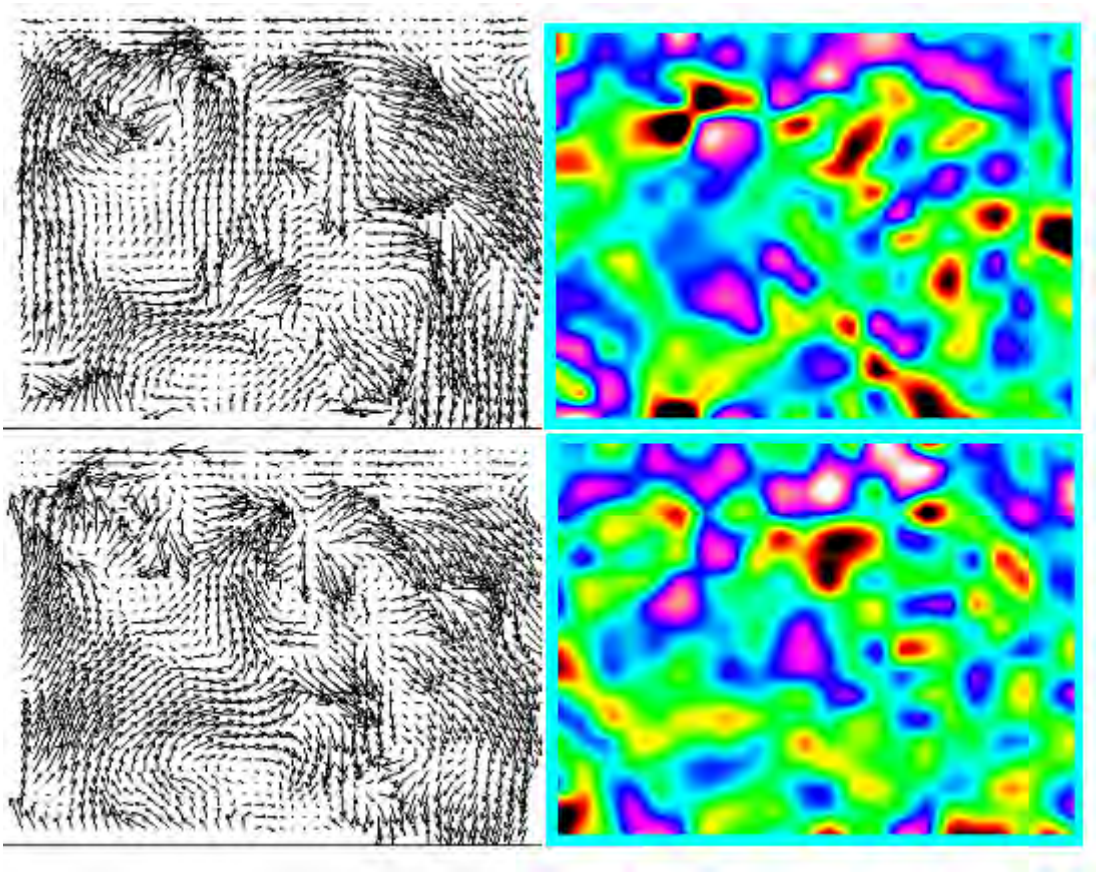

Fig A3.1: Pair of velocity and vorticity images in a lateral grid stirred flow in the Trondheim rotating facility, Ro =0.7 and Ri = 3.2.

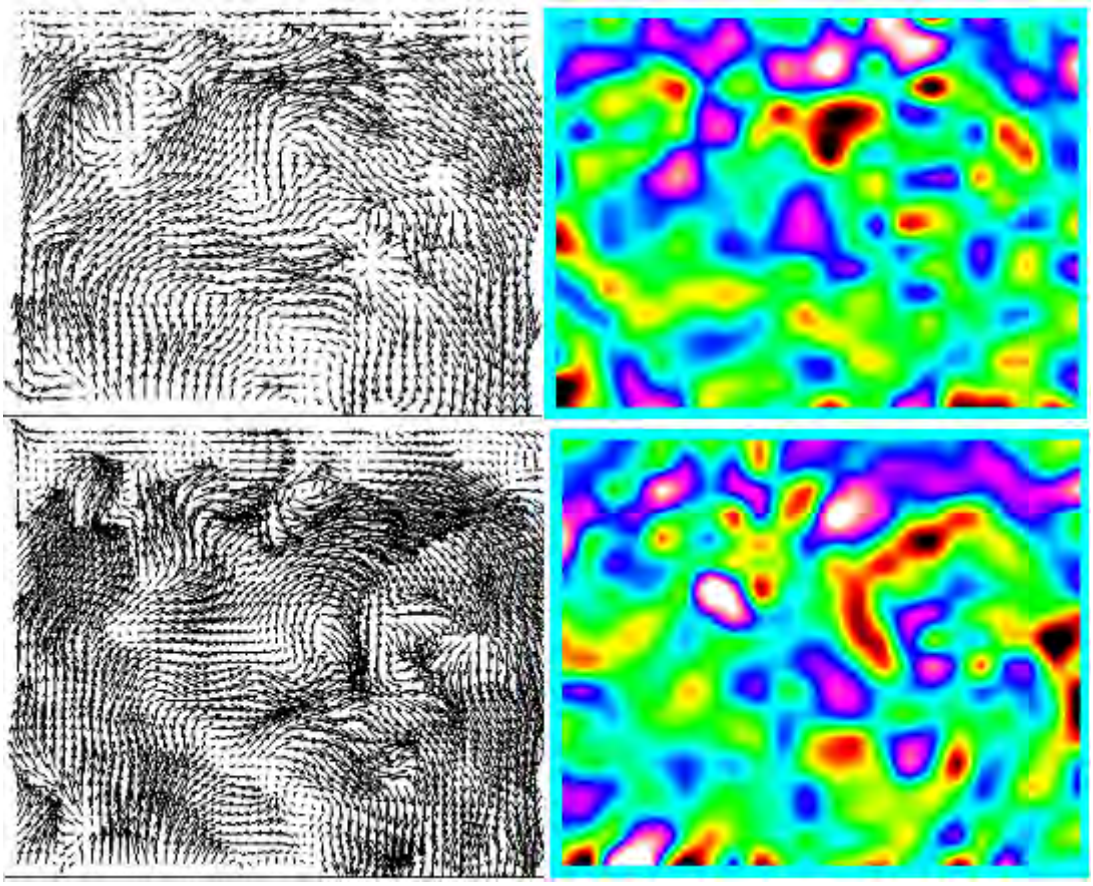

Fig A3.2: Pair of velocity and vorticity images in a lateral grid stirred flow in the Trondheim rotating facility, Ro =0.7 and Ri = 3.2 separated 88 frames i.e. 1.76 s

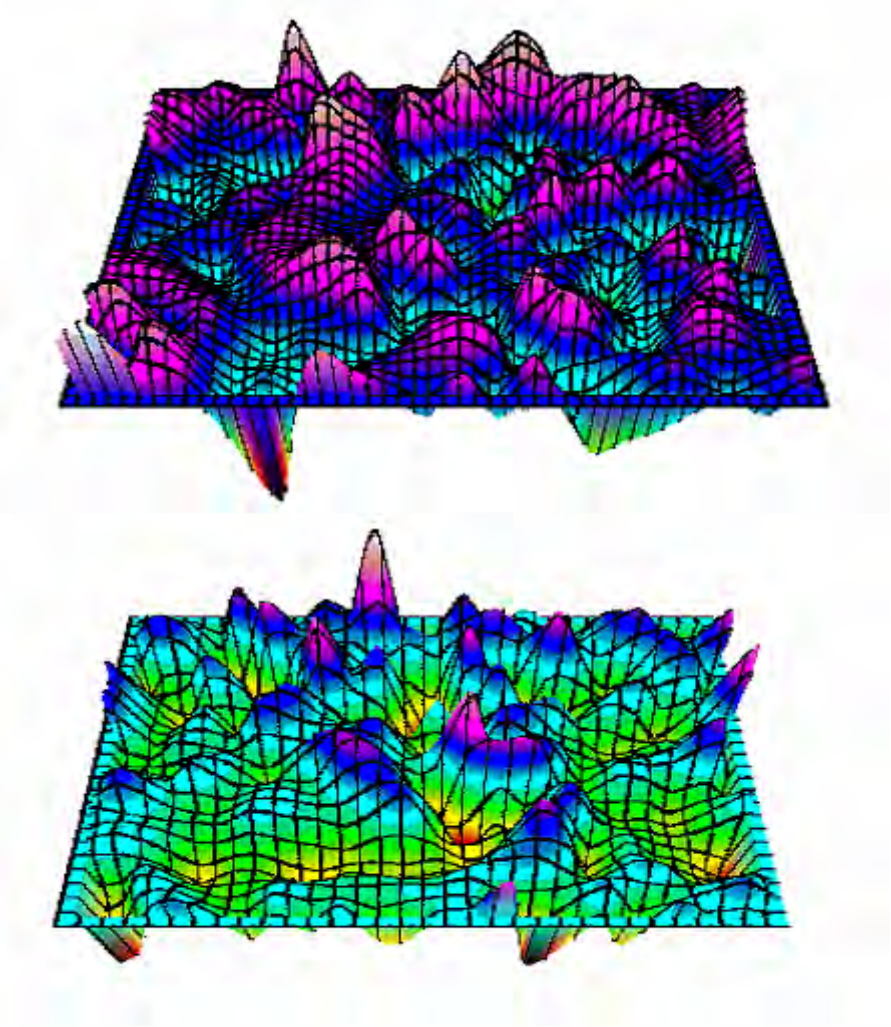

Fig A3.3: Pair of 3D vorticity maps of the images presented at A3.1 lateral grid stirred flow in the Trondheim rotating facility, Ro =0.7 and Ri = 3.2.

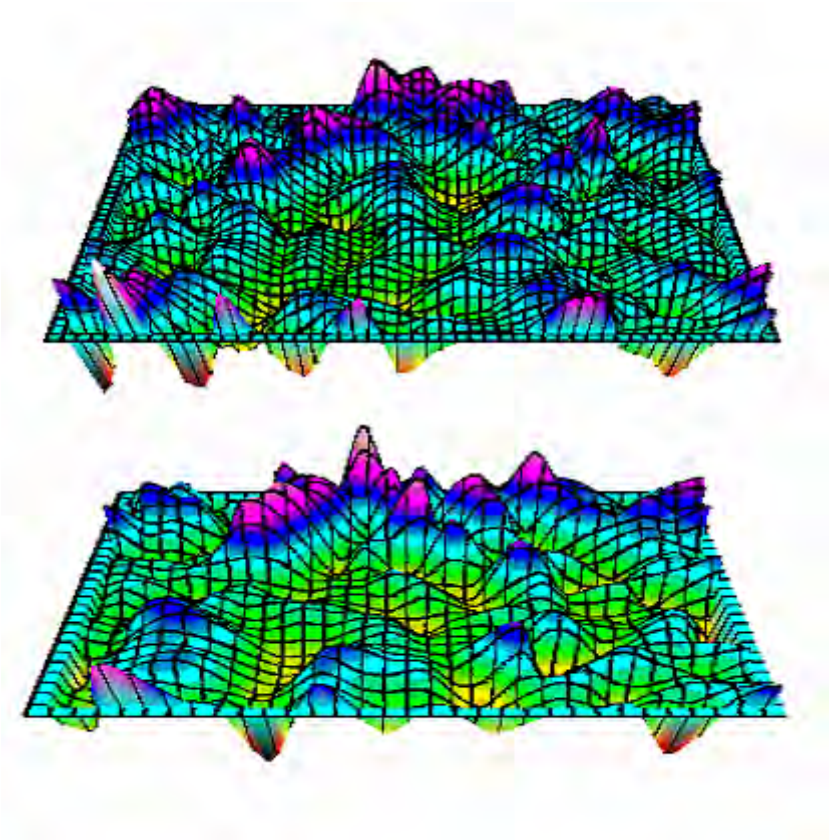

Fig A3.4: Pair of 3D vorticity maps of the images presented at A3.2 in a lateral grid stirred flow in the Trondheim rotating facility, Ro =0.7 and Ri = 3.2.

Fig A3.5: High resolution velocity map of a vertical grid stirred decaying flow in the Trondheim rotating facility, Ro =1.3 and Ri = 0.002 at 2 seconds after the grid drop.

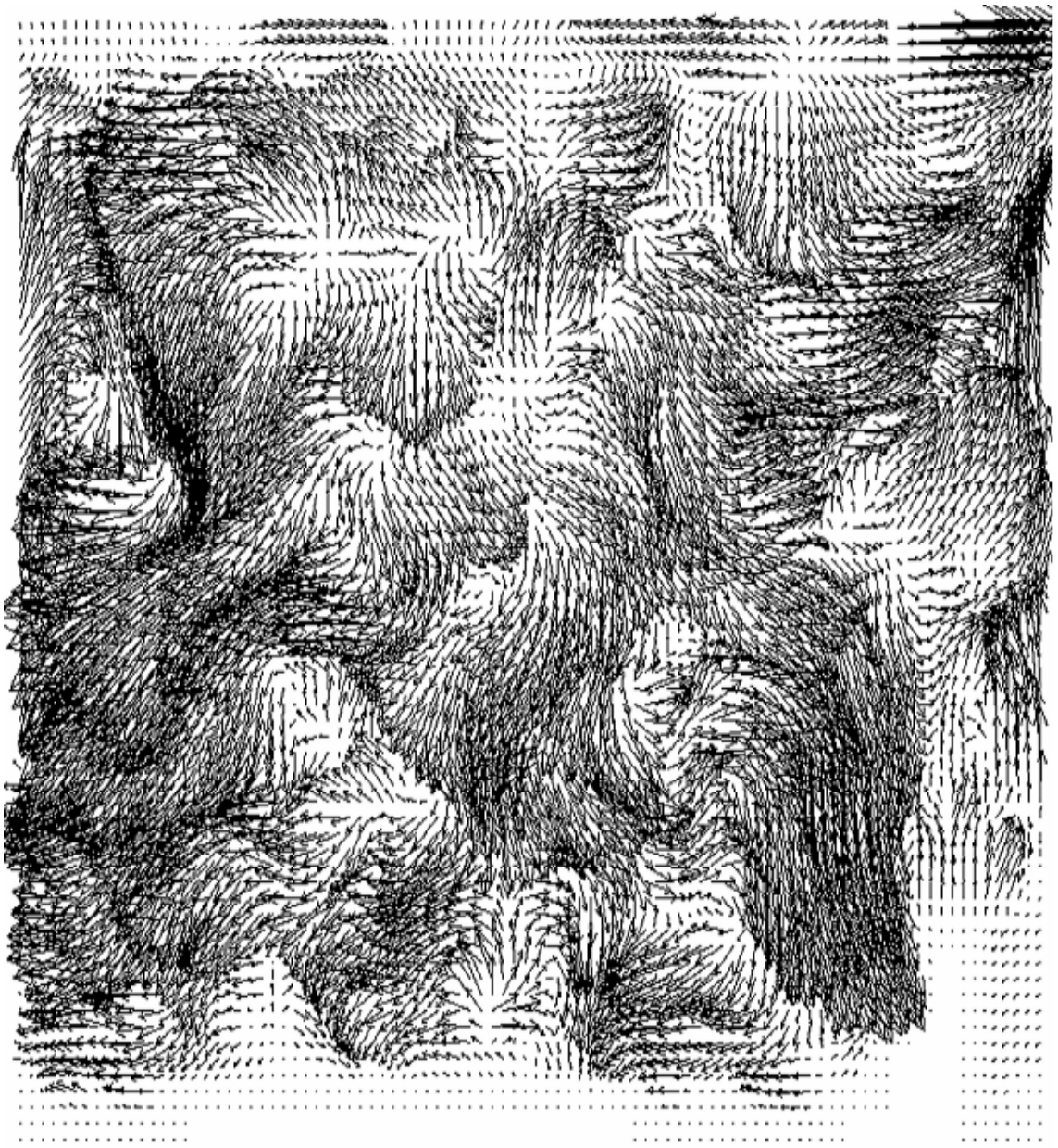

Fig A3.6: High resolution velocity map of a vertical grid stirred decaying flow in the Trondheim rotating facility, Ro =1.3 and Ri = 0.002 at 25 seconds after the grid drop.

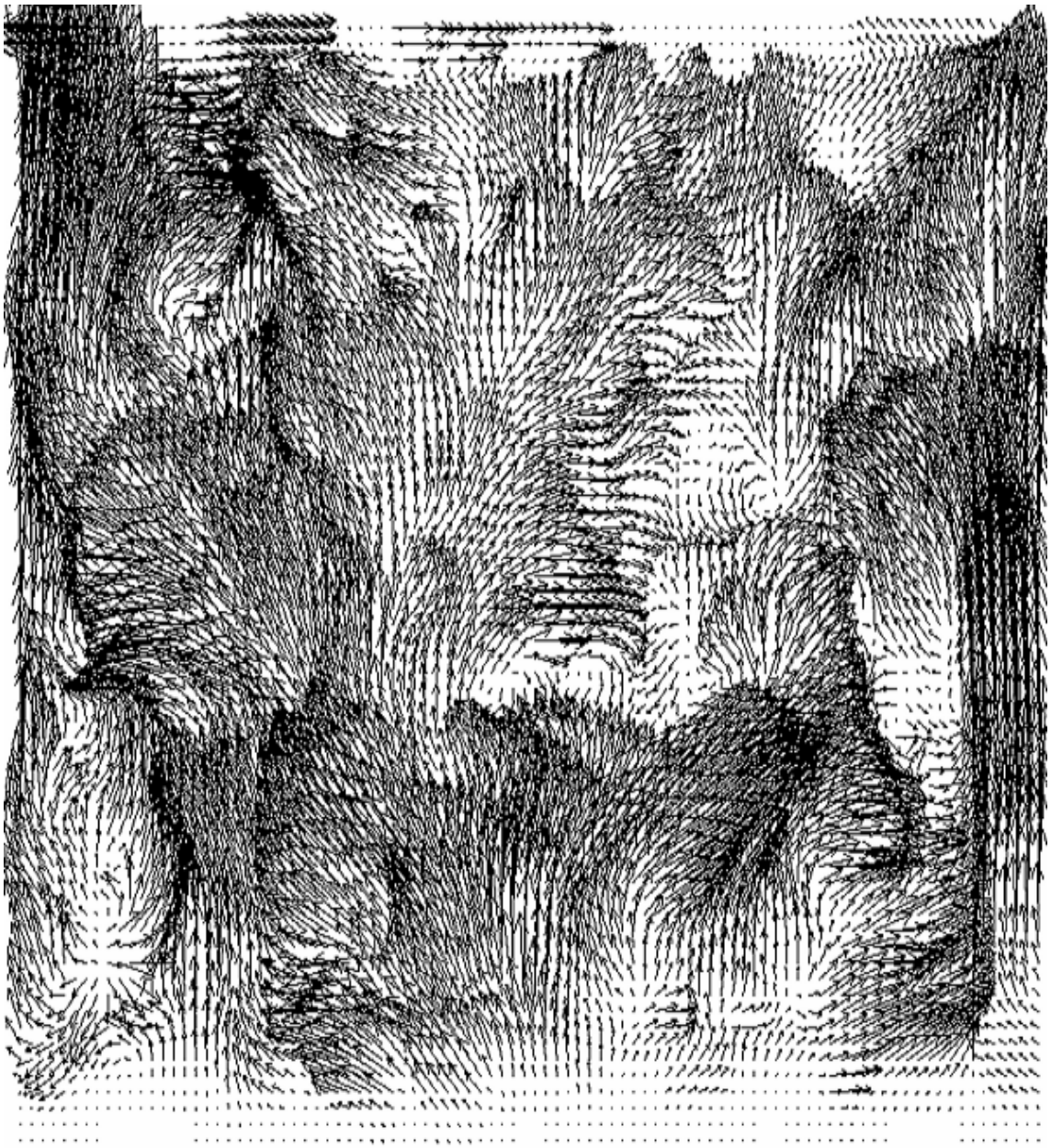

Fig A3.7: High resolution velocity map of a vertical grid stirred decaying flow in the Trondheim rotating facility, Ro =1.3 and Ri = 0.002 at 200 seconds after the grid drop.

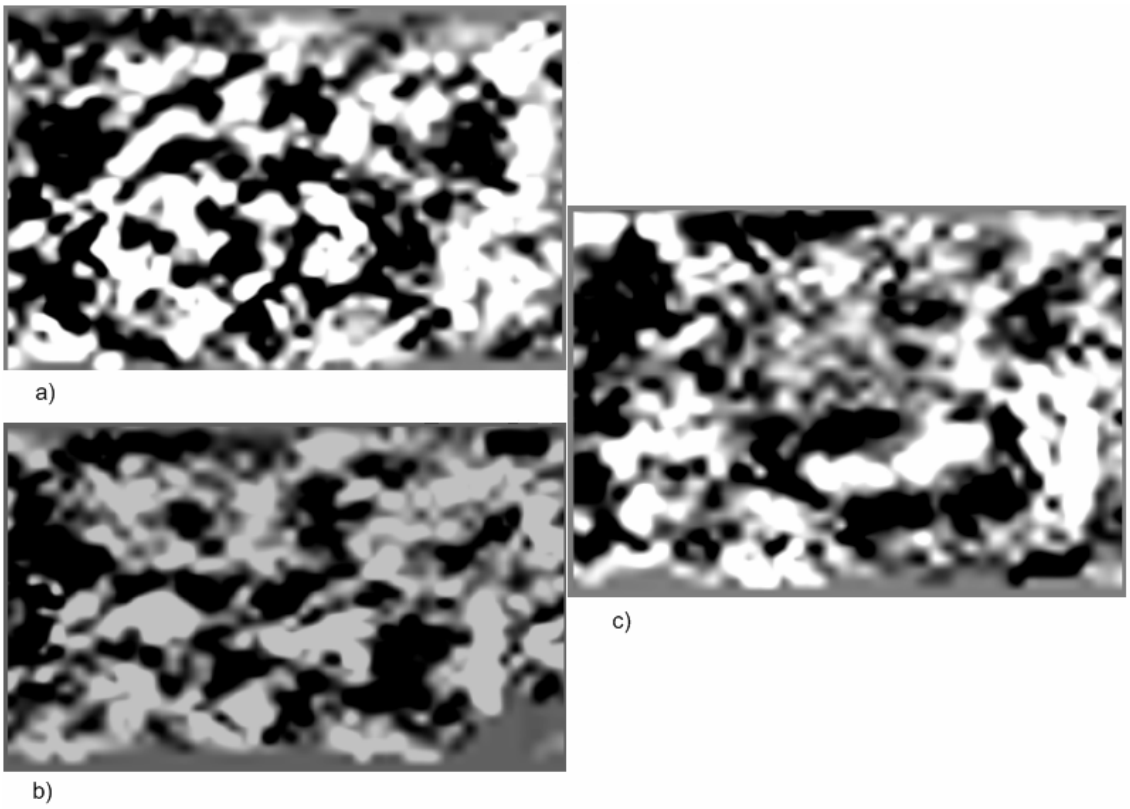

Fig A3.8: Vorticity maps of a vertical grid stirred decaying flow in the Trondheim rotating facility, Ro =1.3, for the three velocity plots seen in figures A3.5, a) A3.6 b) and A3.7 c). The multiscale features were investigated with multifractal analysis (see Chapter 5)

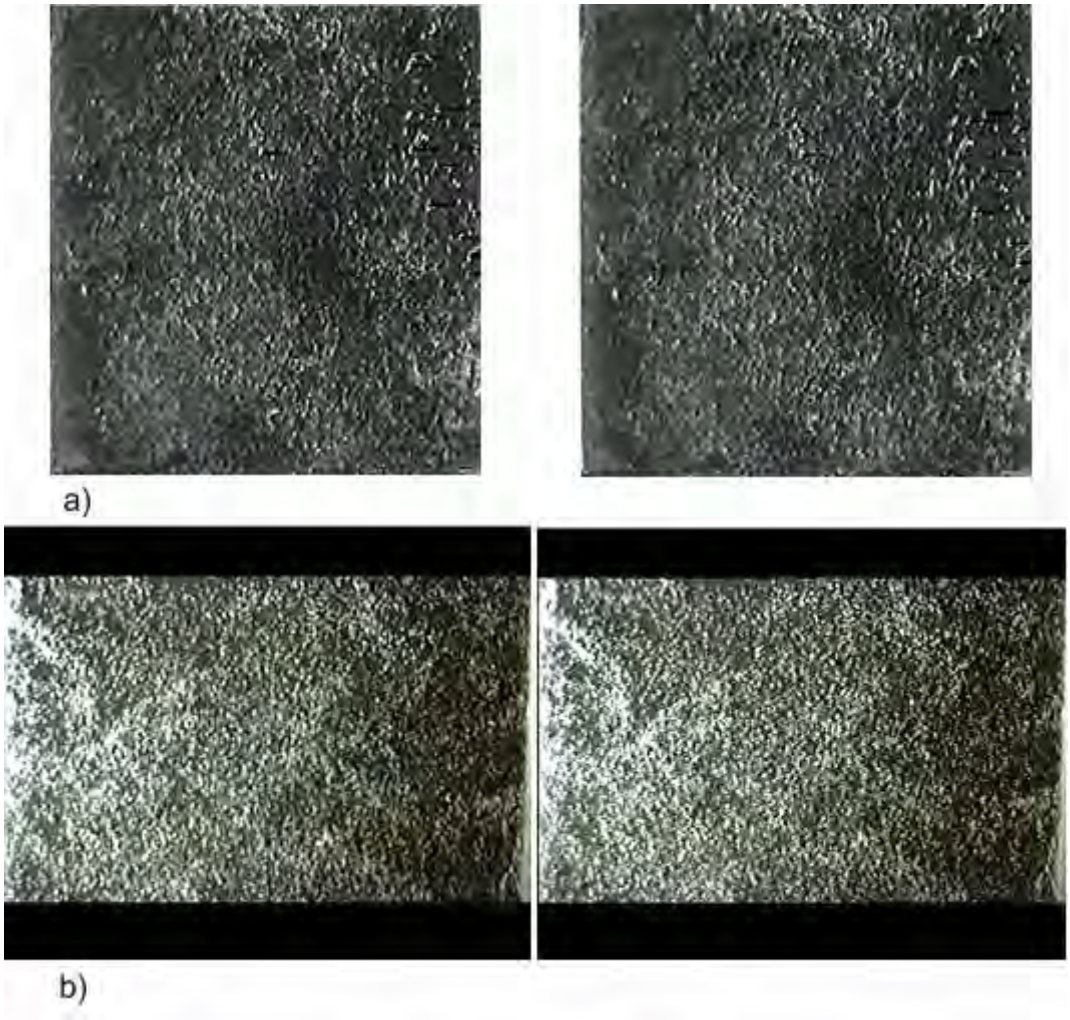

Fig A3.9: Pliolite particle sequences, separated 8 frames at 50 Hz of a) vertical grid stirred decaying flow in the Trondheim rotating facility, Ro =1.3 and Ri = 0.65. b) Non rotating flow in a 1mx1m tank (experiment 2b at 2 seconds after the grid passage.

APPENDIX 4

The Local structure of turbulence for large Reynolds Numbers (Based on Kolmogorov 1941 and Monin and Yaglom 1975)

From a more theoretical view point it is usual to denote

$$u_\alpha(P) = u_\alpha(x_1,x_2,x_3,t), \qquad \alpha = 1,2,3, \tag{A4.1}$$

The (turbulent) components of velocity at time *t* and at point *P* given in Cartesian rectangular coordinates (x_1,x_2,x_3). Considering turbulence, as a complex random process it is natural to assume the components of velocity $u_\alpha(P)$ at each point $P = (x_1,x_2,x_3,t)$ of a four dimensional space/time dominium, $G(x_1,x_2,x_3,t)$ are *aleatory variables i*n the sense of probability theory.

Denoting as $\bar{A}$ the mathematical expectation of the random variable *A*, it is supposed that the variations are smooth, and well behaved, so

$$\bar{u}_\alpha^2 y\left(du_\alpha / dx_\beta\right)^2 \tag{A4.2}$$

are finite and bounded in each sub-dominium within *G*.

Introducing in the four dimensional space (x_1,x_2,x_3,t) new normalised coordinates as:

$$\left.\begin{aligned} y_\alpha &= x_\alpha - x_\alpha^{(0)} - u_\alpha(P^{(o)})(t - t^{(0)}), \\ s &= t - t^{(0)}, \end{aligned}\right\} \tag{A4.3}$$

where

$$P^{(0)} = (x_1^{(0)}, x_2^{(0)}, x_3^{(0)}, t) \tag{A4.4}$$

is a point within space *G*. We note that coordinates y_α of any point *P* depend randomly on variables $u_\alpha\left(P^{(0)}\right)$so they are also random. The velocity in terms of the new coordinates is:

$$w_\alpha(P) = u_\alpha(P) - u_\alpha(P^{(0)}) \tag{A4.5}$$

We also suppose that the $u_\alpha\left(P^{(0)}\right)$ for all $P^{(k)}$, $k = 1,2, \ldots,n$, with coordinates $y_\alpha^{(k)}$ y $s^{(k)}$ lie within dominium G. Then we may define a PDF distribution in a 3n-dimensional space of the probabilities F_n for each

$$w_\alpha^{(k)} = w_\alpha(P^{(k)}), \quad \alpha = 1,2,3; \quad k = 1,2,...,n, \tag{A4.6}$$

where $u_\alpha^{(0)} = u_\alpha(P^{(0)})$ are known.

The distribution of the F_n will depend on parameters $x_\alpha^{(0)}, t^{(0)}, u_\alpha^{(0)}, y_\alpha^{(k)}, s^{(k)}$.

Definition 1:
Turbulence is locally homogenous in domain G, if for each fix $n, y_\alpha^{(k)}$ y $s^{(k)}$ the distribution F_n is independent of $x_\alpha^{(0)}, t^{(0)}$ y $u_\alpha^{(0)}$ if all points $P^{(k)}$ are situated en G.

Definition 2: Turbulence is locally isotropic in domain G, if it is homogenous and also the distribution law is invariant with respect to rotations and reflexions of the system of coordinates (x_1,x_2,x_3).

Comparing with the notion of *isotropic turbulence*, introduced by Taylor (1932), this definition is more restrictive in the sense that F_n needs to be regular since $t^{(0)}$, i.e the regularity in time is wider because the restrictions are imposed on distribution laws of velocity differences and not on velocity.

We assume that in a turbulent flow with sufficiently large Reynolds number $R = \frac{LU}{\nu}$. The hypothesis of local isotropy is observed in small domains G of the four dimensional space (x_1,x_2,x_3,t) where the spatial size is small in comparison with dimensions L for space and in a time given as: $T = \frac{U}{L}$.

Denoting y as the vector with components y_1,y_2,y_3, the variables

$$w_\alpha(y) = w_\alpha(y_1, y_2, y_3) = u_\alpha(x_1 + y_1, x_2 + y_2, x_3 + y_3, t) - u_\alpha(x_1, x_2, x_3, t). \tag{A4.7}$$

are random and assuming local isotropy means that the distribution law is independent of x_1,x_2,x_3, y *t.* so

$$w_\alpha(y) = 0. \tag{A4.8}$$

and considering the second order moments

$$B_{\alpha\beta}(y^{(1)}, y^{(2)}) = \frac{1}{2}\left[B_{\alpha\beta}(y^{(1)}, y^{(1)}) + B_{\alpha\beta}(y^{(2)}, y^{(2)}) - B_{\alpha\beta}(y^{(2)} - y^{(1)}, y^{(2)} - y^{(1)})\right] \tag{A4.9}$$

and then for $B_{\alpha\beta}(y,y)$ we have

$$B_{\alpha\beta}(y, y) = \overline{B}(r)\cos\theta_\alpha \cos\theta_\beta + \delta_{\alpha\beta} B_{nn}(r), \tag{A4.10}$$

where

$$r^2 = y_1^2 + y_2^2 + y_3^2, \quad y_\alpha = r\cos\theta_\alpha, \quad \delta_{\alpha\beta} = 0 \text{ for } \alpha \neq \beta, \quad \delta_{\alpha\beta} = 1 \text{ for } \alpha = \beta, \tag{A4.11}$$

$$\left.\begin{aligned} \overline{B}(r) &= B_{dd}(r) - B_{nn}(r), \\ B_{dd}(r) &= \left[w_1(r,0,0)\right]^2, \\ B_{nn}(r) &= \left[w_2(r,0,0)\right]^2 \end{aligned}\right\} \tag{A4.12}$$

for $r = 0$, we have

$$B_{dd}(=) = B_{nn}(0) = \frac{\partial}{\partial r} B_{dd}(0) = \frac{\partial}{\partial r} B_{nn}(0) = 0, \tag{A4.13}$$

$$\left.\begin{aligned} \frac{\partial^2}{\partial r^2} B_{dd}(0) &= 2\left(\frac{\partial w_1}{\partial y_1}\right)^2 = 2a^2, \\ \frac{\partial^2}{\partial r^2} B_{nn}(0) &= 2\left(\frac{\partial w_2}{\partial y_1}\right)^2 = 2a_n^2. \end{aligned}\right\} \tag{A4.14}$$

These equations were derived without the assumption of incompressibility. If we also make this assumption then

$$r\frac{\partial B_{dd}}{\partial r} = -2\overline{B}, \tag{A4.15}$$

so we may express B_{nn} from B_{dd}. Then it follows that $a_n^2 = 2a^2$. It is easier (assuming incompressibility) to evaluate the dissipation of energy per unit time and per unit mass as:

$$\overline{\varepsilon} = \nu\left[2\left(\frac{\partial w_1}{\partial y_1}\right)^2 + 2\left(\frac{\partial w_2}{\partial y_2}\right)^2 + 2\left(\frac{\partial w_3}{\partial y_3}\right)^2 + \left(\frac{\partial w_2}{\partial y_1} + \frac{\partial w_1}{\partial y_2}\right)^2 + \left(\frac{\partial w_3}{\partial y_2} + \frac{\partial w_2}{\partial y_3}\right)^2 + \left(\frac{\partial w_1}{\partial y_3} + \frac{\partial w_3}{\partial y_1}\right)^2\right] =$$
$$= 15\nu a^2.$$

with the transformation of coordinates

$$y'_\alpha = \frac{y_\alpha}{\eta}$$
$$s' = \frac{s}{\sigma} \tag{4.16}$$

the velocities, kinematic viscosity and the average dispersion of energy are expressed in this new coordinate system as:

$$w'_\alpha = w_\alpha \frac{\sigma}{\eta}$$
$$\nu' = \nu\frac{\sigma}{\eta^2} \tag{4.17}$$
$$\overline{\varepsilon}' = \overline{\varepsilon}\frac{\sigma^3}{\eta^2}$$

The basis hypothesis used by Kolmogorov were first hypothesis of similarity is locally isotropic for turbulence, the distributions F_n are fixed only by properties ν and $\overline{\varepsilon}$. So we have

$$\eta = \lambda = \sqrt{(\nu/\alpha)} = \nu^{\frac{3}{4}} / \bar{\varepsilon}^{\frac{1}{4}}$$
$$\sigma = 1/\alpha = \sqrt{(\nu/\bar{\varepsilon})} \qquad \text{(A4.18)}$$

Being common to assume $\nu' = 1$, $\bar{\varepsilon} = 1$. With the similarity hypothesis the functions

$$B'_{dd}(r') = \beta_{dd}(r') \qquad \text{(A4.19)}$$

should be equal for all cases of locally isotropic turbulence, so we have

$$B_{dd}(r) = \sqrt{(\nu\bar{\varepsilon})}\beta_{dd}(r/\lambda) \qquad \text{(A4.20)}$$

the second moment $B_{\alpha\beta}(y^{(1)},y^{(2)})$ is then expressed only in terms of $\nu, \bar{\varepsilon}$ and the universal function β_{dd}. To determine the behaviour of $\beta_{dd}(r')$ for large distances r' Kolmogorov introduced another hypothesis, called The second hypothesis of similarity where: if the modulus of vectors $y^{(k)}$ and their differences $y^{(k)}$-$y^{(k')}$ (where $k \neq k'$) are large compared with λ, Then the distribution laws F_n are only determined by $\bar{\varepsilon}$ and do not depend on viscosity ν because

$$y''_{\alpha} = \frac{y'_{\alpha}}{k^3}$$
$$s'' = \frac{s'}{k^2} \qquad \text{(A4.21)}$$

where y'_{α} y s' are determined by the above equations, because $k\bar{\varepsilon}' = \bar{\varepsilon}'' = 1$, for large r' in comparison with $\lambda' = 1$ the hypothesis seems valid

$$B''_{dd}(r'') \approx B'_{dd}(r'') = B_{dd}(r'/k^3) \qquad \text{(A4.22)}$$

and we have

$$B''_{dd}(r'') = k^{-2}B'_{dd}(r') = k^{-2}B_{dd}(r'). \qquad \text{(A4.23)}$$

so for large r'

$$B_{dd}(r'/k^3) \approx k^{-2} B_{dd}(r'), \tag{A4.24}$$

Deducing that

$$B_{dd}(r') \approx C(r')^{\frac{2}{3}}, \tag{A4.25}$$

where C is claimed to be an universal constant. So we have for large r compared with λ

$$B_{dd}(r) \approx C\bar{\varepsilon}^{\frac{2}{3}} r^{\frac{2}{3}}. \tag{A4.26}$$

and also

$$B_{nn}(r) \approx \frac{4}{3} B_{dd}(r). \tag{A4.27}$$

On the other hand for small r compared with λ, the relation

$$B_{nn}(r) \approx 2B_{dd}(r). \tag{A4.28}$$

is then obtained.

A4.1. Dissipation of energy in locally isotropic turbulence

Kolmogorov introduced

$$\left.\begin{aligned} B_{dd}(r) &= \left[u_d(M') - u_d(M)\right]^2, \\ B_{nn}(r) &= \left[u_n(M') - u_n(M)\right]^2, \end{aligned}\right\} \tag{A4.29}$$

where r denotes distance between points M and M', $u_d(M)$ and $u_d(M')$ being the components of velocity in the direction $\overline{MM'}$ in points M y M', and $u_n(M)$ y $u_n(M')$ are the components of the velocity in any direction, perpendicular to MM'. So we will need the third order moments

$$B_{ddd}(r) = \left[u_d(M') - u_d(M)\right]^3. \tag{A4.30}$$

and for turbulence, which is locally isotropic and incompressible, then we have equation

$$4\overline{E} + \left(\frac{dB_{ddd}}{dr} + \frac{4}{r}B_{ddd}\right) = 6\nu\left(\frac{d^2B_{dd}}{dr^2} + \frac{4}{r}\frac{dB_{dd}}{dr}\right) \tag{A4.31}$$

similar to Karman equation for isotropic turbulence. Herein $\overline{E}$ denotes the dissipation of energy averaged per unit mass. The above equation may be written as

$$\left(\frac{d}{dr} + \frac{4}{r}\right)\left(6\nu\frac{dB_{dd}}{dr} - B_{ddd}\right) = 4\overline{E} \tag{A4.32}$$

and because of condition $(d/dr)\,B_{dd}(0) = B_{ddd}(0) = 0$, we have

$$6\nu dB_{dd}/dr - B_{ddd} = \frac{4}{5}\overline{E}r. \tag{A4.33}$$

For small r we have:

$$B_{dd} \approx \frac{1}{15}\overline{E}r^2 / \nu, \tag{A4.34}$$

so that

$$6\nu dB_{dd} / dr \approx \frac{4}{5}\overline{E}r. \tag{A4.35}$$

so the second term or the left side is comparable with the first one for small *r* (infinitesimal), but for large values of *r*, the first term may be ignored en comparison with the second one so:

$$B_{ddd} \approx -\frac{4}{5}\overline{E}r. \tag{A4.36}$$

which is the famous 4/5 Kolmogorov law.

It is natural to assume for large *r* the ratio

$$S = B_{ddd} : B_{dd}^{\frac{3}{2}}, \tag{A4.37}$$

so

$$B_{dd} \approx C\vec{E}^{\frac{2}{3}} r^{\frac{2}{3}}, \tag{A4.38}$$

where $C = (-4/5S)^{\frac{2}{3}}$.

In Kolmogorov (1941), this relation was deduced slightly differently, and

$$\eta_k = (\nu^3 / \overline{E})^{\frac{1}{4}} \tag{A4.39}$$

supposing that

$$\left.\begin{aligned} B_{dd}(r) &= \sqrt{(v\overline{E})}B_{dd}(r/\eta_k), \\ B_{nn}(r) &= \sqrt{(v\overline{E})}B_{nn}(r/\eta_k), \end{aligned}\right\} \tag{A4.40}$$

where B_{dd} and B_{nn} are universal functions, so that for small $\rho = r/\eta_k$

$$\begin{aligned} B_{dd}(\rho) &\approx \frac{1}{15}\rho^2, \\ B_{nn}(\rho) &\approx \frac{2}{15}\rho^2 \end{aligned} \tag{A4.41}$$

and for large ρ

$$\begin{aligned} B_{dd}(\rho) &\approx C\rho^{\frac{2}{3}}, \\ B_{nn}(\rho) &\approx \frac{4}{3}C\rho^{\frac{2}{3}}. \end{aligned} \tag{A4.42}$$

In isotropic turbulence in the Taylor sense the distances have to be smaller than the integral lengthscale L of the turbulence, and the correlation coefficients are

$$\left.\begin{aligned} R_{dd}(r) &= \left(u_d(M')u_d(M)\right):b, \\ R_{nn}(r) &= \left(u_n(M')u_n(M)\right):b, \end{aligned}\right\} \tag{A4.43}$$

being b the average of the square of velocity components, which are related with the structure functions $B_{dd}(r)$ y $B_{nn}(r)$ by

$$\left.\begin{aligned} B_{dd}(r) &= 2b(1\text{-}R_{dd}), \\ B_{nn}(r) &= 2b(1\text{-}R_{nn}). \end{aligned}\right\} \tag{A4.44}$$

and we have for r small with respect to L,

$$\left.\begin{aligned} 1-R_{dd} &\approx \left(\sqrt{(v\overline{E})}/2b\right)\beta_{dd}(r/\eta_k), \\ 1-R_{nn} &\approx \left(\sqrt{(v\overline{E})}/2b\right)\beta_{nn}(r/\eta_k), \end{aligned}\right\} \tag{A4.45}$$

If r is small compared with L, but big with respect to λ, then we obtain:

$$1-R_{dd} \approx \frac{1}{2} C \overline{E}^{\frac{2}{3}} b^{-1} r^{\frac{2}{3}},$$
$$1-R_{nn} \approx \frac{2}{3} C \overline{E}^{\frac{2}{3}} b^{-1} r^{\frac{2}{3}}. \qquad \text{(A4.46)}$$

determining the constant C from experimental data which were performed for correlations R_{dd} y R_{nn} by Dryden, using the above equations in the following form.

$$1-R_{nn} \approx 2C(kr)^{\frac{2}{3}},$$
$$k = \overline{E} : (3b)^{\frac{3}{2}}, \qquad \text{(A4.47)}$$

which is named as Dryden equation.

APPENDIX 5

Horizontal non-homogeneous flow: coastal mixing

We present here a series of experimental results linked to the lateral non homogeneous stirring in surface flows and in stratified rotating flows that may be used to model coastal mixing, this is based on Matulka (2003), Matulka et al. (2008), Carrillo et al. (2001) and Redondo et al. (2004).

The sequence shown in figure A5.1 shows the generation of the coastal mixing front from the experiment described in Carrillo et al. (2001) where jets were used to stir a surface flows at one of the sides of the 1m x 1m tank described in chapter 2.

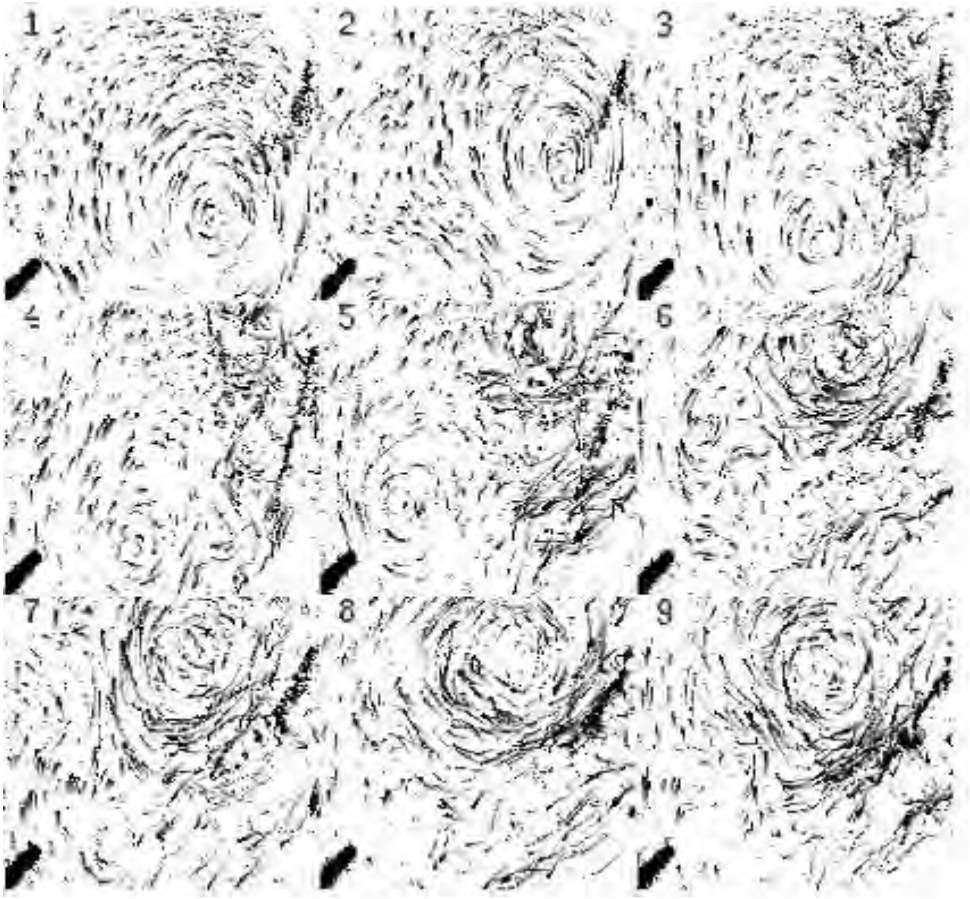

Figure A5.1: Time series from the advance of turbulent horizontal front in the one pump jet experiments. It shows frames during 15 seconds at times 0, 1, 3, 5, 7, 9, 11, 13 and 15 seconds after a steady state had been reached.

The two kinds of experiments developed with coastal current show a slow front advance adverted by the presence of a steady general circulation on the tank. From images such as the sequence shown in figure A5.1 we show the evolution of the front in figure A5.2.

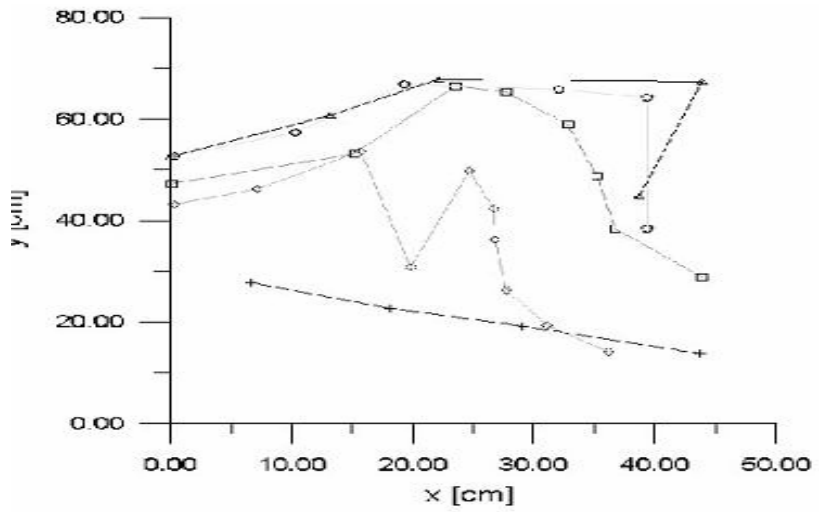

Figure A5.2: Advance of the front on the experiments with a lateral current in the two pump jet experiments, each series shows the average advance at time +: 0, ◊: 10, □: 20, o: 30 and Δ: 40 seconds.

An interesting example of confined circulation, where both stratification and rotation are important is the ocean, and more so in confined seas and in non-homogeneous coastal regions. Okubo (1971), Okubo and Ozmidov et al. (1980) and Ozmidov (1990) performed numerous experiments measuring effective sea surface diffusivities with dye and buoy releases and found the important role of coastal large eddies and coherent structures. In the Black sea there is also a quasi-permanent coastal vortex circulation; these types of coastal flows may be analyzed by satellite images as discussed in chapter 8 by means of different satellite sensors (SAR, Visible, Infrared, Chlorophyll color, Altimetry etc. Benjamin et al. 1999 and Platonov et al. 2005). We show in figure A5.3 from Afanasyev et al. (2003) a combination of in situ ship measurements together with satellite images that exhibits a complex upper layer general distribution, showing some characteristic eddies. In the same way Font (1998) found that in the north Africa Mediterranean Sea similar strong eddy structures were detected in this area. The appearance of distinctive eddies in the NW Mediterranean mostly generated or induced by coastal features and stirring indicates the practical need to investigate in detail these strongly non-homogeneous stratified rotating flows.

Figure A5.3: The main features of the upper layer general circulation, dashed and solid lines indicate recurrent features and eddies detected in the Black sea. From Afanasyev et al (2003).

Figure A5.4 shows a direct comparison of the size distribution of the coastal induced vortices in the NW Mediterranean in the two pump experiments described by Matulka (2003) and Carillo et al. (2001).

We have seen in this experiment the dramatic effect that a strong density interface has both on vertical and horizontal mixing. The effect of density interfaces also tend to spread further the non-homogeneous lateral mixing akin to that taking place near the coastline. An intrusion spreading along the initially sharp interface generates strong vertical vorticity and may be used to define the limit of a coastal mixing front.

The evolution of such coastal mixing, even when there is an overall large scale coastal current may be seen in the sequence of particle tracking streaks. This front grows in time as shown in figure A5.2 and may even destroy the overall large scale circulation creating a new pattern of eddies of multiple sizes.

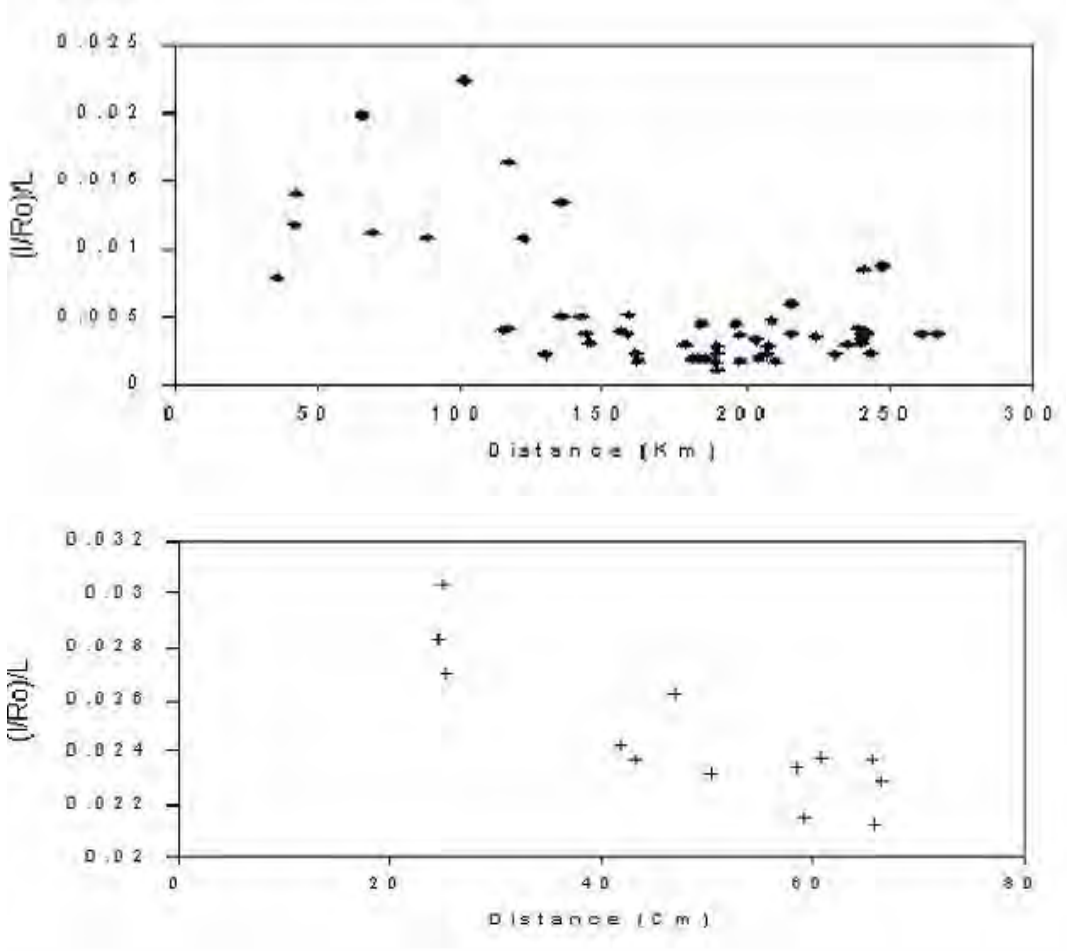

Figure A5.4: top) Histogram of the size distribution of the vortices with respect to the coastal length from Cape Begur during 1997 – 1998. bottom) The same distribution of vortex sizes from the experimental 1 x 1 m tank in the x, y axis, with x the jet stirred side.

There is strong asymmetry in the distribution of the vortices sizes which are caused by the interaction of a mixing front and a coastal current. Those features are seen in the simple non-rotating uniform experiments. The distribution of vortices shown in chapter 8 has to be very carefully parameterized with respect to the relevant non-dimensional numbers; mainly the Reynolds number, the Richardson number and the Rossby number (Redondo et al. 2001, 2006 and 2008) such as shown in figure A5.5.

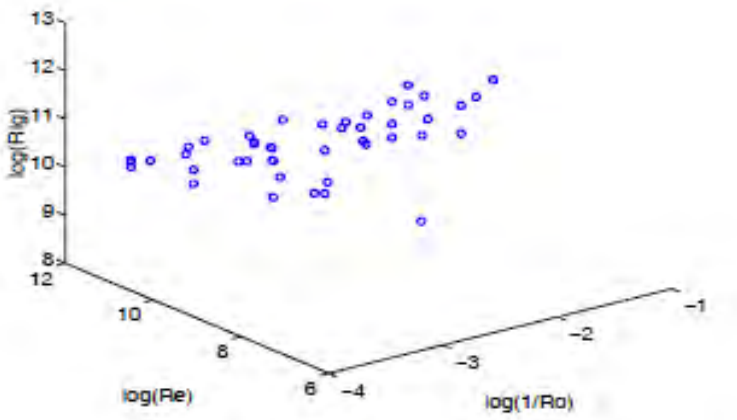

Figure A5.5: Experimental 3D parametric field from Ro, Re and Rig from the rotational experiments performed in the Coriolis table at the SINTEF laboratory.

Further work was performed at the Trondheim Corriolis platform to implement more realistic boundary conditions in the experiments using this time an oscillating grid, some results are presented in Cano et al.(2008).

APPENDIX 6

Molecular mixing and mixing efficiency

From the general equation of turbulent velocity autocorrelations discussed in chapter 2, where the dissipation of energy is derived and the main effect of body forces acting on the bulk of the fluid f_i:

$$\frac{\partial}{\partial t}\left(\frac{\overline{u_i^2}}{2}\right)+U_l\frac{\partial}{\partial x_l}\left(\frac{\overline{u_i^2}}{2}\right)=-\overline{u_i u_l}\frac{\partial U_i}{\partial x_l}-\frac{\partial}{\partial x_i}\left(\frac{\overline{p'u'_l}}{\rho}+\frac{\overline{u_i^2 u_l}}{2}\right)-\varepsilon-f(\nu)+\overline{f'u_i} \tag{A6.1}$$

$$\varepsilon=\nu\overline{\overline{\nabla\vec{u}\cdot\nabla\vec{u}}}$$

with the usual notation, and leaving a general viscous dissipation term *f*(ν) that extracts energy due to molecular viscosity on turbulence. The mass forces (*body forces*), even applying Boussinesq approximation with low inertia are dependent strongly on density fluctuations as well as the possible fluctuations of the actual applied forces, while these effects are considered negligible (i.e. variations of gravity, magnetic fields or rotation).

If we only consider density fluctuations then

$$\overline{u_i f_i}=\overline{u'\rho'}\,\overline{X}\Rightarrow\overline{w'\rho'}g \tag{A6.2}$$

that for gravity corresponds to vertical mixing.

If density diminishes with height, then $\partial\rho/\partial z<0$ so if *w'* is positive, the δενσιτψ φλυχτυατιον has to be negative and vice versa, so their correlation will be negative. Therefore the stable stratification acts as energy sink. When stratification is unstable and the fluid is top heavy then $\partial\rho/\partial z\geq 0$ and then the mixing of densities acts as an energy source. En a situation of negligible diffusion and body forces then turbulent production will balance dissipation.

$$-\overline{u_i u_j}\frac{\partial\overline{u_i}}{\partial\overline{x_j}}=P=\varepsilon \tag{A6.3}$$

with both production and dissipation with dimensions of L^2T^{-3} and we may use

$$\varepsilon\propto\frac{u'^3}{l}\Rightarrow\left[\frac{u'^2}{T}\right]\approx\frac{\left(-\overline{uv}\right)^{3/2}}{L} \tag{A6.4}$$

Relating the Reynolds stresses and a characteristic length scale to dissipation and applying to Navier Stokes equations to the correlation tensor as described in chapter 2 operating as $\overline{NS'_i u'_j} + \overline{u'_i NS'_j}$ leads to the transport equations:

$$\frac{\partial}{\partial t}\left(\frac{\overline{u_i u_j}}{2}\right) + U_l \frac{\partial \overline{u_i u_j}}{\partial x_l} =$$
$$-\left(\overline{u_i u_l}\frac{\partial U_j}{\partial x_l} + \overline{u_j u_l}\frac{\partial U_i}{\partial x_l}\right) + \overline{\frac{p'}{\rho}\left(\frac{\partial u_i}{\partial x_j} + \frac{\partial u_j}{\partial x_i}\right)} - \frac{\partial}{\partial x_l}\left(\overline{u_i u_j u_l}\right) - \frac{1}{\rho}\left(\frac{\partial}{\partial x_i}\overline{p' u'_j} + \frac{\partial}{\partial x_j}\overline{p' u'_i}\right) \quad \text{(A6.5)}$$
$$+\nu\left(\overline{u_i \frac{\partial^2 u_j}{\partial x_l^2}} + \overline{u_j \frac{\partial^2 u_i}{\partial x_l^2}}\right) + \left(\overline{f'_i u_j} + \overline{f'_j u_i}\right)$$

where the terms were explained in figure 4.10: Generation by shear (1), return to small scale isotropy by means of pressure fluctuations *p'* (2), The third rhs term of triple correlations produces transport due to the induced turbulence fluctuations (3). The fourth rhs term is pressure transport (4). The fifth is viscous, irreversible energy drain if the fluid is Newtonian, and the last term is the generation or destruction of turbulent kinetic energy TKE due to body forces, we will use the notation (*f* for rotation as the Coriolis parameter, *g* = *gk* for gravity and *B* for magnetic induced vector forces) (6)

If we restrict the flow to a zero mean flow, where only turbulence fluctuations produce mixing in a gravitation field. The equation of energy and significant change of fluctuations in the vertical axis, such as that of an oscillating grid flow (Redondo 1990), we have a new production term due to the local turbulent oscillations:

$$\frac{1}{2}\frac{\partial q^2}{\partial t} + \frac{\partial}{\partial z}\overline{\left(w'\left(\frac{p'}{\rho} + \frac{q^2}{2}\right)\right)} = -g\frac{\overline{p'w'}}{\rho} - \varepsilon + \overline{u'w'}\frac{\partial \overline{u'(z)}}{\partial z} \quad \text{(A6.6)}$$

If the flow is steady and the vertical transport (second term of the lhs) is balanced, then we can simplify and balance directly local production of TKE, and different sources of dissipation, so:

$$P = -g\frac{\overline{p'w'}}{\rho} - \varepsilon = \varepsilon_M + \varepsilon_W + \varepsilon_\nu \quad \text{(A6.7)}$$

which may be interpreted in a simple way in diagram A6.1; separating the contributions from internal wave radiation, irreversible local molecular mixing and viscous dissipation producing heat.

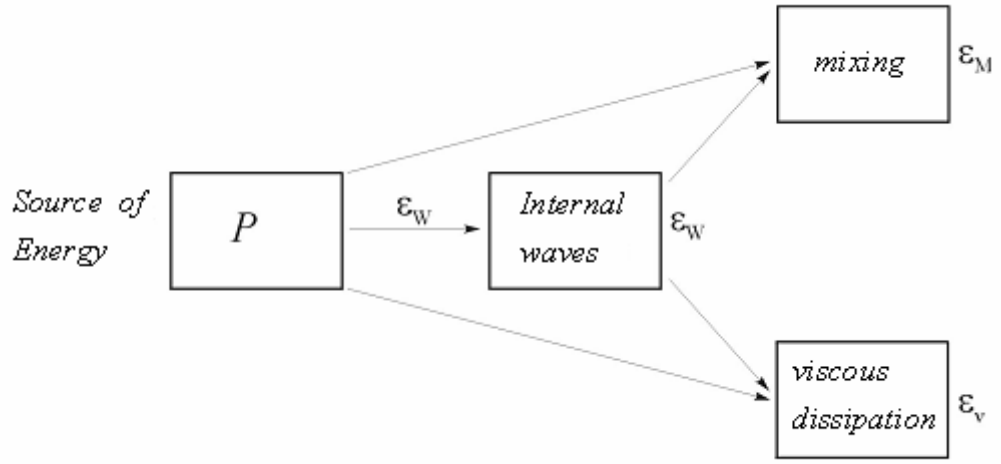

Figure A6.1: Distribution of energy during mixing.

The most variable term will be $\varepsilon_W = f(N)$ as a strong function of the internal wave frequency and its non-linearity, being N the Brunt-Väisällä frequency $N = \left(-\frac{g}{\rho}\frac{\partial \rho}{\partial z} \right)^{1/2}$. This term controls mixing efficiency as a key that regulates the amount of energy available for mixing EAM and the dissipated energy that goes directly into heat. It is important to realize that the different types of dissipation will have different relevant length scales l_i

$$\varepsilon_{M,W,v} = \alpha \frac{u'^3}{l_i} \Rightarrow Actions = u_i l_i \qquad \text{(A6.8)}$$

A6.1. Definition of Mixing Efficiency

From the turbulent kinetic energy equation, comparing buoyancy with the production term

$$\frac{\partial K}{\partial t} = \overline{u' \frac{\partial}{\partial t}\left(\frac{p'}{\rho} + \frac{1}{2} u'u' \right)} + \overline{u'u'} \frac{\partial \bar{u}}{\partial Z} - \frac{g}{\rho} \overline{\rho' \omega'} - \nu \overline{\nabla u' \nabla u'} \qquad \text{(A6.9)}$$

We obtain the Flux Richardson number considered as a local mixing efficiency in stably stratified flows Linden (1979, 1980), in an unstably stratified flow the sign will be negative as described in the review by Fernando (1999)

$$Rf = \frac{g}{\rho} \frac{\overline{\rho' u'}}{\overline{u' \omega'} \frac{\partial \bar{u}}{\partial Z}} \qquad \text{(A6.10)}$$

and the gradient and flux Richardson numbers are related by the ratio of the momentum and scalar turbulent diffusivities, given as a turbulent Prandtl or Schmidt number, Pr_{turb} so that $Rf = \eta = Ri / Pr_{turb}$ is the mixing efficiency, Turner (1973).

The mixing efficiency may also be calculated per unit base area in a practical experimental manner by evaluating the ratio of the gain in potential energy divided by the amount of kinetic energy provided to the fluid during the mixing. It has to be stressed that mixing is a transient process and turbulent structure only occurs between the initial simple structure (two separate fluids) and the final mixed structure (homogeneous, well mixed flow) or linear profile. Most of the interface geometrical descriptors are calculated as averages over the centre region of the interfacial region leaving buffer regions to the sides of the experimental box to avoid lateral influences from the walls. The potential energy at a set time may be evaluated with the following integral (Linden 1979, Redondo 1987):

$$Ep(t) = S \int_0^h g.\rho(z,t).z.dz \qquad \text{(A6.11)}$$

where S the base surface, h is the fluid layer height and $\rho(z,t)$ is the vertical density profile at time t.

Some results of experiments in a top-heavy situation, where the TKE is initially due to the initial potential energy PE, but there is only a maximum available potential energy available for mixing (APE) through a process of conversion first to TKE described fully in Gonzalez-Nieto et al. (2008), Gonzalez-Nieto et al. (2004) and Yague (1992) for convective flows evaluating the overall mixing efficiency calculated from the initial (top heavy) and the final density profiles. The later may be neutral (well mixed), stable with a density step (no mixing) or linearly stratified.

Sometimes instead of using a negative Richardson number, the Atwood number is used. In these experiments a viscous gel was used to modify the available mixing energy AME as a function of a physical parameter, several other geometrical parameters defining the initial conditions, such as the viscoelastic gel viscosity and the separation between the dense layer and the gel were varied. The expression for the mixing efficiency of the top heavy initial profile is based in (Linden & Redondo 1991; Redondo and Linden (1993), Linden, Redondo & Youngs 1994) is both applicable to cases with complete or partial mixing:

$$\eta = 1 - \frac{W_{usefull}}{W_{available}} = 1 - \frac{(\Delta Ep)_{PARTIAL}}{(\Delta Ep)_{NMix}} = 1 - \frac{(\Delta Ep)_{NoMix} + (\Delta W)_{PARTIAL}}{(\Delta Ep)_{NoMix}} = -\frac{(\Delta W)_{PARTIAL}}{(\Delta Ep)_{NoMix}} \quad \text{(A6.12)}$$

where W indicates work, $(\Delta Ep)_{PARTIAL}$ the increase in potential energy for the incomplete mixing situation and $(\Delta Ep)_{NoMix}$ the potential energy change in case of no mixing. After describing some of the situations forced by the viscoelastic layer separating initially the dense and light fluids, the evolution of the density front thickness and the overall mixing efficiencies definitions are discussed.

The mixing efficiency of the overall convective process is particularly simple when the two layers containing the dense and light fluids are of the same height H/2, then if the heavy fluid, initially on top has density $\rho_1 = \rho_2 + \Delta\rho$, with ρ_2 the lighter fluid, there are two limiting cases that will give the maximum and minimum mixing

efficiencies, i.e. when the final profile is constant in height with density $\rho_2 + \Delta\rho/2$, and when there is no molecular mixing and the top and bottom layers just exchange positions.

There are two possible ways to calculate the mixing efficiency assuming that all the kinetic energy used for mixing the flow comes from the available potential energy, so calculating from the integral expression for the potential energy per unit area, the initial potential energy is:

$$Ep(t=0) = \frac{3}{8} g H^2 \Delta\rho \qquad \text{(A6.13)}$$

and the final potential energy if complete mixing has occurred is

$$Ep_{Mix}(t=tf) = \frac{1}{4} g H^2 \Delta\rho \qquad \text{(A6.14)}$$

while if no mixing has taken place, the final potential energy is

$$Ep_{No\,Mix}(t=tf) = \frac{3}{8} g H^2 \Delta\rho \qquad \text{(A6.15)}$$

Similar expressions may be found for other configurations and for unequal depths of the light and heavy fluid. Now there are two different possible definitions of the mixing efficiency:

if the mixing efficiency is defined as

$$\varsigma = \frac{Ep(t) - Ep_{NoMix}}{Ep_{Mix} - Ep_{NoMix}} \qquad \text{(A6.16)}$$

then, the maximum mixing efficiency is ½ as discussed in Linden and Redondo (1991), but if the definition is made considering the actual potential energy used in the process, then the range of mixing efficiency is 0-1 using

$$\eta = \frac{Ep(t) - Ep_{NoMix}}{Ep(to) - Ep(t)} \tag{A6.17}$$

A simple relationship may be found between these two alternative definitions as $\eta = \zeta/2 - \zeta$, and seen in Figure A6.2, with a practical maximum mixing efficiency of 0.33.

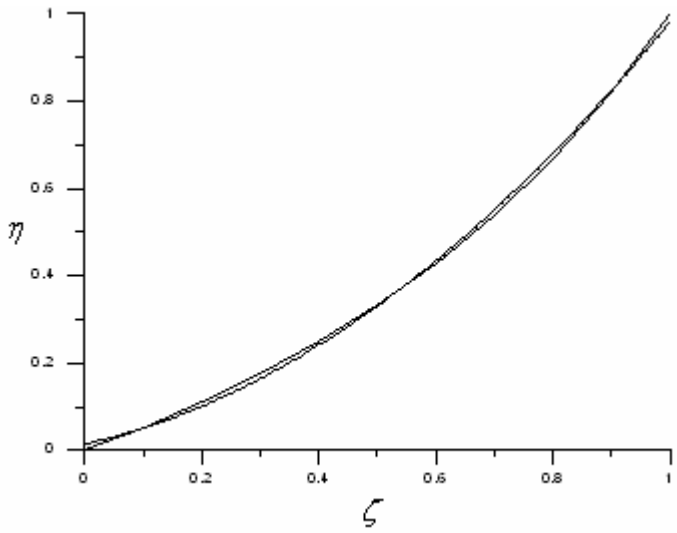

Figure A6.2: Description of the mixing efficiency relationship.

Energetic and thermodynamics of turbulent molecular diffusive mixing can begin to be much more complicated if we include the heat equation and the scalar or solute equation, then it is important to separate the potential energy GPE and internal energy IE) into its available (APE = AGPE+AIE) and non-available (PEr = GPEr + IEr) components, with the IE component being neglected for a Boussinesq fluid, which was the case considered by Winters et al. (1995).

The usefulness of such an decomposition is due to the fact that the background reference state is by construction only affected by adiabatic and/or irreversible

processes, so that understanding how the reference state evolves provides insight into how much mixing takes place in the flow.

In the case of a freely-decaying turbulent Boussinesq stratified fluid with an equation of state linear in temperature, referred to as the Linear-Boussinesq model, Winters et al. (1995) showed that the evolution *n* equations for KE, APE = AGPE, and GPE take a more complicated form (Tailleux 2009) so that:

$$\begin{aligned} d(KE)/dt &= C(KE;APE).D(KE) \\ d(APE)/dt &= C(KE;APE).D(APE) \\ d(GPEr)/dt &= Wr_{mixing} = Wr_{turbulent} + Wr_{laminar} \end{aligned} \qquad \text{(A6.18)}$$

where C(APE;KE) is the so-called *buoyancy flux* measuring the reversible conversion between KE and APE, D(APE) is the diffusive dissipation of APE, which is related to the dissipation of temperature variance, e.g. Holloway (1986); Zilitinkevich et al. (2008), while Wr_{mixing} is the rate of change in GPEr induced by molecular diffusion, which is commonly decomposed into a laminar $Wr_{laminar}$ and turbulent $Wr_{turbulent}$ contribution. All these terms are explicitly defined in Tailleux 2009.

For the Linear-Boussinesq model, as well for a Boussinesq fluid whose thermal expansion increases with temperature, called the NL-Boussinesq model. It is possible to further generalize the corresponding expressions for the fully compressible Navier-Stokes equations with an arbitrary nonlinear equation of state.

Of particular interest in turbulent mixing studies is the behavior of $Wr_{turbulent}$ the turbulent rate of increase in GPEr which so far has been mostly discussed in the context of the Linear-Boussinesq model, for which an important result is: $Wr_{;turbulent}$ = D(APE) which states the equality between the APE dissipation rate and Wr; turbulent. This result is important, because from the known properties of D(APE), it makes it clear that enhanced diapycnal mixing rates fundamentally require:

A) finite values of APE, since D(APE) = 0 when APE = 0;

B) an APE cascade transferring the spectral energy of the temperature (density) field to the small scales at which molecular diffusion is the most efficient at smoothing out temperature gradients. The discussion of the APE cascade, which is closely related to that of the temperature variance, has an extensive literature related to explaining the k^{-3} spectra in the so-called buoyancy subrange, both in the atmosphere, e.g. Lindborg (2006) and in the oceans, e.g. Holloway (1986); Bouruet- Aubertot et al. (1996). Note

that because APE is a globally defined scalar quantity, evaluation of APE cascades requires the introduction of the so-called APE density, for which a spectral description is possible, e.g. Holliday & McIntyre (1981); Roullet & Klein (2009); Molemaker & McWilliams (2009).

This model exhibits only one type of reversible conversion, namely the buoyancy flux associated with the APE=KE conversion, and three irreversible conversions, viz., D(KE), D(APE), and $Wr_{;mixing}$, the first one caused by molecular viscous processes, and the latter two caused by molecular diffusive processes. A primary goal of turbulence theory is to understand how the reversible C(APE;KE) conversion and irreversible D(KE), D(APE), Wr_{mixing} are all inter-related. Turbulent diffusive mixing, for the understanding of viscous dissipation constitutes somehow a separate issue with its own problems, e.g. Gregg (1987). The nature of these links is usually explored by estimating the energy budget of a turbulent mixing event, defined as a sudden period of intense mixing preceded and followed by laminar conditions, for which there is a vast literature of observational, theoretical, and numerical studies.

Integrating the above energy equations over the duration of the turbulent mixing events thus yields:

$$\begin{aligned} KE &= C(KE;APE).D(KE) \\ APE &= C(KE;APE).D(APE) \\ GPEr &= Wr_{mixing} = Wr_{turbulent} + Wr_{laminar} \end{aligned} \qquad \text{(A6.19)}$$

where S and the overbar denote respectively the net variation and the time-integral of a quantity over the mixing event. Summing the KE and APE equation yields the important available mechanical energy equation:

$$KE + APE = \left[D(KE) + D(APE)\right] < 0 \qquad \text{(A6.20)}$$

which states that the total available mechanical energy ME = KE+APE undergoes a net decrease over the mixing event as the result of the viscous and diffusive dissipation of KE and APE respectively. A schematic of the APE dissipation process, which provides a diffusive route to KE dissipation, is illustrated in figure A6.3.

For mixing efficiency in turbulent stratified fluids it is clear that turbulent diapycnal mixing (through D(APE)) participates in the total dissipation of available

mechanical energy ME = KE+APE. Since D(APE) is non-zero only if APE is non-zero, turbulent diapycnal mixing therefore requires having as much of ME in the form of APE as possible. The classical concept of \mixing efficiency, reviewed above, seeks to provide a number quantifying the ability of a particular turbulent mixing event in dissipating ME = KE +APE preferentially diffusively rather than viscously. From a theoretical viewpoint, it is useful to separate turbulent mixing events into two main archetypal categories, corresponding to the two cases where ME is initially entirely either in KE or APE form. These two cases are treated separately, before providing a synthesis addressing the general case.

At a fundamental level, quantifying the mixing efficiency of a turbulent mixing event requires two numbers, one to measure how much of ME is viscously dissipated, the other to measure how much of ME is dissipated by turbulent mixing. While everybody seems to agree that D(KE) is the natural measure of viscous dissipation, it is the buoyancy flux C(APE;KE), rather than D(APE), that has been historically thought to be the relevant measure of how much of ME is dissipated by turbulent mixing, since it is the term in Eq. (A6.1) that seems to be removing KE along with viscous dissipation. For mechanically-driven turbulent mixing events, it is easy to see that APE = 0 and ME = KE, the efficiency of mixing has been classically quantified by means of two important numbers. The first one is the so-called flux Richardson number Rf, by Linden (1979) defined above as the fraction of the change in available kinetic energy which appears as the potential energy of the stratification as defined above.

Energetic and thermodynamics of turbulent molecular diffusive mixing e.g., Osborn (1980), and the second one is the so-called mixing parameter as:

$$\gamma = \frac{Buoyancy}{dissipation} = \frac{gw'\rho'/\rho}{\varepsilon} \qquad \text{(A6.21)}$$

It is now recognized, however, that the buoyancy flux represents only an indirect measure of irreversible mixing, since it physically represents a reversible conversion between KE and APE, while furthermore appearing to be difficult to interpret empirically, e.g. see Barry & al. (2001) and references therein. Recognizing this difficulty, Caulfield and Peltier (2000) and Staquet (2000) suggested to replace C(KE;APE) by a more direct measure of irreversible mixing in the above definitions of Rf and mixing. Since turbulent diapycnal mixing is often diagnosed empirically from

measuring the net changes in GPEr over a mixing event, e.g. McEwan (1983a,b); Barry et al. (2001); Dalziel and al (2008), a natural choice is to use $Wr_{turbulent}$ as a direct measure of irreversible mixing, which leads to theoretical new possible definitions justified from the fact that in the Linear-Boussinesq model, the following equality holds:

$$C(APE;KE) = D(APE) = Wr_{turbulent} \tag{A2.22}$$

when APE = 0 and only mechanical mixing is initially available.

When buoyancy is the source of mixing, the modified flux Richardson number RGPEr used by Tailleaux 2009 may also be used as discussed above. Rayleigh-Taylor instability has the peculiar property that GPEr; max, the maximum possible increase in GPEr achieved for the fully homogenized state, is only half the initial amount of APE, e.g. Linden and Redondo (1991); Dalziel et al (2008) (at least when Rf = 1, i.e., in the context of the L-Boussinesq model).

Physically, it means that less than 50 % of the initial APE can actually contribute to turbulent diapycnal mixing, and hence that at least 50 % of it must be eventually viscously dissipated.

Experimentally, Linden and Redondo (1991) reported values of Rf=0.3-0.4, while Dalziel et al (2008) reported experiments in which the maximum possible value Rf = 0.5 was reached. Owing to the peculiarity of the Rayleigh-Taylor instability, however, one should refrain from concluding that mixing is perfect or that in general Rf = 0.5 represent the maximum possible values for mixing and Rf in turbulent stratified fluids. To reach a general conclusions about mixing and Rf, more general examples of buoyancy-driven turbulent mixing events should be studied. It would be of interest, for instance, to study the mixing efficiency of a modified Rayleigh-Taylor instability such that the unstable stratification occupies only half or less of the spatial domain, as in Gonzalez-Nieto et al. (2008) so that GPEr;max > APEj. In this case, all of the initial APE could in principle be dissipated by molecular diffusion, which would correspond to the limits Rf = 1 and mixing = +1. Of course, such limits cannot be reached, as it is impossible to prevent part of the APE to be converted into KE, part of which will necessarily be dissipated viscously, but they are nevertheless important in suggesting

that values of mixing > 1 can in principle be reached, which sets an interesting goal for future research, specially the roles of waves on mixing efficiency.

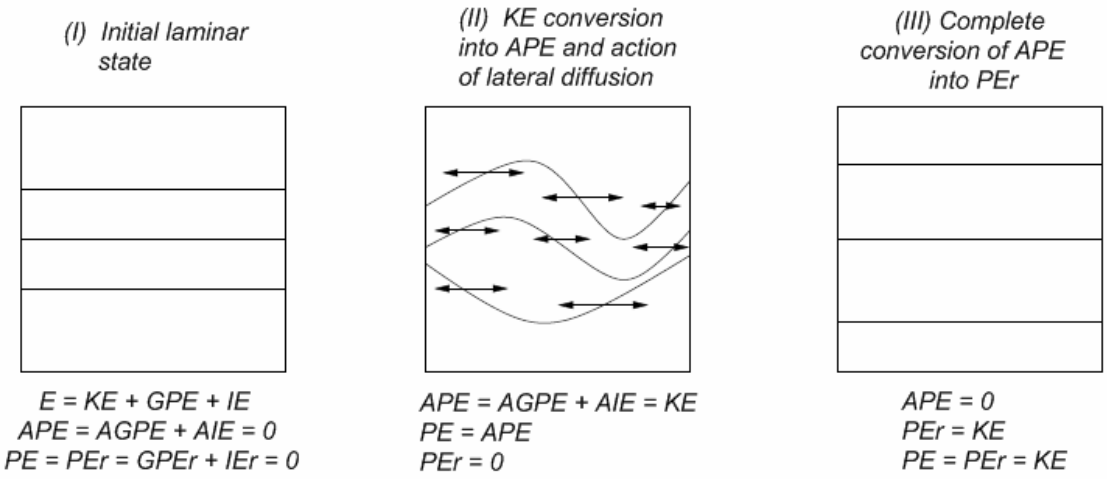

Figure A6.3: Idealized depiction of the diffusive route for kinetic energy dissipation. (I) represents the laminar state possessing initially no AGPE and AIE, but some amount of KE. (II) represents the state obtained by the reversible adiabatic conversion of some kinetic energy into APE, which increases APE but leaves the background GPEr and IEr unchanged; (III) represents the state obtained by letting the horizontal part of molecular diffusion smooth out the isothermal surfaces until all the APE in (II) has been converted into background PEr = GPEr + IEr. be fundamentally correlated because they are both controlled by molecular diffusion (Tailleux 2009).

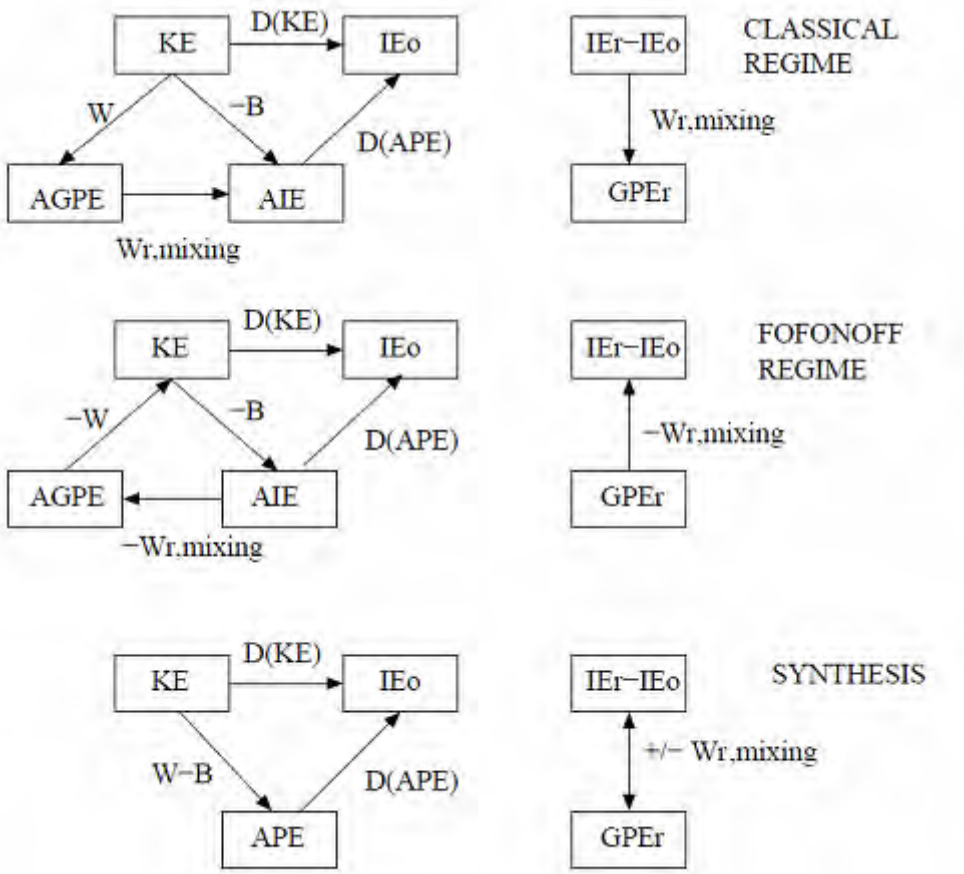

Figure A6.4: The energetics of freely decaying turbulence for the classical regime (top panel), the Fofonoff regime (middle) panel, and a synthesis of both regimes obtained by subsuming AGPE and AIE into APE alone (Tailleux 2009).

Figures A6.4 to A6.6 present different possible mixing routes proposed by Tailleux (2009) in the different mixing situations.

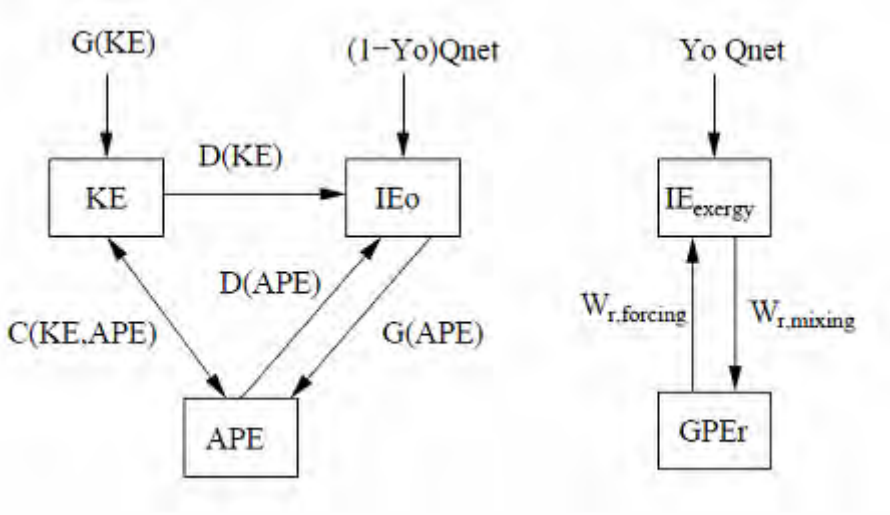

Figure A6.5: Energy flowchart for a mechanically - and buoyancy – driven thermally-stratified fluid, where $Q_{net} = Q_{heating} - Q_{cooling}$. At leading order, the "dynamics" (the IE_{exergy} / GPE_r system). The dynamics/thermodynamic coupling occurs through the correlation between $D(APE)$ and $W_{r,mixing}$, as well as through the correlation between $G(APE)$ and $W_{r,forcing}$ (Tailleux 2009).

Turbulent flow consists of a superposition of eddies of every size. The rate at which the turbulent kinetic energy is transfer from bigger eddies to smaller eddies is called the dissipation ε. The energy cascade, however, can not be extended infinitely because of the viscous forces. The smaller an eddy, the greater the velocity gradient inside the eddy and the greater the viscous stress that counteracts the eddying motion. Consequently, there is a statistical lower limit of smallest eddy size that corresponds to a minimum scale of turbulence and maximum frequency in the turbulent motion. At this limit this kinetic energy of the major part of the turbulent kinetic energy is contained in the large but not the largest eddies. The large eddies are, therefore, often called energy containing eddies. The length and time scale of those eddies are further important scales. The size of energy containing eddies depends on the geometry of a spatial domain and on the local intensity of turbulence. This size can be related (it is not exactly the same) to the integral turbulent length scale that can be determined from the two-point spatial correlation functionfor statistical steady (time independent)

turbulence. Here, *Lij* denotes the length scale tensor. For homogenous isotropic turbulence the integral length scale is independent of the direction.

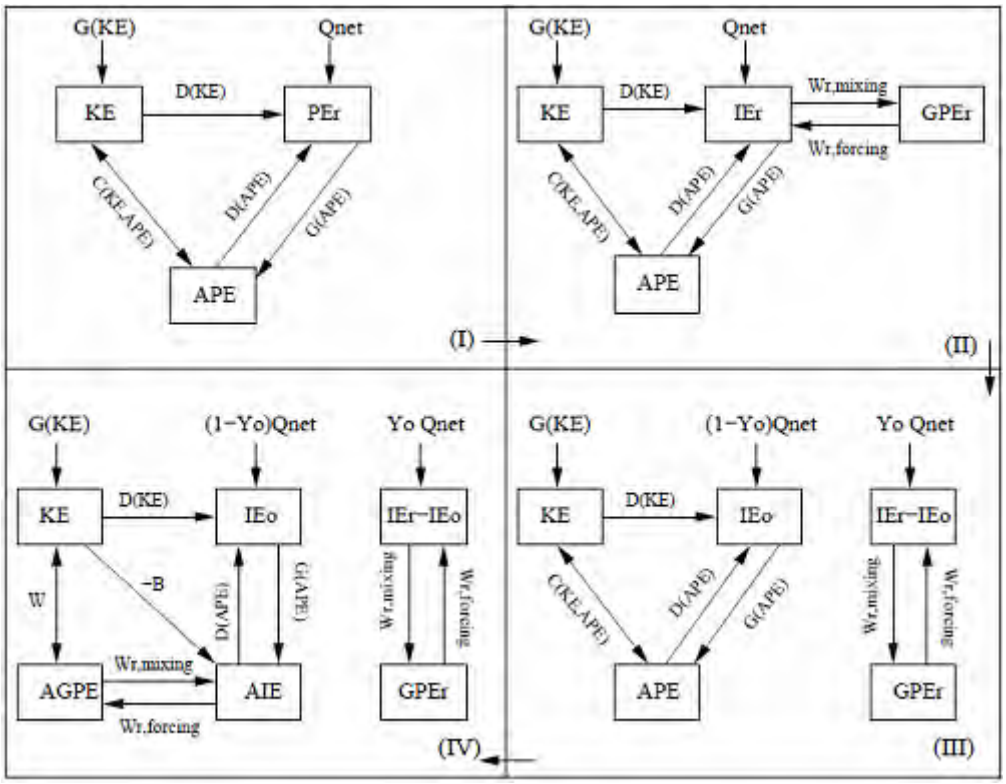

Figure A6.6: Successive refinements of the energetics of a forced/dissipated stratified fluid. Panel (I): $KE / APE / PE_r$ representation. Panel (II): Decomposition of PE_r into $IE_r + GPE_r$. Panel (III): Decomposition of IE_r into a dead part IE_0 and exergy part $IE_{exergy} = IE_r - IE_0$. Panel (IV): Decomposition of APE into AIE and $AGPE$, revealing the link between $C(KE, APE)$ to the density flux W and work of expansion/contraction B (Tailleux 2009).

This two-point velocity correlation function for homogenous isotropic turbulence and the corresponding integral turbulent length scale are schematically shown in Figure A6.7. Two-point velocity correlation functions versus the distance between two points Δx for homogenous isotropic turbulence. *Lij* is a measure for the correlation of velocity fluctuation at the point x and $x + \Delta x$, thereby indicating to which degree the turbulent proportion of two points with distance Δx influence each other. *lI* is located where the

shaded areas above and below the two-point velocity correlation are of equal size. Hence the integral length scale *l* can be interpreted as the length scale from which point on the velocity fluctuation are predominantly uncorrelated. The corresponding time scale can be determined from the known time correlation function Qualitatively the integral turbulent time scale can be interpreted as an averaged inverse rotational frequency of the typical big eddy appearing in the spatial location *x*.

Though turbulence in practical flows is neither isotropic nor homogenous, the idealized integral length scale provides at least coarse quantitative information about spatial correlation and sizes of typical energy containing eddies in turbulent flows. Quantitatively the integral turbulent length scale can be interpreted as an averaged radius of typical big eddy appearing in the spatial location.

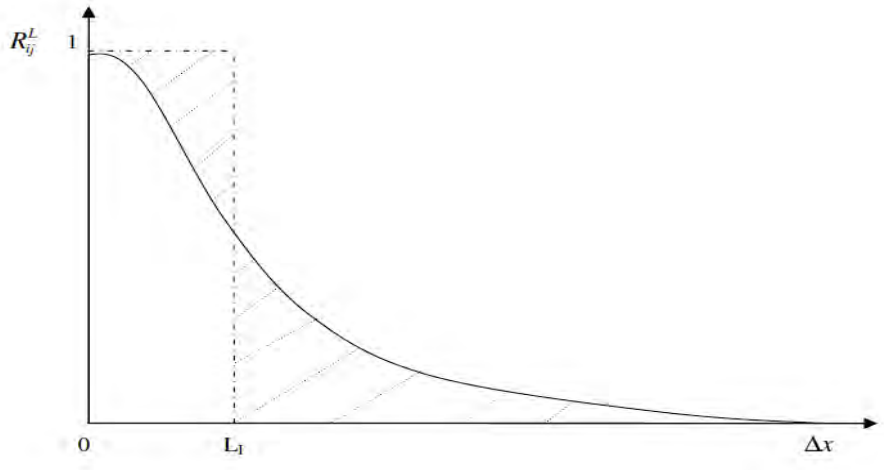

Figure A6.7: Definition sketch of the integral scale

Other widely used length scales are Taylor microscale defined in chapter 2 which can be determined by autocorrelation functions near the origin. In terms of the longitudinal autocorrelation function *Rf(r,t)* and the transversal autocorrelation function two corresponding quantities can be defined at the Taylor microscale level as the longitudinal Taylor microscale and the transversal Taylor microscale. A Taylor-time microscale can also be defined analogously.

The turbulent kinetic energy spectrum obtained from the Fourier transfer of the spatial isotropic two-point correlation *Lij R* function is schematically plotted in Figure A6.8 the ordinate indicates kinetic energy density per wave number *k* or the inverse turbulent length scale. The maximal value of log E(k) corresponds to the energy containing scale that related to the turbulent integral length scale *l=LI*. The eddies of

size smaller than the energy containing eddied build the inertial sub-range, where Taylor microscale is located between *LI* and *LK*, according to $LT = \mathrm{Re}\, LK$. As it was shown by (Kolmogorov 1941), the energy transfer from the large to small scale within the inertial subrange is independent on the scale size

A6.2. Scales of Turbulent Mixing

In many physical situations one encounters a scalar φ advected by turbulent flow fields like temperature and pollutants in air and water. Similar to the velocity field, there is a statistical lower limit of smallest scale of turbulent mixing and maximum frequency in mixing processes. Such smallest scale is called Batchelor scale $B\,L\varphi$ and defined in terms of the Kolmogorov scale and Schmidt number, *Sc*, Like the Kolmogorov scale in a turbulent flow, the Bachelor scale characterizes the smallest scalar eddies wherein molecular diffusion is balanced by turbulent mixing. For most gases, the Schmidt is number is approximately one, so the smallest scalar lengths are approximately equal to Kolmogorov scale. For liquids, *Sc* can be on the order of 10^3 or greater, so that the scalar field contains much more fine-structures than the velocity field. The scales at which diffusion is occurring are much smaller. Then computational requirements to numerically solve these scales and thus accurately describe the mixing process are correspondingly increased. For scalar eddies much larger than the Batchelor scalar, molecular diffusion is negligible. Thus, initially premixed scale fields will remain segregated at scales larger than the Batchelor scale.

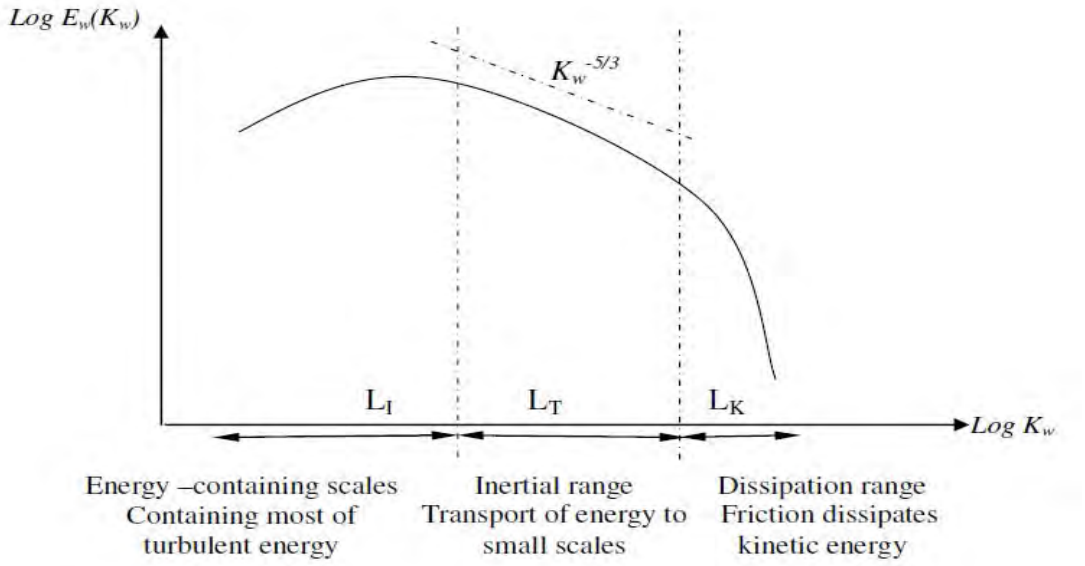

Figure A6.8: Schematic turbulent kinetic energy spectrum.

This has important consequences for turbulent reaction flows because it implies that the chemical source term will be strongly coupled to turbulent mixing for many chemical reactions of practical importance. At high Reynolds numbers, the small scales

of scalar field are usually assumed to be nearly isotropic (Kang & Meneveau 2001 showed that scalar fields at small level are not so isotropic as assumed.) and will evolve on a time scale that is much smaller than that of the large scales. Moreover, for a passive scalar, the characteristic time scales for mixing at length scales above the Batchelor scale will be determined solely by turbulent flow. The largest structures in the scalar field is also named as scalar integral scale, and is primarily determined by two processes: (1) initial condition of the scalar field can be initialized with a characteristic $I_{L\varphi}$ that is completely independent of turbulence field, and (2) turbulent mixing where the energy containing range of a turbulent flow will create "scalar eddies" with characteristic integral scales calculated for a scalar φ in the same way as for the velocity spatial correlation function and then integrating. The scalar spatial correlation function provides the length scale information about the underlying scalar field. For homogenous scalar fields, the scalar spectrum is related to the scalar spatial correlation function also through the Fourier transform. Figure A6.9 is an example of scalar energy spectrum for a range of Schmidt numbers plotted for *Re=500* [84]. The schematic velocity spectrum is included in the figure for comparison. Analogous to the velocity field, the scalar mixing in inertial convective sub-range can be interpreted as a cascade process. The inertial sub-range exhibits the same profile (~5/3) similar to velocity field for moderate Schmidt numbers. For low Schmidt number, the scale spectrum falls off much faster than the velocity spectrum. For high Schmidt number, viscous convective/diffusive sub-range (Batchelor spectrum) with (~1) scaling is evident

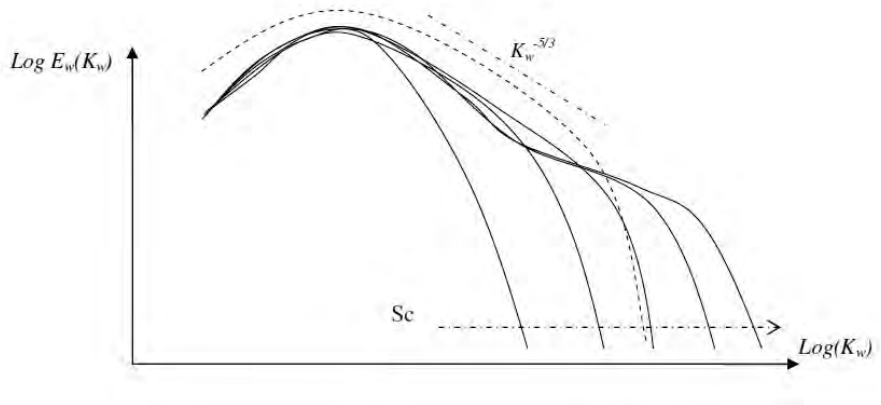

Figure A6.9. Different power spectra as a function of the Schmidt number.